Design, Channel Modeling and Simulation of LED-Based Short-Range Underwater Optical Communication Systems

Dissertation

zur Erlangung des akademischen Grades eines Doktors der Ingenieurswissenschaften (Dr.-Ing.) der Technischen Fakultät der Christian-Albrechts-Universität zu Kiel

vorgelegt von:

Jan Sticklus

aus

Esbjerg

Kiel, 2023

Tag der Einreichung: 20.07. 2023

Tag der Disputation: 18.12. 2023

Berichterstatter: Prof. Dr.-Ing. Peter A. Höher
Prof. Dr.-Ing. Kevin Köser

Preface

I still remember the first time I met Prof. Dr.-Ing. Peter A. Höher, at an autonomous underwater vehicle test in the naval base of Eckernförde. To this time I have been working for more than two decades for the GEOMAR Helmholtz Center for Ocean Research Kiel as an engineer in laboratories and in the AUV-Team on worldwide operations at sea, and I was still looking for new challenges...

My fields of interest, the underwater LED illumination, light measurement and pressure-neutral technology matched to the research topic of underwater optical communication of the Information and Coding Theory Group of the Faculty of Engineering of the Christian-Albrechts-University of Kiel. Prof. Höher gave me the opportunity to work as an external doctorate student in his group. Throughout this time, he offered guidance, support and encouragement. He enabled constructive discussions and provided valuable suggestions, but also admitted independent work. In all these years I have learned an incredible amount and also discovered my own limit.

For all this, I would like to express my deepest gratefulness to my supervisor.

My very special thank belongs to Dr. Jo-Anne Wartho and Prof. Dr. Colin Devey from the GEOMAR Magmatic and Hydrothermal Systems group, for their kindness and tolerance towards me and my research activities side by side with the geochronology-laboratory work. My sincere thank goes to my supporter from the very first hour Dr. Tom Kwasnitschka.

I am very grateful for the material provisioning by the Robex-project and the GEOMAR technology-transfer, without this work could not have been conducted.

Furthermore, I would also like to thank the GEOMAR Oceanic Vision Group, as well as Dr. Martin Hieronymi and Dr. Rüdiger Röttgers from the Optical Oceanography group of the Helmholtz-Zentrum Hereon, and of course the ICT group of the Faculty of Engineering for fruitful discussions and support. Additionally I thank Prof. Dr. Kevin Köser, Prof. Dr. Michael Höft and Prof. Dr. Stephan Pachnicke for their willingness to serve the board of examiners.

Finally, I thank my wife Svenja and my daughters Liv and Mie for their endless patience over all the years.

Eckernförde, July 2023

Jan Sticklus

Abstract

The number and complexity of subsea applications is constantly increasing, as are the demands on data traffic. Fast underwater optical wireless communication (UOWC) represents a solution for shorter distances. This thesis focuses on the adaption of this technology to the challenging conditions in the channel.

Oceanic water features a narrow spectral window of least attenuation in the blue regime, which changes to green for coastal waters. In conjunction with the spectral properties of the LEDs emission and the detectors responsivity, this results in a threefold relationship. In order to enable an energy-efficient system design in coastal waters and to bypass the green-gap in LEDs, the use of converted-green LEDs is proposed and investigated. Since the majority of deployments will not take place in the deep dark ocean, natural ambient light will be present in varying forms and strengths. The effect and the constraints of optical filtering to suppress this disturbance is examined, a model is developed, and simulations for optimization are carried out. Well selected thin film filters represent an effective solution. Since the signal-to-noise ratio is very important for subsequent signal processing in an UOWC system, in-depth noise analyses are performed, comprising different detector types and various operating conditions. The applicability is compared and presented in detail. LEDs can be used as photodetectors, and this is examined for single-color power LEDs in terms of a potential dual-use in UOWC. The properties are thoroughly investigated in the spectral, temporal and spatial domains. An unexpected high responsivity and a distinct bandpass characteristic is discovered, and a potential for low-cost applications is clearly identified. Housings and ports are inevitable for optical underwater devices, but pressure-neutral embedding can be an alternative. A comprehensive survey of these technologies is given and the optical path is analyzed. The total characteristics of assemblies in various configurations are determined by underwater goniometric measurements and compared to calculations. Design considerations are extracted and the implementation of multiple segmented transducers is discussed. The exact prediction of the link budget relies on individual system attenuation coefficients k_{sys}, but these exhibit many dependencies. In order to generate first spectral curve sets of these coefficients for different water types, extensive Monte Carlo simulations of the underwater light field are conducted. Impact factors are identified and systematically examined. The magnitude of the occurring temporal dispersion is determined for realistic worst-case scenarios. Additionally, a method for experimental determination of k_{sys} is developed and field tests are conducted. This work provides concepts and answers to essential questions in the optical and electrical domains of UOWC for developers and users.

Keywords: Underwater optical communication, thin film filter, converted green LED, spectral adaption, noise analysis, dome port, pressure-neutral potting, Monte Carlo simulation.

Kurzfassung

Die Anzahl und Komplexität von Unterwasseranwendungen nimmt ständig zu, ebenso wie die Anforderungen an den Datenverkehr. Schnelle optische drahtlose Unterwasserkommunikation (UOWC) stellt eine Lösung für kürzere Distanzen dar. Diese Arbeit befasst sich mit der Anpassung dieser Technologie an die herausfordernden Bedingungen in diesem Kanal.

Ozeanisches Wasser weist ein schmales spektrales Fenster mit der geringsten Dämpfung im blauen Bereich auf, das bei Küstengewässern in den grünen Bereich übergeht. In Verbindung mit den spektralen Eigenschaften der LED-Emissionen und der Empfindlichkeit des Detektors ergibt sich eine dreifache Abhängigkeit. Um ein energieeffizientes Systemdesign auch in küstennahen Gewässern zu ermöglichen, und die grüne Effizienzsenke von LEDs zu umgehen, wird die Verwendung von konvertiert-grünen LEDs vorgeschlagen und untersucht. Da die meisten Einsätze nicht in der dunklen Tiefsee stattfinden werden, bleibt das natürliche Umgebungslicht in unterschiedlicher Form und Intensität existent. Die Wirkung und die Grenzen optischer Filter zur Unterdrückung dieser Störung werden untersucht, ein Modell entwickelt und Simulationen zur Optimierung durchgeführt. Gut angepasste Interferenzfilter können eine effektive Lösung darstellen. Da das Signal-Rausch-Verhältnis für die nachfolgende Signalverarbeitung in einem UOWC-System sehr wichtig ist, wurde eine eingehende Rauschanalyse durchgeführt, die verschiedene Detektortypen und unterschiedlichste Betriebsbedingungen umfasst. Die Anwendbarkeit wird verglichen und im Detail vorgestellt. LEDs können auch als Photodetektoren eingesetzt werden, dieses wird für einfarbige Hochleistungs-LEDs im Hinblick auf eine mögliche Doppelnutzung in der UOWC untersucht. Es findet eine eingehende Analyse der Eigenschaften im spektralen, zeitlichen und räumlichen Bereich statt. Eine unerwartet hohe Ansprechempfindlichkeit und eine ausgeprägte Bandpass-Charakteristik wird nachgewiesen, ein Potenzial für kostengünstige Anwendungen ist deutlich erkennbar. Gehäuse und Fenster sind für optische Unterwasser-Instrumente unumgänglich, ein druckneutraler Verguss kann dazu eine Alternative darstellen. Es wird ein umfassender Überblick über diese Technologien gegeben und der optische Pfad analysiert. Die Gesamtcharakteristik von Baugruppen in verschiedenen Konfigurationen wird durch goniometrische Unterwassermessungen ermittelt und mit Berechnungen verglichen. Überlegungen zum Design werden extrahiert und die Implementierung von mehrfach segmentierten Sende- und Empfangseinheiten wird diskutiert. Die genaue Vorhersage des Budgets einer Verbindung hängt von den individuellen Systemdämpfungskoeffizienten k_{sys} ab, welche jedoch viele Abhängigkeiten aufweisen. Um erstmals spektrale Kurvensätze dieser Koeffizienten für verschiedene Wassertypen zu erzeugen, werden umfangreiche Monte Carlo-Simulationen des Unterwasser-Lichtfeldes durchgeführt. Die Einflussfaktoren werden ermittelt und systematisch untersucht. Das Ausmaß der auftretenden zeitlichen Streuung wird für die ungünstigsten Fälle realistischer Szenarien bestimmt. Zusätzlich wird eine Methode zur experimentellen Bestimmung von k_{sys} entwickelt und entsprechende Feldversuche werden durchgeführt. Diese Arbeit liefert Entwicklern und Anwendern Konzepte und Antworten auf wesentliche Fragen im optischen und elektrischen Bereich der UOWC.

Stichwörter: Optische Unterwasserkommunikation, Interferenzfilter, konvergiert grüne LED, spektrale Anpassung, Rauschanalyse, Kuppelport, druckneutraler Verguss, Monte Carlo Simulation.

Contents

Chapter 1

Introduction

1.1 Background

The oceans are one of the most elementary and important parts for life on Earth and for human existence. More than two-thirds of our planet is covered by water, and the oceans contain over 97 % of the planet's water. All depth zones of the oceans have their respective influence on the ecosystems of Earth. The harsh environmental conditions and the average depth of the oceans of almost 3700 meters make it unsurprising that the sea is largely unexplored [1].

The motivation of research, industry and military to explore and use the space underwater may vary, but they have an increasing demand for communication in common, as advanced physical sensors, high quality imaging and sophisticated navigation require moderate to high bandwidth for real-time operation as well as for the transfer of large amounts of collected data in short time. For fixed structures and nodes, cables and fibers can fulfill this task, but utilization can be difficult. For mobile underwater applications like vehicular use, wireless communication is indispensable. Figure 1.1 shows potential fields of applications for the use of underwater optical wireless communication (UOWC).

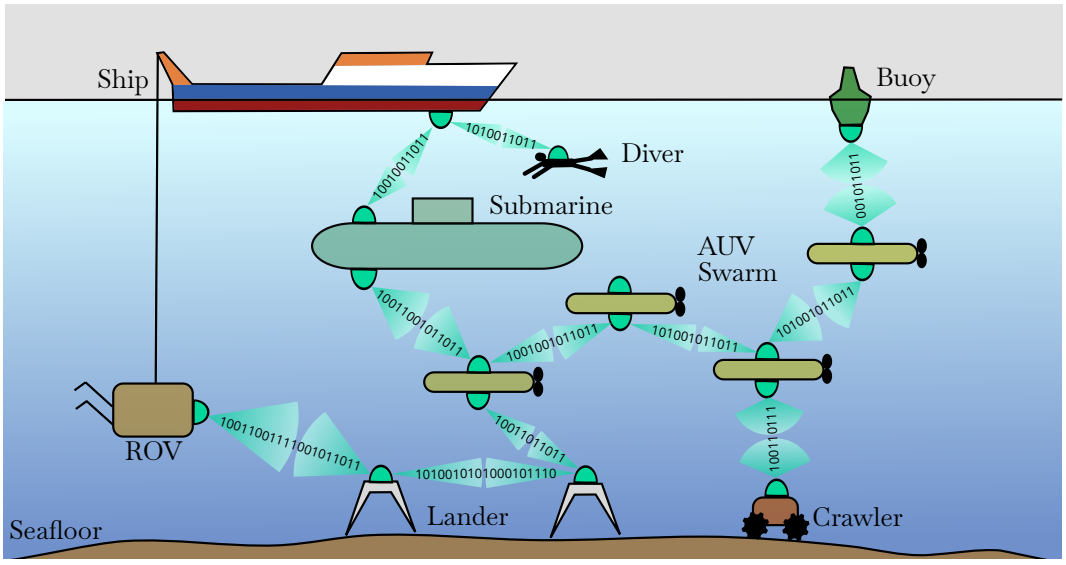

Figure 1.1: Typical scenarios for possible UOWC usage, including remotely operated vehicles (ROVs) and autonomous underwater vehicles (AUVs).

Common nowadays and widely used is acoustic technology, with typical applied frequencies up to tens of kHz and achievable ranges of kilometers, but with the drawback of a generally low bandwidth and an attenuation increasing with frequency. Nevertheless the acoustic underwater channel has the widest operational range. For further information the interested reader may refer to [2, 3].

Electromagnetic waves (EM) are applicable for wireless underwater communication. The radio frequencies (RF) are in the range of extremely low frequencies (ELF) to medium frequencies (MF),

corresponding to signals from 3 Hz to 3 MHz. Moderate data rates can only be achieved at very short distances, as longer ranges suffer from a strong attenuation in saltwater. Furthermore, large antennas are required and only very low data rates are provided. More detailed information can be found in [4, 5]. A promising alternative is the realisation through magnetic induction (MI). This technology has recently drawn attention due to its advantages of low latency, low energy consumption and predictable links. Detailed information are given in [6, 7, 8, 9, 10, 11, 12]. In the past two decades the interest and research in UOWC as a special case of free space optics (FSO) communication has increased significantly. Optical waves in the blue to green color regime are preferably used, since seawater typically shows a relative minimum of attenuation in this range. Frequently employed transmitting light sources are light emitting diodes (LEDs), lasers and laser diodes (LDs), and their common feature is short switching times. Since several fast detector types are also available, a combined application promises high bandwidths underwater. Seawater is an element with highly variable properties, varying from clear ocean to murky harbor water. Depending on the type of seawater and its absorption and scattering properties, communication ranges from a couple of meters up to a few hundred meters in maximum are possible. Figure 1.2 gives a general overview of the acoustic, MI, RF and optical wireless technologies capabilities. Comprehensive and comparative overviews are presented in [13, 14, 15, 16, 17].

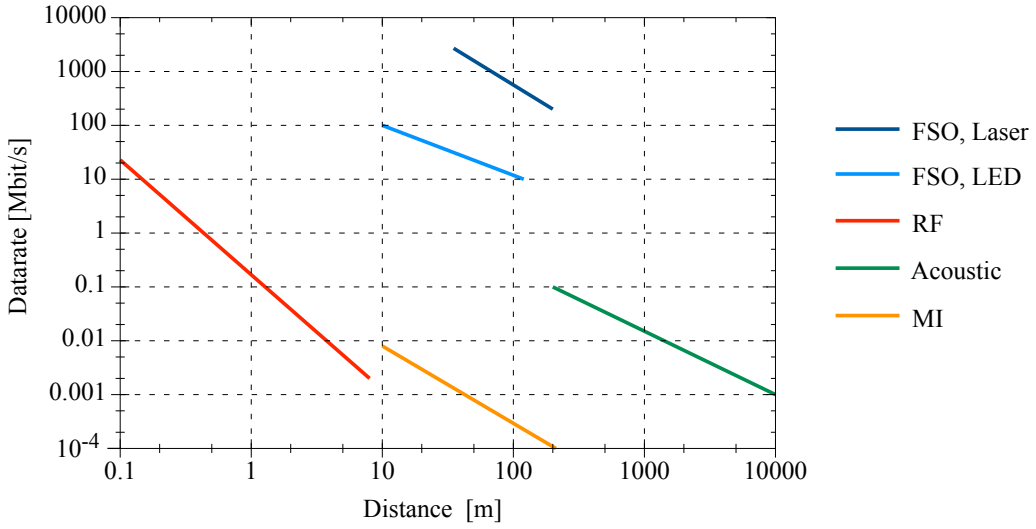

Figure 1.2: Rough estimate of the achievable performance from the main technologies for underwater wireless communications in seawater, adopted from [18, 19]. A more detailed version is depicted in [20].

1.2 State of the Art

Especially in the last decade, an increase in research in the field of UOWC can be recognized. Many studies, beside simulations also include laboratory experiments, tank or basin tests and field tests of prototypes. Parameters like data rates, bit error rates (BER) and ranges are stated. Care should be taken when interpreting these data, because of a lack in comparability since physical system specifications and environmental parameters are not completely reported [21]. An overview about performance values of specific UOWC systems can be found in [13, 22]. Even if many studies are using lasers or laser diodes as sources, pointing and tracking is still a problem, and thus impedes vehicular use and most applications at present [23, 24]. Driven by the rapid development of LEDs, these light sources are becoming a key technology in lighting, imaging and communications.

Recent advances and remaining challenges of the UOWC technology include:

- Sensor networks, node networks.
- Swarm intelligence.
- Energy harvesting.
- Simultaneous information and power transfer.
- Adaptable systems to environmental conditions.
- Efficient transmission techniques.
- Mitigating link misalignment.
- Disruption tolerance.
- Minimal packaging.
- Low costs.
- Hybrid communication systems (RF, MI, and acoustic).

These topics are extracted from [25, 26, 27, 28], and more details can also be found here. Worth mentioning in this context are multi-hop relaying technology [29] and smart transmitters [30]. Another aspect of the state of the art can be market investigation. The outcome of the analysis about which systems are commercially available is given in Tables 1.1 and 1.2.

Table 1.1: Overview of UOWC systems on the market in early 2021, with electrical and performance properties.

Manufacturer Type	Tx Color	Rx Type	Data rate, Range	Port type	Power
Aquamodem OP	LED, cyan	n/a	10 kbit/s, 1 m	serial	n/a
Hydromea 100	LED, blue	n/a	115 kbit/s, 2 m	serial	5 W
Hydromea 250LP	LED, blue	n/a	250 kbit/s, 7 m	serial	5 W
Hydromea 5000ER	LED, blue	n/a	500 kbit/s, 50 m	serial	5 W
Hydromea LumaX	LED, blue	n/a	10 Mbit/s, 50 m	serial, Ethernet	5 W
Marinelink WOCS 40220	LED, blue	APD	25 Mbit/s, 10 m	Ethernet	50 W
Sonardyne Bluecomm 100	LED, blue	PIN PD	5 Mbit/s, 15 m	Ethernet	30 W
Sonardyne Bluecomm 200	LED, blue	PMT	10 Mbit/s, 150 m	Ethernet	25 W
Sonardyne Bluecomm 200UV	LED, UVA	PMT	10 Mbit/s, 75 m	Ethernet	40 W

It compares some basic data of the few manufacturers products in terms of type of source and detector, optical and electrical ports, performance, housing technology and offered variations. The prices claimed for the available UOWC sets are in the small to medium five figure amount (in Euros). Despite more than 20 years of research activity on the UOWC topic, the small range of products on the market reflects the technical challenges. It is remarkable that there is currently no laser-based UOWC version on the open market, but the situation may be different in the military

Table 1.2: Overview of UOWC systems on the market in early 2021, with optical and mechanical properties.

Manufacturer Type	Optical Port, Beam angle	Housing type, Depth rating	Housing size
Aquamodem OP	flat, 17°	PH, 3000 m	29 cm x 7 cm diam.
Hydromea 100	cast, 120°	PN, 6000 m	10 cm x 5 cm x 3 cm
Hydromea 250LP	cast, 120°	PN, 6000 m	10 cm x 5 cm x 3 cm
Hydromea 500ER	cast, 120°	PN, 6000 m	10 cm x 5 cm x 3 cm
Hydromea LumaX	cast, 120°	PN, 6000 m	10 cm x 6 cm diam.
Marinelink WOCS 40220	dome, 90°	PH, 1000 m	36 cm x 20 cm diam.
Sonardyne Bluecomm 100	dome, 120°	PH, 4000 m	25 cm x 13 cm diam.
Sonardyne Bluecomm 200	dome, 180°	PH, 4000 m	Tx: 20 cm x 13 cm diam. Rx: 38 cm x 13 cm diam.
Sonardyne Bluecomm 200UV	dome, 180°	PH, 4000 m	Tx: 20 cm x 13 cm diam. Rx: 38 cm x 13 cm diam.

Data in Tables 1.1 and 1.2 are extracted from [31, 32, 33, 34]. Abbreviations: avalanche photo diode (APD), positive intrinsic negative photo diode (PIN PD), multiplier tube (PMT), pressure housing (PH), pressure neutral (PN), receiver (Rx), transmitter (Tx).

sector. However, no information is available on this. The intended use of the offered systems is mainly for vehicle to fixed node data transfer, e.g., ROV to an anchored sensor carrying deep sea observatories.

1.3 Scope and Aim

The scope of this thesis is focused on UOWC, based on systems with LEDs as transmitters and photodiodes as receivers. The development of such systems takes place in many steps and iterations. Assemblies consist of several components, and designing, modeling and simulation are interrelated. The underwater environment with its variety of influencing factors represents a challenging surrounding. Even though a lot of research has been done in the field of UOWC, there are still a number of less considered areas. The following topics will be covered in this dissertation: LED wavelength adaption, ambient light filtering, optimized detector selection, LEDs in dual-use, underwater housing technology, assembly light path characteristics, and Monte Carlo (MC) underwater lightfield simulation, including the generation of system related attenuation coefficients.

This work aims to support engineers and developers in understanding the UOWC systems relations and provides support in many aspects from design to operation. The objectives are feasible, versatile and affordable units for different communication purposes under harsh conditions. Furthermore, their compact sizes allow integration into vehicles, at all ranges of depths, and offers energy efficiency in battery powered vehicles or anchored systems. The goal is to decrease time expenditure and iterations during the engineering process of adapted UOWC assemblies and to shorten the necessary operational tests, to ultimately get a system that fulfills the requirements. Furthermore, a goal is to take this fascinating technology a step further towards the physical implementation of underwater swarm communication.

1.4 Author's Contributions

The major contributions of this work can be split into six main topics. These, and the respective link to the author's peer reviewed scientific publications are given below.

LED color apdaption Most UOWC-publications are limited to the use of blue LEDs, because of their efficiency and suitability for oceanic waters. The least attenuation window of coastal waters like the Baltic Sea is in the green wavelength range, just where the so-called 'green gap' of LEDs is located. The adaption of LED colors to water types and photodetector (PD) responsivities is examined in general, and in particular the use of converted green LEDs as an efficient alternative. Parts of this topic within Chapter 3 have been published in [35].

Ambient light suppression In most studies on UOWC, a deep dark ocean without ambient light is assumed. However, only a certain part of the applications will take place in this environment, and coastal waters are likely to be much more common. Natural ambient light can penetrate to depths of more than 100 meters. The various properties of this light field and related suppression by different optical filters is investigated in detail. Parts of this topic within Chapter 3 have been published in [36].

Noise and detector applicability The signal-to-noise ratio (SNR) in the electrical domain is an important parameter for signal processing. In order to optimize this with regards to UOWC, an in-depth noise analysis is carried out for different detector types and sizes using separated signal and interference light levels. Underwater ambient light circumstances are transferred and operating conditions are varied, thus targeting the subject comprehensively and as close to reality as feasible. Parts of this topic within Chapter 3 have been published in [35].

LEDs as PDs The reverse mode of LED operation is known in principle but is not very common. With emphasis on a potential dual-use in UOWC, single-color power LEDs exhibiting large die areas are examined here. The measurements in the spectral domain yielded unexpected results. The LEDs applied as photodetectors provided impressive responsivity values and pronounced bandpass characteristics, thus they represent an low-cost alternative to PD filter combinations. Parts of this topic within Chapter 3 have been published in [37].

UOWC assemblies Housing and port technologies are essential for underwater optical applications. Outside the field of imaging, where ports are recognized due of the distortions, these technologies are given little notice. Here, the criteria, concepts and aspects relating to UOWC are compiled and presented in a integrated form. The light path is investigated, the characteristics of the assemblies are examined, and theoretical results are supported by practical measurements. Parts of this topic within Chapter 4 have been published in [17, 38].

System attenuation coefficient This value is of decisive importance when determining the link budget in UOWC. In many publications in the field, only very common coefficients are applied for calculations or simulations. While the water types are still roughly distinguished, the wavelength and the system properties are often not further considered. Here, Monte Carlo simulations are applied to generate sets of curves for system-related attenuation coefficients as function of the wavelength and for various beam angles. Further dependencies are additionally investigated. A method for an experimental determinaton is also developed. Parts of this topic within Chapter 5 have been published in [35].

1.5 Thesis Outline

The remainder of this dissertation is organized as follows.

Chapter 2 gives an insight into the topic of optics in the underwater area. Fundamentals are provided and a system overview is given. The medium water and its properties, the environmental conditions and impacts are explained. In addition, a general model as well as some communication technology basics are given.

Chapter 3 examines the optimization of selected underwater optical communication elements. The first item discussed is the LED color adaption to water properties, the second item is a filter optimization for ambient light suppression, and the third item is the improved selection of photodetector types related to the signal-to-noise ratio. The last item introduces the application of LEDs as photodetectors.

Chapter 4 presents different underwater housing concepts for optical applications. The light path of flat and dome ports, as well as for transparent embedding is examined. Both the influences of fundamental parameters and geometric conditions are investigated. The spatial characteristics of the source and detector and the port properties are merged into assembly characteristics, measurements and calculations of these are compared. Finally, considerations for the design of assemblies are given and the implementation of multiple segmented transducers is discussed.

Chapter 5 describes Monte Carlo simulation, and the implementation and the constraints are discussed. For typical underwater optical communication system configurations, sets of related attenuation coefficients are generated. Potential influencing parameters are examined. This is followed by a description and evaluation of an experimental determination of the system related coefficient.

Chapter 6 contains the conclusions and identifies potential subjects for future work.

Chapter 2

Fundamentals

2.1 Underwater Optical Communication Systems Description

A subsea optical communication system is characterized by the transmission of modulated optical signals over a certain distance through the medium water for the purpose of data transfer. This is generally carried out in the wavelength area where the water shows a relatively low attenuation, often stated as "transparent window". This includes mostly the ultraviolet (UV) and the visible (VIS) wavelength range, see Fig. 2.1.

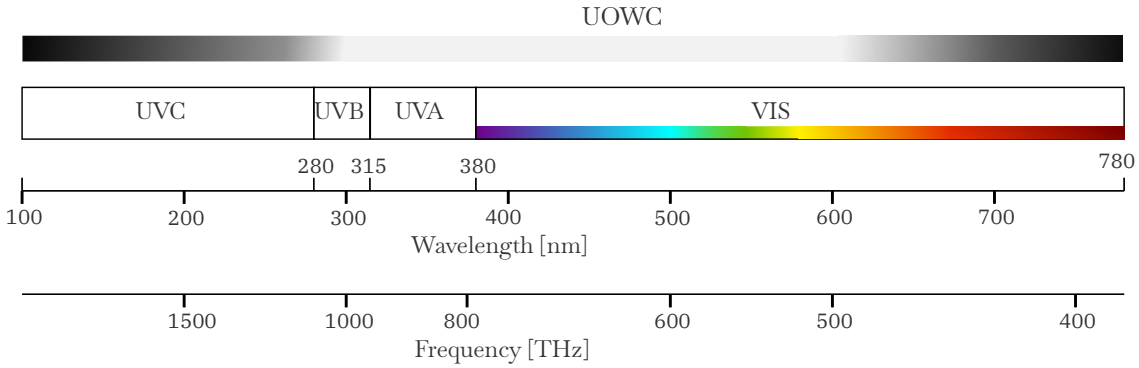

Figure 2.1: Section of the electromagnetic spectrum containing the spectral range applicable for UOWC.

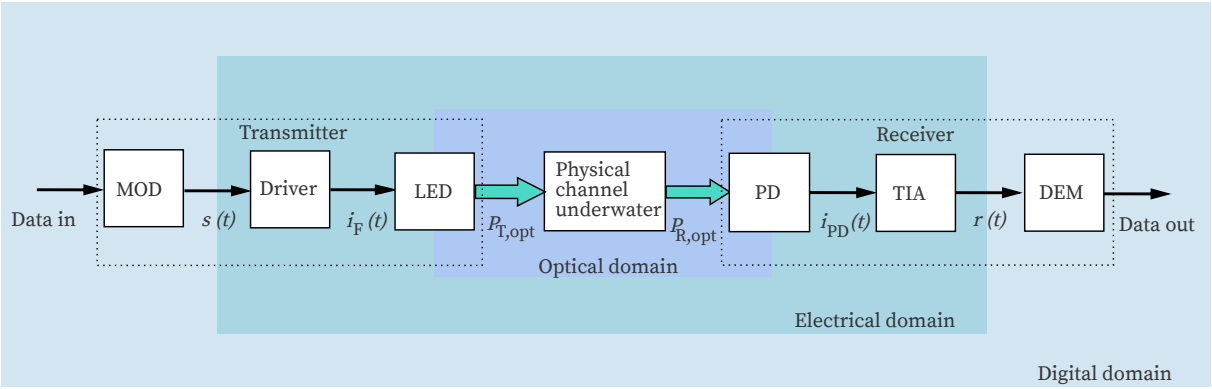

Figure 2.2: Underwater wireless communications transmission scheme, in compliance to the block diagram given in [39].

As depicted in the block diagram in Fig. 2.2, an UOWC system consists of the main elements transmitter (Tx) and receiver (Rx), separated by the physical channel. The transmitter includes a modulator (MOD) in the digital domain, a driver in the electrical domain followed by an LED as a light source entering the optical domain. Digital input data are converted by the modulator

to a waveform signal $s(t)$ which is the input for the driver. The driver delivers the forward current $i_{\mathrm{F}}(t)$ for the LED that outputs a radiant power $P_{\mathrm{T,opt}}(t)$, also stated as radiant flux $\Phi_{\mathrm{T}}(t)$. This optical power penetrates the water and is attenuated according to the distance traveled until it partially hits the photodetector (PD). On the receiver side, the optical domain ends at the PD and is followed by a transimpedance amplifier (TIA) in the electrical domain, and finally by a demodulator (DEM) in the digital domain. This means the received optical power $P_{\mathrm{R,opt}}(t)$, respectively $\Phi_{\mathrm{R}}(t)$, is converted to a photocurrent $i_{\mathrm{PD}}(t)$, which is amplified to an output voltage $r(t)$ and the digital data is finally restored from this.

In a wider context, this scheme can be seen as the first layer or the physical layer in common communication models [40]. This work focuses on the optical domain and the adjacent electrical domain on the receiver side.

2.1.1 Optical Front Ends

In electro-optical systems for underwater applications, a separation of electrical components from the medium water is indispensable. This applies to all natural waters, especially seawater as it is very conductive and corrosive. Materials used for this purpose must not only be insulating but also optically transparent. In case of UOWC, four different material or media are generally involved: air, water, glass, and plastics. The corresponding typical refractive indices are listed in Table 2.1.

Table 2.1: Typical refractive indices of selected media in the VIS wavelength range.

Material, media	Refractive index
Air	1.0
Water	1.34
Glass	1.45 - 1.7
Plastics	1.5 - 1.6

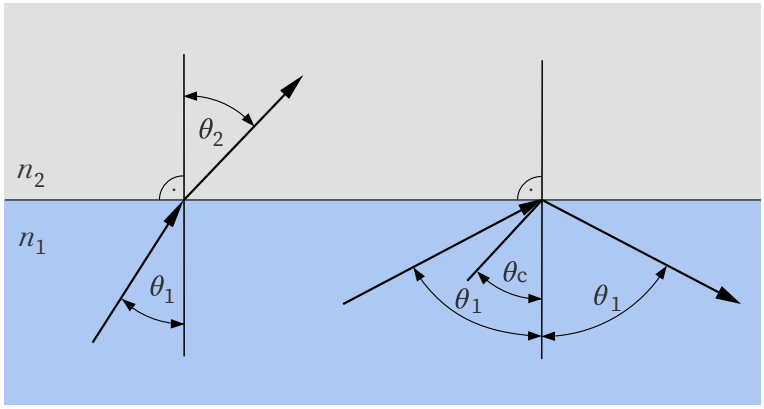

Figure 2.3: Refraction of light at an interface of two media with $n_1 > n_2$ on the left side and total reflection on the right, including the corresponding angles valid for $n_1 > n_2$.

If light crosses the boundary of two different media of refractive indices n_1 and n_2, the incident ray is refracted, see Fig. 2.3. The incident angle θ_1 and the refraction angle θ_2 are measured from the normal of the interface, and the relationship is known as Snell's law [41]:

$$\frac{\sin(\theta_2)}{\sin(\theta_1)} = \frac{n_1}{n_2} \ . \tag{2.1}$$

If $n_1 > n_2$ and the incident angle θ_1 exceeds the critical angle θ_c, total reflection occurs:

$$\theta_\mathrm{c} = \arcsin\left(\frac{n_2}{n_1}\right) . \tag{2.2}$$

The phase velocity v of light in a medium is given by the ratio of the light speed in the vacuum $c_0 = 2.998 \cdot 10^8$ m/s and the refractive index n of the medium:

$$v = \frac{c_0}{n} . \tag{2.3}$$

Incident light of $\Phi_\mathrm{i}(\lambda)$ passing the boundary of two media is not only refracted, but generally a partial reflection of $\Phi_\mathrm{r}(\lambda)$ occurs, which leads to a reduced transmission of $\Phi_\mathrm{t}(\lambda)$, see also Fig. 2.4. This is described by the transmittance $T(\lambda)$ and reflectance $R(\lambda)$:

$$T(\lambda) + R(\lambda) = 1. \tag{2.4}$$

For unpolarised light, like from LEDs, and small incident angles (less than 30°) the following approximation can be used [41]:

$$R(\lambda) = \left(\frac{n_2 - n_1}{n_2 + n_1}\right)^2 . \tag{2.5}$$

It should be noted that the wavelength dependence of the refractive index of the tabulated materials above in the visible wavelength range (VIS) is small. This is in the order of one percent, with slightly higher values for small wavelengths. It should also be mentioned, that the internal absorption of these materials is typically less than half a percent in the VIS range for thicknesses in the millimeter range, thus negligible in most cases. A typical air-glass interface with perpendicular incident light shows a transmittance of 96 %.

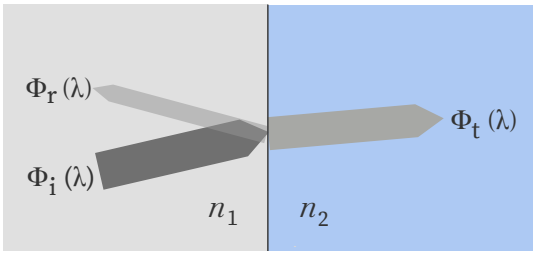

Figure 2.4: Partial reflection of light at an interface of two media with $n_1 > n_2$.

Transmitter Side

The optical path from the light source to the medium water commonly contains several stages, cf. Fig. 2.5. The core of the LED (die) is in most cases covered with potting compound, either flat or shaped as a lens, which forms the primary optic. The general integration into the LED housing is considered as one stage, with characteristics provided by data sheets. The rather weak concentrated beam characteristic in this stage can be used directly without further concentration. Frequently, the beam is further formed by secondary optics. This includes convex, total internal reflection (TIR), Fresnel lenses or reflectors in a wide range of designs. Before the light reaches the environmental medium water, it usually passes an optical port. In rare cases this can be represented directly by the primary or secondary optics, but mainly these are flat or hemispherical ports or a layer of casting material. To describe the transmitter, it is useful to combine the characteristics of the individual components in the light path. This is comparable to an underwater goniometer measurement, which delivers the angular intensity of the whole setup. The radiant intensity I_e describes the power or radiant flux per unit solid angle, and the SI unit is Watt/sr.

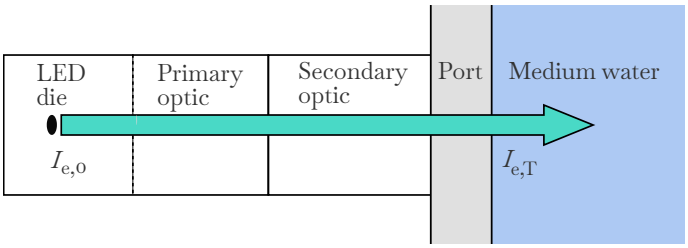

Figure 2.5: General light path in the optical domain of the transmitter side of an UOWC system.

For this directional radiometric quantity, the index 'e' (energetic) is used to prevent confusion with the basic formula symbol I for electric current. According to the "Ten Times Law" [41] with an operating distance much larger than the die diameter, the LED can be interpreted as a point source. Furthermore, a rotational symmetry can be assumed. A pronounced spectral characteristic of the radiant intensity $I_e(\lambda)$ is to be expected with the LED. With lenses, reflectors and transparent window materials, on the other hand, these are only to be expected to a limited extent within the partial VIS wavelength regime used from UOWC systems. The resulting transmitted intensity at the port-water interface $I_{e,T}$ depends of course on the initial $I_{e,0}$ value and the gain G_{opt} of lenses or reflectors, which generally leads to a reduced beam angle. The full beam angle is represented by β. The directional components of the intensity are referred to the inclination from the centerline, given by γ_T, see Fig. 2.6. Along with the wavelength dependence, this results in the term $f(\lambda, \gamma_T)$. Rotational symmetry is assumed, as it is found in most practical cases. To make a distinction from the term "field of view", which is often used on both sides, the denomination "beam angle" is used on the transmitter side, and "field of view" is only used on the receiver side. Each transition through the interface of two media results in a loss L_{opt}. This yields the formal description of:

$$I_{e,T} = I_{e,0} \cdot G_{opt} \cdot L_{opt} \cdot f(\lambda, \gamma_T), \text{ for } -\beta_{1/2} < \gamma_T < \beta_{1/2}, \text{ else } I_{e,T} = 0\ . \tag{2.6}$$

Expressed in a practical form, using a normalized angular distribution function $S_{T,norm}(\gamma_T)$, valid

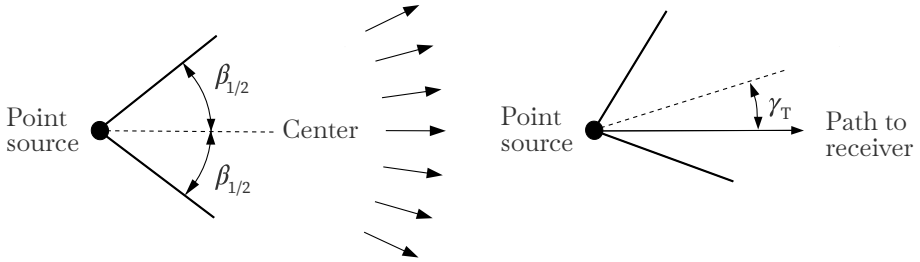

Figure 2.6: Basic transmitter geometry. Angle β is representing the beam angle, directional components relate to the inclination angle γ_T.

for one wavelength and within the beam angle, gives:

$$I_{e,T}(\gamma_T) = I_{e,Tmax} \cdot S_{T,norm}(\gamma_T). \tag{2.7}$$

The $S_{T,norm}(\gamma_T)$ function can be determined either by calculation or by measurements with an underwater goniometer. Here the radiant intensity of the transmitter setup is measured at varying angles and a fixed distance. Since such sensors are rare and only relative values are necessary, in practice irradiance sensors are often used in combination with apertures, tubes and baffles. To obtain the function, the achieved values at the different angles γ_T are normalized with the encountered maximum value, which in most cases occurs at γ_T=0°.

Receiver Side

The light path on the receiver side is similar to the transmitter side, but in reverse order, see Fig. 2.7. The first stage of the light is leaving the medium water through an optical port, which can be either flat or hemispherical, or a layer of casting material. The next stages may contain an optical concentrator and filter before the rays respectively photons are reaching the photodetector. Optical concentrators (OC) similar to reflectors can have different shapes such as a truncated cone concentrator (TCC), paraboloid profile concentrator (PPC) or compound parabolic concentrator (CPC). Of course lenses can also be used as concentrators. Optical filters of different types and characteristics are mainly used for ambient light suppression.

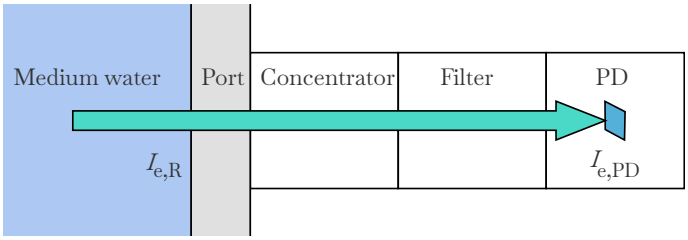

Figure 2.7: General light path in the optical domain of the receiver side of an UOWC system.

The description of the receiver side is related to that of the transmitter. The incoming radiant intensity $I_{e,R}$ at the water-port interface has to pass several stages of transition before it finally becomes $I_{e,PD}$ at the photodetector. Here it undergoes gains G_{opt} from concentrators and losses L_{opt} from media transitions and filters in the passband. A strong wavelength dependence is of course to be expected for the filters, and similarly detectors can also exhibit this to a certain extent. With lenses, concentrators and transparent window materials, this dependence is generally minor. The rays are accompanied by refraction when passing the media boundaries on route from the water to the PD, which has a particular effect with larger inclination angles γ_R. The intensity $I_{e,PD}$ that reaches the active surface of the photodetector within the field of view α, determines the power received and finally the current generated. The wavelength and inclination dependencies are expressed with the term $f(\lambda, \gamma_R)$. The geometry is given in Fig. 2.8, and a rotational symmetry is assumed. A generalized description including gains and losses is given by:

$$I_{e,PD} = I_{e,R} \cdot G_{opt} \cdot L_{opt} \cdot f(\lambda, \gamma_R), \text{ for } -\alpha_{1/2} < \gamma_R < \alpha_{1/2}, \text{ else } I_{e,PD} = 0\ . \tag{2.8}$$

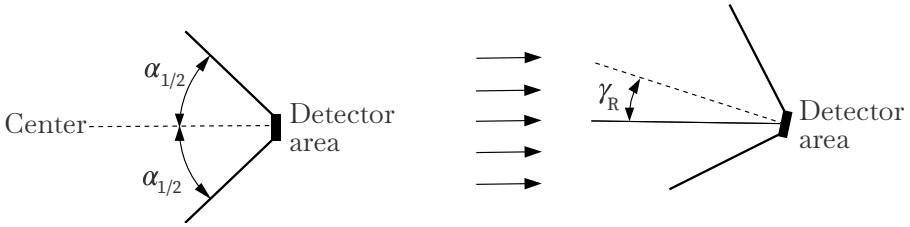

Figure 2.8: Basic receiver geometry. Angle α represents the field of view, directional components relate to the inclination angle γ_R.

A more applicable form of the equation above employing an angular distribution function $S_R(\gamma_R)$, that includes gains and losses, valid for one wavelength and within the field of view is:

$$I_{e,PD}(\gamma_R) = I_{e,R} \cdot S_R(\gamma_R). \tag{2.9}$$

$I_{e,R}(\gamma_R)$ is the incoming radiant intensity at inclination γ_R. The $S_R(\gamma_R)$ function needs to be calculated. Related to the center of a dome port in an underwater environment, for example, this

would result in values slightly below 1 for all angles within the hemisphere. Section 4.2 contains the modeling of the light path for different underwater housing concepts.

2.1.2 Underwater Optical Link Configurations

In the case of UOWC, three different link configurations are generally distinguished:

- Line-of-sight (LOS) link.
- Non-line-of-sight (NLOS) link.
- Retro-reflecting link.

Line-Of-Sight Link

The most common link configuration is line-of-sight (LOS). This direct link represents an unobscured straight line between the transmitter and receiver within the beam angle and the field of view, respectively, as depicted in Fig. 2.9. Misalignment is an issue in the point-to-point configurations, and related discussion can be found in [42, 43, 44]. A closer look at the link budget is outlined in Section 2.1.4. Direct UOWC links can be interrupted or disturbed by a variety of

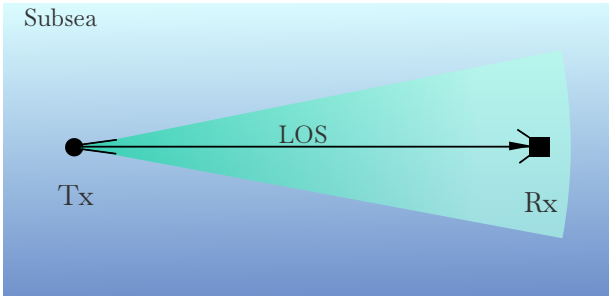

Figure 2.9: Direct line of sight link of UOWC.

possibilities, for example, by objects such as vehicles, fish, algae and bubbles. The effect of blocking and shadowing on UOWC in the LOS setup has been studied in [45]. In the literature, the LOS link type is sometimes referred to as diffuse link for larger transmitter beam angles such as those found in LEDs. This probably serves the simple purpose of differentiation from laser-based systems, as stringent LEDs do not produce diffuse light, but instead yield incoherent directed light.

Figure 2.10 illustrates LOS scenarios including surface and seafloor reflections as well as particulate scattering. Surface reflections in UOWC only occur when a system is operated close to the surface and the angle θ_S exceeds the critical angle θ_c. In the seawater-air boundary this is approximately 48°, cf. (2.2). Seafloor reflections are negligible in most cases due to strong absorption and minor reflectance of the ground. Particular reflection on the other hand, can occur anywhere in the water column and depends on the water type and thus the number of scattering components. Even the clearest oceanic waters are containing scattering constituents. Particulate scattering in natural waters takes place mostly in a forward direction at small angles. For more information refer to Section 2.2.1. The order of magnitude of scattered signal components reaching the receiver depends on the distance, the density of scatters and the field of view. Reflected signal components generally cover a longer distance than the direct ones, so they arrive at the receiver with a delay compared to the straight ones. This can lead to bit errors and inter symbol interference (ISI), respectively. The entire scattering process has an effect on the impulse response, and related research can be found in Section 5.2.6 and [46, 47, 48]. Due to the high speed of light in water, given

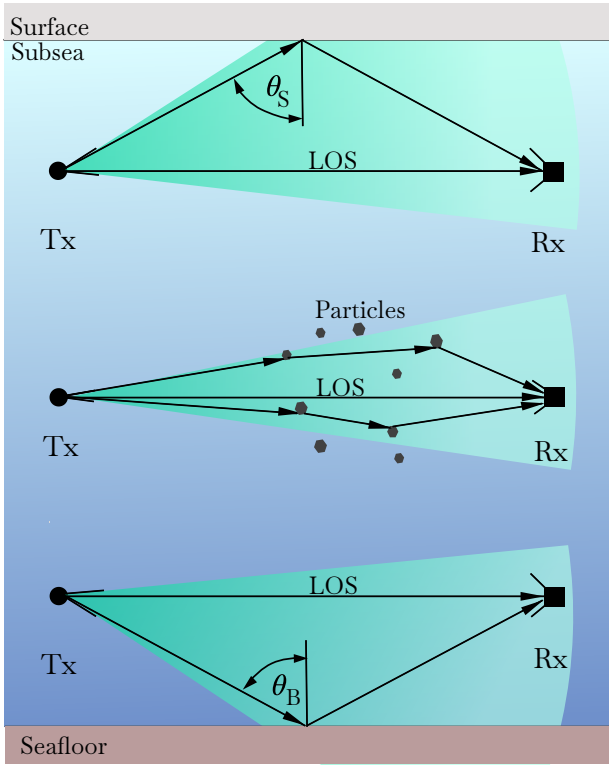

Figure 2.10: Line of sight scenario of UOWC with multipath caused by surface, particles or seafloor reflections, with respective illustrations from top to bottom.

by (2.3), the delay times are very short (in the nanosecond range) at typical maximum distances of tens of meters for LED based systems. Since the bandwidth of power LEDs generally is at most in the range of tens of MHz, there will be hardly any multipath related interference. In much faster laser based systems, however, the temporal dispersion leading to ISI can play a major role, see [49, 50, 51, 52]. Spatial dispersion is a serious issue for laser-based systems, but for shorter ranging LED based applications with comparatively large beam angles it is less significant.

Non-Line-Of-Sight Link

The NLOS link is based on reflection, and there is no direct path between transmitter and receiver within their beam angle and the field of view. The origin of the reflections are either particles in the water column or the medium change at the water surface, as depicted in Fig. 2.11.

However, the application of these two indirect links is limited. The advantage is the insensitivity to the alignment. The disadvantage of the particulate reflection is the low efficency and need for the presence of enough particles. Therefore, this application is for shorter distances in turbid coastal waters or in harbours. This topic is covered by [53, 54]. The approach of total surface reflectance is influenced by the wind-induced strongly-varying surface conditions and in particular is limited due to the unavoidable surface proximity. Related literature is given in [55, 56].

Another possible configuration would be to use reflections from the seafloor similar to the surface reflections to establish an indirect link. This approach is probably more of a theoretical nature, since the ground is likely to be highly absorbent and only slightly reflective in most cases. The author is not aware of any case in the literature where this effect is intentionally used in UOWC.

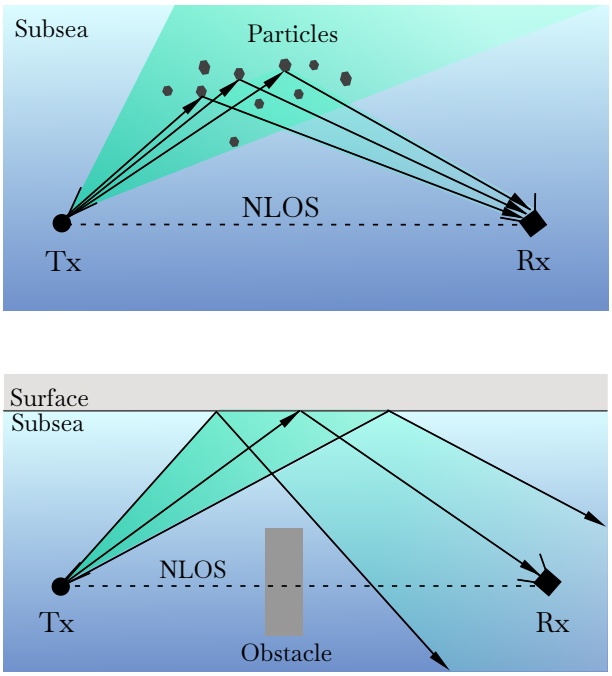

Figure 2.11: Reflective non-line-of-sight scenario of UOWC based on particular scattering in the upper drawing and on surface reflections in the lower.

Retro-Reflecting Link

For the sake of completeness, the retro-reflecting link should not remain unmentioned. Such systems use modulable micro-mirrors and are usually laser-based and therefore have increased requirements in pointing and tracking. Further information is gathered in [57].

Link Orientation

The link orientation can have a certain impact on UOWC systems. This occurs in particular in the vertical direction near the surface and in coastal regions. The reasons for this are, (a) the distribution of optically active components, and (b) the gradient of refraction due to large salinity and temperature changes, please refer to Section 2.2.1 and [58].

2.1.3 Environmental Conditions and Channel Impacts

The underwater optical channel is subject to a wide range of impacts. Ambient light from the sun is generally the major one, which can be direct, diffused by clouds or reflected by the moon at night. More details to this topic are given in Sections 2.2.4 and 2.2.5. In principle, the deep ocean can be considered as dark, but a source of disturbance can be from artificial light of parallel operated light-based instrumentation. For example imaging methods using video or flash lights for cameras on vehicles. Since the entire visible light spectrum is used in most cases, and thus a spectral separation is not possible, a temporal separation remains as alternative. Interference effects due to light reflections are most likely to take place on the surface, but can also take place on the bottom, depending on the nature of the seabed.

Another source of interference can be due to fluorescence, bioluminescence and Raman scattering, a brief description can be found in Section 2.2.6. Disturbances of a different kind are due to blocking, shadowing or obscuration of the light path. Fish and other marine life can be attracted to light, and jellyfish and marine growth (e.g., algae) can represent obstacles. This is more likely to happen in the biologically more active upper zones of the ocean. For long-term underwater

deployment of optical devices, biofouling can be a serious problem. The growth of a biofilm leads to decreasing transmittance through transparent port components. This can occur within hours in the worst case and at depths up to a few hundred meters, depending on the environmental conditions like availability of nutrients, water temperature and sunlight. A good way to solve this issue is the use of ultraviolet (UV) LEDs [38]. Even though these LEDs are now quite efficient and are operated intermittently, the energy issue always remains in the foreground with this type of application.

2.1.4 UOWC Link Budget

One of the most important contexts in UOWC is the relation of power fed into the channel to that received, i.e., the link budget. Related literature can be found in [59, 60]. In the following, this core formula is developed based on [61]. It is valid for one wavelength in LOS configuration, as given in Fig. 2.12, within the beam angle and field of view in the optical domain. It refers to a point source and a planar detector. Not included are the transitions from the electrical domain into the optical and vice versa at the receiving end, as described by the LED's radiant efficiency and by the photodetector's responsivity, respectively. Beer-Lambert's law describes the exponential

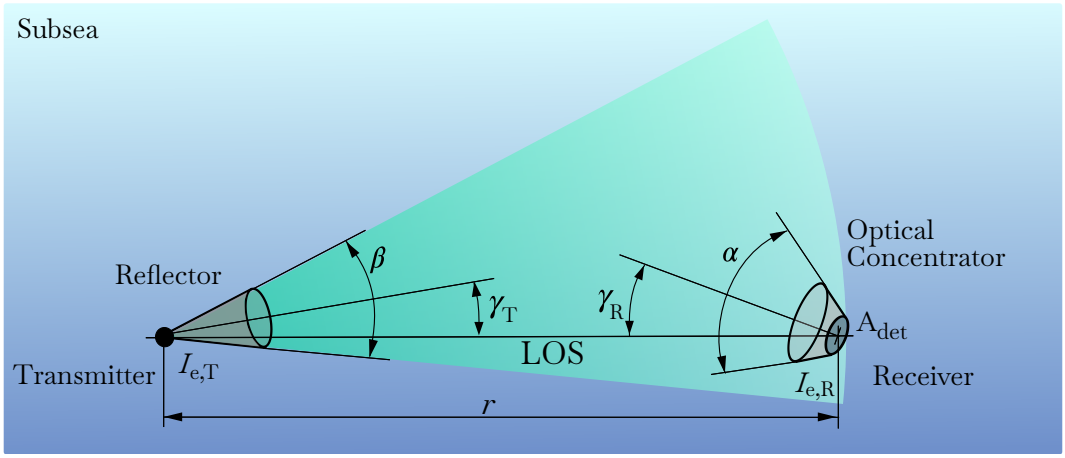

Figure 2.12: Line of sight scenario in UOWC with transmitter and receiver separated by the distance r. On the transmitter side the beam angle is β, the inclination is γ_T, and on the receiver side the field of view is α and the inclination is γ_R. The detectors active area is A_det.

decrease of radiant flux and similarly of radiant intensity in a medium with attenuation coefficient c and for a distance r. With $I_\mathrm{e,T}$ as the transmitted radiant intensity and $I_\mathrm{e,R}$ as the received intensity, the following relation results:

$$I_\mathrm{e,R} = I_\mathrm{e,T} \cdot e^{-cr}. \tag{2.10}$$

The inverse square law describes the development of the irradiance E in $\mathrm{W/m^2}$ from a radiant intensity I_e as function of the distance r within a unit solid angle Ω_0:

$$E = \frac{I_\mathrm{e}}{r^2} \cdot \Omega_0. \tag{2.11}$$

Inserting and rearranging results in:

$$E_\mathrm{R} = I_\mathrm{e,T} \cdot \Omega_0 \cdot e^{-cr} \cdot \frac{1}{r^2}. \tag{2.12}$$

The power P_PD in W at a PD of area A_det in $\mathrm{m^2}$ inclinated by angle γ_R and irradiated with E in $\mathrm{W/m^2}$ is:

$$P_\mathrm{PD} = E \cdot A_\mathrm{det} \cdot \cos(\gamma_\mathrm{R}), \tag{2.13}$$

and inserting and solving for P_{PD} leads to:

$$P_{\mathrm{PD}} = I_{\mathrm{e,T}} \cdot \Omega_0 \cdot e^{-cr} \cdot \frac{1}{r^2} \cdot A_{\mathrm{det}} \cdot \cos(\gamma_{\mathrm{R}}). \tag{2.14}$$

The directionality of the transmitter is described by the maximum radiant intensity $I_{\mathrm{e,Tmax}}$ and the normalized angular distribution $S_{\mathrm{T}}(\gamma_{\mathrm{T}})$. The angle dependent characteristic of the receiver path is given by $S_{\mathrm{R}}(\gamma_{\mathrm{R}})$. Due to refraction, the outer angle of incidence (AOI) at the port, i.e., the inclination, can be different from the inner AOI of rays reaching the PDs surface. Therefore it is advantageous to integrate the cosine of Lambert's law into the $S_{\mathrm{R}}(\gamma_{\mathrm{R}})$ function, yielding $S_{\mathrm{R}}(\gamma_{\mathrm{R,cos}})$. Finally the power arriving at the detector P_{PD} for a LOS system with transmitter and receiver inclination within the beam angle and field of view and valid for one wavelength equals to:

$$P_{\mathrm{PD}} = I_{\mathrm{e,Tmax}} \cdot S_{\mathrm{T,norm}}(\gamma_{\mathrm{T}}) \cdot \Omega_0 \cdot e^{-cr} \cdot \frac{1}{r^2} \cdot S_{\mathrm{R}}(\gamma_{\mathrm{R,cos}}) \cdot A_{\mathrm{det}}. \tag{2.15}$$

It is clear that the received power is strongly dependent on the distance. On the one hand it is inversely proportional to the distance squared, on the other hand it is exponential in the attenuation term.

2.1.5 Photonic Devices and Amplifiers

LED Light Source

The range of LEDs on the market is known to be large and very diverse, but the market share of LEDs suitable for UOWC systems is comparatively small. This application is mainly limited to single-color LEDs in the power to high-power range of watts to tens of watts. The color spectrum is bounded due to the water attenuation properties in the blue to amber color regime, equivalent to 450 nm to 600 nm wavelength. Depending on the LED series, there are typically only three to five different colors available in this wavelength region. The color of emitted radiation is changed by different composition of the semiconducting material, which changes the bandgap energy E_{g} of the semiconducting material. Using the Planck constant h and the speed of light c_0, the wavelength can be calculated by:

$$\lambda \sim \frac{hc_0}{E_{\mathrm{g}}}. \tag{2.16}$$

The spectral power distribution of single-color LEDs is given in Fig. 2.13. The spectral bandwidth is defined at 50 % of the maximum intensity, generally termed as full width at half maximum (FWHM) and ranges from 15 nm to 35 nm for direct color LEDs in the visible range. The spectra are not particularly narrow banded as in the case with laser diodes, moreover the spectra are widely overlapping. A separation into three independent physical channels can barely be achieved by optical bandpass filtering, even in the case of using only blue, green, and amber colored LEDs.

Indium gallium nitrite (InGaN) semiconductors typically generate blue to green light, whereas aluminum gallium indium phosphide (AlGaInP) produces light in the spectral region from yellow to red [64]. The zone between these two bands, the so-called green-yellow gap of LEDs, is characterized by low efficiency in terms of the ratio of emitted optical power to electrical power. The radiant efficiency of green and yellow LEDs is considerably lower to that of blue or red LEDs. This is particularly disadvantageous for the use in coastal waters, since they show the lowest attenuation in this wavelength area [35]. More efficient alternatives are available on the market, the so-called converted green or converted amber LEDs. The principle is analogous to the widely-used white LEDs, which consist of high efficient blue LEDs combined with a phosphor conversion layer. This layer converts the blue light to green or amber. A disadvantage of these converted color types for the use in UOWC, is the substantially higher optical bandwidth, which hinders ambient light filtering. Another drawback is the significantly longer rise and fall times in pulsed

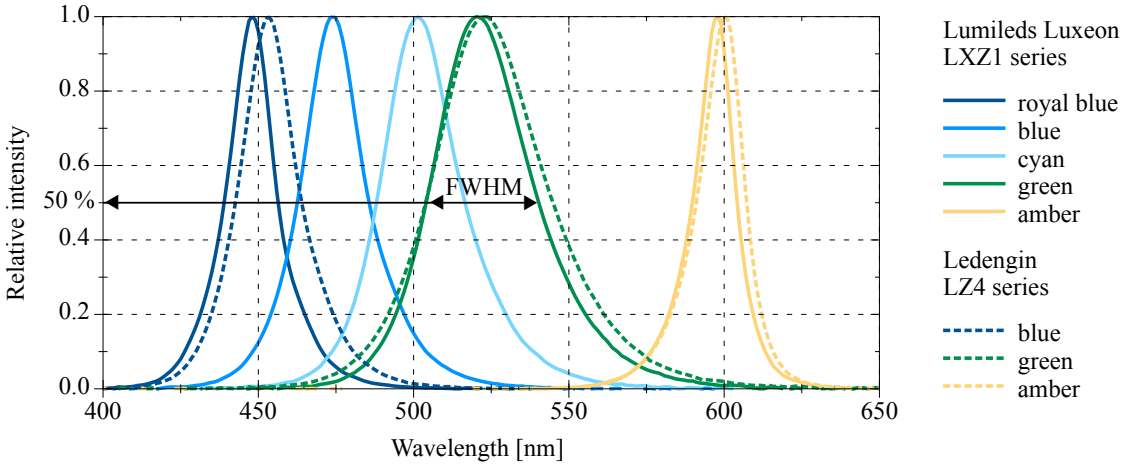

Figure 2.13: Spectral intensity distribution in normalized presentation of single-color power LEDs. Two LEDs series in the blue to amber color regime are shown. The data were determined with a Gigahertz Optics BTS256 spectrometer for Lumileds Luxeon Z Series [62] at forward current of I_f=350 mA and for Ledengin LZ4 series [63] at I_f=700 mA, both at 25 °C.

operation. The bandwidth of converted color LEDs is limited to only a few MHz. In contrast, direct color power LEDs are much faster and are able to achieve tens of MHz bandwidth. Spectral broadband white LEDs are not used for communication purposes under water, as the red spectral components would fall victim to absorption in the water and make ambient light filtering almost impossible. The topics of LED color and filtering are covered in more detail in the Sections 3.1 and 3.2.

In addition to speed properties, the irradiation characteristic is also important in case of UOWC. Most off-the-shelf power LED components are of a planar-type, without additional optical beam shaping. Therefore they offer a wide and smoothly decreasing radiation characteristic of typically 120° FWHM. In many applications, including UOWC, there is a need to sharpen the directionality through lenses or reflectors, which simultaneously leads to an increase of the irradiance and reduction of the beam angle. More detailed information is available in Section 4.3.1.

A this point, other LED technologies and their possible applicability within UOWC is briefly discussed. Quantum-dot LEDs (QLEDs) are promising, with spectrally narrowband, efficient, and tuneable light emitting features. The origin is a small scale display technology, but discrete single-color power components are not available at present. Micro LED (µLED) arrays have been introduced as a promising alternative in high speed visible light communication (VLC) and UOWC. These efficient gallium nitride (GaN) based LEDs have demonstrated bandwidths in the low GHz range in several experiments [65, 66]. The emitted blue to cyan colored light has a generally suitable wavelength for underwater applications. Since the currently achievable power is only in the range of milliwatts, µLED arrays need further development and optimized optics before they can be used as a light source in future UOWC systems. Organic LEDs (OLEDs) are fundamentally different from widely used semiconductor LEDs. The operating principle is based on a layer of organic compound, which emits light in response to an electric current. This technology is more of areal type, the achievable radiance is relative low. The typical response time of 1 µs to 10 µs is fast in terms of display technology but is not in terms of communications. Disadvantages in comparison to semiconductor based LEDs include a limited lifespan, the risk of water damage, and low efficiency.

Photodetectors

The task of a photodetector is the conversion from light, i.e., photons, into an electrical current. The general mode of operation of semiconductor PDs can be described as follows: photons hit the area near the pn-junction and generate electron-hole pairs, and these carriers are drifting and generate a current when the PD is connected in reverse direction to a voltage source. In photomultiplier tubes the photons hit the cathode material under high voltage, which ejects electrons into the evacuated tube, which is followed by a multiplication via the secondary emission process that becomes the photocurrent. The following groups of detector types are suitable for the application in high-speed UOWC systems:

- Positive intrinsic negative photodiode (PIN-PD).
- Avalanche photodiode (APD).
- Photomultiplier tube (PMT).
- Silicon photomultiplier (SiPM).

The main criteria for selection of these components are generally responsivity, dynamic range, active area, wavelength range, speed, and noise. Due to the distinct different characteristics exhibited by the PDs, it is necessary to look carefully at the particular environmental and operational conditions. A system performance test in a water basin and a perfectly dark lab is clearly different from establishing a robust optical communication within a swarm of robots in coastal waters during daylight. Even though photodetectors are generally linear over many decades of

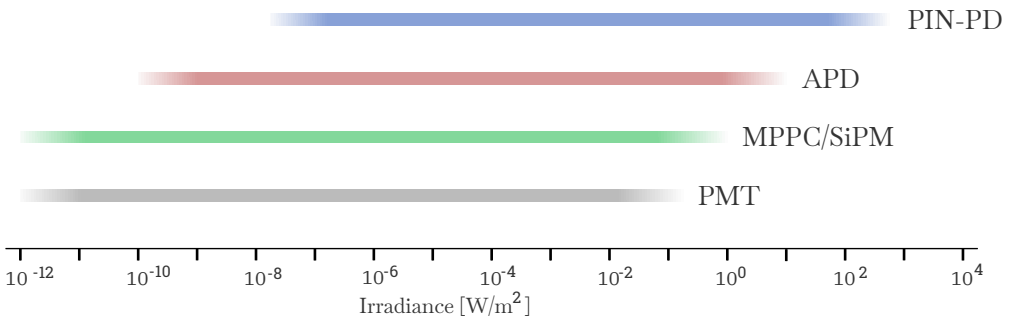

Figure 2.14: Typical light level operating ranges for different photodetector types. Data valid for a wavelength of 555 nm [67].

light level, the irradiance reaching the PDs active area is important for the decision about the type, cf. Fig. 2.14.

In comparison, PIN-PDs and APDs are suitable for higher light levels occurring in real operations, such as remaining ambient light even after filtering in shallow waters and signal irradiances in short ranges of a few meters. Thus they are predestined for use in the first generations of swarm robotics, encompassing deployments outside the deep dark ocean. The different properties in terms of responsivity of both variants are shown in more detail in Fig. 2.15. PIN-PDs are generally cheap and robust, but if the missing gain is compensated by large areas, the increasing junction capacitance reduces the speed. They basically cover a wide spectral range, with weaknesses in the blue to green area. APDs have an internal gain, but need high reverse voltages to operate, are temperature sensitive, and are noisier. Due to the gain, smaller areas are needed which allows higher speeds. The costs of large area PIN-PDs and comparable smaller sized APDs are in the same range. Both variants are available in relatively small flat packages. More in-depth discussion of this topic is included in Section 3.4.

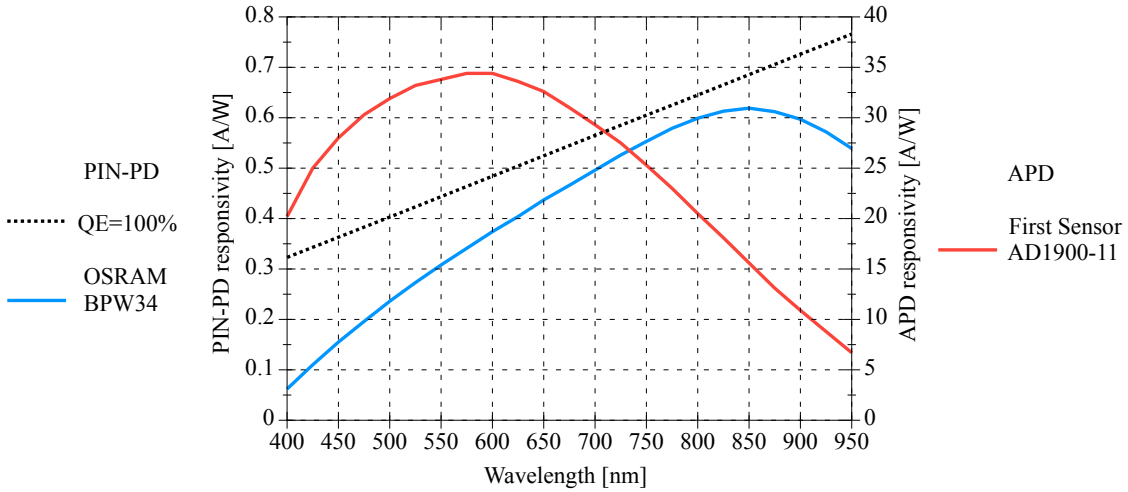

Figure 2.15: Spectral responsivity $\mathcal{R}$ of a standard PIN-PD, and for comparison the quantum efficiency (QE) theoretical maximum bound of QE=100 % on the left y-axis [68]. To illustrate the differences, the spectral progression of an APD at a gain of M=100 is given on the right y-axis. Data are extracted from corresponding data sheets [69, 70].

For low-light high-speed applications, PMTs and the group of SiPMs are generally appropriate. A PMT is in most cases a classic evacuated glass tube operated at high voltages. They offer advantages like high gain, speed and sensitivity, but high operating voltages and low mechanical robustness are the drawbacks. Recently, a leading manufacturer introduced a series of PMT-modules tailored for underwater optical communications [71]. The modern semiconductor counterpart of the PMTs is represented by the group of SiPMs. Within this group there are several names and abbreviations. Essentially, a silicon photomultiplier (SiPM), also called multi-pixel photon counter (MPPC), is an array of single photon avalanche diodes (SPADs). These SPADs, also known as the single-pixel photon counter (SPPC), are basically APDs operated above the breakdown voltage, in the so-called Geiger mode. SiPMs are best suited for pulse counting of low intensity very short signals in the nanosecond range, but in other cases the signal processing can get challenging [72].

Utilizing the PMT- or SiPM-technology in the dark clear ocean enables UOWC in the 100 m range for LED-based systems. But their individual drawbacks, such as high operating voltage, temperature sensitivity, noise, mechanical robustness, size, and costs needs to be taken into account. Nevertheless, SiPM detectors are a promising new technology in UOWC [73].

As a special case of PDs, single-color LEDs can be operated as optical receivers and act similar to a photodiode [37]. This is particularly valid for high-power LEDs, since they have relatively large active areas comparable with medium-sized PDs. Another unique feature is their intrinsic bandpass filtering characteristic, combined with potential dual use as transmitting and receiving element, they may be an interesting option for extraordinary applications or in the low-cost area. Studies on this are described in the Section 3.5.

Operational and Transimpedance Amplifiers

Operational Amplifiers (OpAmps) are DC-coupled high-gain voltage amplifiers. In almost all cases they are integrated circuits (ICs) and come with a differential input and usually a single ended output. These OpAmps are versatile electronic parts, because their characteristics can be determined by a few external components. Of course, there is a wide range on the market, but also versions with special properties such as low-noise and high-speed. These in particular are

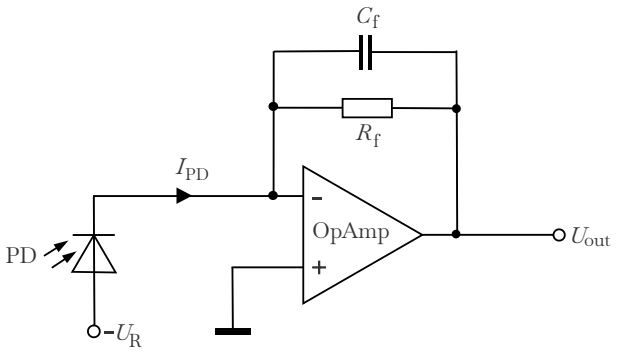

Figure 2.16: Elementary circuit of a one-stage transimpedance amplifier as commonly utilized for PIN-PDs and APDs. The discrete devices R_f and C_f are the feedback resistor and the feedback capacitor, respectively. A reverse voltage U_R is applied to the anode in order to reduce the capacitance of PIN-PDs, or in case of APDs, to enable the avalanche effect.

suitable for use in the receiver front end of UOWC systems.

Photodetectors like PIN-PDs and APDs have a wide linear operating range, and the generated photocurrent therefore includes many orders of magnitude. These tiny currents, typically ranging from microamps to nanoamps in UOWC environments, need transformation into voltages suitable for subsequent signal processing, primarily A/D conversion. This is commonly performed by one-stage and sometimes by two-stage transimpedance amplifiers (TIAs). One-stage TIAs mainly consist of an OpAmp, a feedback resistor R_f, and a feedback capacitor C_f, as depicted in Fig. 2.16. The feedback resistor determines the amplification and the acceptable light level before saturation of the amplifier. The dimensioning of C_f must be done very carefully, because it has a significant influence on the stability, the impulse response, and the cut-off frequency. The required capacitance values are often in the range of a few picofarad, and the stray capacitances can be correspondingly significant, so it is advisable to make measurements in addition to simulations with appropriate tools like [74].

At this point, an example will serve to illustrate the relationships and the development of these values. For this purpose, a simplified simulation for a point light source of power P_opt and for a PD of area A_det and responsivity $\mathcal{R}$ is carried out at different distances r for coastal oceanic water. The parameters are specified in Table 2.2. Further simulation conditions include an ideal source with uniform distribution, no inclination of source and PD, and no ambient light. The exponential attenuation of the medium water is taken into account, and the attenuation coefficient applied is the widely used c, which is generally valid for beams. The attenuated source power is spread over the surface of a spherical cap, represented by the lower term in the formula, and forms the irradiance E_PD at the detector [35]:

$$E_\mathrm{PD} = \frac{P_\mathrm{opt} \cdot e^{-cr}}{2\pi r^2 (1 - \cos(\beta/2))}. \tag{2.17}$$

The optical power at the detector surface P_PD yields:

$$P_\mathrm{PD} = \frac{P_\mathrm{opt} \cdot e^{-cr}}{2\pi r^2 (1 - \cos(\beta/2))} \cdot A_\mathrm{det}. \tag{2.18}$$

The generated detector current I_PD and the output voltage U_out are given by:

$$I_\mathrm{PD} = E_\mathrm{PD} \cdot A_\mathrm{det} \cdot \mathcal{R} \tag{2.19}$$

$$U_\mathrm{out} = I_\mathrm{PD} \cdot R_\mathrm{f}. \tag{2.20}$$

Table 2.2: Simulation parameters.

Transmit optical power	P_{opt}	5	W
Beam angle	β	70	°
Wavelength	λ	514	nm
Attenuation coefficient	c	0.3	1/m
Responsivity	$\mathcal{R}$	0.37	A/W
Detector area	A_{det}	10	mm^2
TIA feedback resistor	R_{f}	100	kΩ

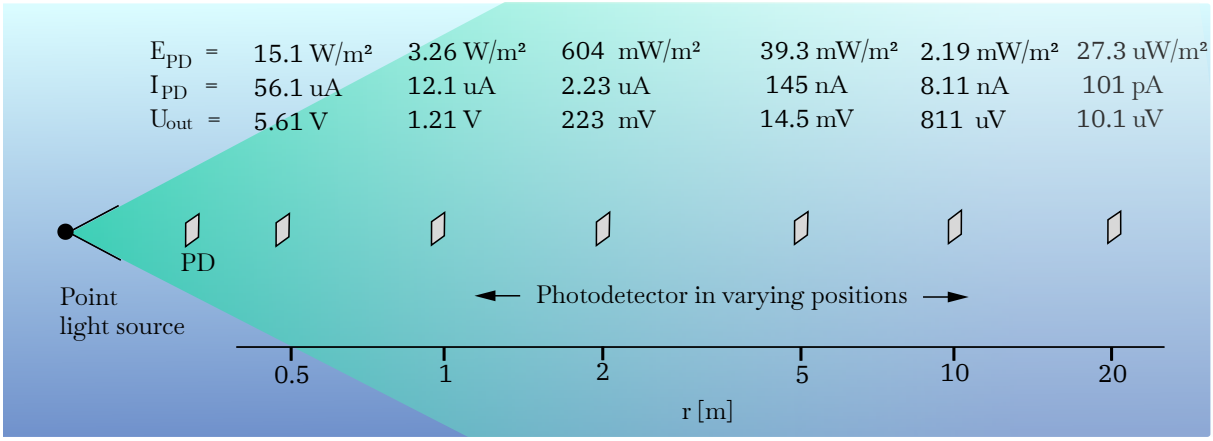

Figure 2.17: Dependence of the irradiance E_{PD} reaching the PD, the generated photocurrent I_{PD}, and the output voltage U_{out} on the distance r. System parameters for the corresponding simulation are chosen to be typical realistic values as given in Table 2.2.

As a result, the simulation shows the drastic changes of the relevant values over many decades within a realistic operating range of 0.5 to 10 meters, see Fig. 2.17. As it can be seen from (2.17), the power is attenuated as a function of the distance r by the square law and exponentially by Beer's law. The useful range of the TIA is limited at the upper end by the saturation of the amplifier and at the lower end by the noise. Apart from the signal component, the saturation can also be influenced to a considerable extent by possible ambient light, despite optical filtering. To ease subsequent signal processing, such as A/D conversion and electrical filtering, approaches like logarithmic amplification or switchable respectively programmable gain can be pursued. In turn, however, some attention must be paid to the C_{f} dimensioning and impulse response, as well as to the modulation scheme in case of signal superposition, for example. In principle, of course, there is also the possibility of saturation of the photodetector, generally less with the PIN-PDs than with the APDs.

The second important aspect is the noise. In the case of UOWC, especially the area where the signal-to-noise ratio (SNR) is just sufficient for transmission with an admitted error rate. Three predominant noise sources can generally be identified: thermal noise, shot noise, and amplifier noise. Thermal noise (Johnson-noise) is generated by the thermal agitation of charge carriers, it is present in all electrical circuits, and increases with temperature. Shot noise is caused by the random fluctuation of photons per unit time hitting the detector area. The origin makes no difference for the PD, and there is no distinction between signal and ambient light. The third main component to be considered in the examination of noise is the amplifier noise. This is described by the parameters of voltage noise density and current noise density, which are specified as electrical characteristics in the amplifier's data sheet. Low-noise amplifiers are of course preferable for

TIA applications. The use of suitable simulation tools is recommended to handle the plurality of variables. A general remark at this point is that the detector dark current noise is negligible in most cases.

Usually PIN-PD-based systems are more robust to ambient light conditions, but they are slower and less sensitive, whereas APD-based systems cope worse under ambient light conditions due to shot noise, but offer comparatively better sensitivity and higher speed, cf. [75]. More in-depth discussion of this topic is included in Section 3.4.

2.1.6 Relevant Aspects of Digital Communications in UOWC

Intensity Modulation and Direct Detection

An LED based UOWC system follows the intensity modulation and direct detection (IM/DD) principle. Intensity modulation can be generated by varying the LED forward current. Direct detection is achieved by a photodetector in the receiver, which converts the optical power reaching the surface to an electrical current. Features which should be mentioned at this point are that LEDs as non-coherent light sources prohibit the use of any phase information. Furthermore this is a baseband technique without frequency conversion. The waveform signal $s(t)$ must be real-valued and non-negative. The LED forward current and emitted power are not entirely proportional, at least not for large signal variations. In the optical domain of UOWC we find a proportionality between the transmitted power P_{Topt} and the received power P_{Ropt}. In the electrical domain, the received power is proportional to the square of the photodetector current. The fundamental relationship between the received powers in the optical domain P_{Ropt} and in the electrical domain P_{Rel} is given by:

$$P_{\mathrm{Rel}} \sim \kappa \mathcal{R}^2 P_{\mathrm{Ropt}}^2. \tag{2.21}$$

Herein, $\mathcal{R}$ is the reponsivity of the photodetector, and this is a device and wavelength dependent parameter. The shaping gain factor κ depends on properties of a signal $x(t)$, which corresponds to $s(t)$ used here, and is given by:

$$\kappa \triangleq \frac{\overline{x^2}}{\bar{x}^2}. \tag{2.22}$$

Large amplitude fluctuations and thus high κ ratios lead into better power efficiency of the modulation scheme for the same received power. More detailed information can be obtained in [39, 76, 77].

AWGN Channel Model

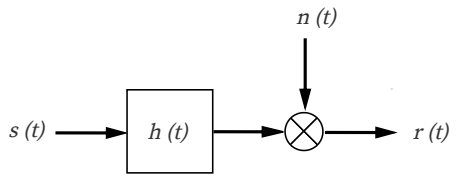

Figure 2.18: Additive white Gaussian noise (AWGN) channel model.

The AWGN channel model is a fundamental in communication technology [78, 79]. As depicted in Fig. 2.18, $s(t)$ is the intensity modulated input signal, $h(t)$ is the channel transfer function, $n(t)$ is the additive white Gaussian noise, and $r(t)$ the channel output signal. The corresponding formula is (* denotes linear convolution):

$$r(t) = s(t) * h(t) + n(t). \tag{2.23}$$

To the signal a noise process is added, which has a flat spectral power noise density over the bandwidth, the so-called white noise. This noise is Gaussian distributed, and it has a zero mean. Based on AWGN, the Shannon-Hartley theorem states the channel capacity, which is of large interest for communication systems. The theoretical maximal channel capacity is a function of the channel's bandwidth and the signal-to-noise ratio, and can be approximated for intensity modulation by appropriate formulas. The electrical SNR and not the optical is included here. Since there is no well established theoretical model for the UOWC channel [80], the AWGN channel model is often used for UOWC systems, even if its validity is limited. One limitation has its cause in the noise contribution from the shot noise, which is signal dependent. In case of UOWC, this signal is generated by the LED source. Ambient light also causes shot noise, which is independent from the LED source. The shot noise distribution shifts from Poisson with small number of events, to similar to Gaussian for large numbers. Transferred to the number of incident photons at the photodetector, this means leaving the (single) photon counting regime at increasing irradiances. Another limitation is that the Shannon-Hartley theorem assumes Gaussian distributed channel input symbols. This assumption violates the constraint of non-negative channel inputs. Nonetheless, Shannon-Hartley theorem can be used as a rough estimate in UOWC, particularly when the noise sources are separately analyzed and the thermal noise contribution or the amplifier noise are clearly dominant over the shot noise contribution. A noise analysis for different exemplary operating conditions is provided in Section 3.3.3.

UOWC Modulation Schemes

The selection of the modulation scheme has a large impact on the respective system performance, this implies a careful consideration of the mutually influencing criteria:

- Bandwidth performance.
- Power efficiency.
- Signal to noise (SNR) requirements.
- Bit error rate (BER) specification.
- Implementation effort.

Highest possible data rates also require large bandwidth, but these are generally limited by the LED and the PD capacitance. Since mobile underwater devices and also anchored systems are almost exclusively battery-powered, the energy efficiency is the key to long operating times. This applies not only to the LED and the absolute transmitted power, but also to the modulation scheme. While the BER is a systemic boundary condition, the SNR strongly depends on the distance Tx-Rx. A high design complexity and the resulting implementation effort are also relevant to cost, space and energy. Modulation schemes for non-coherent IM/DD UOWC systems are in most cases single-carrier types with two amplitude levels. These so-called bi-phase schemes are hardware friendly due to the switching process. Non-return-to-zero On-Off-keying (NRZ-OOK) and pulse-position-modulation (PPM) are often used, the first because of good bandwidth properties and the simplest implementation, and the second because of low SNR requirements. The generally popular pulse-width-modulation (PWM) is rarely used in this area because of its poor power efficiency. At this point, the asynchronous digital pulse interval modulation (DPIM) should be mentioned [81], as well as the differential pulse position modulation (DPPM) [82]. More in-depth literature is given in [39, 83].

For an accurate function a certain bit error rate (BER) needs to be fulfilled. Without channel coding this targeted bit error rate threshold is mostly set to a value in the range of 10^{-2} to 10^{-6}. Different modulation schemes require individual SNRs in order to achieve the targeted BER. The most commonly applied modulation schemes in UOWC, NRZ-OOK and PPM, need an SNR in the

Table 2.3: Comparison of common modulation schemes for UOWC. Values for SNR extracted from graphics given in [39].

	NRZ-OOK	4-PPM	8-PPM	16-PPM
Bandwidth efficiency	$R_\mathrm{b} = B$	$R_\mathrm{b} = 0.5B$	$R_\mathrm{b} = 0.375B$	$R_\mathrm{b} = 0.25B$
SNR				
for 10^{-2} BER	7.2 dB	5.0 dB	4.0 dB	3.2 dB
for 10^{-3} BER	9.8 dB	7.3 dB	6.0 dB	5.2 dB
for 10^{-4} BER	11.4 dB	8.8 dB	7.4 dB	6.4 dB
for 10^{-5} BER	12.6 dB	9.9 dB	8.4 dB	7.4 dB
for 10^{-6} BER	13.5 dB	10.7 dB	9.3 dB	8.2 dB
Power efficiency κ	2	4	8	16

Data rate R_b, bandwidth B

electrical domain roughly in the range of 5 dB to 15 dB for a certain BER, cf. Table 2.3. The values of the SNR per bit (E_b/N_0) are taken as the basis instead of the SNR per symbol (E_s/N_0), since these are the more practical choice in the case of bandwidth limited systems and thus constant time slots or chip durations. Assuming the average power is constrained, the $L-$PPM scheme shows better immunity against noise with increasing cardinality L, and this higher sensitivity leads into larger achievable distances in practice [83]. To avoid the communication suffering from drop outs when the required SNR is undercut, an adaptive system could change the modulation scheme to a less noise sensitive one. For example from NRZ-OOK to 8-PPM, though at the expense of bit rate. Reducing the distances under otherwise identical conditions quickly leads to a significant improvement in the SNR, and thus to reliable communication down to very short distances, which then can lead into saturation problems. It is worth mentioning at this point, that channel coding can correct a limited number of errors in a received message. This leads into an reduction of the BER to arbitary low values. In comparison to the uncoded case, this corresponds to an improvement of the SNR or increase of the distance, respectively. UOWC systems applying forward error correction (FEC) like Reed Solomon (RS) coding are presented in [80, 84]. General overviews of modulation schemes and related topics are gathered in [13, 15, 17].

Input Output Architectures

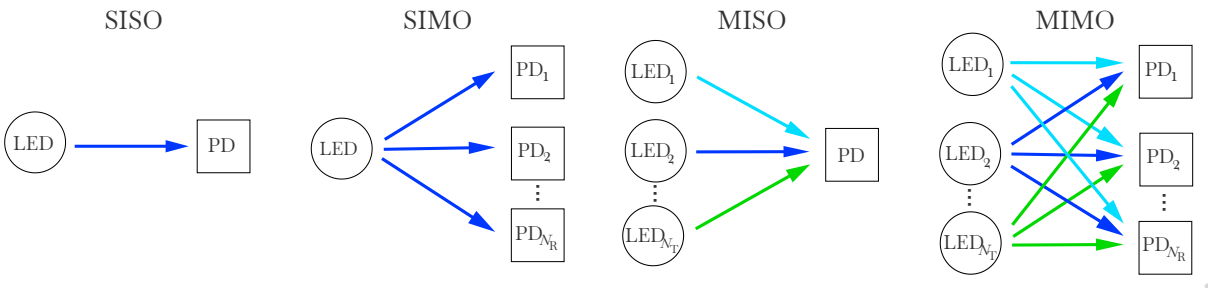

Figure 2.19: Drawing depicts the four general input-output schemes from single-input single-output (SISO) to multiple-input multiple-output (MIMO). N_T is the number of elements on the transmitter side and N_R on the receiver side.

The basic system in optical transmission comprises one light source and one photodetector as

the receiving element, which is also known as single-input single-output system (SISO). This is clearly the most widely used and frequently compared type in the UOWC sector. If several light sources are used on the transmitter side and several photodetectors on the receiver side, this is referred to as multiple-input multiple-output (MIMO) technology, see Fig. 2.19. Special cases of MIMO are the single-input multiple-output (SIMO) and multiple-input single-output (MISO) systems, which only use one light source or one photodetector, respectively, [39]. MIMO enables an improvement of the system availability (spatial diversity) and data rate (spatial multiplexing), either by transmitting the same or different information by all sources, respectively. Further characteristics and features on the use of MIMO technology in the field of UOWC are that the Rx and Tx elements can be arranged close or spatially separated, and one or different colors can be used. Furthermore single-user or multi-user communication is feasible, and localization is possible. Since most UOWC applications will be mobile, thus needing hemispherical or even spherical Rx and Tx characteristics, which leads to considerably overlapping segments in the practical implementation. This automatically creates a MIMO system in certain areas. For energy-critical applications like mobile UOWC, the SIMO architecture is preferable to the MISO in most scenarios. A comprehensive introduction to the entire topic is given in [17]. A comparative performance analysis of the different architectures including LED based UOWC was carried out in [85], and a study dedicated to SIMO is given in [86]. The feasibility of implementing MIMO capable UOWC transmitters is presented in [30].

2.2 Light in the Medium Water

Natural waters as medium of the underwater optical channel are challenging for UOWC system designers due to their widely varying parameters. The optical properties of water are grouped into two classes, inherent optical properties (IOP) and apparent optical properties (AOP) [87]. IOPs depend on the medium itself like its composition and present particles, and the absorption and scattering coefficients are two prominent examples. AOPs depend on the medium itself and on the structure of illumination, the directionality of the light field, such as the diffuse attenuation coefficient for instance, more details are given in [88].

2.2.1 Absorption, Scattering and Attenuation

Absorption

Compared to air, water is a strong absorbing medium for light. Photons of the penetrating light are irreversibly removed from their path and the energy is converted by the water molecules or other absorbing constituents. These effects show a high spectral dependency. With respect to Mobley [87], the spectral absorption coefficient is defined as depicted in Fig. 2.20 and by following equation:

$$a(\lambda) = \lim_{\Delta r \to 0} \frac{\Phi_\mathrm{a}(\lambda)}{\Phi_\mathrm{i}(\lambda)} \cdot \frac{1}{\Delta r}. \tag{2.24}$$

The main optically active absorbing components in natural waters are:

- a_w, absorption by the water itself.
- a_phyt, absorption by phytoplankton.
- a_CDOM, absorption by colored dissolved organic matter.
- a_NAP, absorption by non-algae particles or detritus.

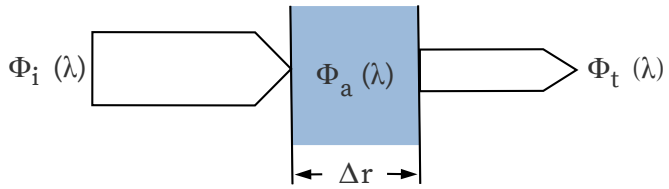

Figure 2.20: Geometry to define spectral absorption in a volume of water as given by Mobley. $\Phi_a(\lambda)$ is the part of the monochromatic incident beam $\Phi_i(\lambda)$ which is absorbed in a layer of water with thickness Δr, $\Phi_t(\lambda)$ is the transmitted power, and units are W/nm.

The total spectral absorption coefficient $a(\lambda)$ can be expressed as the sum of these grouped absorbing constituents [89]:

$$a(\lambda) = a_w(\lambda) + a_{phyt}(\lambda) + a_{CDOM}(\lambda) + a_{NAP}(\lambda). \tag{2.25}$$

The unit of absorption coefficient is 1/m. Due to the different spectral progression and variability of these constituents, this requires a closer look. The absorption by the water $a_w(\lambda)$ itself is given in Figs. 2.21 and 2.22 for pure water and pure seawater with a salinity of 35 ‰, respectively. A strong rise in absorption can be registered in the range above 600 nm. The difference between both types is relatively small, and the dependence on temperature and salinity is known to be low [87].

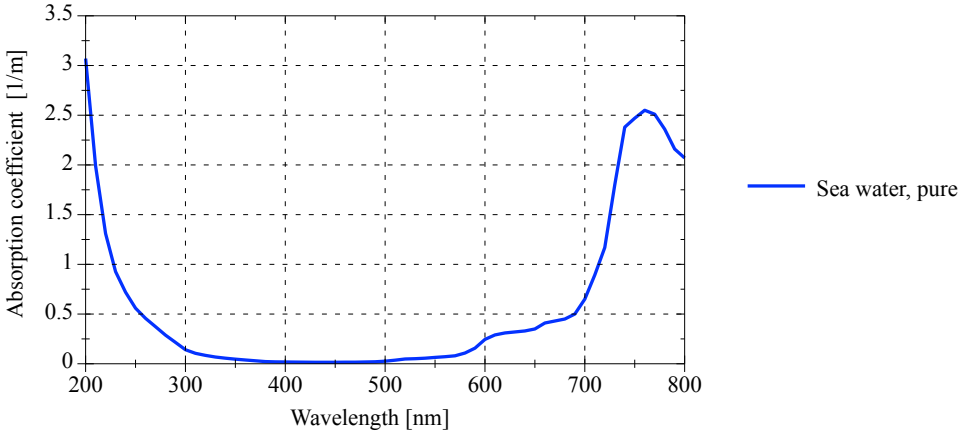

Figure 2.21: Spectral absorption $a_w(\lambda)$ of pure sea water. The so-called transparent window is clearly identifiable. Plotted from tabulated data given in [90].

Phytoplankton is the generic term for living microalgae containing chlorophyll pigments. Characteristic for phytoplankton is the strong absorption in the blue wavelength regime and a peak in the deep red. Due to a variable mixture of species in natural waters the spectral behavior also varies. A spectral absorption model was developed by Bricaud et al. [92], given as tabulated numerical constants $A_{phyt}(\lambda)$ and $B_{phyt}(\lambda)$, and is shown in (2.26). A chlorophyll concentration related general absorption spectra can be calculated by:

$$a_{phyt}(\lambda) = A_{phyt}(\lambda) \cdot \langle chl \rangle^{-B_{phyt}(\lambda)}. \tag{2.26}$$

The chlorophyll concentration *chl* ranges roughly from 0.1 mg/m^3 for clear oceanic waters to 10 mg/m^3 in productive coastal areas, and can rise up to 100 mg/m^3 in lakes, see also Fig. 2.23.

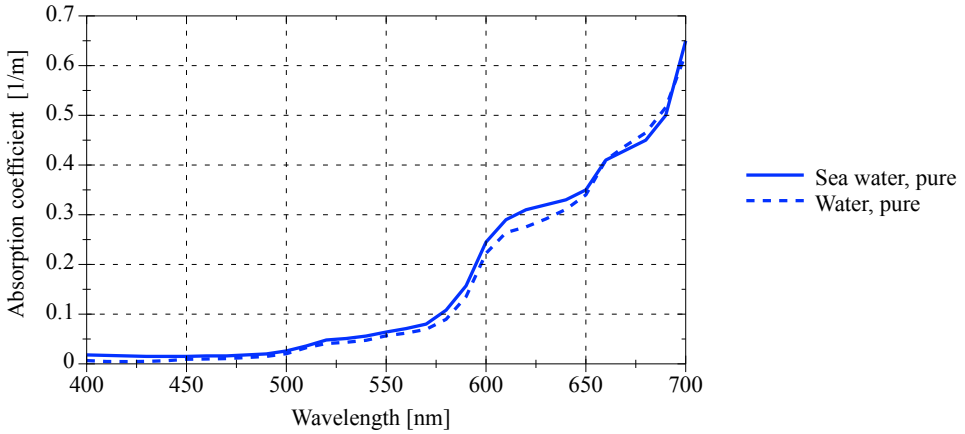

Figure 2.22: Spectral absorption $a_{\mathrm{w}}(\lambda)$ of pure water and pure sea water. Plotted from tabulated data given in [90, 91].

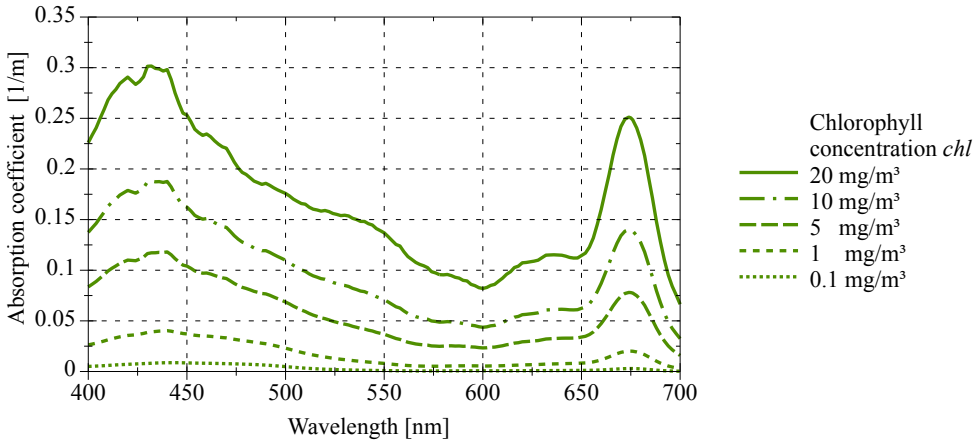

Figure 2.23: Spectral absorption of phytoplankton $a_{\mathrm{phyt}}(\lambda)$ in sea water as function of the chlorophyll concentration. Values calculated and plotted based on [92].

Colored dissolved organic matter (CDOM) are decaying organisms, also named yellow substances or gelbstoff. The absorption generally exponentially decreases with wavelength, and values depend on the concentration and the specific type of yellow substances. The spectral characteristic of this absorbing constituent can be modeled by (2.27), according to Bricaud et al. [93]. Exponential coefficients S_{CDOM} and reference values $a_{\mathrm{CDOM}}(\lambda_{\mathrm{ref}})$ can be found in [87, 89]:

$$a_{\mathrm{CDOM}}(\lambda) = a_{\mathrm{CDOM}}(\lambda_{\mathrm{ref}}) \cdot e^{(-S_{\mathrm{CDOM}}(\lambda-\lambda_{\mathrm{ref}}))}. \tag{2.27}$$

Non-algae particles (NAP) or detritus, also described as debris of plankton and sediments form another absorbing constituent. The spectral progression is similar to the course of CDOM, but with typically smaller slopes. The equation of the model (2.28), as well as exponential coefficents S_{NAP} and reference values $a_{\mathrm{NAP}}(\lambda_{\mathrm{ref}}$ are given in [89, 94]:

$$a_{\mathrm{NAP}}(\lambda) = a_{\mathrm{NAP}}(\lambda_{\mathrm{ref}}) \cdot e^{(-S_{\mathrm{NAP}}(\lambda-\lambda_{\mathrm{ref}}))}. \tag{2.28}$$

The CDOM and NAP absorption reference values are often given at wavelengths λ_{ref} of 400 nm to 443 nm, respectively, and exponential coefficients are mostly in the range of 0.01 to 0.02.

Figs. 2.24 and 2.25 show the total spectral absorption and the constituents modeled for the Atlantic Ocean and the Baltic Sea, representing oceanic and coastal waters, respectively.

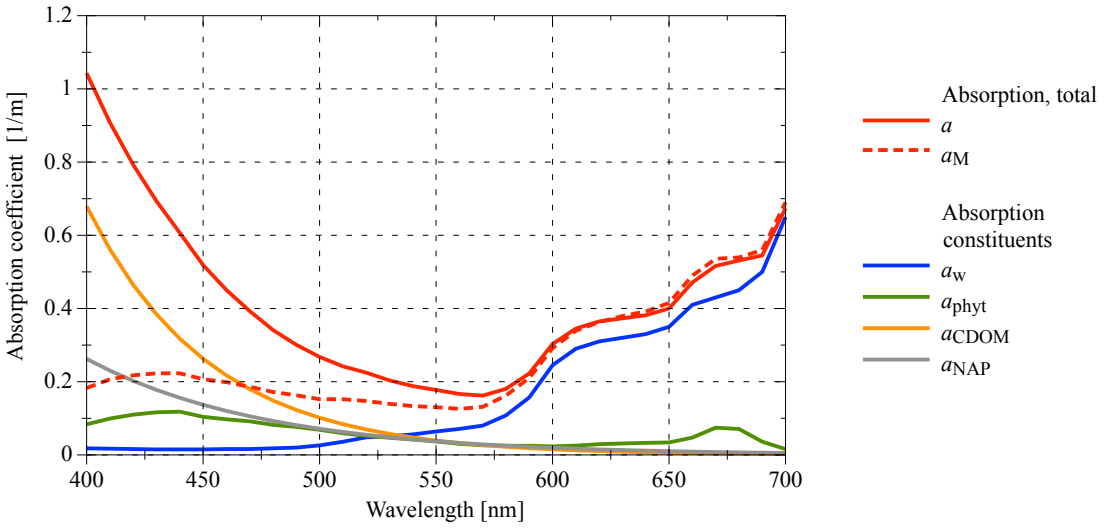

Figure 2.24: Modeled total spectral absorption $a(\lambda)$ and its constituents as well as the total of the simplified model $a_{\mathrm{M}}(\lambda)$ for the Baltic Sea. Parameters are extracted from [94] and represent typical values for this area. (Sea water, chl=5 mg/m^3, $a_{\mathrm{CDOM}}(433)$=0.3 1/m and S_{CDOM}=0.019, $a_{\mathrm{NAP}}(433)$=0.15 1/m and S_{NAP}=0.013).

To ease modeling, Morel [95] presented a simplified model based on the work by Prieur and Sathyendranath [96], given as (2.29). This model for the total absorption $a_{\mathrm{M}}(\lambda)$ only needs the spectral water absorption coefficient $a_{\mathrm{w}}(\lambda)$, the chlorophyll concentration chl, and one tabulated chlorophyll specific spectral value $A_{\mathrm{chl}}(\lambda)$:

$$a_{\mathrm{M}}(\lambda) = [a_{\mathrm{w}}(\lambda) + 0.06 \cdot A_{\mathrm{chl}}(\lambda) \cdot chl^{0.65}] \cdot [1 + 0.2 \cdot e^{(-0.014(\lambda - 440))}]. \tag{2.29}$$

Since the relationship to other constituents like CDOM is fixed, the preferable usage is limited to phytoplankton dominated oceanic waters. For illustration, the curves created according to this model have been integrated in Figures 2.24 and 2.25. In case of the CDOM-rich Baltic the difference of the two modeled total absorptions is obvious.

The absorbing components are subject to natural fluctuations due to depth and the season of the year, which applies in particular to the chlorophyll-containing phytoplankton [95, 97]. The chlorophyll concentration and accordingly the absorption can show pronounced peaks in the vertical water column at the photic zone up to 150 m depth. This of course corresponds to UOWC with vertical links, and this topic is investigated in [98]. A good general reference of absorption values and their variability for different areas is given in [94].

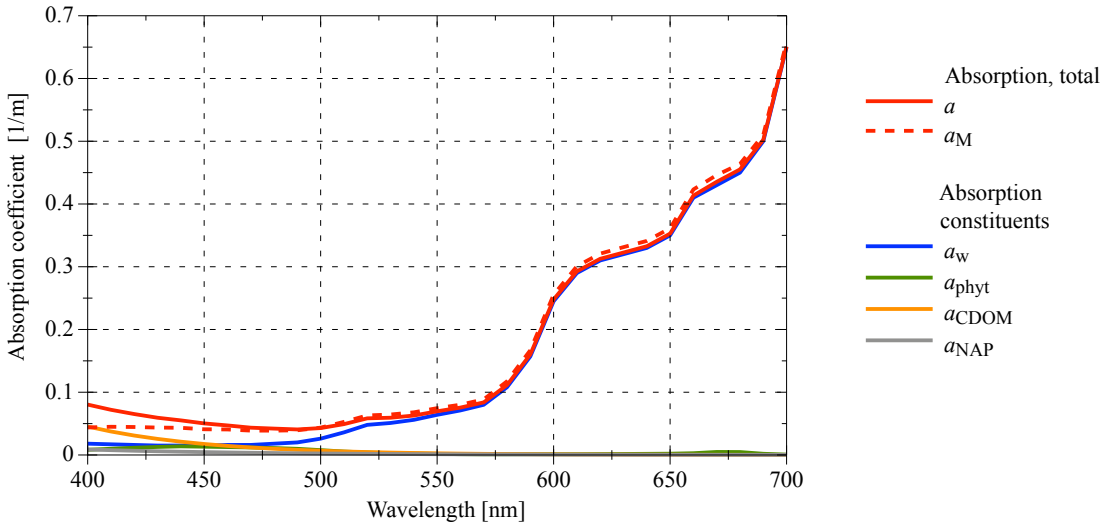

Figure 2.25: Modeled total spectral absorption $a(\lambda)$ and its constituents as well as the total of the simplified model $a_{\mathrm{M}}(\lambda)$ for the Atlantic Ocean. Parameters are extracted from [94] and represent typical values for this area. (Sea water, chl=0.2 mg/m^3, $a_{\mathrm{CDOM}}(433)$=0.02 1/m and S_{CDOM}=0.019, $a_{\mathrm{NAP}}(433)$=0.05 1/m and S_{NAP}=0.013).

Scattering

The effect of scattering of light in water can be described as the process when the path of a photon is changed in a direction by interaction with molecules or particles. This causes spatial and temporal dispersion, and the latter is discussed at the end of this subsection. With respect to Mobley [87], the spectral scattering coefficient is defined as depicted in Figure 2.26 and by following equation:

$$b(\lambda) = \lim_{\Delta r \to 0} \frac{\Phi_s(\lambda)}{\Phi_i(\lambda)} \cdot \frac{1}{\Delta r}. \tag{2.30}$$

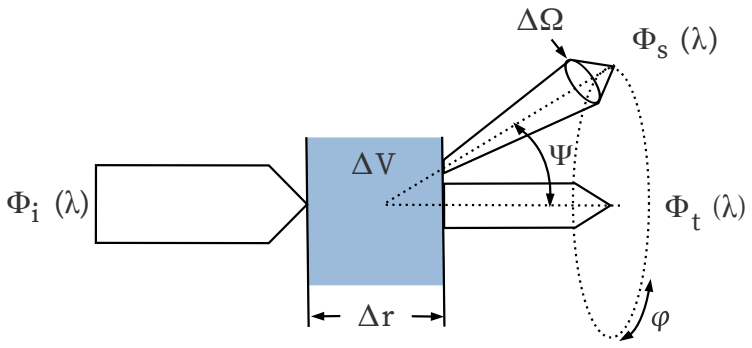

Figure 2.26: Drawing shows the geometry to define spectral scattering in a volume of water as given by Mobley. $\Phi_{\mathrm{s}}(\lambda)$ is the part of the monochromatic incident beam $\Phi_{\mathrm{i}}(\lambda)$ that is scattered in a volume ΔV of water with thickness Δr, $\Phi_{\mathrm{t}}(\lambda)$ is the transmitted power, and units are W/nm. The light is scattered into a solid angle $\Delta\Omega$ in direction of Ψ, and the azimuthally symmetry of these events is depicted by φ.

Mobley [87] categorizes scattering into three size-related domains:

- b_w, molecular scattering by the water itself ($<< \lambda$).
- b_p, scattering by large organic and inorganic particles ($> \lambda$).
- scattering by turbulence, i.e. changes in refractive index ($>> \lambda$).

The total spectral scattering coefficient $b(\lambda)$ was modeled by Haltrin [99], as the sum of scattering by the water itself and scattering based on particles, and is given by:

$$b(\lambda) = b_w(\lambda) + b_p(\lambda). \tag{2.31}$$

The unit of the scattering coefficient is 1/m, it only gives the strength of scattering and does not consider the angular distribution. Scattering due to turbulence is not included, and a description of this topic is given in Chapter 2.2.3. The molecular scattering can be described as elastic scattering by Raleigh equations, assuming spherical particles. The modeling of the spectral scattering by the water itself $b_w(\lambda)$ can be performed by [99]:

$$b_w(\lambda) = b_w(\lambda_0) \cdot \left(\frac{\lambda_0}{\lambda}\right)^{4.332}. \tag{2.32}$$

Reference values are given in [100]. The spectral distribution and the magnitude are shown in Fig. 2.27. The contribution of molecular scattering to the total scattering is relatively small.

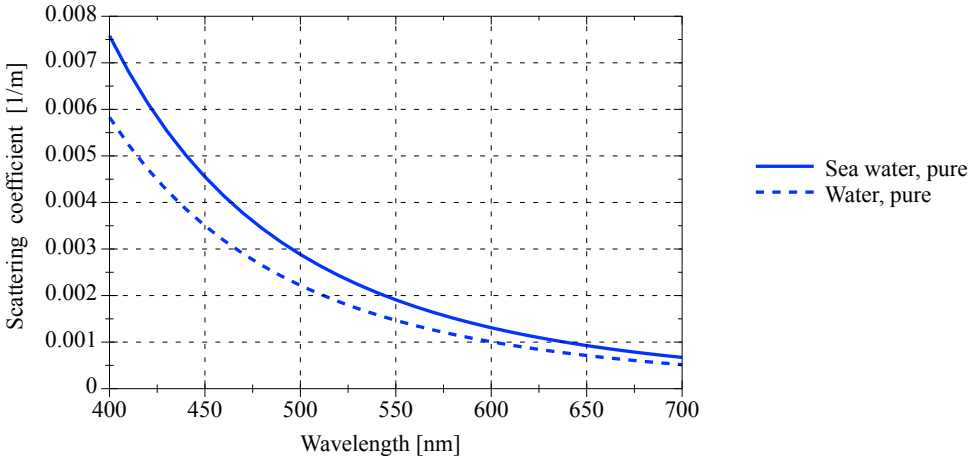

Figure 2.27: Spectral scattering $b_w(\lambda)$ of pure water and pure sea water. Plotted with values calculated from (2.32) and parameters $b_w(\lambda_0)$=0.00583 1/m for pure water, $b_w(\lambda_0)$=0.00758 1/m for pure sea water and λ_0=400 nm.

The scattering due to particles $b_p(\lambda)$ depends on the size and concentration. Modeling is mostly based on the Mie theory. With respect to the model of Haltrin [99], as given in (2.33), the size is divided into two fractions and expressed as:

$$b_p(\lambda) = b_s(\lambda) \cdot C_s + b_l(\lambda) \cdot C_l. \tag{2.33}$$

The first are small particels less than 1 μm in size and of mineral origin, the NAP. The second are large particles over 1 μm in size and of biological origin, like phytoplankton. The contribution of CDOM to scattering is mostly neglected [101]. The specific scattering coefficients for small and large particles b_s and b_l, both in m^2/g, are given by:

$$b_s(\lambda) = 1.1513 \cdot \left(\frac{400}{\lambda}\right)^{1.7} \tag{2.34}$$

and

$$b_{\mathrm{l}}(\lambda) = 0.3411 \cdot \left(\frac{400}{\lambda}\right)^{0.3}. \tag{2.35}$$

Values for particle concentrations in different water types can be found in [102]. These concentrations for the fraction of small particles C_{s} and for large particles C_{l}, both in g/m^3, can also be expressed through the chlorophyll concentration *chl*:

$$C_{\mathrm{s}} = 0.01739 \cdot chl \cdot e^{0.11631 \cdot chl} \tag{2.36}$$

$$C_{\mathrm{l}} = 0.76284 \cdot chl \cdot e^{0.03092 \cdot chl}. \tag{2.37}$$

The range of validity for chlorophyll concentrations *chl* is from 0 to 12 mg/m^3. Integrating equations (2.34)-(2.37) into (2.33) allows us to express the particulate scattering by one parameter - the chlorophyll concentration. A corresponding example is shown in Fig. 2.28. These models of the particulate scattering and the parametrization through chlorophyll concentrations are approximate. Real measurements and modeled values can show large differences, since particles size distributions and refraction indices vary naturally and cannot be sufficiently parameterized by the concentrations [87]. The role of scattering seawater constituents is detailed described in detail by [103]. At this point it should be noted again, that chlorophyll carrying seawater constituents can be subject to strong seasonal changes and show vertical peaks in the upper oceanic zone.

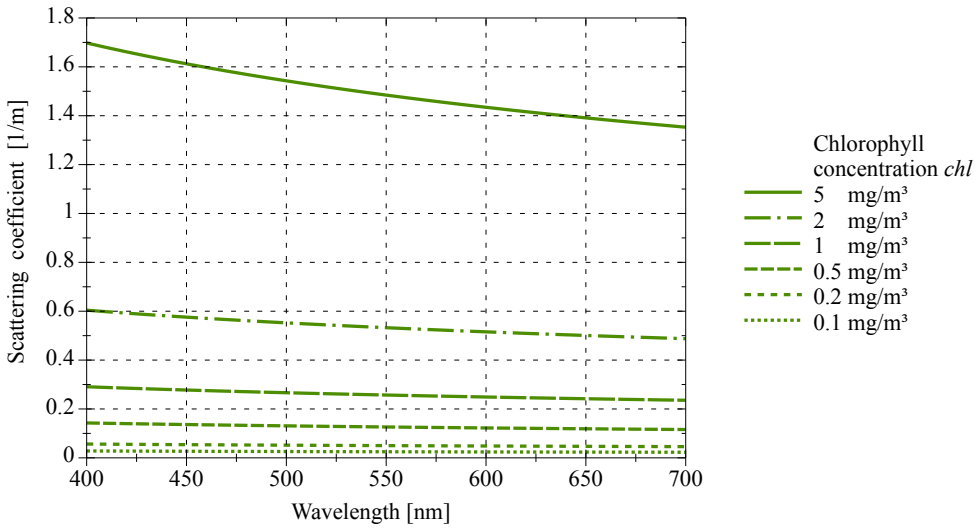

Figure 2.28: Spectral scattering $b_{\mathrm{p}}(\lambda)$ of particles in sea water expressed by varying chlorophyll concentrations *chl*. Plotted with values calculated from (2.33)-(2.37).

The second characteristic feature of scattering is the angular distribution of the scattered photons, which is presented in Fig. 2.26 and described by the volume scattering function (VSF):

$$\beta(\lambda, \Psi) = \lim_{\Delta r \to 0} \lim_{\Delta \Omega \to 0} \frac{\Phi_{\mathrm{s}}(\Psi, \lambda)}{\Phi_{\mathrm{i}}(\lambda) \Delta r \Delta \Omega}. \tag{2.38}$$

The physical description of the VSF is the scattered intensity per unit incident irradiance per unit volume of water [104]. An extensive mathematical derivation can be found in [87].

Almost five decades ago, Petzold carried out precise scattering measurements for different types of water [105]. The obtained total VSFs, $\beta(\Psi)$ are still widely cited and used as references, cf. Fig. 2.29. Since the measurements were only conducted at one fixed wavelength $\lambda = 514$ nm, the variable λ is omitted. The wavelength dependence of the VSF in the blue to green color regime is

generally small [106], and will therefore not be considered in the following. The total VSF $\beta(\Psi)$ is the sum of the contributions by the particulate scatter $\beta_{\mathrm{p}}(\Psi)$ and scattering by the water itself $\beta_{\mathrm{w}}(\Psi)$:

$$\beta(\Psi) = \beta_{\mathrm{p}}(\Psi) + \beta_{\mathrm{w}}(\Psi). \tag{2.39}$$

The molecular scattering by the water itself is orders of magnitude smaller than scatter from particles and can be neglected in most cases, except in the clearest natural waters at large backscattering angles. According to Mobley [87], the main statements about the progression of the VSF in natural waters are the following: it shows a strong peak in forward direction, one half of the total scattering happens within 0° and less than 10°, and backscattering is typically a few percent of the total scattering. To generate a typical phase function from Petzold's VSFs for different water types, the water part is subtracted from each curve, then each curve is normalized by the corresponding particle scattering coefficients b_{p}, see (2.40). Then an average is calculated, resulting in the particle phase function $\tilde{\beta}_{\mathrm{p}}(\Psi)$ which can be physically interpreted as a probability distribution of scattering as function of angle Ψ, or in other words as a probability density function (PDF):

$$\tilde{\beta}_{\mathrm{p}}(\Psi) = \frac{\beta(\Psi) - \beta_{\mathrm{w}}(\Psi)}{b_{\mathrm{p}}}. \tag{2.40}$$

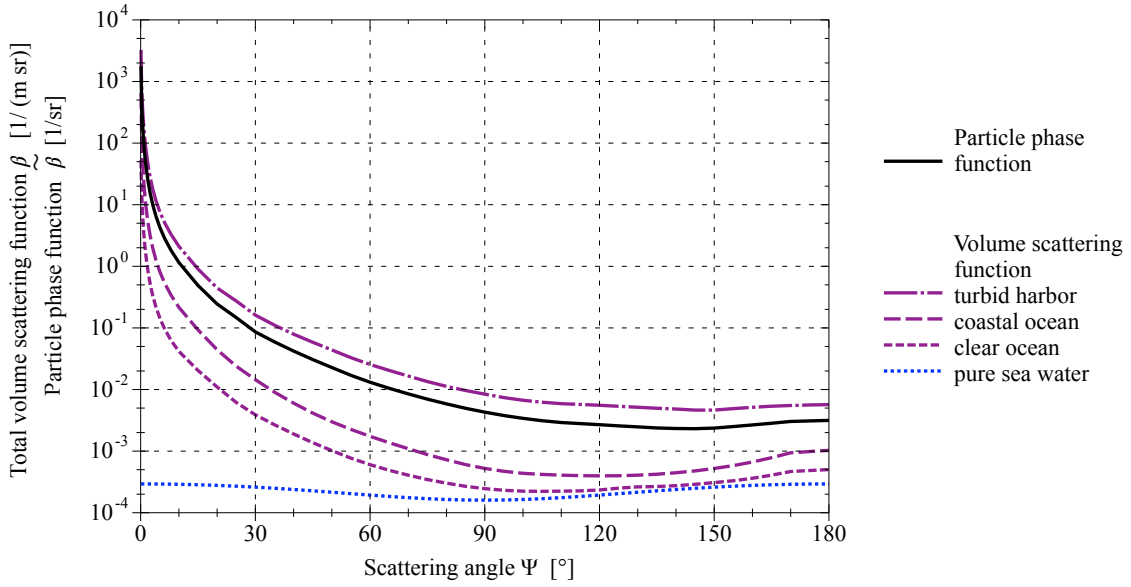

Figure 2.29: Petzold's measured volume scattering functions for different water types and the calculated phase function, based on tabulated data from [87]. The graphs clearly show that the forward scattering takes place predominately with small angles of Ψ and that backscatter with $\Psi > 90°$ occurs rarely.

Precise measurements of scattering functions are generally demanding. Consequently they have not been performed very often in the field. Since they are a basic requirement for modeling the light propagation under water, different models of the phase function models have been developed. The most commonly used include the one- and two-term Henyey-Greenstein (OTHG, TTHG) models, the Fournier-Forand (FF) and the Sahu-Shanmugam (SS) model [107, 108, 109, 110]. Experiments are often required in addition to numerical simulations. Since sea trials are costly and laboratory tests with different types of sea water are impractical, tank tests with fresh water and scattering agents simulating ocean water can be used instead [104, 111]. Commercial antacid (e.g., Maalox) was successfully used as a scattering medium, as its phase function is close to real oceanic water types, and the attenuation can be adjusted by using different concentrations of the agent. Investigations to achieve more realistic simulated water parameters can be found in [112].

Attenuation

The sum of the spectral absorption and scattering coefficients is giving the spectral beam attenuation coefficient $c(\lambda)$:

$$c(\lambda) = a(\lambda) + b(\lambda). \tag{2.41}$$

For an exemplification, the total absorption of the examples given in Figs. 2.24 and 2.25 and the related particulate spectral scattering are merged, neglecting the molecular scattering. The results in Figs. 2.30 and 2.31 show a typical spectral attenuation curve for a coastal and an oceanic water, respectively. These examples are representatives for oceanic and coastal waters and depict the different total values as well as the spectral dominant constituents. It is worth mentioning that the meaning of scattering in the context of attenuation is that a photon is scattered off the straight line path from transmitter to receiver and is lost, i.e. without multiple scattering back to the track. This is analogous to the absorption of photons which are also lost in terms of countability.

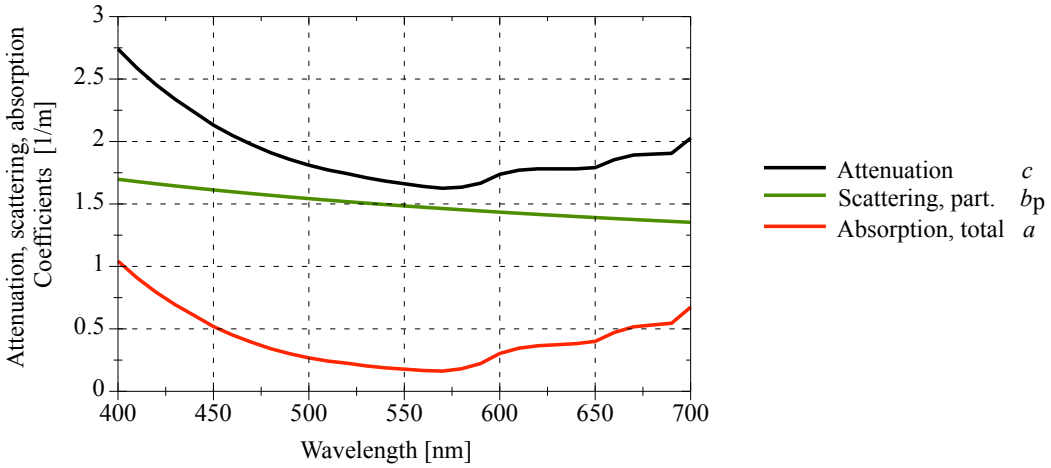

Figure 2.30: Spectral attenuation $c(\lambda)$ as a sum of its components total absorption $a(\lambda)$ and particulate scattering $b_\mathrm{p}(\lambda)$, representing typical values for the Baltic Sea as an example for coastal waters, cf. Figs. 2.24 and 2.28. The attenuation is mainly determined by the scattering.

Commonly used in conjunction with attenuation is the spectral scattering albedo $\omega_0(\lambda)$, which represents the relation of scattering to attenuation:

$$\omega_0(\lambda) = \frac{b(\lambda)}{c(\lambda)}. \tag{2.42}$$

The values of ω_0 at a wavelength of 514 nm roughly range from 0.2 for clear oceanic water to 0.85 for turbid harbor water. The beam attenuation coefficient $c(\lambda)$ is used in Beer's law, which describes the remaining radiant flux Φ in W of an initial value Φ_0 after traveling a distance of r through a medium with $c(\lambda)$:

$$\Phi(r, \lambda) = \Phi_0(\lambda) \cdot e^{-c(\lambda) \cdot r}. \tag{2.43}$$

The term $c(\lambda) \cdot r$ is often stated as the attenuation or e-folding length, and one attenuation length $c(\lambda) \cdot r = 1$, meaning that $e^{(-1)}$ is equivalent to a decrease in intensity of ~63 %. For example, one attenuation length of water with c=0.4 1/m is 2.5 meters, whereas a more turbid water with c=2.2 1/m is only 0.45 meters.

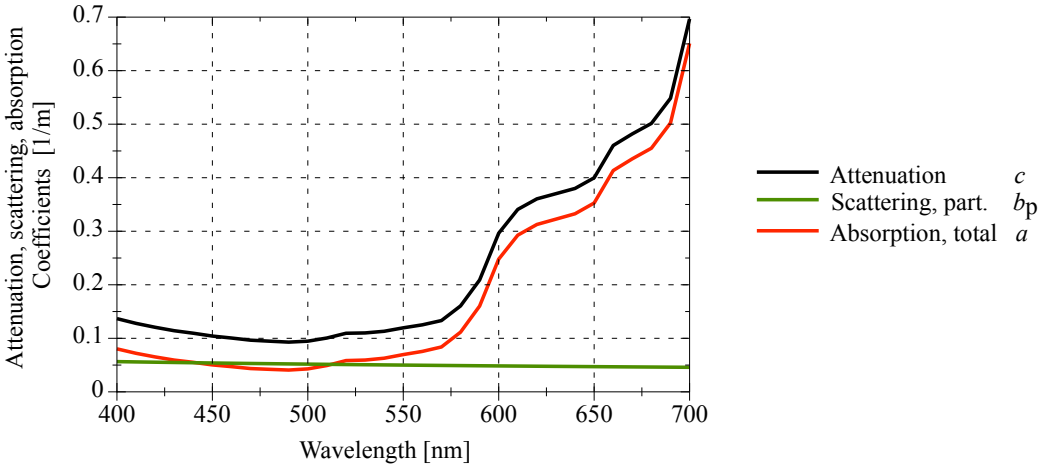

Figure 2.31: Spectral attenuation $c(\lambda)$ as a sum of its components total absorption $a(\lambda)$ and particulate scattering $b_p(\lambda)$, representing typical values for the Atlantic as an example for oceanic waters, cf. Figs. 2.25 and 2.28. It is evident that the attenuation is dominated by the total absorption at longer wavelengths.

2.2.2 Classification of Water Types

More than 50 years ago, N.G. Jerlov developed a classification of water bodies based on the AOP, more specifically on the spectral optical attenuation depth, which is the inverse of the spectral diffuse attenuation coefficient $K_d(\lambda)$ [101]. The water types were divided into five typical oceanic spectra I, IA, IB, II, III and nine typical coastal spectra 1C through 9C, from low to high attenuation, respectively. A graphical overview is given in Figure 2.32.

In contrast to the diffuse attenuation coefficient $K_d(\lambda)$, which is based on the downwelling irradiance of sunlight, the spectral beam attenuation coefficient $c(\lambda)$ is based on IOP and is valid for collimated narrow photon beams [87]. Please refer to Fig. 2.32 and note difference of diffuse and beam related values for the same class. The share of the attenuation component is shown in Fig. 2.33.

The strict allocation into classes should be viewed with some caution, as the parameters of natural waters may vary by seasonal fluctuations, as well as local occurrences. The values of the classes should be interpreted as a mean with smooth transitions. The global distribution of water types as a general overview can be found in [113], and a more detailled map of northern seas is given in [114]. Values obtained from these should only serve as a rough guide for open seas. Waters closer to the coast or even habour waters are often murkier and more variable in optical parameters, due to underlying influence factors such as shifting tides or fresh water entries.

Another commonly used classification is the splitting into Case-1 and Case-2 waters. Most oceanic waters with phytoplankton dominated IOPs are of Case-1 category, and globally this applies to more than 80 % of all waters. Coastal, inland and all other waters belong to Case-2, where CDOM and NAP also are significant constituents [115].

Furthermore, a simple subdivision into oceanic, coastal and habour waters is widely used in the literature, based on samples and measurements from Petzold in 1972 and supplemented by Mobley [100], cf. Table 2.4.

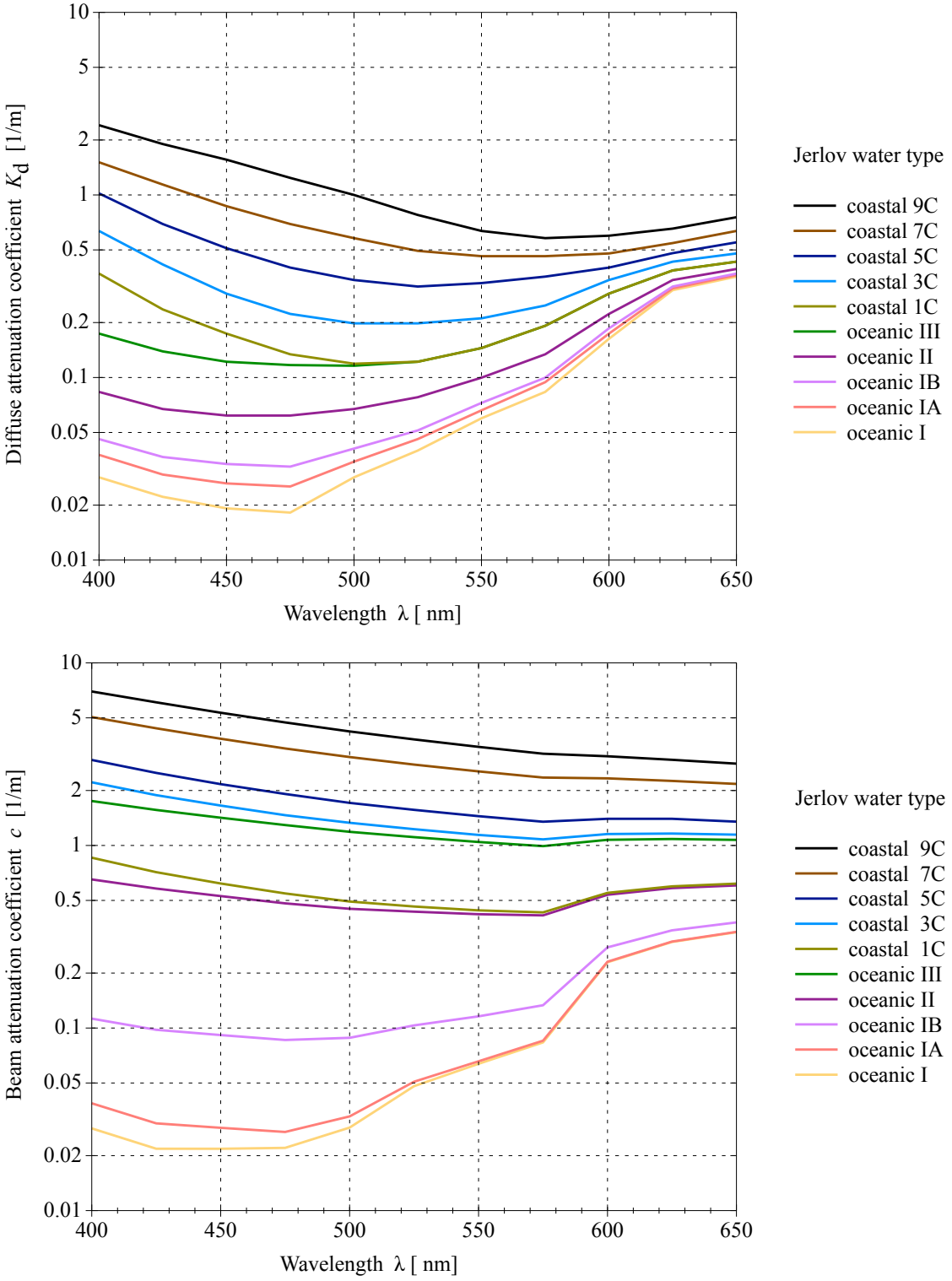

Figure 2.32: Spectral diffuse attenuation K_d shown in the upper diagram, and beam attenuation c in the lower, both for Jerlov water types I to 9C. Plotted from database of [102], (data of 5C for 600 nm to 650 nm are interpolated).

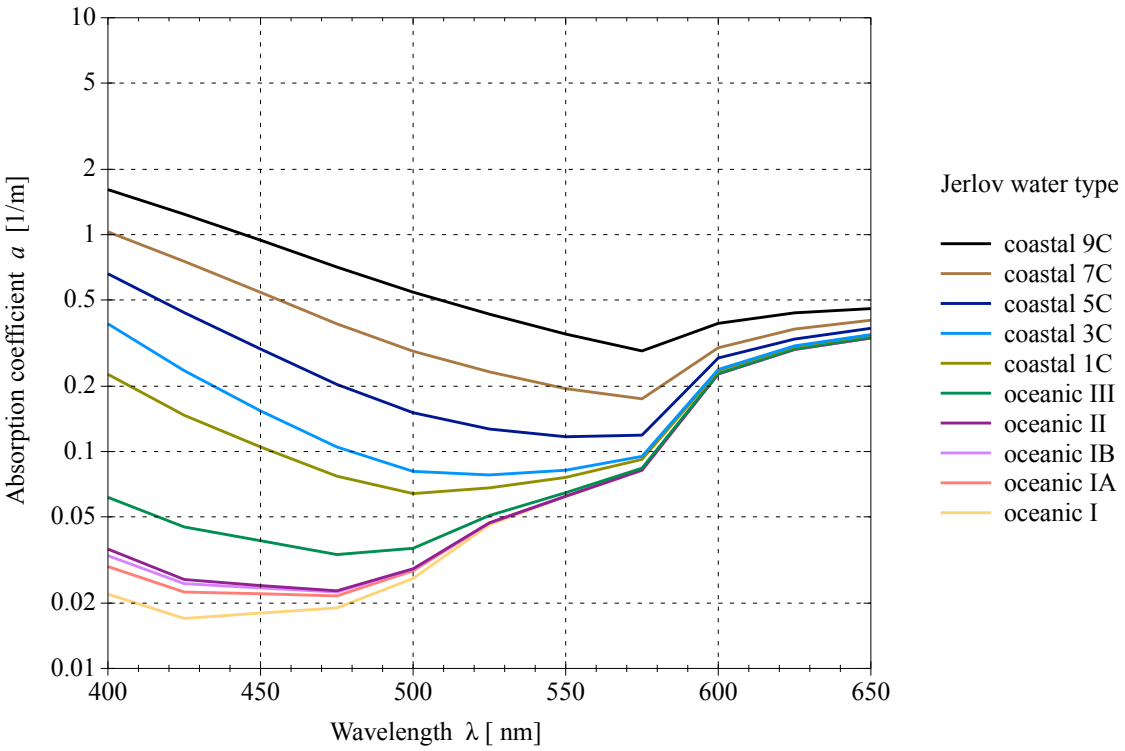

Figure 2.33: Spectral absorption a for Jerlov water types I to 9C. Plotted from database of [102], (data of 5C for 600 nm to 650 nm are interpolated).

Table 2.4: Properties for three different waters at $\lambda = 514$ nm.

Class	Absorption a [1/m]	Scattering b [1/m]	Attenuation c [1/m]	Albedo ω_0
clear oceanic	0.114	0.037	0.151	0.245
coastal ocean	0.179	0.219	0.398	0.550
turbid habour	0.366	1.824	2.190	0.833

In the case of widely varying oceanic optical parameters a classification can only provide a rough estimate of values, and a significant improvement can be achieved through measurements. The variability of water optical parameters for UOWC systems is described in [116] and a general overview of instrumentation for ocean monitoring is given in [117]. Measurements of optical water parameters can be carried out with in situ underwater transmissiometers [118]. Instruments of these type can be deployed at variable depths and are able to record the attenuation and absorption values, for single wavelengths or spectral, depending on the version. Since optical water properties have a large impact on UOWC systems, is it recommendable to make such measurements and state the values as they are essential for performance assessments. An experiment in the field including such measurements is described in Section 5.3.

2.2.3 Refractive Index, Turbulence and Scintillation

Inhomogeneity of a material or medium like seawater causes changes in the refractive index n and induces scattering. Beside suspended particles and seawater molecules, this is another cause of scattering. The refraction index of seawater is dependent of the parameters temperature T, salinity ϵ, wavelength λ and pressure p (i.e., density change by water depth). More details can be

found in [119, 120]. The variation of these parameters is represented as refractive index diagrams in Figures 2.34, 2.35 and 2.36. The refractive index of seawater shows a relative linear increase with rising salinity and pressure.

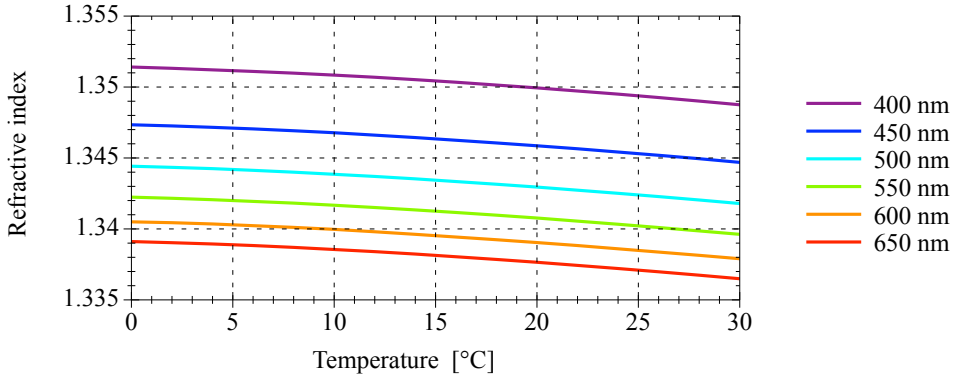

Figure 2.34: Spectral refraction index of seawater for temperature variation. Valid for a depth of 0 meters and a salinity of 35 ‰. Plotted from tabulated data of [119].

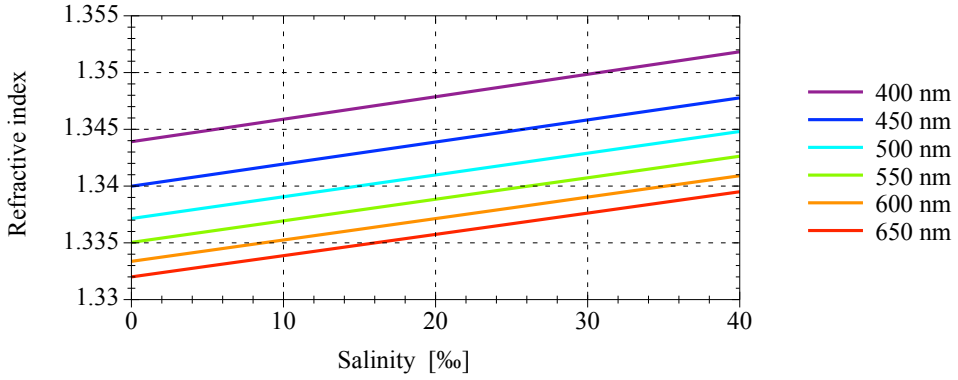

Figure 2.35: Spectral refraction index of seawater for salinity variation. Valid for a depth of 0 meters and a temperature of 10°C. Plotted from tabulated data of [119].

Generally, the refractive index shows a slow and spacious change, but the sensitivity to these parameters is ultimately based on the naturally occurring variation. Eddies are temporary loops of swirling water, and circular currents. Large eddies cascade down to smaller and smaller ones until they finally lose their energy. Within these eddies the diffusing temperature and or salinity zones form curved boundaries with focusing and defocusing effects, and the oceanic turbulence thus generates optical turbulence. The effect on the refractive index is known as scintillation. The fluctuation of the optical intensity is given by the scintillation index σ^2, which is defined as the normalized root mean square deviation of the intensity I_e:

$$\sigma^2 = \frac{(\langle I_e^2 \rangle - \langle I_e \rangle^2)}{\langle I_e \rangle^2}. \tag{2.44}$$

Weak turbulent regimes are indicated by $\sigma^2 << 1$ and strong ones by $\sigma^2 >> 1$, cf. [121, 122].

Scintillation can have a serious influence on the UOWC systems performance, the BER can increase and in turn the range can reduce accordingly. Some literature has been published on this

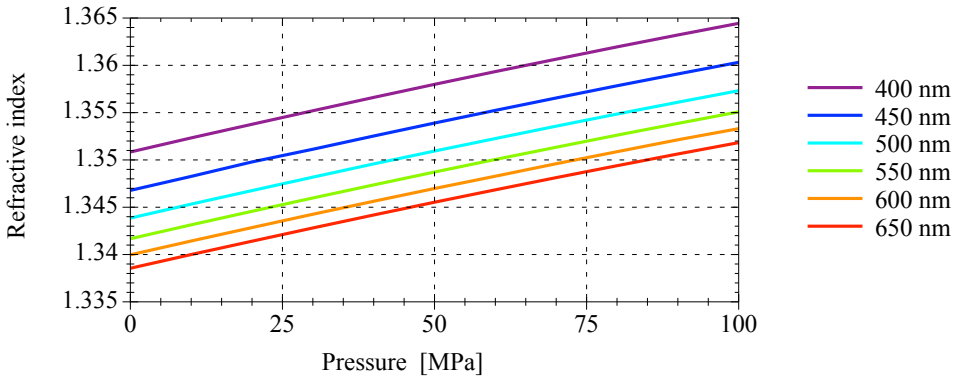

Figure 2.36: Spectral refraction index of seawater for pressure variation. Valid for a salinity of 35 ‰ and a temperature of 10°C. A pressure of 10 MPa equals to 100 bar and an approximate depth of 1000 meters. Calculated and plotted from tabulated data of [119].

topic in the recent years, but is mostly related to laser-based systems, since these are generally more affected due to typically longer ranges and pointing issues compared to LED-based systems. Further information on laser-based systems can be obtained from [123, 124, 125, 126, 127, 128]. Publications on the impact of turbulence to LED-based systems are rare, in [86] investigations were carried out with more extreme parameters, whereas in [129] moderate parameters were used, resulting in relatively small values σ^2 of < 0.08. For practically achievable distances of a few tens of meters in maximum these values are even less, and this clearly indicates a limited influence of weak turbulence to LED-based UOWC systems.

Investigations on the turbulence of the moving ocean and propeller induced scintillation can be found in [130, 131]. Bubbles are another possible reason for turbulence, and research on this topic is given in [85, 132, 133, 134].

2.2.4 Solar Spectral Irradiance and Ambient Light Underwater

In many publications regarding UOWC and related simulations darkness is considered. This assumption is generally correct for the deep sea in the bathypelagic zone (midnight) at depths of 1000 meters and more. In the adjacent mesopelagic zone (twilight) from 200 meters to 1000 meters and particularly in the epilagic zone (sunlight) or photic zone from the surface to 200 meters depth, sunlight penetrates the water column and is important for marine life, but can be a hurdle for UOWC systems.

The ambient light underwater is the result of naturally occurring solar irradiance, and a reference spectrum is given in Fig. 2.37. The solar radiation's magnitude and spectrum has strong influencing factors, such as the zenith angle of the sun, cloud coverage, wind speed or moisture level in the atmosphere. The characteristic of the distributed light reaching the sea surface changes from directed in clear skies to diffuse in overcast conditions, as well as the magnitude of irradiation is decreased to a tenth. Within the water, directed light travels longer distances or penetrates to larger depths, and it becomes increasingly diffuse due to scattering. Within the water column light is distinguished between up- and downwelling irradiance, and each contains all directions in a hemisphere, cf. Fig. 2.38. The amount of the downwelling irradiance can be orders of magnitude larger than the upwelling, the viewing direction of a sensor can therefore be of great importance.

The area of least light attenuation of seawater is rougly in the range from 400 to 600 nm, and the maximum of solar radiation approximately 450 nm to 600 nm. To reduce or avoid solar disturbance, the gaps in the spectrum (Fraunhofer lines) theoretically could be used, but their bandwidth is very narrow. An efficient utilization of LEDs is therefore not feasible. Lasers should

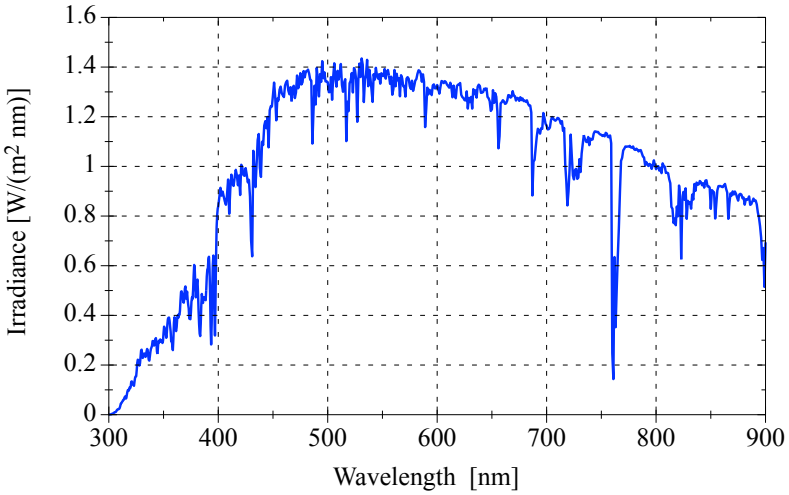

Figure 2.37: Direct spectral solar irradiance at the Earth's surface for normal direction at a solar zenith angle of 48.2° and standard atmospheric conditions. Plotted from tabulated data of Reference Solar Spectral Irradiance ASTM G-173-03 [135].

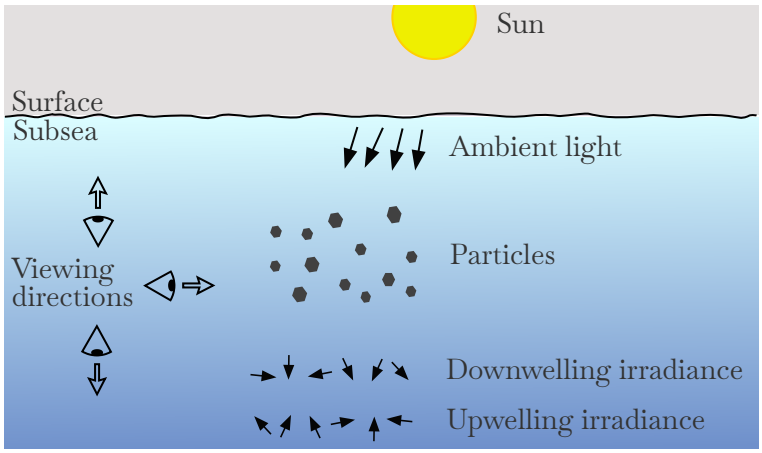

Figure 2.38: Directions and structure of ambient light underwater.

have exactly the same wavelength, and extremly narrow bandpass filters would be necessary, which is difficult to achieve in reality. Another approach has been investigated by Farr [136]. The use of short wavelengths in the band of 350 nm to 400 nm where the solar radiation drops off. Kedar [137] examined the application of UV light of 200 nm to 280 nm for UOWC in the so-called solar blind range below 300 nm. Both attempts have to battle the increased seawater attenuation and availability of efficient light sources, to be able to operate in the region of reduced or even without solar radiance. Simulations of UOWC networks under realistic environmental conditions that explicitly include different solar illumination can be found in [138, 139]. More in-depth information and further research on ambient light filtering is provided in Section 3.2.

2.2.5 Underwater Light Field Fluctuations

Air-sea interactions, in conjunction with sunlight can have a strong influence on the variability of the underwater light field. Wind and induced waves generate a dynamic surface at the medium change from air to water for direct sunlight. This causes focussing and defocussing effects in the near surface water. Arising radiance peaks in shallow waters can have a factor of 10 compared

to the mean values, the time scale can be in the range of 1 ms to 10 s, and the spatial extent is from 1 cm to 100 m [140]. However, in depths of 30 m fluctuations of 50 % can still be observed [141]. These effects are generally stronger in the yellow-red spectral regime compared to the blue-green one [142]. UOWC systems operated in shallow water can be disturbed by such occurrences through increased noise levels for short time intervals, or even worse the system can be driven into saturation.

2.2.6 Bioluminescence, Fluorescence and Raman Scattering

Another source of possible disturbance for UOWC can be light induced by effects like bioluminescence, fluorescence and Raman scattering. Although the amount of light of these effects is generally small, when they take place in close proximity to the receiver they may be able to generate noteworthy disturbances, especially when the communication signal is weak and the detector is very sensitive. These effects can be significant in the dark at large water depths or at night. Implications are more likely to be expected in multicolor or unfiltered applications.

Bioluminescence is the term for light emitted by marine organisms, sized from fish down to bacteria. The occurrence can be in all depths as well as all geographic zones of the oceans. The color is species dependent and is in the blue to yellow regime, where the light attenuation of the oceans is also least. The spectral bandwidth of the emission can take on values from 26 nm to 100 nm FWHM, and the duration varies from tens of milliseconds to continuous emission.

Raman scattering is the event of inelastic scattering of photons in matter, in this case by water molecules. The photons path is redirected and energy is exchanged, the wavelength shifts from λ' to a longer wavelength λ. For instance blue light with λ' =450 nm will be Raman redistributed in seawater to green in a relative narrow band of 20 nm at $\lambda = 530$ nm. Calculations can be done by using the Raman wavelength redistribution function.

Fluorescence is also an inelastic scattering process of noteworthy relevance in the water medium. Incident photons are absorbed by molecules of substances in the water, and after a very short time (in the order of nanoseconds to picoseconds) they are emitted again with a longer wavelength. Basically it can be seen as an absorption followed by an emission. As an example, the excitation of seawater containing yellow matter and chlorophyll with λ' or $\lambda_{ex} = 450$ nm, would result in an emission λ or λ_{em} with a wider band from approximately 450 nm to 600 nm for yellow matter and with a narrower band from 660 nm to 720 nm for chlorophyll. An extensive explanation of these topics is given in [87, 143].

2.3 Chapter Summary

In this chapter, the fundamental principles and impacts of underwater optical wireless communication channels have been described. This includes the optical path between the source and the detector when entering or leaving the water medium. Refraction, transmittance and reflectance are significant here. The link between transmitter and receiver can be established in different configurations, and the direct line-of-sight represents the major type and the base for subsequent examinations. The resulting link budget has been developed, and two distance-dependent terms have a decisive influence, which are the exponential decrease by the Beer-Lambert law and the inverse square law.

Relevant basics of photonic devices like spectral characteristics and the operating ranges of LEDs and photodetectors with respect to UOWC were given, as well as the required transimpedance amplification and some aspects of digital communications. A simulation example using basic parameters has demonstrated the orders of magnitude to be expected with respect to irradiance, photocurrent and distance.

As key elements of large impact, the inherent optical properties of the water, the absorption and the scattering have been described more in detail. This concerns the constituents, modeling,

spectral properties and the resulting attenuation. The classification of a wide range of natural waters to several oceanic and coastal types with respect to Jerlov have been presented. Temperature, salinity and depth influences on the water's refractive index are discussed, which can lead to turbulence and scintillation. Other potentially disturbing effects like bioluminescence, fluorescence and Raman scattering are presented.

Since UOWC does not only take place during dark nights or in large water depths, interfering ambient light due to solar irradiance must be considered. The challenges here arise from the broad spectrum, comparatively large intensities, a variable structure, and a distinct directionality.

Chapter 3

Examination and Optimization of Selected UOWC System Components

3.1 Influencing Factors of the LED Wavelength Selection

In the field of the UOWC, the choice of the operating wavelength or color is commonly based on two realities: the least attenuation window of seawater lies in the blue to green color area and within this range blue LEDs are the most efficient. The short wavelength region on the left side of the least attenuation window was examined by [136], where the application of near ultraviolet (NUV) LED sources has been proposed for UOWC. The solar irradiance decreases in this UV range compared to the visible spectral range, thus leading to a higher tolerance to daylight, with the disadvantage of increased absorption by the water. In [144] the optimum wavelength for UOWC in highly turbid habour water has been experimentally investigated. Red LED light turned out to be the best choice under such extreme conditions. The red light is also subject to a very strong attenuation, which only allowed very low ranges.

In our own publication [35] the potential of using converted green LEDs in coastal waters was examined. Based on this work, the following section takes a broader look at this topic. The question of the optimal LED wavelength does not always offer a simple answer, therefore this makes it necessary to take a closer look at the relevant aspects. In the case of UOWC, the goal can be described as follows: the electrical power used on the transmitter side should generate as much current as possible in the detector on the receiver side, after the medium has been passed. In the following, the electrical and physical characteristics of the LED source, the medium water and the photodetector are presented in more detail. Subsequently, the wavelength-dependent threefold relationship of efficiency, responsivity, and attenuation is provided as a context.

3.1.1 Propagation Window in Natural Waters

The spectral characteristic of light attenuation for different seawater types (Jerlov water types) is typically given in tables or logarithmic scaled graphics, cf. [102] and Section 2.2.2. Besides the different water types and the wavelength, the structure of the incident light must be taken into account. Of the three parameters normally available, the attenuation coefficient c is valid for collimated beams, the diffuse attenuation coefficient K_d is related to diffuse downwelling sunlight, and the absorption coefficient a is independent from the light structure. Of course the question arises, which exponential coefficient should be applied for extinction calculations of LED-based underwater systems. Depending on the type and the optics used, LEDs exhibit beam angles ranging from a few degrees to more than a hundred degrees, as well as different patterns or intensity distributions. As point sources LEDs are essentially not diffuse, but rather more or less directed, although not strongly collimated like a laser beam. Therefore, at first it can be stated that the beam attenuation c represents the upper bound of the exponential coefficient, and the absorption a is the lower limit. The use of the interjacent value K_d can only represent a compromise for LED utilization underwater, and an individual system related value K_sys would be more accurate. Simulations are the best way to illustrate the impact of applying the different extinction coefficients. The results according to (2.17) for the irradiance at the receiver for one

oceanic and one coastal water type each, at two wavelengths and the same initial optical power and without inclination, are shown in Figs. 3.1 and 3.2. The parameters used are given in Tables C.1 and C.2, which can be found in the appendix.

In order to obtain the ranges of least attenuation for the different water and extinction coefficients, it is necessary to evaluate the corresponding table values and the graphs generated from them, cf. Figs. 2.32 and 2.33. A combined representation of these attenuation minimum areas is contained in Fig. 3.3, based on a two-sided margin of 20 %. The change in beneficial wavelength from blue in clear oceanic waters to cyan and further to green in intermediate coastal waters is confirmed. Furthermore it can be observed from the progression, that in very turbid coastal waters yellow is getting the most advantageous color. An imagined continuation of the trend for even more turbid waters, as found in habours or lakes, indicates wavelengths even in the orange to red regime to be suitable.

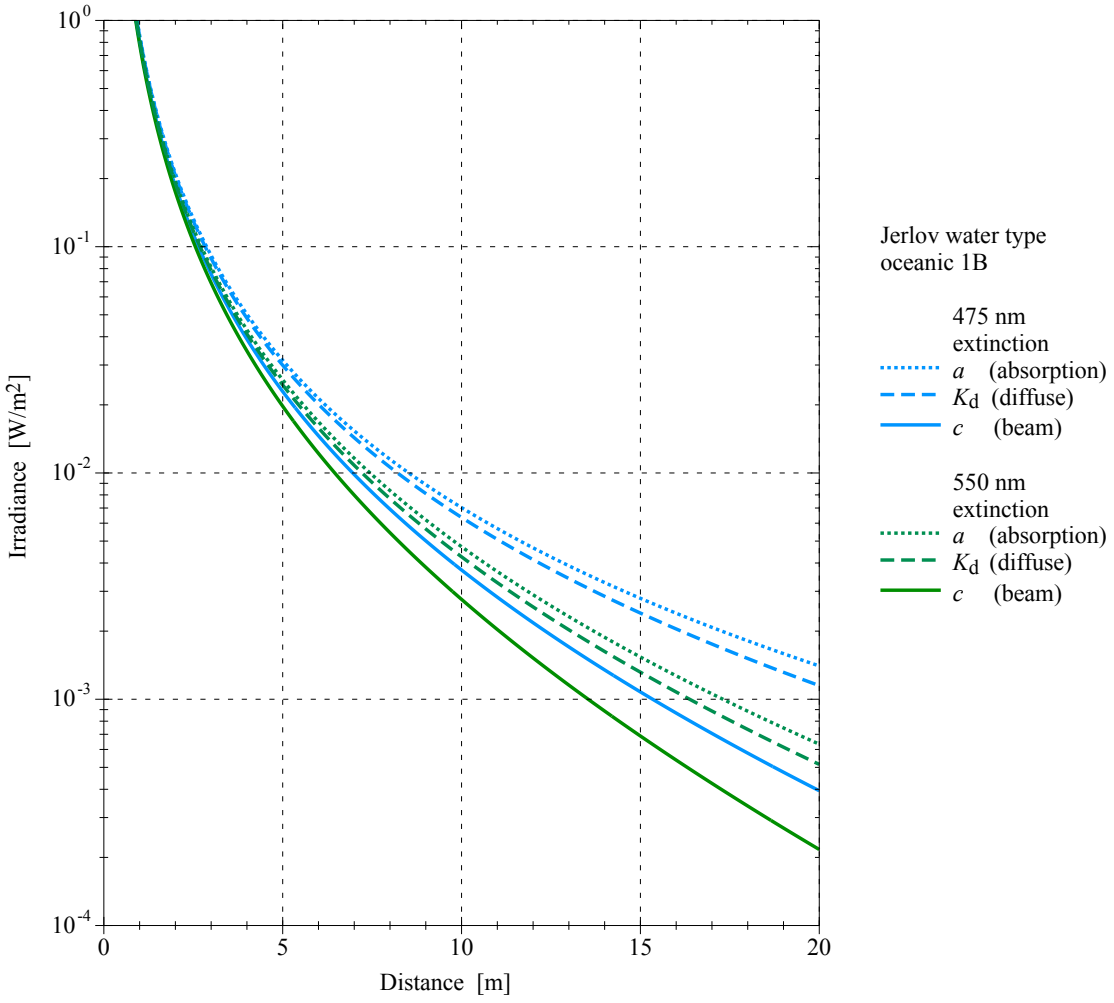

Figure 3.1: Simulated irradiances at the receiver for oceanic water. Calculation for two source wavelengths and different extinction coefficients and otherwise equal source characteristics. Detailed parameters are given in Tables C.1 and C.2.

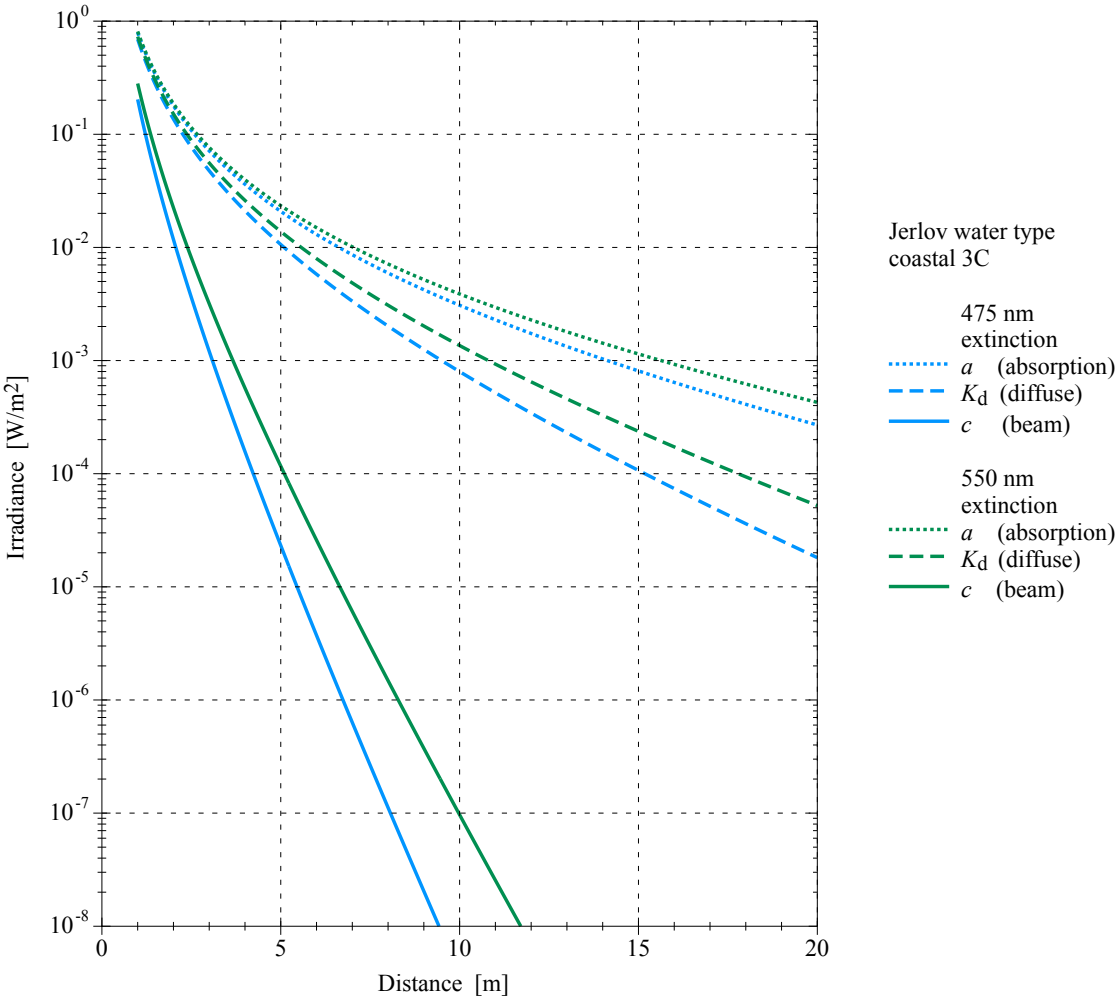

Figure 3.2: Simulated irradiances at the receiver for coastal water. Calculation for two source wavelengths and different extinction coefficients and otherwise equal source characteristics. Detailed parameters are given in Tables C.1 and C.2.

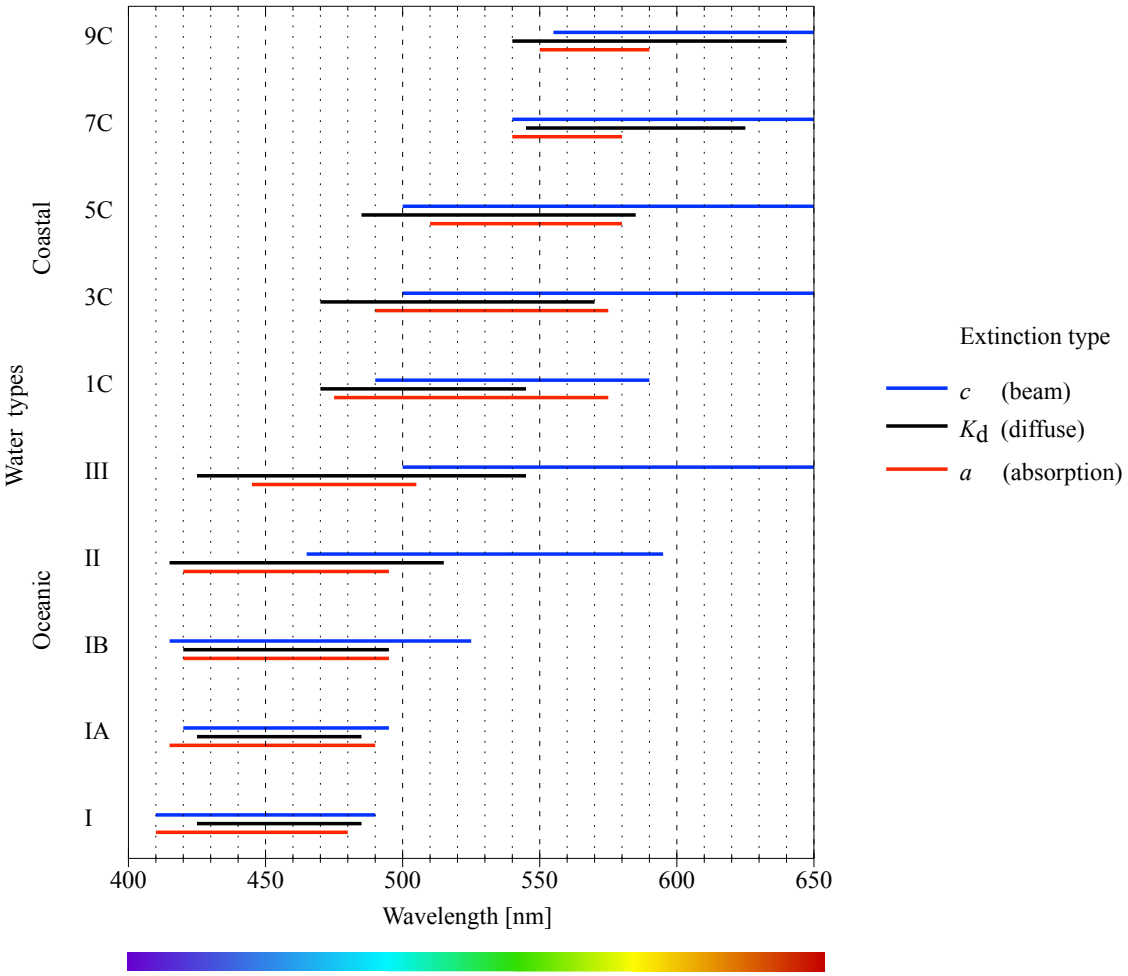

Figure 3.3: Wavelength areas of attenuation minima for different Jerlov water types and different extinction types, including color scale for simplified allocation. Areas identified for oceanic waters I to III, coastal waters 1C to 9C, each from clear to murky.

3.1.2 LED Properties and Availabilty

After some fundamentals of LEDs in UOWC have been presented in Section 2.1.5, they will be followed up more specifically in this section. In terms of LEDs utilized in UOWC three drawbacks can be identified:

- Limited color selection for power LEDs.
- Green-yellow gap in efficiency.
- Spectral bandwidth.

The market for LEDs seems to be overwhelming, but on closer inspection, the range is relatively small in terms of non-converted single-color power LEDs series. This is due to the fact that these do not play a role for general illumination like converted white LEDs. In addition, the available series only offer a few colors in the blue to yellow spectrum. For further investigation the series with probably the largest range of single-colors was chosen - the Lumileds Luxeon Z color line. Depending on the LED manufacturer, the following terms are also used in place of single-color: direct-, primary-, true- or native-color, as well as direct emission.

The energy efficiency is a significant property, especially in mobile communications. In LEDs it is termed wall-plug efficiency or radiant efficiency η_{el} and is defined as the ratio of emitted optical power P_{opt} to the electrical input power P_{el}:

$$\eta_{\mathrm{el}} = \frac{P_{\mathrm{opt}}}{P_{\mathrm{el}}}. \tag{3.1}$$

The electrical power can be directly accessed by the product of forward current I_{f} and forward voltage U_{f} at the operating point. The radiant power is generally only given in data sheets for wavelengths shorter than 450 nm (deep blue) or longer such as 650 nm (deep red). For wavelengths within this range luminous flux is commonly documented. This makes sense for human-centric applications where the eyes are the receiver, since these values in lumen are weighed by the photoptic (daytime) human eyes sensitivity curve [145]. This CIE curve, originated in the year 1924, has undergone some minor modifications over the years, especially in the short wavelength (blue) range. For technical applications, where photodetectors are the receiving elements, a conversion is needed. For a single wavelength a simple conversion can be done by using the luminous efficiency factor of 683 lm/W at 555 nm and the wavelength dependent factor from the corresponding curve or table. In case of LEDs such a conversion would be inaccurate, since LEDs are not monochromatic light sources, they rather show a spectral distribution with an approximate Gaussian-shaped distribution. The required task is to derive the radiant power from the given typical luminous flux values and normalized intensity spectrum. To achieve this, an initial assumed power value is divided into power fractions for 1 nm width, corresponding to the intensity spectrum. These values are then weighted by the luminous function and integrated over the full spectrum. The power value is then changed iteratively, until the obtained sum of the luminous flux fractions approximates the total flux provided by the data sheet.

The outcome is depicted in Fig. 3.4, and the parameters used are tabulated in Table C.3 of the appendix. The "green-yellow gap" in single-color LEDs is clearly evident, and is obviously just in the wavelength area where the attenuation in coastal waters is lowest. The result of the manufacturer's efforts to close this gap with converted green and converted amber/yellow types is clearly visible: the radiant efficiency of the converted types is approximately doubled compared to the single-color version. Another way to present the "green-yellow gap" more comprehensively is by measuring the absolute spectral intensity at the same electrical input power of the different colored LEDs, see Fig. 3.5. In addition to the height of the peaks, these graphs also provide information on the width and the asymmetry.

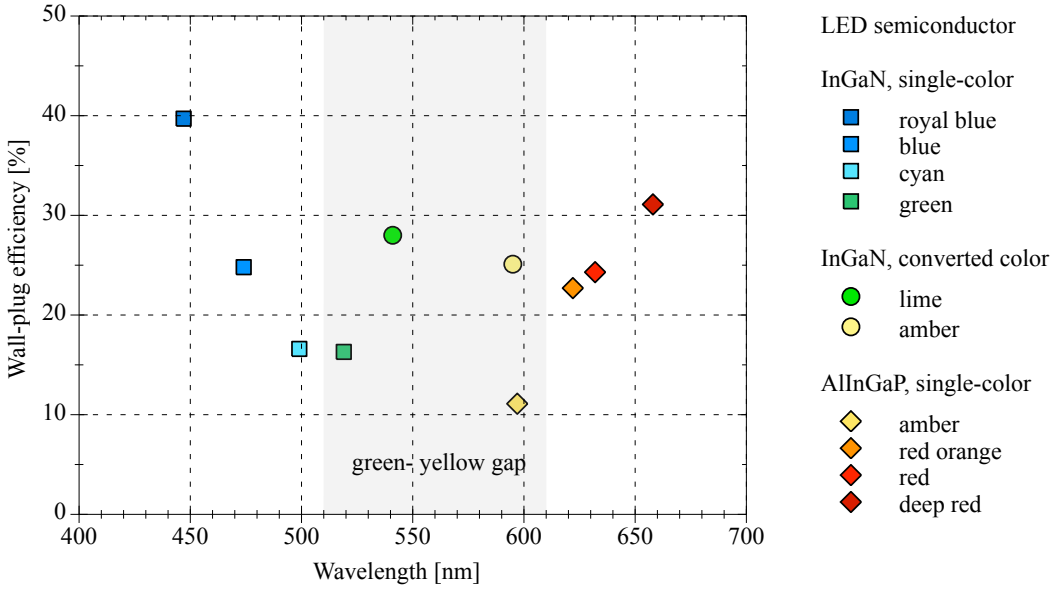

Figure 3.4: LED wall-plug efficiency of Luxeon Lumileds Z series at a forward current of 500 mA and at 25°C. Data points calculated for typical values as given in [62].

Table 3.1: Key parameters of examined converted green LEDs.

Manufacturer, Type	Peak wavelength [nm]	FWHM [nm]	Wallplug efficiency (@500mA)
Lumileds LXZ1 PM01	541	104	28.0 %
Luminus SFT10CG	525	98	28.4 %
Osram LCG H9RN	516	98	37.5 %

Due to the relative high efficiency in the green-yellow band, the converted types appear interesting for UOWC in coastal waters. Therefore, a more comprehensive examination of the properties is indicated. An essential part of this is a comparison of the relative intensity as a function of wavelength. As given in Fig. 3.6, the rarely available converted green and amber high power types are compared to direct color counterparts. The much larger spectral bandwidth of the converted types is immediately apparent, and the FWHM values are at approximately 100 nm.

While the three converted green types only show small portions of the spectrum outside the "least attenuation window" of coastal waters, the main portion of the converted amber types is just located there, so their use in coastal waters would be inefficient. Key parameters of the examined converted LEDs are given in Table 3.1 and published in data sheets [62, 147, 146].

For further comparison, the converted green Osram LCG H9RN LED was chosen because this product is the most promising one incorporating the highest radiant efficiency and lowest peak wavelength. A known property of converted LEDs in general is the relative slow phosphor-mediated conversion process due to long photoluminescence lifetimes. As only electrical bandwidths of a few MHz are achievable, this is about one order of magnitude less than for single-color LEDs [148, 149]. Own experiments utilizing the Lumileds LXZ1 PM01 have resulted in a bandwidth of slightly over 2 MHz [35]. The large optical bandwidth can be another disadvantage, as it can hinder the optical filtering of ambient light. Please refer to Section 3.2 for discussion of this topic.

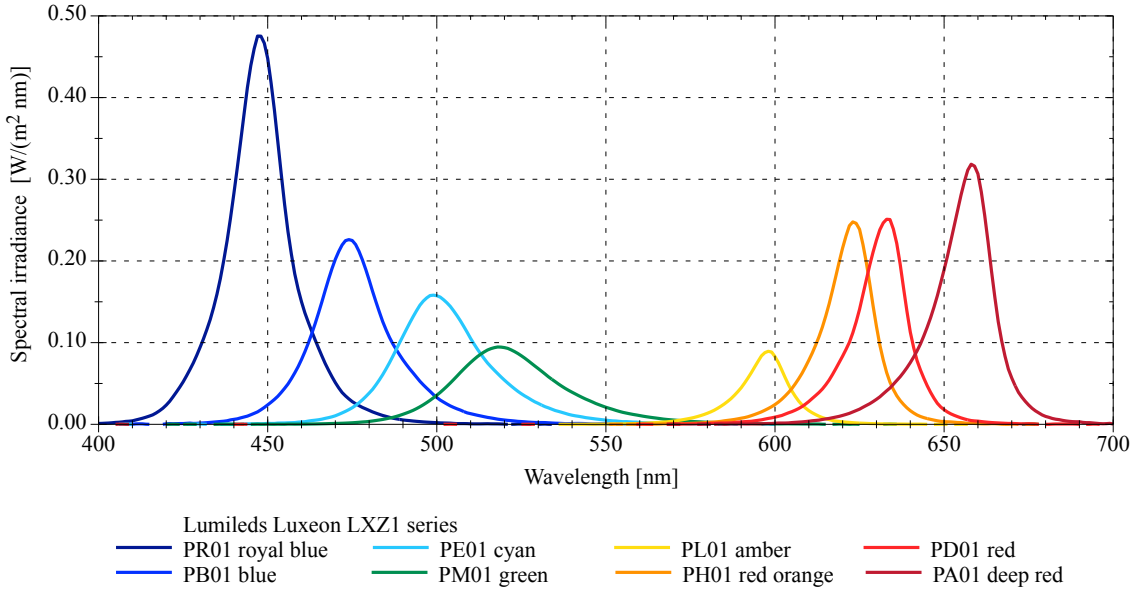

Figure 3.5: Spectral irradiance of Luxeon Lumileds Z series single-color LEDs at 0.9 Watt electrical input power, measured with Gigahertz Optic BTS256 spectrometer under otherwise identical conditions. Intensity values interpolated for equal power consumption on a small scale only to preserve linearity.

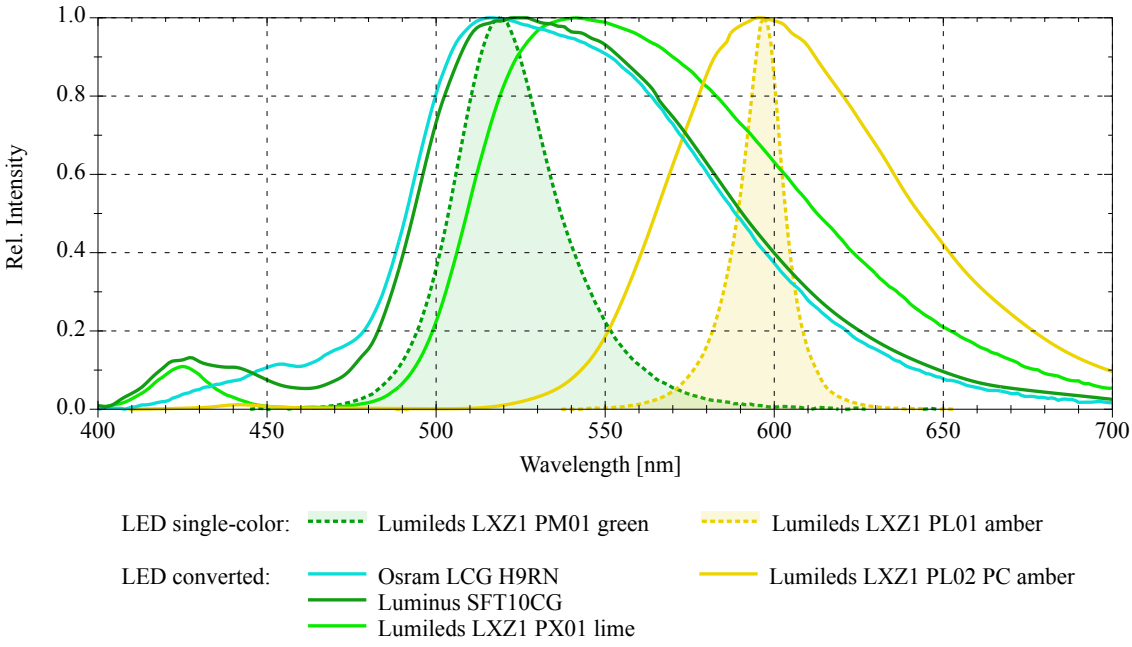

Figure 3.6: Relative spectra of converted LEDs in the green yellow regime, also given for comparison green and amber single-color LEDs. Spectra measured at forward currents of 300 mA at 25°C and for Lumileds PC amber at 500 mA. Spectrum of Luminus at 700 mA retrieved from data sheet [146].

3.1.3 Spectral Progression of Responsivity

The third element of the threefold relationship is the photodetector's responsivity. Corresponding to the water's attenuation window and the possible LED colors, only a narrow spectral range from approximately 450 nm to 600 nm is significant for UOWC. Generally, blue enhanced silicon photodetectors are best suitable for the these applications. These are available as Si-PIN-PDs or as APDs, albeit they are relatively rare. Beside silicon, only gallium phosphide (GaP) is suitable as another semiconductor material for this wavelength range. Generally, such PDs offer only small responsivity values and are considered as exotic parts.

The theoretical bound of responsivity for silicon, where the so-called quantum efficiency is 100 %, and a selection of curves from leading manufacturers for blue-enhanced and non-enhanced Si-PIN-PDs are given in Fig. 3.7. In the range used, the responsivity increases relatively steadily with the wavelength, and this is presented in a standardized way for better illustration for PIN-PDs and APDs in Fig. 3.8. Between 450 nm and 550 nm the responsivity increases by a factor of 1.2 to 1.5, in contrast to the LED's wall plug efficiency that drops in this range. The operational wavelength range of these detectors extends over a much wider band than required for UOWC, see Fig. 2.15. This area requires filtering in ambient light conditions, see Section 3.2. In the case of APDs as active elements, the intrinsic lower sensitivity at short wavelengths can be compensated by increasing the reverse voltage and thereby the gain. However, this would also negatively influence the noise.

PMTs and SiPMs will not be reviewed further here, but there are versions available for the blue spectral range with a moderately narrow spectral band, for general information refer to Section 2.1.5.

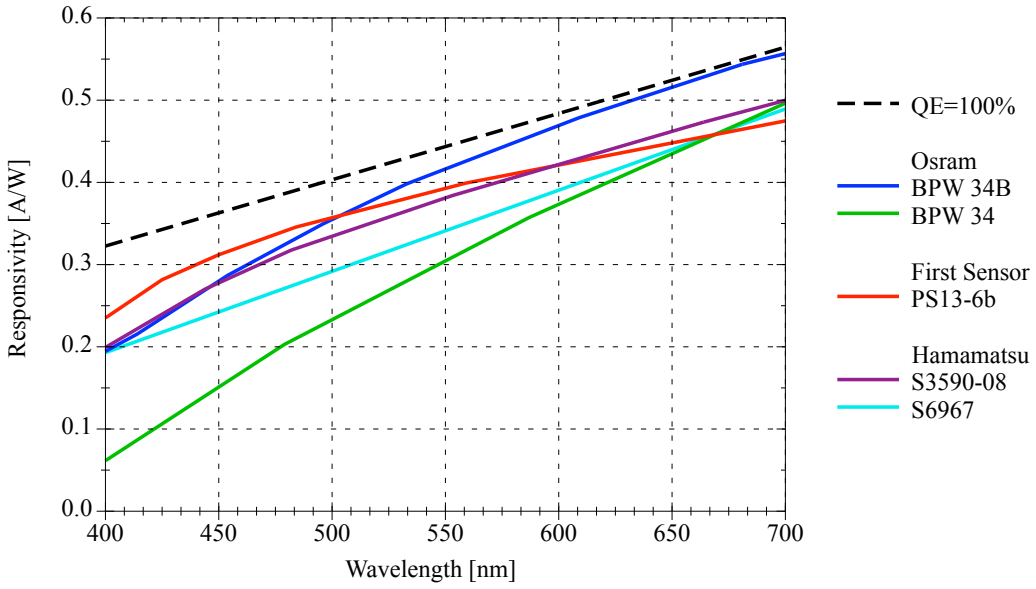

Figure 3.7: Responsivity of sophisticated blue enhanced Si-PIN photodetectors, particularly suitable for UOWC. For comparison, the theoretical limit (dashed line) and that of a non-enhanced type (green line) are given. Data extracted from data sheets [69, 150, 151, 152, 153].

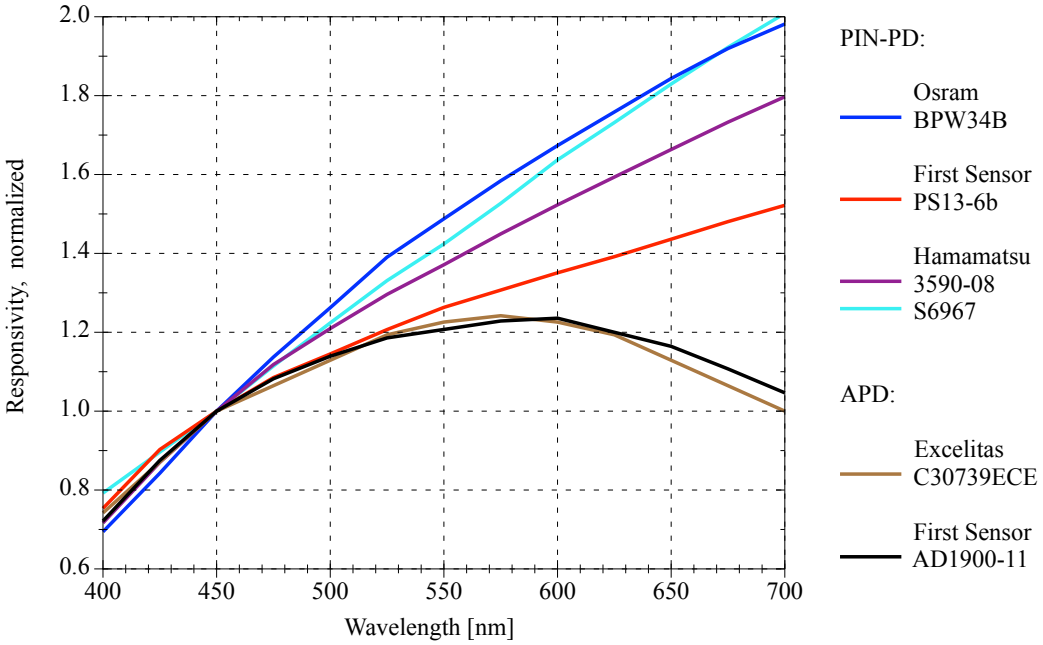

Figure 3.8: Responsivity of Si-PIN and avalanche photodetectors, normalized at 450 nm. Additional data was extracted from data sheets [70, 154].

3.1.4 Threefold Relationship of Efficiency, Attenuation and Responsivity

The interaction of the three wavelength-dependent components is best presented by a comprehensive simulation. By combining (2.19), (2.17) and (3.1), the following formula can be generated as a basis for further simulations:

$$I_{\mathrm{PD}}(\lambda) = \frac{P_{\mathrm{opt}}(\lambda) \cdot e^{-K_{\mathrm{d}}(\lambda) r} \cdot A_{\mathrm{det}} \cdot \mathcal{R}(\lambda)}{2\pi r^2 (1 - \cos(\beta/2))}. \tag{3.2}$$

In order to examine the overall efficiency of the combination of these three components, the distance-dependent obtained detector current is calculated for the same electrical input power and geometrical conditions, representative for two fundamentally different water types and various LED emission wavelengths. However, first, a look at the individual components and parameters is necessary. For the LED source an electrical input power of 10 watt is chosen, the radiant power P_{opt} accordingly results of the radiant efficiency from each LED color of the examined Lumileds Z series.

Simulations are carried out for single wavelengths, since the responsivity values only change little within the narrow optical bandwidth of the direct color LEDs (typ. 20 nm to 30 nm FWHM) and practically no shift of the graphs are expected. In case of the converted green LED (typ. 100 nm FWHM), an additional curve (stroke dotted line) is calculated by splitting the power into five spectral bands. The beam angle β is set to a practical value of 70° equally distributed through an imaginary ideal reflector and without inclination. As intermediate oceanic water type Jerlov IB is selected, and Jerlov 3C as a coastal water type. For the extinction calculation, the coefficient K_{d} is applied to be a compromise for LED utilization. On the detector side a Si-PIN-PD is used, with an area A_{det} of 10 mm^2, also without inclination. A typical blue enhanced curve is adopted for the responsivity $\mathcal{R}$, comparable to the Hamamatsu S3590-08 detector. Detailed parameters are given in Tables C.4 and C.5 in the appendix.

The resulting curves are shown in Fig. 3.9. The progression of the photocurrent in areas of larger distances is basically more interesting for the UOWC, because with increasing distance the SNR constantly decreases, until finally the communication can no longer be maintained.

Table 3.2: Achievable distances at a photocurrent of 10 nA for two water types.

Wavelength, LED color	Jerlov 1B, oceanic Distance [m]	Jerlov 3C, coastal Distance [m]
450 nm, deep blue	21.3	8.31
475 nm, blue	19.1	8.92
500 nm, cyan	16.3	9.07
520 nm, green	14.9	9.24
515 nm, conv. green	18.4	11.1

Table 3.3: Attainable photocurrents and ratios at 8 m distance in coastal water and 16 m distance in oceanic water.

Wavelength, LED color	Jerlov 1B, oceanic Photocurrent [nA]	Jerlov 3C, coastal Photocurrent [nA]
450 nm, deep blue	21.8 (0.0 dB)	11.9 (0.0 dB)
475 nm, blue	15.8 (-2.8 dB)	15.6 (+2.4 dB)
500 nm, cyan	10.5 (-6.4 dB)	15.9 (+2.5 dB)
520 nm, green	8.18 (-8.5 dB)	16.9 (+3.0 dB)
515 nm, conv. green	15.3 (-3.1 dB)	35.7 (+9.5 dB)

Assuming that a signal current of 10 nA provides a necessary distance from the noise floor and thus a sufficient SNR can be achieved, the ranges attainable by the various LEDs can be determined from the diagrams. Likewise, the photocurrents achievable by the different LEDs can be extracted for a certain distance, e.g., for 8 m in coastal water and 16 m in oceanic water. Based on this a comparison in decibels can be made. Tables 3.2 and 3.3 show the results.

The upper diagram for oceanic water confirms the expectation that deep blue is the most favorable color for longer distances in this water, due to the high wall-plug efficiency of the deep blue LED and the low attenuation at this wavelength, despite the comparatively low responsivity. A change of colors from blue to cyan and green leads to increasing deterioration. The converted green variant gives better results than the green but is worse than the blue at greater distances. In the case of the converted green LED, an overestimation is evident if it is not simulated in spectrally split power.

In coastal water, the expectations are different, as the converted green LED is assumed to be the most favorable version related to intensity, since the attenuation is lowest and the responsivity is highest in this wavelength area and the wall-plug efficiency also show high values. Despite the low wall-plug efficiency of the direct-color green LED, it performs second best at longer distances in the important area, to the right of the intersection point, cf. Fig. 3.9. Although the performance is significantly lower than that of the converted green version, the blue colors are still slightly below the non-converted green. In terms of intensity, the converted green LED is clearly the most favorable choice for this water type. The main drawback is the low electrical bandwidth due to the limited speed of the conversion process. The second drawback is the large optical bandwidth, that is disadvantageous for narrow optical filtering, which in turn benefits the noise component in the SNR. Furthermore, the narrow filtering would burden the efficiency advantage. The utilization of multiple colors and the appropriate filtering is basically a similar issue for adaptive or multiplex systems.

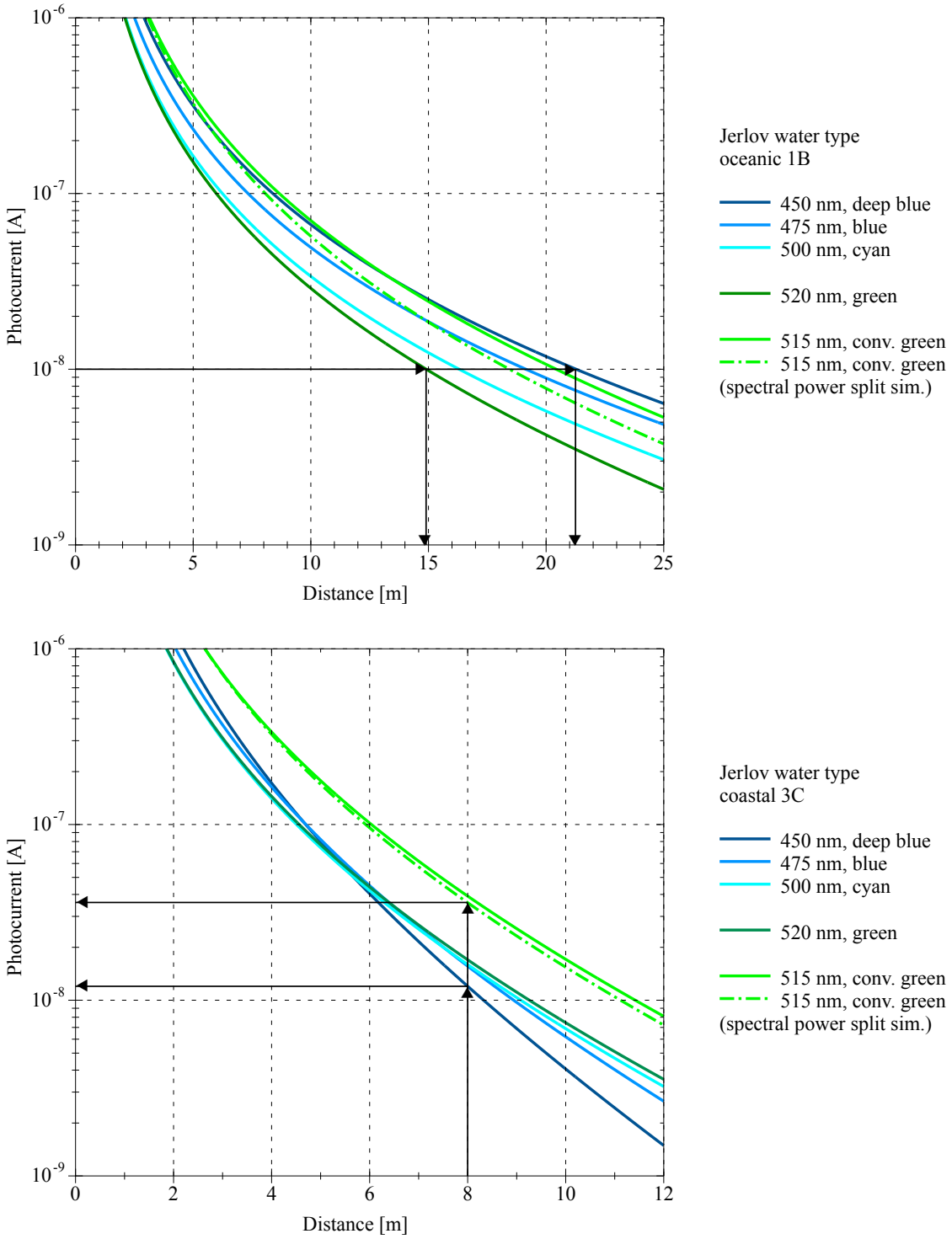

Figure 3.9: Simulation of threefold relationship from responsivity, attenuation and radiant efficiency for two water types and five LED colors. The upper graph depicts the achievable ranges at the same photocurrent in an oceanic water, the lower graph depicts the obtainable photocurrents at the same distance in coastal water.

3.2 Optical Filtering for Ambient Light Suppression

Nowadays, subsea operations utilize advanced sensor technology and therefore demand sophisticated underwater communication. In the past, the acoustic channel was almost entirely used in untethered mobile underwater applications. The dominance is still unbroken, and the large range certainly contributes to this, but a low data rate must be accepted, see also Fig. 1.2. For well over a decade, attempts have been ongoing to utilize the optical underwater channel complementary for communication applications, promising higher data rates at the expense of lower achievable distances in comparison to the acoustic technique [13, 15].

In underwater scenarios, mobile vehicles play a steadily increasing role. These include remotely operated vehicles (ROVs), autonomous underwater vehicles (AUVs), gliders and crawlers. Potential communication applications in scientific and commercial exploration missions can be located in all depth ranges: near the surface, in the mid water or close to the seafloor. The communication can take place between ship hulls, divers, buoys, anchored observatories and the full range of underwater vehicles, as depicted in Fig. 1.1. In most cases, vehicles will be involved. Optical communication between fixed points may be conceivable, but could alternatively be realized by means of cables or fibers. Inter-swarm communication can be seen as the most challenging task.

The majority of the available vehicles are assigned to smaller depth ratings. The reasons for this can be seen in the costs and the fundamentally greater interest in coastal areas. Field tests are therefore to be expected in the upper zones of coastal and oceanic waters utilizing mid-size AUVs with a limited depth rating and payload. Apart from special operations, during dark nights or in the deep sea, underwater optical communication systems are exposed to a certain portion of ambient sunlight. As an unavoidable source of disturbance in terms of saturation and noise, this ambient light can restrict the serviceability. These unwanted effects can be reduced by equipping matching optical filters to the detectors. Mobile applications generally require wider fields of views (FOVs) for transmitting and receiving to avoid pointing and tracking issues. To achieve a favored hemispherical or even spherical characteristic, a combination of multiple off-the-shelf parts with intermediate FOVs is self-evident [30, 155, 156, 73]. Intrinsic hemispherical detectors for underwater applications are only known as photo multiplier tubes (PMTs) [157]. Light sources, such as lasers and laser diodes (LD) are mostly used in the special case of stationary setups, because of their narrow beam and high demands with respect to pointing and tracking. Due to their high performance in terms of speed and range, they play a certain role in visible light communication (VLC) and also in underwater communications [59, 49]. On the other hand, the speed and power density of LEDs is significantly lower. They also require more optical bandwidth, but provide a wider radiation pattern [65]. Nevertheless, LEDs are considered to be an eligible low cost light source without a recent alternative. A review of the different photodetector types with regard to their spectral properties and suitability for ambient light is obligatory.

The topic of ambient light disturbance in the area of optical communication has been addressed in [79] for the infrared radiation (IR) range, and subsequently for VLC in [158, 159, 160]. The assumption of total darkness is used in most studies in the field of UOWC. To the author's best knowledge, there are only a few studies available, which address the solar noise impact in UOWC in the visible [75, 161, 162] and the ultraviolet (UV) light range [136, 137]. In [162, 163] two thin film filters were deployed for use in an UOWC system due to impairment of solar radiation. The design of thin film filters for multi color VLC was investigated in [164], albeit more in terms of cross color interference. A recently published work on the effectivity of optical filters in UOWC is given in [165]. Another way of optical interference suppression by the use of an liquid cristal display (LCD) as a filter is presented in [166, 167, 168]. The intention of the following section is to bring system designers closer to the impact of ambient light, in order to create efficient, feasible, and versatile layouts.

3.2.1 Underwater Ambient Light

As already presented in Section 2.2, the optical properties of natural waters are very diverse. The clarity of natural waters is commonly classified in the Jerlov classification scheme, under the assumption of a homogeneous vertical distribution of water constituents within the upper mixed layer of the sea, clear sky, and high solar altitudes. In the following, the light field properties of three widespread water types are examined more closely for the oceanic types IB and III, as well as for the coastal type C3.

Jerlov's classification is based on only one parameter: the irradiance transmittance in surface water. From a comparatively simple depth-profile measurement of downwelling plane irradiance $E_\mathrm{d}(z,\lambda)$, one can determine the diffuse attenuation coefficient of downwelling irradiance:

$$K_\mathrm{d}(z,\lambda) = -\frac{1}{E_\mathrm{d}(z,\lambda)} \cdot \frac{dE_\mathrm{d}(z,\lambda)}{dz}. \tag{3.3}$$

The irradiance transmittance $T(z,\lambda)$ at wavelength λ from the surface to depth z, is related to (the assumed depth-constant) attenuation coefficient K_d via

$$T(z,\lambda) = e^{-K_\mathrm{d}(\lambda)z}. \tag{3.4}$$

K_d is an apparent optical property of a water body that varies systematically with wavelength and is rather insensitive to external environmental conditions such as solar zenith angle variations [102]. K_d is basically the measure of how sunlight and skylight is attenuated in the water body. The corresponding curves of the Jerlov water types are given in Fig. 2.32. Solonenko and Mobley [102] estimated the fundamental inherent optical properties, i.e., absorption and scattering coefficients of the water constituents, of all Jerlov water types. These parameters were used to run radiative transfer simulations with Hydrolight (version 5.2, Numerical Optics Ltd., Devon, UK), please refer to [87] and to Appendix C.2. The numerical model computes the in-water radiance distribution as a function of depth and wavelength, and provides other quantities like up- and downwelling irradiances.

Fig. 3.11 shows the computed decline of spectral downwelling irradiance with water depth for the three water types. In these simulations, the sky is cloud-free with the sun at a 30° zenith angle (corresponding to a sun elevation during noon at summer in central Europe) and a gentle wind breeze of 5 m/s. Additional Hydrolight simulations were carried out with different sun zenith angles (30°, 50°, and 70°) as well as for clear sky and overcast atmospheric conditions.

Table 3.4: Downwelling E_d and upwelling E_u irradiances for different water types and depths in the spectral range from 350 nm to 750 nm.

Depth [m]	Jerlov 1B E_d [W/m^2]	oceanic E_u	Jerlov III E_d [W/m^2]	oceanic E_u	Jerlov 3C E_d [W/m^2]	coastal E_u
2	319	9.0	306	51	236	20
5	240	8.0	187	37	110	12
10	175	6.6	92	20	37	4.5
20	107	4.5	25	5.9	5.3	0.7
50	32	1.5	1.0	0.27	0.04	0.006
100	4.7	0.24	0.03	0.009	0.0002	n. a.
200	0.14	0.007	0.0001	n. a.	n. a.	n. a.

The underwater light field and its change with depth is an important factor for further investigations of optical filters. Near the surface, the upwelling irradiances have values from a few

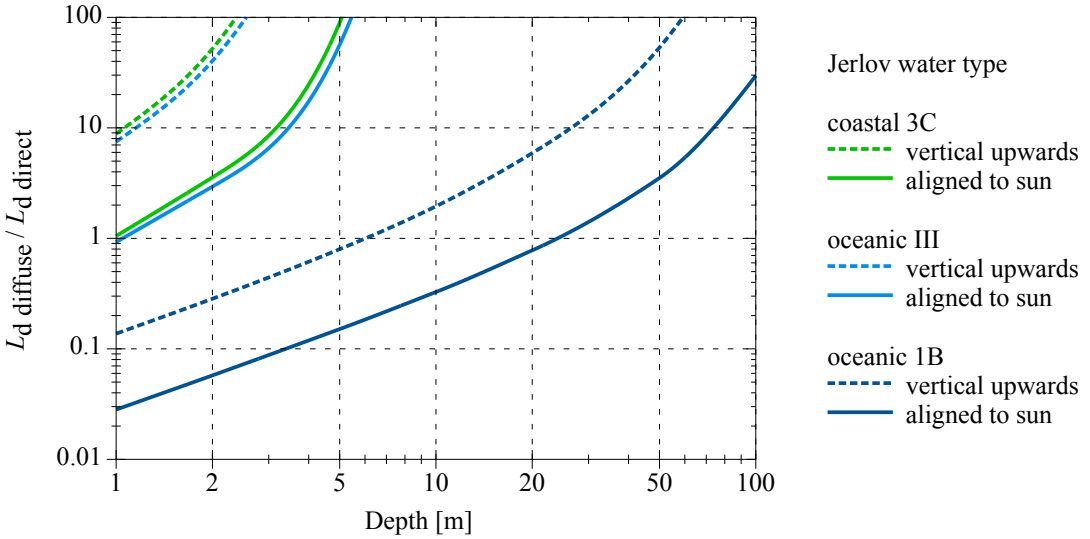

Figure 3.10: Ratio of the diffuse to the direct downwelling radiances as a function of the water depth for oceanic and coastal water, for a sensor looking vertical upwards or aligned direct into the sun. Data were generated with Hydrolight for a specific wavelength of 450 nm, cf. [36].

percent up to a third of that of the downwelling irradiance, see also Table 3.4. With increasing depth, the shape of the downwelling radiance field gradually transforms from being directed (with a radiance maximum from the sun zenith direction) to diffuse. Fig. 3.10 shows how the impact of the direct downwelling radiance blurs with depth for the three water types and two viewing directions. The downwelling radiance field is mostly diffuse at 2 m depth for 3C, 5 m for III, and 20 m for IB. Notably, and as a rough guide for practical estimates, an overcast sky reduces the downwelling irradiance to a quarter, and provides completely diffuse conditions. The shift in sun elevation from noon to evening also leads to a reduction to one quarter.

In addition to the time-averaged radiance distribution that Hydrolight computes, one has to deal with extreme radiance fluctuations due to sunlight focusing and defocusing of sea surface waves, see also Section 2.2.5. Thus, radiance fluctuations, mainly from the direction of the direct sun, can be a significant source of disturbances in shallow depths. This fact has to be considered in UOWC operations, but is not included in simulations. Apart from wave-induced light fluctuations and the sensor pointing direct into the sun direction, the sensor orientation facing upwards is generally the worst case for ambient light exposure and thus the main point of consideration, but substantial portions are also to be expected in the horizontal case. In the upper zones, remarkably high downwelling values of up to hundreds of watts per square meter can occur, and thus LED generated values are exceeded, and ambient light filtering becomes important.

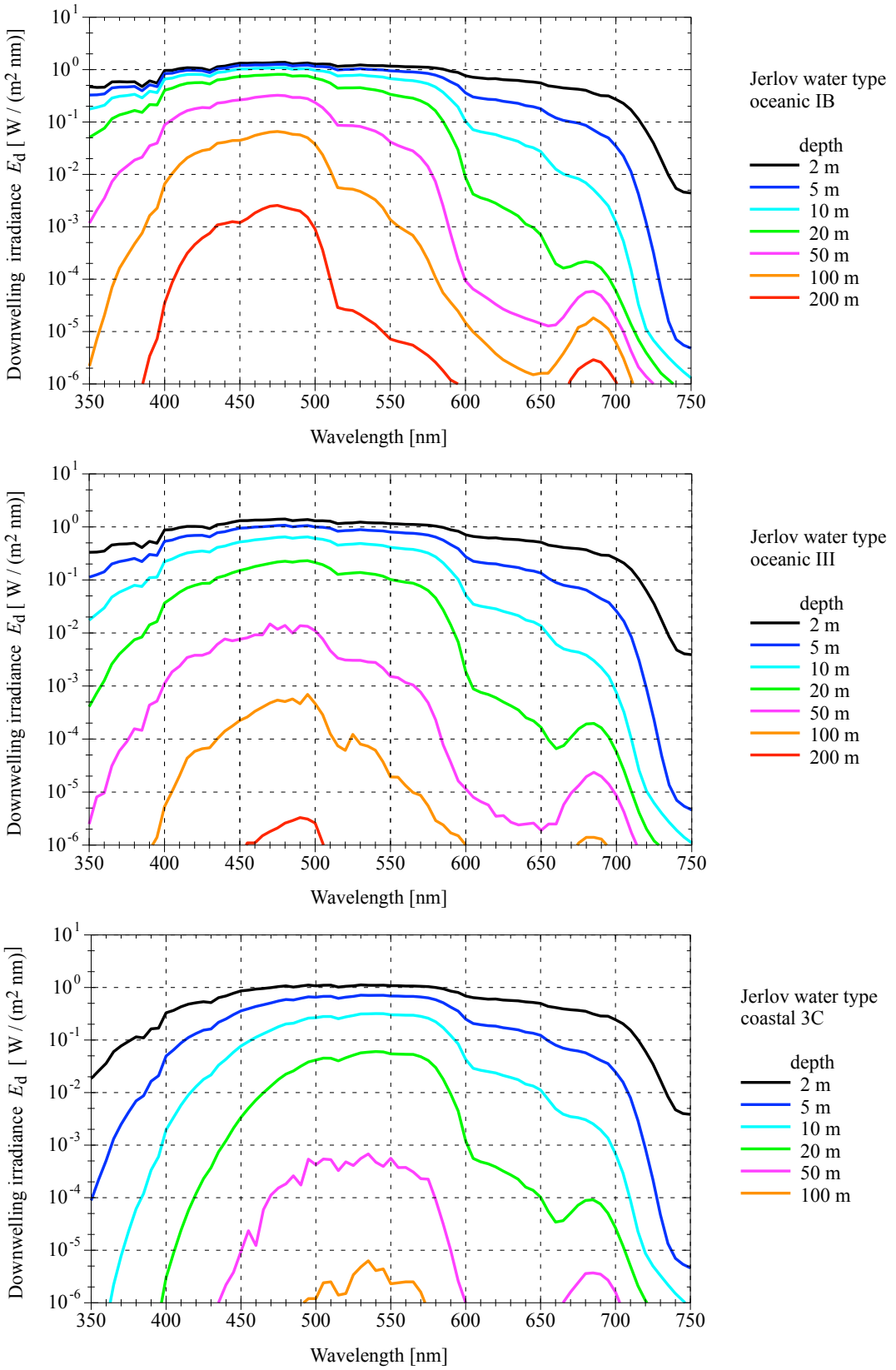

Figure 3.11: Plots show the downwelling spectral irradiance for various depths, valid for three Jerlov water types under 30° sun zenith angle, clear skies and 5 m/s windspeed. Plotted from the database generated by Hydrolight. More information is collected in [36].

3.2.2 LED Based Light Source

Based on the LED fundamentals and on the wavelength selection of LEDs for UOWC, see Sections 2.1.5 and 3.1, the study of filtering options requires a closer look at the spectral properties. As an area of least attenuation of light in natural waters, a spectral band of wavelengths in the blue to green range can be identified. Due to their generally high electro-optical efficiency and speed, blue LEDs are a suitable choice and are frequently used as UOWC transmitters [35]. For further investigation deep blue LEDs in the 450 nm range are chosen, whereby the results are basically transferable to other colors at respective wavelengths. The spectral emission of these single-color LEDs is roughly Gaussian shaped with a full width at half maximum (FWHM) of typically 15 nm to 30 nm. Influencing factors of the LED peak wavelength are temperature, current and binning, which are basically color-depended. Both the typically small negative current gradient (in -nm/A) and the minor temperature gradient (in nm/K) only lead to small deviations of at most single nanometers, at least under realistic operating conditions. In contrast to these operating parameters, the selection parameter, the so-called binning, can have a more significant influence. Generally, LEDs are assorted by the manufacturer depending on flux and wavelength values. For example, for a royal blue LED this means four bins or groups, ranging from 440 nm to 460 nm. Such a variation of several or tens of nanometers to the nominal value can cause problems in combination with narrow bandwidth optical filters, so a careful system design is recommended.

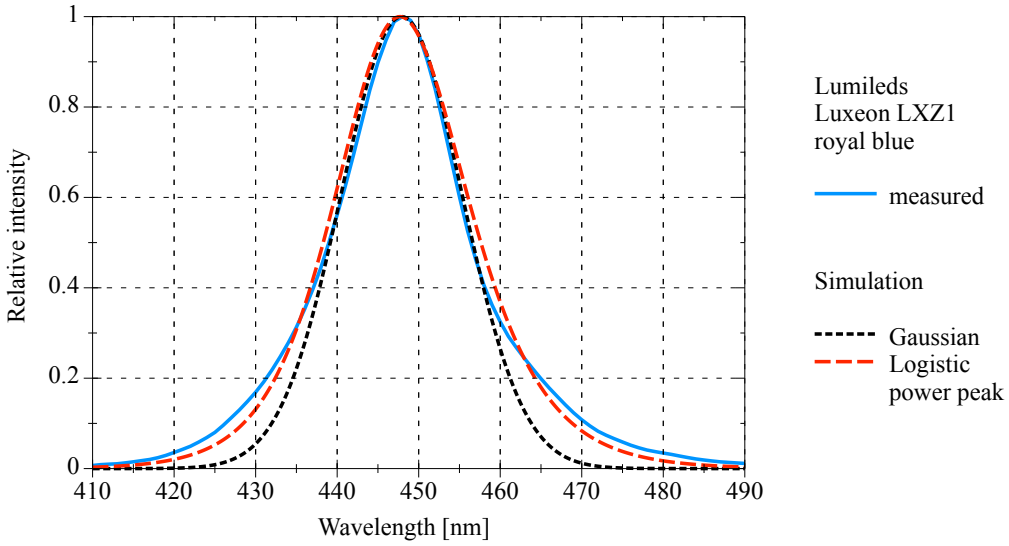

Figure 3.12: Curves of measured and simulated relative intensity for a deep blue LED. For model functions, parameters and measurement information refer to the Section C.3.

The utilization of the LED radiant emission also depends on the spectral coverage. Fig. 3.12 gives the measured relative spectral emission of a deep blue LED, which is slightly asymmectrical. It is compared to the commonly used Gaussian approximation and the better matching logistic power peak model function [169]. Due to the deviation in simple models, the use of measured spectra is worthy of consideration. To identify the differences in the shape of the spectral emission from diverse LED colors, not only the intensity can be normalized, but also the wavelength, with the intention of stretching to equal the FWHM, cf. Fig. 3.13. For example, here it is shown that green is more suitable for filtering than yellow.

A major issue in filtering these bell-shaped intensity distributions is efficiency or coverage. This can be represented by combining an ideal bandpass with variable transmission range and the

same central wavelength with the LED. A set of such curves is given in Fig. 3.14. A second series (Ledengin LZ4) of another manufacturer showed comparable color-related results. For example, comparing yellow and green at a passband to FHWM ratio of 1, results in 60 % and 70 % coverage, respectively.

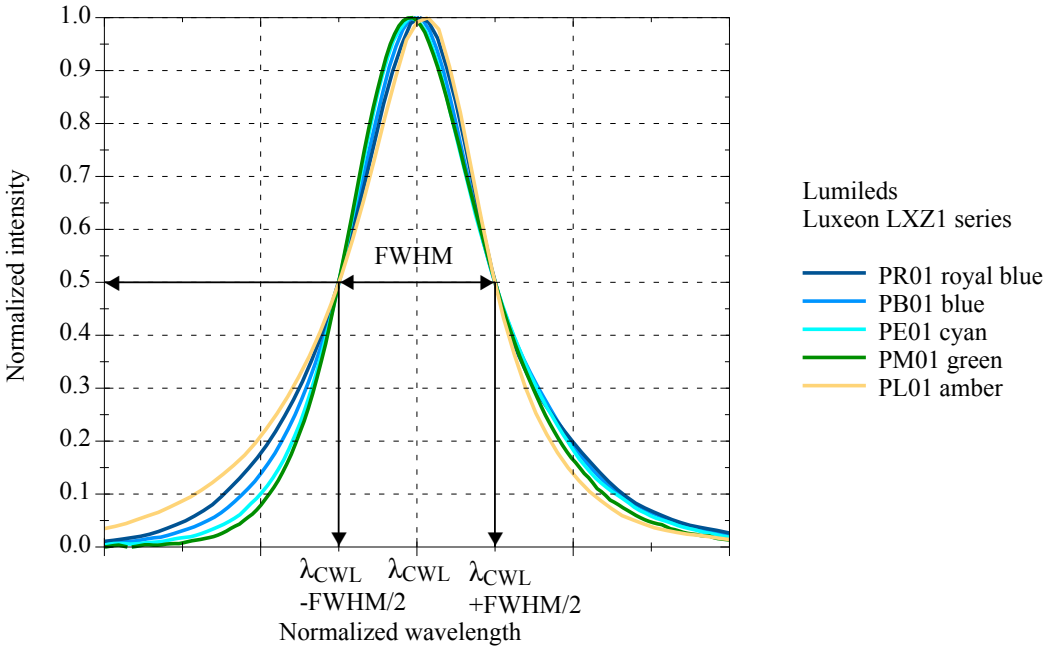

Figure 3.13: Intensity of different colored LEDs within one series as a function of the wavelength in a double normalized way. Based on measured and normalized spectra of Fig. 2.13.

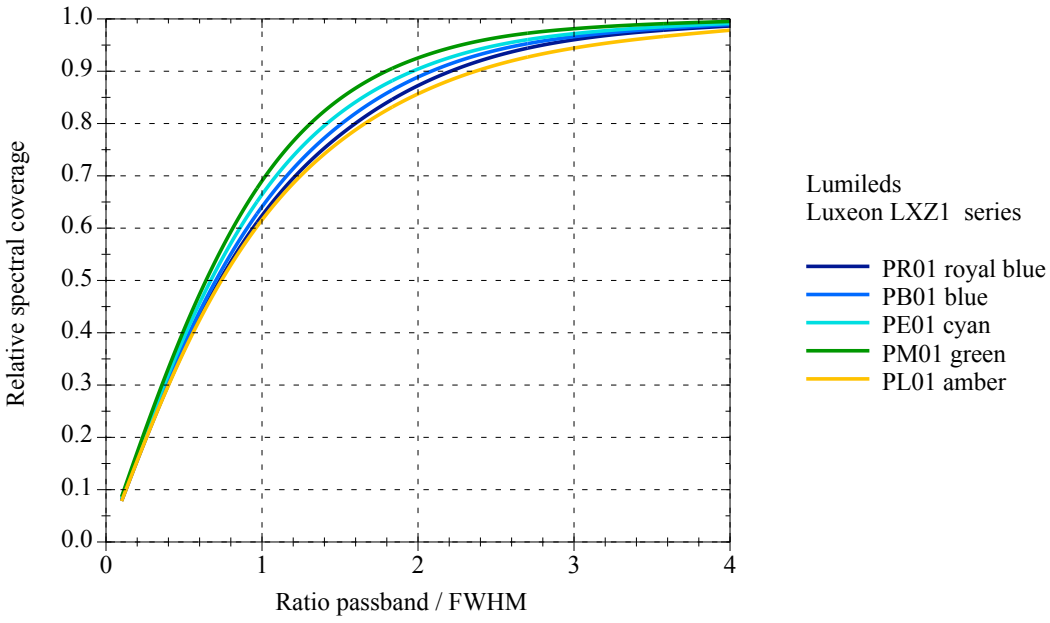

Figure 3.14: Relative spectral coverage as function of the ratio of an ideal filters passband to the LEDs FWHM for different colors of a power LED series (Lumileds Z) at normal incidence.

3.2.3 Photodetector

Types and Characteristics

The four main photodetector types used in UOWC are PMTs, SiPMs, APDs and PIN-PDs, and an introduction is given in Section 2.1.5. In common, they have an optical bandwidth of several hundred nanometers, where PMTs and SiPMs (depending on the variant) are generally somewhat narrower, and PIN-PDs are a bit wider-banded. Underwater, the ambient light that occurs has a depth-dependent bandwidth of approximately 350 nm to 700 nm, while the optical bandwidth used by the LED transmitter is only up to a few tens of nanometers. In order to protect the photodetector as much as possible from the interfering ambient light, an appropriately adapted bandpass filter should be used, which allows the signal component to pass and blocks the ambient light to a certain extent. For medium light conditions, found in shallow or medium underwater depths, large-area Si PIN-PDs and APDs can be an appropriate choice. Furthermore, they are cheap and robust, and have a low integration effort. The higher sensitivity offered from the other types such as SiPMs and PMTs is not advantageous in these shallow operating environments, not even under filtered conditions. But under almost perfect darkness in the deep oceans they achieve the highest performance and largest ranges [75].

Alternative photodetectors for the lower part of the visible spectrum could be in gallium phosphide (GaP) technology, but these specialized products generally offer lower sensitivities and higher capacitances comparable to silicon PIN-PDs. Pre-assembled PIN-PD filter combinations are rare on the market and are only available for specialized applications. In most instances they are filtered for photo-optical light measurements by reproducing the International Electrotechnical Commission (IEC) curve of human eye color sensitivity, or with a flat response over a wide range for radiometric measurements.

In this section, the overlaps of the wavelength ranges of LED, PD and ambient light are a precondition, however other properties or technical data of the detector are not required, since only the filter placed in front is examined.

3.2.4 Optical Bandpass Filters

Terminology

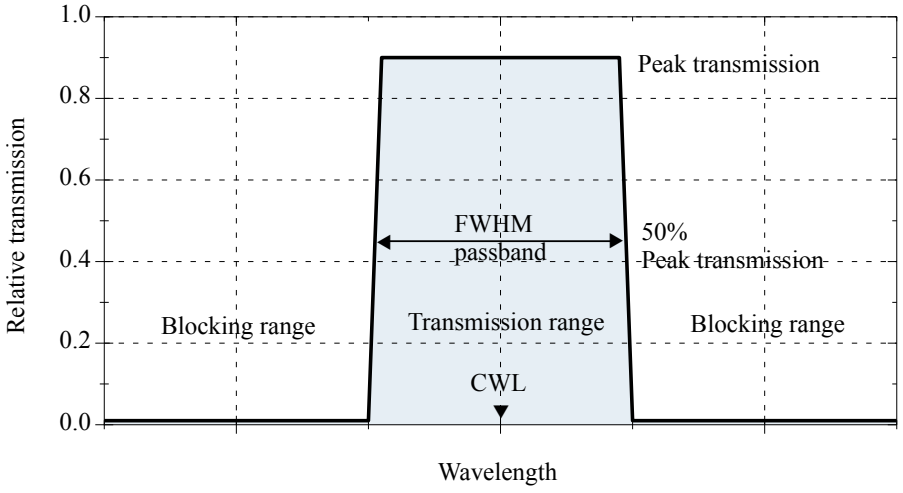

Figure 3.15: Graphic is showing an idealized bandpass filter.

Optical bandpass filters are generally identified by their center wavelength (CWL) and their bandwidth in the passing range at 50% of the peak transmission, denoted as FWHM or passband

width (PB), see Fig. 3.15. Depending on the type, real bandpasses can show ripples in the distribution, smooth rounded slopes, or side lobes.

Colored Glass Filters

Optical filters made of colored glass are widely used due to their simplicity, robustness and low price. The main effect of these filter types is more or less selective absorption in a certain wavelength range [41]. As bandpass filters at visible wavelengths, these filters show relatively large transmission losses and weak slopes. Further disadvantages can be fluorescent effects and side lobes, i.e. unwanted transmission at higher wavelengths, cf. Fig. 3.21. Generally, these filters are available off the shelf in different thicknesses and in a moderate variety. Types are generally not custom-made, due to the industrial casting production in huge batches. A market survey of bandpass filters shows only an availability in the blue or green range. The search for a filter matching approximately the deep blue LEDs center wavelength of 450 nm provides only a few results. Many products are only compatible with each other, limiting the number of discrete types. Since the well matching filter BG 28 of the manufacturer Schott is unfortunately discontinued, the B440 type produced by Hoya was chosen for further investigation; please refer to Fig. 3.16 and [170]. An appreciated feature is the relatively low dependence to the angle of incidence (AOI), due to a slowly increasing effective thickness at rising angles from the perpendicular of the incident directed light. The characteristic of a particular glass filter can be changed by the material thickness. Increasing it will reduce the transmission and narrow the width of the bandpass. Production related issues may cause slight variations in thickness and differences between glass batches. The quality of the filter's transmission can generally be influenced by the light structure, such as diffuse or directed from a point source. The colored glass filter shows a certain robustness against this alteration. Measurements confirmed only a minor deviation of the curve for diffuse conditions compared to small AOIs. For further information on measurements, please refer to Appendix C.4.

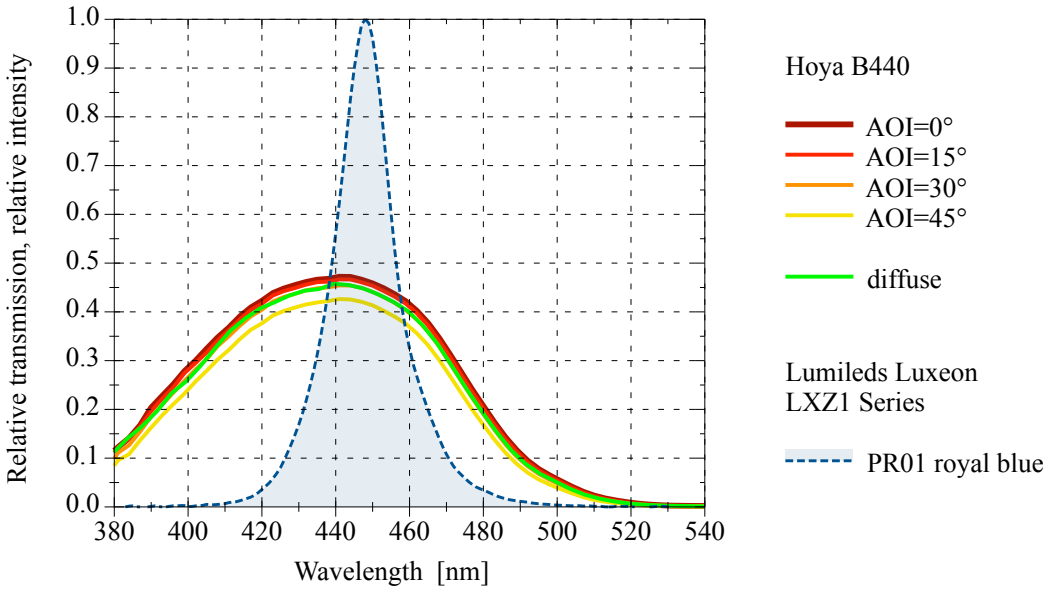

Figure 3.16: Measured spectral transmission curves for a colored glass bandpass filter Hoya B440 with a directed light source at different AOIs and with a diffuse light source. The measured relative intensity distribution of a deep blue LED of approx. 450 nm CWL is also given as a filled curve to illustrate the overlap.

Thin Film Filters

Thin film filters, also named dichroic or interference filters, are made of many stacked thin layers of alternating high- and low-index material evaporated on a substrate such as glass. Depending on the wavelength, light interferes differently in these layers; it is transmitted or reflected. Generally, these filters are available in a large number of variations, and as individually designed types, but they are typically cost intensive.

Their main advantages are high transmission values and steep slopes [171]. The disadvantage as bandpass filters is the AOI-dependent spectral shift of the transmission zone, which leads to a disintegration of the good characteristics at larger AOIs. This shift at non-normal angles of incidence φ can be calculated based on (3.5), as given in [172]. The effective index of refraction n_{eff} is given in the respective data sheet. Please refer to Fig. 3.17 for the curves of typical values of n_{eff}.

$$\lambda(\varphi) = \lambda_0 \cdot \sqrt{1 - (\sin(\varphi)/n_{\text{eff}})^2} \tag{3.5}$$

Furthermore, thin film filters show an increasing sensitivity with rising AOIs to the polarization direction of light. This only applies to light sources such as lasers or LDs, but not LEDs. A selection of filters with different properties suitable for deep blue LEDs are available off the shelf. Three types will be presented and examined in this section: a narrow 10 nm bandpass and a wider low-cost 40 nm type, both selected to encounter the center wavelength of the LED spectrum. The third filter is a high-quality 50 nm bandpass, a few nanometers out of alignment towards higher wavelengths to compensate for the AOI-related spectral shift. This provision is denoted as the shift margin (SM) in the following. The characteristics of these filters are shown in Fig. 3.18. For further information on filter data please refer to [173, 174, 175], and for information on measurements see the Appendix C.4.

Another drawback of thin film filters is a certain sensitivity to the structure of the incident light; the steep slopes and the transmission degrade in diffuse light as shown in Fig. 3.19. A comparison of measured and simulated values for demanding conditions of a large AOI is shown in Fig. 3.20.

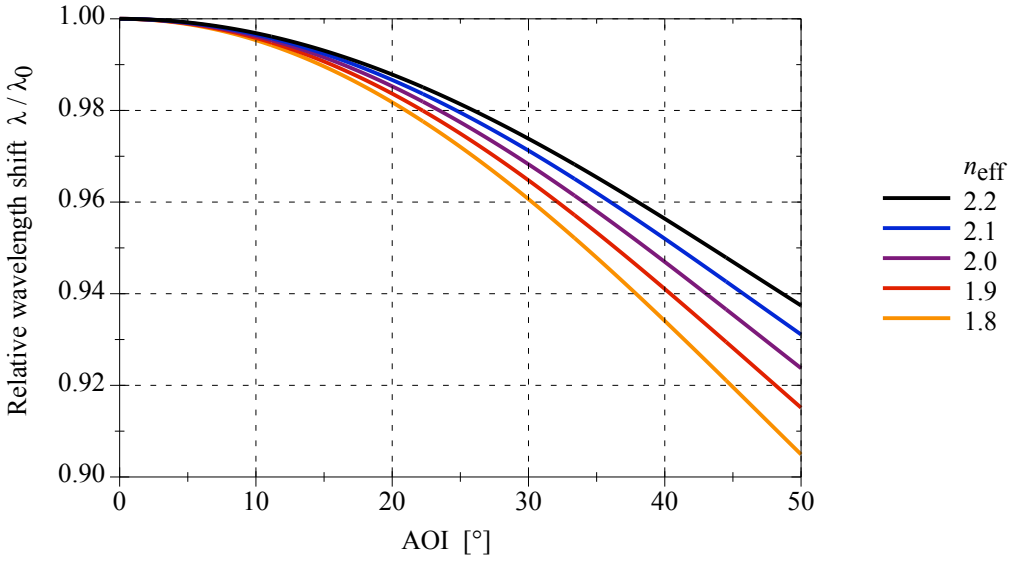

Figure 3.17: Relative wavelength shift of thin film filters with different effective indices of refraction at non-normal angles of incidence.

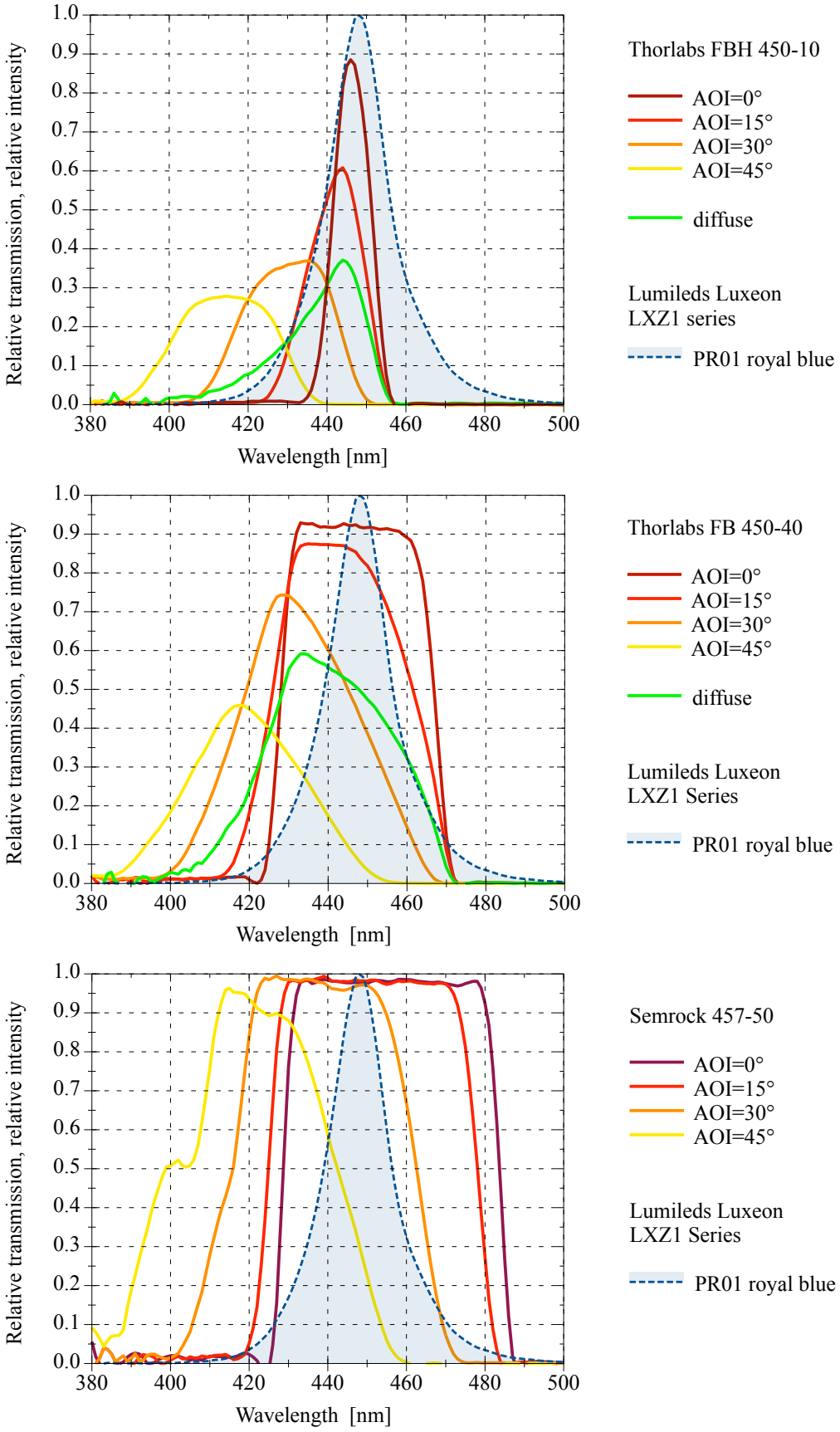

Figure 3.18: Relative transmission of three thin film filters for varying angles of incidence and relative intensity of a deep blue LED.

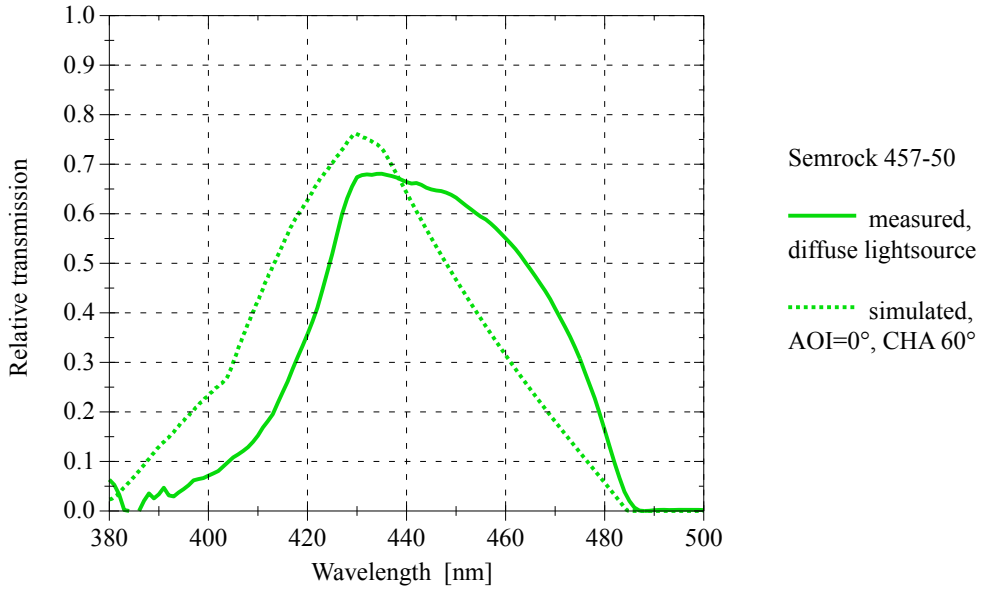

Figure 3.19: Measured spectral transmission curve for a thin film bandpass filter Semrock 457-50 with a diffuse light source, and for comparison the simulated curve employing a light source with a beam half angle or cone half angle (CHA) of 60°.

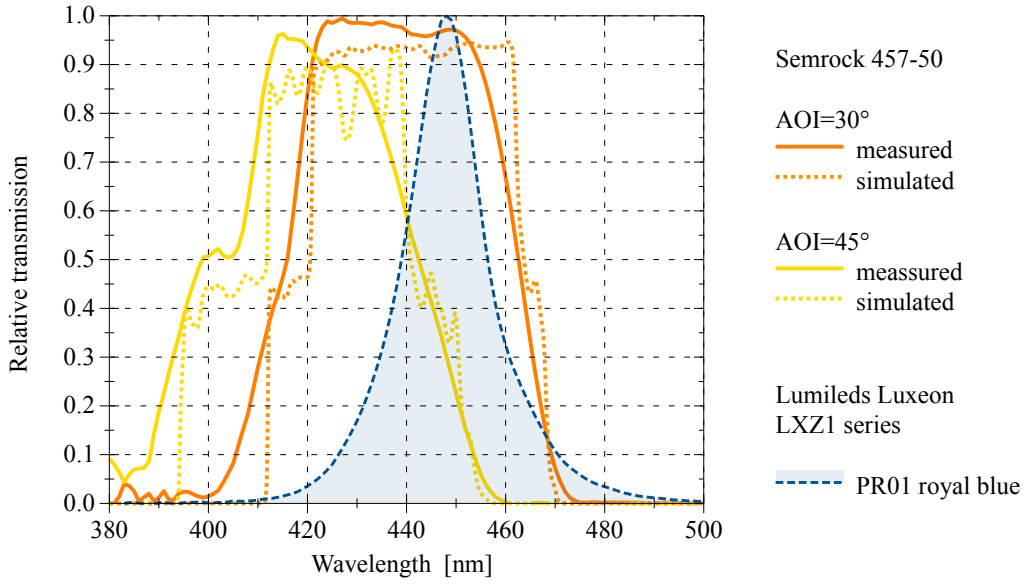

Figure 3.20: Comparison of measured and simulated spectral transmission curves for a thin film bandpass filter Semrock 457-50 for a large AOI. Additionally shown is the relative intensity of a deep blue LED.

Selection and Setup of Filter Components

To approach the desired goal of an effective filtering inside a large FOV for each single receiving element, many parameters need to be considered and aligned. Starting at the environmental conditions such as location, water type, operating depth, wavelength of least attenuation, spatial orientation, and continuing with the light source properties such as LED type, CWL, binning, FWHM and intensity curve. This is followed by the filter attributes including type, center wavelength, passband width, AOI range, coverage of LED radiant emission, filter quality, tolerances and possible side lobes. These side lobes, which occur with colored glass as well as with thin film types, can be critical when positioned spectrally inside the sensitivity curve of the detector and the ambient light distribution range, see Figure 3.21. In underwater operations, side lobes above approximately 750 nm are not considered critical, as the water absorption is large in this range. Other types of filters like gelatine or polyester foil are available, but they are not suitable for the harsh humid environment. Proceeding with the photodetector and its spectral sensitivity and directional characteristics, and finally with the choice of the underwater housing technology, this matching process may need some iterations, since many dependencies exist, including mutual ones.

Anti-reflection coatings can help to reduce losses in transitions to air and make fragile filter surfaces more mechanically robust and resistant. Filters should not be exposed directly to seawater, especially thin film filters, as they are sensitive to dirt. Further optimization can be done by using index matching gel to bond the planar PD to the filter to avoid an additional glass-air-glass transition, see also Section 2.1.1.

To set up an optical system for underwater operations it is common to use pressure housings with flat- or dome-ports made of glass or plastics, and as alternative components can be cast in optical transparent materials such as silicone, polyurethane, or epoxy. The applicability of the respective material depends on the pressure-resistant or pressure-neutral method of construction [17, 36, 176]. Common to all is the need to avoid the number and the order of transitions of optical density, since they may generally influence the transmission and the FOV. This topic is discussed in detail in Section 4.3.1.

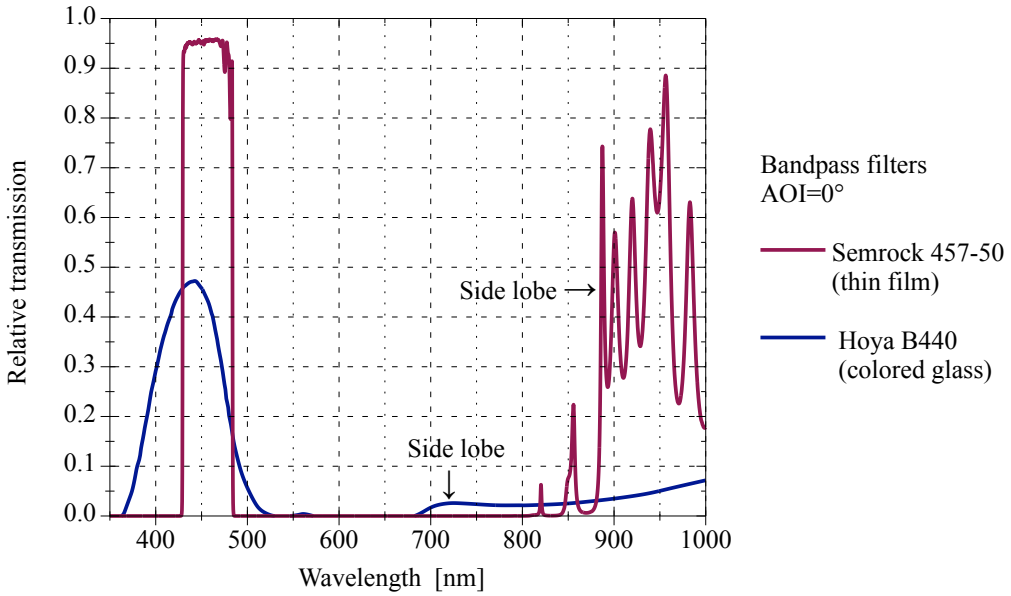

Figure 3.21: Transmission curves of a colored glass bandpass filter Hoya B440 and a thin film bandpass filter Semrock 457-50. Side lobes can be identified on the right side.

3.2.5 Influence on Optical Signal-to-Noise Ratio and Optimization

OSNR

The filter implemented in front of a PD should let pass the signal from the LED light source and block the ambient light as much as possible. It is unavoidable that the filter also passes the part of the ambient light spectrum which is within the passband. This as unwanted component represents the optical noise.

In Figure 3.22 different underwater situations are shown for the case of a straight upward looking sensor, basically the worst case scenario. An exception would be the sensor viewing directly into the sun, which can occur in shallow clear waters. The upwelling irradiance is not relevant for the upwards looking sensor and likewise the other way round. More information on the influence of the detector orientation is given in Section 3.4.2.

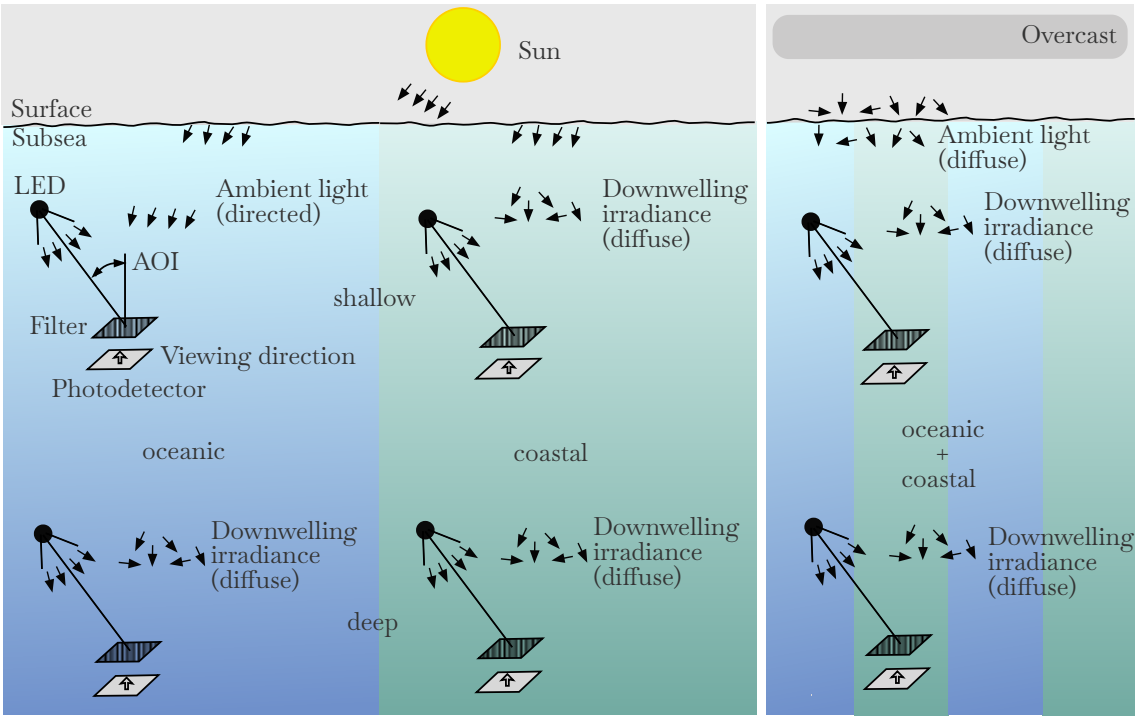

Figure 3.22: Illustration is showing the general scenario and illustrates the environmental circumstances including the variation of water type, depth and sun brilliance/overcast.

The optical SNR is defined in (3.6) and more specifically in (3.7), with the power of the LED as signal P_{sigLED} and the power of the ambient light as noise P_{ambLight}. The spectral measurements or simulations are delivering irradiance values E in watts per unit area. For relative calculations, the transition from E to the power P in watts is correct, as long as the reference area is the same and constant, as for the PD in this case:

$$OSNR = \frac{P_{\text{opt.Signal}}}{P_{\text{opt.Noise}}} \tag{3.6}$$

$$OSNR = \frac{P_{\text{sigLED}}}{P_{\text{ambLight}}}. \tag{3.7}$$

To examine the effectivity of a filter, the relative change in the optical signal-to-noise ratio (OSNR) is sufficient, and absolute values are not required. This can be calculated as expressed in (3.8), where E_{LED} is the relative irradiance of the LED and $T_{\text{Filterdir}}$ is the relative transmittance

Table 3.5: Calculated relative rates of passed radiated power for different LED-filter combinations at various AOIs, based on measured LED spectra and filter transmission curves. Additionally, the corresponding values of signal power loss in decibel caused by the optical filter are shown. The LED is Lumileds LXZ1 series in royal blue.

AOI	Colored glass Hoya B440	Thin film Thorlabs 450-10	Thin film Thorlabs 450-40	Thin film Semrock 457-50
0°	44.1 % -3.56 dB	37.2 % -4.30 dB	82.4 % -0.84 dB	92.9 % -0.32 dB
15°	43.6 % -3.61 dB	29.4 % -5.32 dB	72.1 % -1.42 dB	94.0 % -0.27 dB
30°	42.3 % -3.73 dB	11.9 % -9.23 dB	40.6 % -3.91 dB	85.1 % -0.70dB
45°	39.5 % -4.03 dB	1.64 % -17.85 dB	9.43 % -10.25dB	33.4 % -4.77 dB

of the filter for directed light. In the lower part of the fraction, E_d is the irradiance of the ambient light, which is in most cases diffuse, and therefore the transmittance of the filter for diffuse light $T_\mathrm{Filterdiff}$ is used. To achieve values in the more practical unit decibel, (3.9) can be used.

$$\Delta\mathrm{OSNR} = \frac{\dfrac{\int_{350\ \mathrm{nm}}^{750\ \mathrm{nm}} E_\mathrm{LED}(\lambda)\cdot T_\mathrm{Filterdir}(\lambda)\ \mathrm{d}\lambda}{\int_{350\ \mathrm{nm}}^{750\ \mathrm{nm}} E_\mathrm{LED}(\lambda)\ \mathrm{d}\lambda}}{\dfrac{\int_{350\ \mathrm{nm}}^{750\ \mathrm{nm}} E_\mathrm{d}(\lambda)\cdot T_\mathrm{Filterdiff}(\lambda)\ \mathrm{d}\lambda}{\int_{350\ \mathrm{nm}}^{750\ \mathrm{nm}} E_\mathrm{d}(\lambda)\ \mathrm{d}\lambda}} \tag{3.8}$$

$$\begin{aligned}\Delta\mathrm{OSNR}\ [\mathrm{dB}] = {} & 10\cdot\log\left(\frac{\int_{350\ \mathrm{nm}}^{750\ \mathrm{nm}} E_\mathrm{LED}(\lambda)\cdot T_\mathrm{Filterdir}(\lambda)\ \mathrm{d}\lambda}{\int_{350\ \mathrm{nm}}^{750\ \mathrm{nm}} E_\mathrm{LED}(\lambda)\ \mathrm{d}\lambda}\right) \\ & -10\cdot\log\left(\frac{\int_{350\ \mathrm{nm}}^{750\ \mathrm{nm}} E_\mathrm{d}(\lambda)\cdot T_\mathrm{Filterdiff}(\lambda)\ \mathrm{d}\lambda}{\int_{350\ \mathrm{nm}}^{750\ \mathrm{nm}} E_\mathrm{d}(\lambda)\ \mathrm{d}\lambda}\right)\end{aligned} \tag{3.9}$$

Please find further information regarding the calculations in Appendix C.5. The upper term of the main fraction in (3.8) represents the relative passed irradiation of the LED through the filter. Values for four examined different filters with varying AOIs are given in Table 3.5. The lower term refers to the relative ambient light attenuation by the filter. Since the ambient light spectral composition is a function of the depth and the water type, this is considered in the scope of Table 3.6. By taking values from Tables 3.5 and 3.6 and using (3.9), the improvement in OSNR can be calculated for a specific filter, at a certain depth of a given water type for a desired angle of incidence. This has been performed to achieve the curves presented in Figs. 3.23 and 3.24.

Table 3.6: Calculated ambient light suppression for the four different filters in three exemplary water types at varying depths, up to meaningful remaining light values. Generally calculated with filter characteristics for diffuse light, with the exception for very shallow water of 2 m to 5 m depths in the clear water type IB. Here the characteristics of the dominating directed light were used for thin film filter (AOI = 15°), please refer to Fig. 3.10. Values for the thin film filters in water type IB at a depth of 10 m were not calculated, since the filter characteristic either for diffuse or directed light were applicable.

Water type	Depth	Colored glass Hoya B440	Thin film Thorlabs 450-10	Thin film Thorlabs 450-40	Thin film Semrock 457-50
Jerlov 1B	2 m	-8.53 dB	-14.21 dB	-9.05 dB	-6.87 dB
	5 m	-7.75 dB	-13.38 dB	-8.22 dB	-7.05 dB
	10 m	-7.14 dB	n.a	n.a	n.a.
	20 m	-6.54 dB	-12.98 dB	-8.55 dB	-6.40 dB
	50 m	-5.74 dB	-12.11 dB	-7.61 dB	-5.40 dB
	100 m	-5.31 dB	-11.76 dB	-7.15 dB	-4.82 dB
	200 m	-5.23 dB	-12.09 dB	-7.29 dB	-4.64 dB
Jerlov III	2 m	-8.47 dB	-14.90 dB	-10.62 dB	-8.47 dB
	5 m	-7.85 dB	-14.31 dB	-9.96 dB	-7.77 dB
	10 m	-7.47 dB	-13.99 dB	-9.56 dB	-7.31 dB
	20 m	-7.28 dB	-13.99 dB	-9.45 dB	-7.03 dB
	50 m	-6.22 dB	-12.92 dB	-8.40 dB	-5.88 dB
	100 m	-6.58 dB	-14.57 dB	-9.51 dB	-6.38 dB
Jerlov 3C	2 m	-9.51 dB	-15.89 dB	-11.64 dB	-9.36 dB
	5 m	-10.10 dB	-16.83 dB	-12.49 dB	-9.92 dB
	10 m	-11.40 dB	-19.07 dB	-14.73 dB	-11.56 dB
	20 m	-13.70 dB	-22.79 dB	-19.43 dB	-14.98 dB
	50 m	-13.99 dB	-24.25 dB	-22.64 dB	-16.30 dB

The analysis of Tables 3.5 and 3.6 and of the Figs. 3.23 and 3.24 shows that the colored glass filter offers the lowest OSNR gain, but also the smallest AOI dependence. The effectiveness may not be so high - but compared to a configuration without a filter, it is attractive, as well as robust and cheap, and will thus will be used in many cases. As demonstrated, the narrowest tested thin film Thorlabs 450-10 filter shows the best OSNR for small AOIs, but drops off for larger AOIs. The thin film filter Semrock 457-50, which has a wider passband and some shift margin, performs at a more balanced level thus represents the best choice of the tested components. The attenuation of the LEDs signal is low, with a simultaneous tolerance of larger AOIs. This result would allow energy efficient applications with 60° FOV with comparatively high improvement of the OSNR, compared to a colored glass filter. This is important, since in many practical situations the ambient light will be significantly less, such as for overcast, periods outside of high sun, horizontal or downwards looking sensors and larger operation depths.

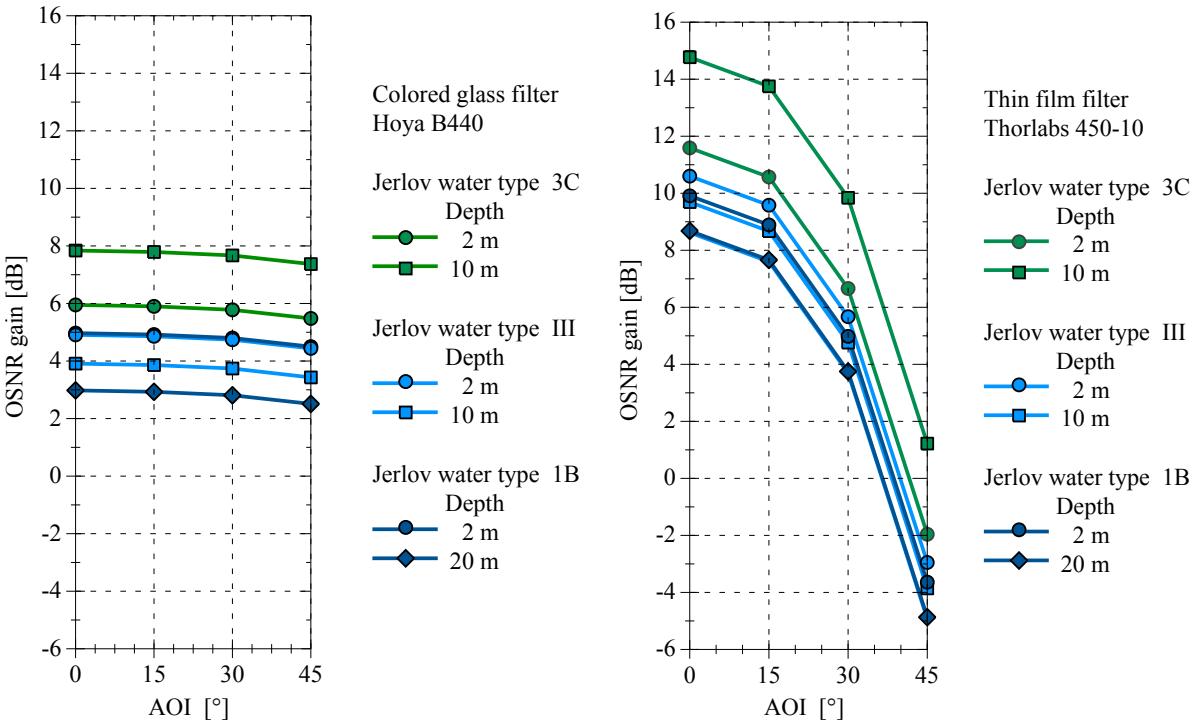

Figure 3.23: Gain in OSNR due to utilization of a colored glass and a narrow band thin film filter in different waters and depths for varying angles of incidence.

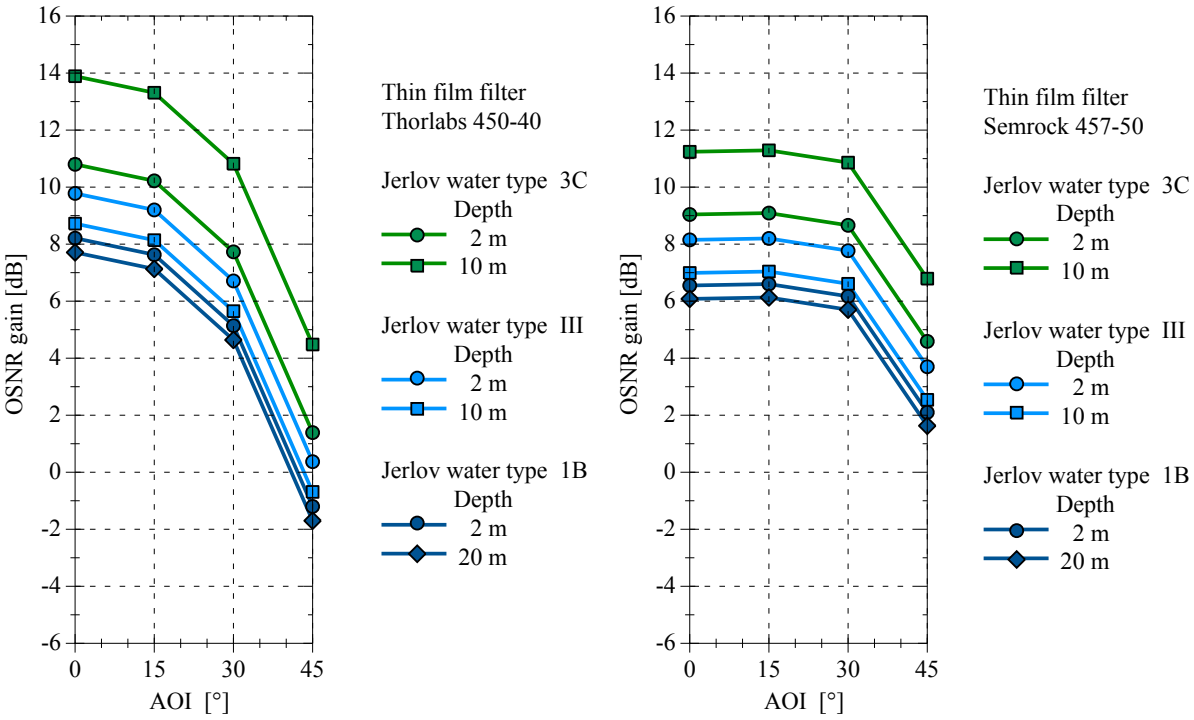

Figure 3.24: Gain in OSNR due to utilization of two thin film filter of intermediate passband width in different waters and depths for varying angles of incidence.

Attempt of Generalization

Due to the limited availability of thin film filters with different passband widths (PB) for the same center-wavelength from stocks, only a small selection of filters was accessible for testing purposes. In addition, the filters exhibit different qualities in terms of maximum transmission, edge steepness and roundings. This allows certain basic principles to be identified, but no optimizations can be derived. There are basically two questions that arise from the above issue. The first is how the behavior changes by adding different shift margins (SM). The second is the question of an optimum in terms of OSNR as a function of the ratio of the filter passband width to the LED FWHM. To answer these questions, simulations are best suited.

For this purpose, the properties and behavior of the thin film filter must be represented in a model. For the case of directed light impacting perpendicular to the filter's and the PD's surface, as well as the fact that real filter transmissions can reach value of close to 1, this is leading to:

$$T(\lambda) = 1 \quad \text{for} \quad \lambda_{\mathrm{PB_{lower}}} \leq \lambda \leq \lambda_{\mathrm{PB_{upper}}}, \ \text{else} \ T(\lambda) = 0 \tag{3.10}$$

with

$$\lambda_{\mathrm{PB_{lower}}} = \lambda_{\mathrm{PB_{center}}} - \frac{PB}{2} \quad ; \quad \lambda_{\mathrm{PB_{upper}}} = \lambda_{\mathrm{PB_{center}}} + \frac{PB}{2}. \tag{3.11}$$

The application of this thin film filter model to the spectral coverage of an LED, including the shift margin is shown in Fig. 3.25 for better clarification.

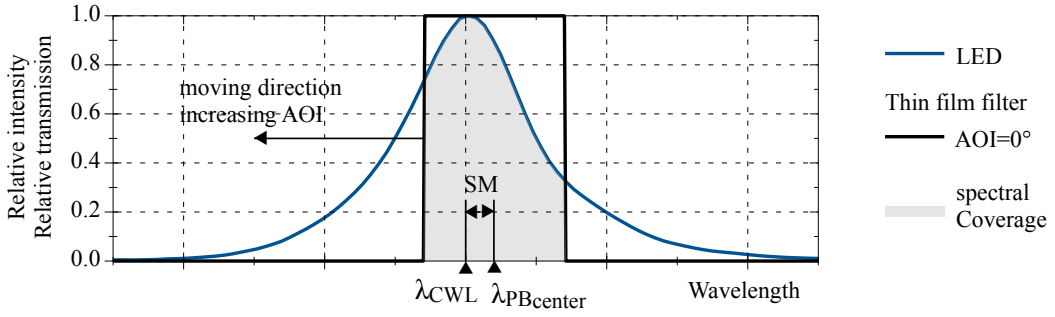

Figure 3.25: Spectral coverage of an LED from idealized thin film filter including the shift margin.

The base of the model for the behavior of the thin film filter under diffuse light conditions consists of two parts. The first part are the author's own spectral measurements of the available filters by utilizing a diffusor sheet, and the second part are transmission simulations for various filters of different passband widths under large cone angles, see Section 3.2.4 and Appendix C.4. This yields the following model, and Fig. 3.26 shows the interrelationships graphically:

$$T(\lambda) = 0 \quad \text{for} \quad \lambda < \lambda_{\mathrm{diff_{lower}}} \tag{3.12}$$

$$T(\lambda) = 0.2 + \frac{0.2 \cdot PB}{FWHM_{\mathrm{LED}}} \cdot \frac{(\lambda - \lambda_{\mathrm{diff_{lower}}})}{(\lambda_{\mathrm{diff_{center}}} - \lambda_{\mathrm{diff_{lower}}})} \quad \text{for} \quad \lambda_{\mathrm{diff_{lower}}} \leq \lambda \leq \lambda_{\mathrm{diff_{center}}} \tag{3.13}$$

$$T(\lambda) = 0.2 + \frac{0.2 \cdot PB}{FWHM_{\mathrm{LED}}} \cdot \frac{(\lambda - \lambda_{\mathrm{diff_{upper}}})}{(\lambda_{\mathrm{diff_{center}}} - \lambda_{\mathrm{diff_{upper}}})} \quad \text{for} \quad \lambda_{\mathrm{diff_{center}}} \leq \lambda \leq \lambda_{\mathrm{diff_{upper}}} \tag{3.14}$$

$$T(\lambda) = 0 \quad \text{for} \quad \lambda > \lambda_{\mathrm{diff_{upper}}}. \tag{3.15}$$

The model described in (3.12) to (3.15) is valid for ratios of the filter passband PB to the LED optical bandwith $FWHM_{\mathrm{LED}}$ of 0.2 to 4, and same center wavelengths λ_{CWL} of the LED and

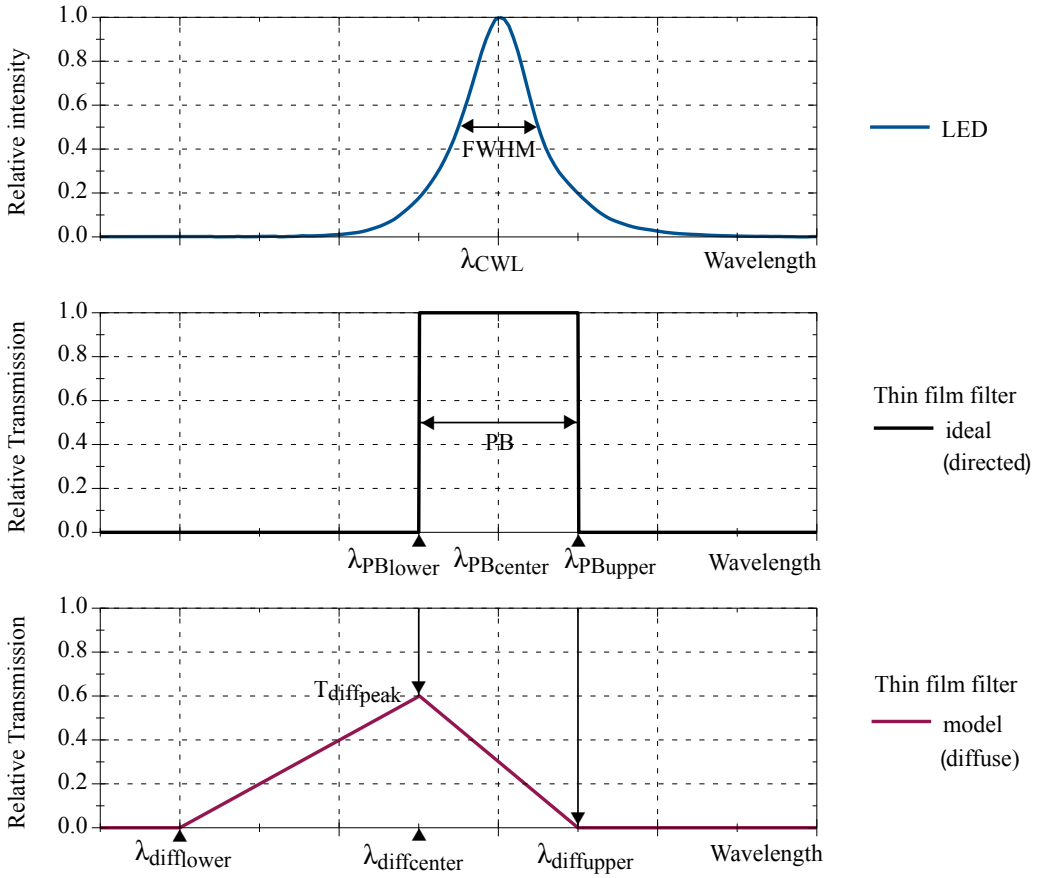

Figure 3.26: Modeling of the thin film filters transmission for diffuse incident light. Example shows the filter's passband being two times the FWHM of the LED.

$\lambda_{\mathrm{PB_{center}}}$ of the filter. These values also represent the given ones. The significant wavelengths of the diffuse transmission curve are given by:

$$\lambda_{\mathrm{diff_{upper}}} = \lambda_{\mathrm{PB_{upper}}} \quad ; \quad \lambda_{\mathrm{diff_{center}}} = \lambda_{\mathrm{PB_{lower}}} \quad ; \quad \lambda_{\mathrm{diff_{lower}}} = 0.9 \cdot \lambda_{\mathrm{PB_{lower}}}. \tag{3.16}$$

The factor of 0.9 in (3.16) results from (3.5) at an effective refraction index of 2 and an AOI of 60°. The model does not take into account the slight asymmetry of the spectral intensity course of the LED, so the peak is centered within the optical bandwidth.

After introducing the modeling, this section then goes back to the first question of the shift margins effect. The SM denotes the amount of shift of the filter center wavelength $\lambda_{\mathrm{PB_{center}}}$ compared to the LED center λ_{CWL} towards higher wavelengths, to compensate for the AOI related shift in direction of lower wavelengths. The result of several simulations comprising different passband widths as well as shift margins is given in Fig. 3.27. In order to represent a middle case as far as possible, the LED chosen for simulation is Luxeon Z series blue, due to an intermediate spectral course within colors of the series, cf. Fig. 3.13. Likewise, a filter with an intermediate effective index of refraction of 2 is selected. The relative spectral coverage is represented by the upper term of (3.8). The calculation is done by summation of discrete elements with 1 nm width.

The curves shown indicate the following relationships. In principle, larger AOI can be achieved by inserting some shift margin, but at the expense of transmission values with small AOIs. This is more pronounced with narrowband filters. The simulation is based on ideal filter shapes for all AOIs, but in reality these degrade with increasing AOI. This is more distinctive for narrowband and simpler designs, and many high-quality filters can hold the shape well up to 30°. The effect

of this degradation is a smaller spectral coverage. All in all, applying a shift margin is a useful method to reduce the effects of viewing angle dependency, but overdoing can be counterproductive.

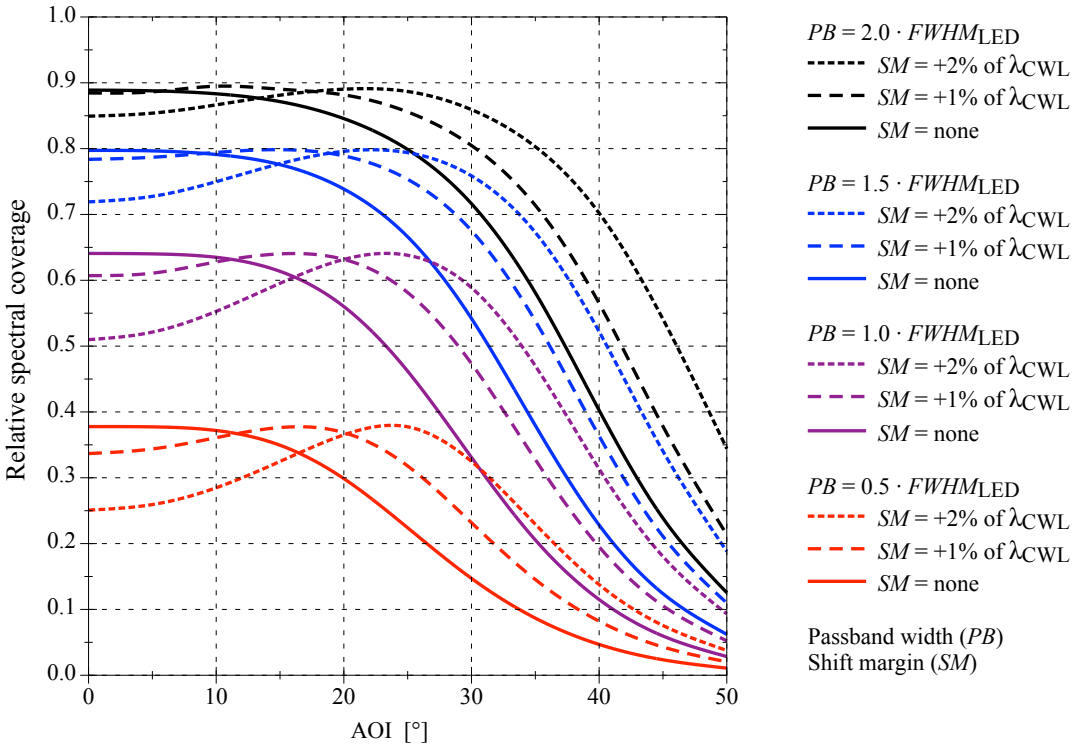

Figure 3.27: Relative spectral coverage as afunction of the angle of incidence for ideal filters with different passband widths and different added wavelength shift margins, both using realistic scales.

The second open question is related to a possible optimum in terms of OSNR by variation of the filters passband width. The following conditions are applied for the simulation: upwards looking sensor, perpendicular incidence, LED type Lumileds Z royal blue with a λ_{CWL} of 448 nm and a FWHM of 17.4 nm, equal filter passband center and LED center wavelength, and ambient light conditions given as downwelling irradiance within a bandwidth of 350 nm to 750 nm, see Fig. 3.11. A simulation range of the PB_{Filter} to $FWHM_{\mathrm{LED}}$ ratio from 0.2 to 4 results in filter passbands from 3.5 nm to 70 nm.

The upper diagram in Fig. 3.28 gives the simulated suppression of the LED light by the filter, utilizing the direct light filter model of (3.10) and the left term of (3.9). This corresponds in principle to the non-logarithmic version in Fig. 3.14. For the calculation of the ambient light suppression of the oceanic Jerlov IB water at a depth of 2 m, the direct filter light model and the right term of (3.9) needs to be applied. Diffuse ambient light situations are found in the remaining water types and depths, such as Jerlov IB 20 m, III and 3C. The diffuse filter model as given in (3.12) to (3.15) needs to be used here, as well as the right term of (3.9) again.

The lower diagram in Fig. 3.28 depicts the combination of the signal component suppression and ambient light suppression by the thin film filter. In addition to the simulated curves, calculated points from three real filters (based on measured transmission values) are given for comparison, cf. Fig. 3.18. For the predominantly occurring diffuse ambient light situation underwater, an OSNR gain maximum results at a ratio of the filter's passband to the LED FWHM of approximately 1. In the case of directional ambient light, small ratios provide better OSNR gain values.

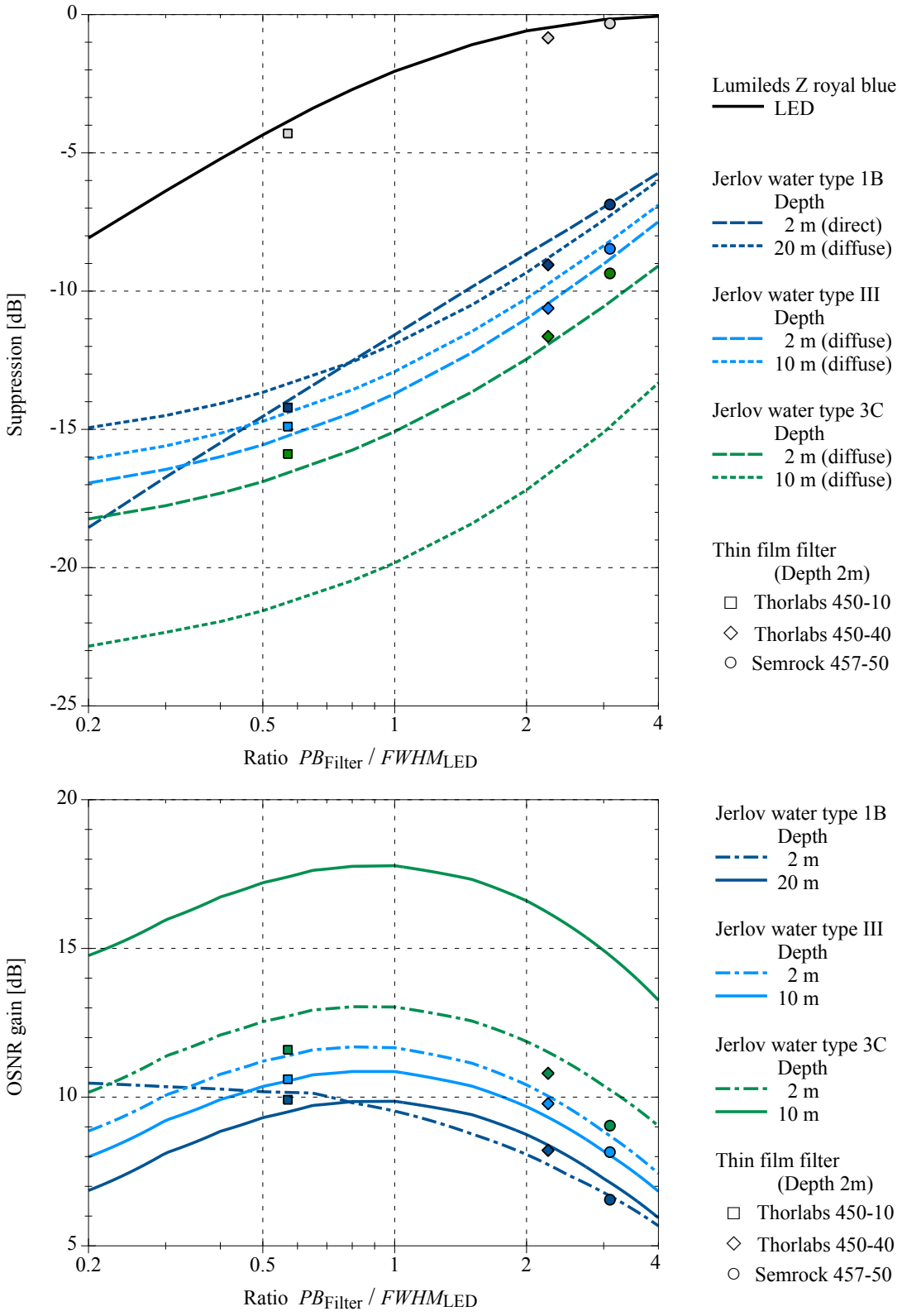

Figure 3.28: The upper diagram depicts the suppression of ambient light by a modeled ideal filter for different water types and depths, as well as the residual power of the LED after filtering. The combination of both is given in the lower diagram, which corresponds to the delta in OSNR for these circumstances. Added calculated points based on measured filter curves are shown for three real thin film filters.

3.3 Noise Sources and Noise Properties

3.3.1 From Optical to Electrical SNR

The optical signal to noise ratio (OSNR) is given in (3.7) as the ratio of signal to ambient irradiance or power. This ratio can be improved by filtering, but this improvement or gain cannot be directly applied to the electrical domain. The signal-to-noise ratio (SNR) in the electrical domain is given as the ratio of average received power to the average noise power at the same position within the chain [39]:

$$SNR_{=}\frac{P_{\mathrm{Rel}}}{N_{\mathrm{Rel}}}. \tag{3.17}$$

A comparison of the numerators and denominators of (3.7) and (3.17) shows why a direct transfer from OSNR to the electrical SNR breaks, which is also indicated by (2.21).

The photodetector cannot distinguish between wanted signal light and unwanted ambient light, and all incident light will be transferred into an electrical current by the responsivity $\mathcal{R}$. Generally, there are different proportionalities of the received powers P_{Ropt} and P_{Rel} in their domains. In the optical P_{Ropt} is proportional to the detector's effective area A_{eff}, in the electrical domain P_{Rel} is proportional to ${A_{\mathrm{eff}}}^2$. The ratio of these two powers is further dependent on the signal shape, which is described by the shaping gain factor κ, cf. Section 2.1.6.

The denominator consists of statistically independent thermal and shot noise:

$$N_{\mathrm{Rel}} = N_{\mathrm{shot}} + N_{\mathrm{therm}}. \tag{3.18}$$

Both of these components can be dominant in UOWC, for example the thermal noise in a deep dark environment, and the shot noise under ambient light conditions.

A binary intensity modulation contains two signal states, H and L, which in the simple common case correspond to optical power on and off, respectively. Extracting the minimum required SNR for the most common NRZ-OOK modulation scheme from Table 2.3, results in a value of 13.5 dB for an ambitious BER value of 10^{-6}, and a shaping gain factor of 2. This SNR is based on signal and noise averages, in simulations both states are considered separately in most cases, the more relevant state is generally with the signal set at peak power. In the case of a dominant signal independent noise (thermal) and a κ value of 2 this leads to a 3 dB increase in SNR, giving a total of 16.5 dB for the ON state. In the other case of dominant signal dependent noise (shot) the ratio stays at 13.5 dB. Modulation schemes of higher power efficiency like 4-PPM, or lower BER values are requiring less SNR. Generally, the SNR values are seen as minimum requirements. Thus, an average SNR value of 15 dB represents the requirement under the conditions mentioned, and is therefore used as a base for the following investigations.

3.3.2 TIA Amplification

A basic description of the PD and TIA, as well as some basic formulas for calculations, are given in Section 2.1.5. Additional relationships required for more in-depth investigations are provided in the following section. The electrical front end of the receiver in UOWC normally consists of the PD itself and a one-stage low-noise wideband preamplifier in a transimpedance configuration, as given in Fig. 3.29. The dynamic range is limited by noise with small signals on the low side, and by saturation on the high side, due to ambient light or even very large signals.

Two topologies in the TIA stage are common: the photovoltaic and the photoconductive mode, respectively. In the photovoltaic mode, the PD anode is grounded, and the reverse voltage U_{R} is hereby zero. Correspondingly, the PD is virtually short-circuited by the OpAmp. A possible positive impact on the darknoise contribution can promote high sensitivity applications. In the photoconductive mode, U_{R} is > 0, which leads to a junction capacitance reduction because the effective gap increases between the differently doped semiconductor layers. Typically achievable

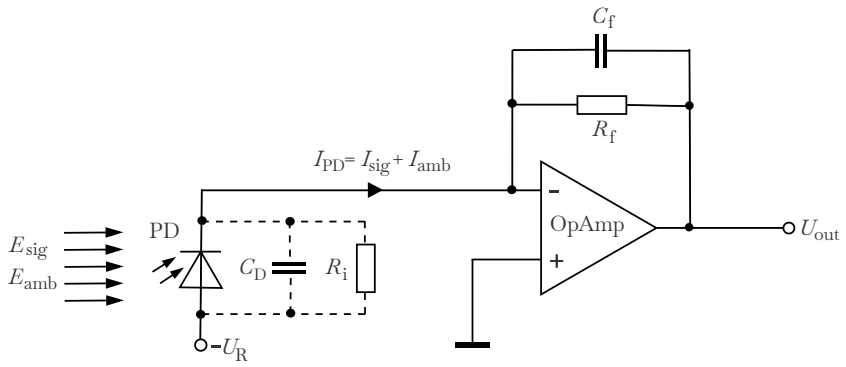

Figure 3.29: One-stage TIA utilized for PIN-PD or APD. The discrete devices R_f and C_f are the feedback resistor and the feedback capacitor, respectively. The PD junction capacitance is symbolized by C_D, the shunt resistance by R_i.

capacity reductions are in the range of a factor 2 to 10. Since the capacitance is the generally limiting factor of the speed or the bandwidth, this reduction plays a big role in most applications. APDs must always be operated with a high reverse voltage, otherwise the avalanche effect will not occur. However, due to the internal gain, only smaller areas are usually required, which means that the resulting capacities are smaller. More detailed information about the transimpedance amplifier (TIA) and other circuit configurations can be found in [79, 177]. Calculations and simulations of TIA can be conducted with [74, 178].

The irradiation reaching the PD represents a superposition of the signal and ambient components, which differ spectrally but also temporally. The signal part consists in most cases of fast binary or step intensity changes, and the ambient part is usually a constant amount with relatively slow changes. The output voltage U_{out} is accordingly determined by the sum of the respective currents I_{sig} and I_{amb} generated by the PD and the feedback resistor R_f:

$$U_{out} = U_{sig} + U_{amb} = (I_{sig} + I_{amb}) \cdot R_f. \tag{3.19}$$

The respective voltage components U_{sig} and U_{amb} can also be expressed by the corresponding irradiances E_{sig} and E_{amb} and the PD parameter responsivity $\mathcal{R}$, gain G and detector area A_{det}:

$$U_{sig} = \mathcal{R} \cdot G \cdot A_{det} \cdot E_{sig} \cdot R_f \tag{3.20}$$

$$U_{amb} = \mathcal{R} \cdot G \cdot A_{det} \cdot E_{amb} \cdot R_f. \tag{3.21}$$

The SNR in decibels is given by the following equation, where U_{n_sum} represents the sum of the noise from different sources:

$$SNR = 20 \cdot \log\Big(\frac{U_{sig}}{U_{n\_sum}}\Big) \text{ [dB]}. \tag{3.22}$$

The achievable cut-off frequency of the TIA stage is given by:

$$f_{-3dB} = \sqrt{\frac{GBW}{2\pi \cdot R_f \cdot (C_D + C_f)}}. \tag{3.23}$$

The gain bandwidth product GBW is a characteristic value of the amplifier used. C_D is the PD junction capacitance, and R_f and C_f are the components dimensioned according to the desired amplification and quality or overshoot in the pulse response behavior. A required GBW can be approximated by:

$$GBW \approx f^2_{-3dB} \cdot 2\pi \cdot R_f \cdot C_D. \tag{3.24}$$

3.3.3 Noise Sources

With respect to the achievable communication speed and bit error rates of an UOWC system, the signal-to-noise ratio (SNR) is the most relevant parameter. The signal power in LED-driven and battery-supplied systems is limited and also attenuated geometrically and exponentially by the water with increasing distance.

This implies special attention to the noise, for which several sources can be identified. A clear dominant role cannot be assigned to one type of noise, as it depends on many environmental conditions and component parameters. The examination of the noise should always take place at the same position within the chain or circuit, here the respective voltages at the output across the resistor R_f are used. Of course the respective currents can also be evaluated as well as the powers, which are then referred to as noise equivalent power (NEP) [161, 179]. The formulas in the following are valid for PIN-PDs, and later they will be extended to include APDs.

The Johnson or thermal noise, which is caused by the thermal agitation of charge carriers (electrons or holes) in a conductor, is present in all passive resistive elements. The thermal noise of the feedback resistor R_f expressed as a voltage $U_{\mathrm{n\_th}}$ is given in (3.25), where T is the absolute temperature in Kelvin, k_B=1.38 10^{-23} Ws/K is the Boltzmann constant, and NBW is the related noise bandwidth. The noise contributions of the op-amp itself are represented by the voltage noise density e_n in nV/$\sqrt{\mathrm{Hz}}$, whereby e_n represents the thermal noise of the internal resistors. The respective voltage $U_{\mathrm{n\_e_n}}$ is given in (3.26). The thermal noise contribution of R_i can be neglected due to typically very high values where $R_\mathrm{i} >> R_\mathrm{f}$.

$$U_{\mathrm{n\_th}} = \sqrt{\frac{4 \cdot k_\mathrm{B} \cdot T \cdot NBW}{R_\mathrm{f}}} \cdot R_\mathrm{f} = \sqrt{4 \cdot k_\mathrm{B} \cdot T \cdot R_\mathrm{f} \cdot NBW} \tag{3.25}$$

$$U_{\mathrm{n\_e_n}} = e_\mathrm{n} \cdot \sqrt{NBW_{\mathrm{e_n}}} \tag{3.26}$$

Shot noise is caused by the random fluctuation of the number of photons hitting the PD surface and generating charge carrier pairs, and this form is known as quantum shot noise. The electronic shot noise is based on charge carriers crossing a potential barrier in p-n junctions. With a photodiode, in general the two types cannot be distingushed and follow a Poisson distribution, and the descriptive equation is the same for both [3, 39]. Shot noise will be generated in the photodetector by its dark current I_d, and the currents induced by the ambient and the signal incident light, I_amb and I_sig, respectively. The corresponding noise voltages are given by (3.27) to (3.29), where the elementary charge is e_0=1.60 10^{-19} As. The shot noise of the amplifier input bias currents is given by the current noise density i_n in pA/$\sqrt{\mathrm{Hz}}$. The respective voltage $U_{\mathrm{n\_i_n}}$ is given in (3.30).

$$U_{\mathrm{n\_shot\_dark}} = \sqrt{2 \cdot e_0 \cdot I_\mathrm{d} \cdot NBW} \cdot R_\mathrm{f} \tag{3.27}$$

$$U_{\mathrm{n\_shot\_amb}} = \sqrt{2 \cdot e_0 \cdot I_\mathrm{amb} \cdot NBW} \cdot R_\mathrm{f} \tag{3.28}$$

$$U_{\mathrm{n\_shot\_sig}} = \sqrt{2 \cdot e_0 \cdot I_\mathrm{sig} \cdot NBW} \cdot R_\mathrm{f} \tag{3.29}$$

$$U_{\mathrm{n\_i_n}} = i_\mathrm{n} \cdot \sqrt{NBW} \cdot R_\mathrm{f} \tag{3.30}$$

Thermal and shot noise are so-called white noise. They are spectrally flat, and show a constant magnitude of power over the frequency. Other noise sources can generally be identified, but are not taken into account here due to their minor nature. For example noise due to imperfections in the semiconductor material, which shows 1/f character and is called pink noise [177].

The noise bandwidth NBW limits the effective range of a white noise process. The equivalent noise bandwidth is seen as a so-called "brick-wall" filter, which replaces the integration over all

frequencies of the transfer function. The NBW depends on the cut-off-frequency and the quality factor Q, which describes the slope in the frequency transfer function and the shape in the pulse response. For the common case of a maximal flat response the Q is 0.7, which leads to a NBW of the cut-off-frequency $f_{-3\mathrm{dB}}$ multiplied by 1.1. The NBW, valid for most contributions, can be calculated as follows:

$$NBW = \frac{\pi}{2} \cdot Q \cdot \sqrt{\frac{GBW}{2\pi \cdot R_\mathrm{f} \cdot (C_\mathrm{D} + C_\mathrm{f})}}. \tag{3.31}$$

An exception is the $NBW_{\mathrm{e_n}}$ of the voltage noise density contribution, which is larger due to gain peaking in the frequency dependent noise gain profile. It can be approximated by:

$$NBW_{\mathrm{e_n}} \approx NBW \cdot GBW \cdot 2\pi \cdot (R_\mathrm{f} \parallel R_\mathrm{i}) \cdot (C_\mathrm{D} + C_\mathrm{f}). \tag{3.32}$$

To calculate the sum $U_{\mathrm{n\_sum}}$ of the different uncorrelated noise voltages, they need to be added as root-sum-of-squares:

$$U_{\mathrm{n\_sum}} = \sqrt{{U_{\mathrm{n\_th}}}^2 + {U_{\mathrm{n\_shot\_dark}}}^2 + {U_{\mathrm{n\_shot\_amb}}}^2 + {U_{\mathrm{n\_shot\_sig}}}^2 + {U_{\mathrm{n\_i_n}}}^2 + {U_{\mathrm{n\_e_n}}}^2}. \tag{3.33}$$

Avalanche photodiodes are characterized by an internal gain G and additional noise compared to the PIN-PDs. Excess noise is added during the internal multiplication process, represented by the excess noise factor F, which is gain and wavelength dependent. In most cases data sheets only specify for one wavelength, and further values need to be requested from the manufacturer. More information on the APDs noise calculation can be obtained in [68, 180]. For other than the referenced gain in the data sheet, an approximation of F can be made by using the excess noise index x in:

$$F \approx G^x. \tag{3.34}$$

The shot noises resulting from different currents are thus affected by an increase. In case of the ambient and signal currents for APDs the corresponding extended equations for the noise voltages are:

$$U_{\mathrm{n\_shot\_amb}} = \sqrt{2 \cdot e_0 \cdot G \cdot F \cdot I_\mathrm{amb} \cdot NBW} \cdot R_\mathrm{f} \tag{3.35}$$

$$U_{\mathrm{n\_shot\_sig}} = \sqrt{2 \cdot e_0 \cdot G \cdot F \cdot I_\mathrm{sig} \cdot NBW} \cdot R_\mathrm{f}. \tag{3.36}$$

For APDs, the dark current I_d needs to be separated into two components, the not-multiplied surface leaking current and the multiplied bulk leaking current:

$$I_\mathrm{d} = I_\mathrm{ds} + I_\mathrm{db} \cdot G. \tag{3.37}$$

Thus, the according noise voltage $U_{\mathrm{n\_shot\_dark}}$ is given by:

$$U_{\mathrm{n\_shot\_dark}} = \sqrt{2 \cdot e_0 \cdot (I_\mathrm{ds} + I_\mathrm{db} \cdot G^2 \cdot F) \cdot NBW} \cdot R_\mathrm{f}. \tag{3.38}$$

Since the components of the dark current are normally not indicated individually and the APD is typically operated at higher gains of 10 to 100, the I_ds becomes insignificant in most cases, which leads to:

$$U_{\mathrm{n\_shot\_dark}} \approx \sqrt{2 \cdot e_0 \cdot (I_\mathrm{d} \cdot G \cdot F) \cdot NBW} \cdot R_\mathrm{f}. \tag{3.39}$$

3.3.4 Simulation of TIA-Amplified Photodetectors

The two most known photodiode-TIA calculators are given in [74, 178]. They both only include the PIN-PD photodetectors. The former offers attractive graphics but does not allow free parametrization of the PD and TIA, and the latter only allows the definition of one light source. For a detailed comparison of PIN-PD and APD, the influence of amplifier parameters and the simulation of different signal and ambient light conditions must be considered, therefore they are only of limited use. To investigate these topics, which are particularly important for the design of UOWC systems, it is necessary to set up a spreadsheet or a stand-alone program, which integrates (3.19) to (3.39) and allows an extensive parametrization.

As a starting point for the calculations, the parameters of suitable common components are used in order to create an image that is not distorted by extreme values of any unreal parts. The same applies to parameter variations to reproduce more sophisticated properties, and these are also derived from real parts. The parameters of the initial setup of the chosen TIA and photodetectors are given in Tables 3.7 and 3.8, respectively.

Table 3.7: TIA parameters used in the simulation.

Gain bandwidth product	GBW	19	MHz
Voltage noise density	e_n	6	$\mathrm{nV}/\sqrt{\mathrm{Hz}}$
Current noise density	i_n	0.0005	$\mathrm{pA}/\sqrt{\mathrm{Hz}}$
Feedback resistor	R_f	100	kΩ
Temperature	T	293	K
Quality factor	Q	0.707	

Table 3.8: Photodetector parameters used in the simulation.

Type		PIN-PD	APD	
Manufacturer		Osram	Hamamatsu	
Partnumber		BPW34B	12053-10	
Area	A_det	7.45	0.785	mm^2
Responsivity	$\mathcal{R}$	0.28	16	A/W
Capacitance	C_D	15	15	pF
Reverse Voltage	U_R	10	150	V
Gain	G	1	50	
Excess noise factor	F	-	1.7	

Values are valid at a wavelength λ of 450 nm.

Some remarks are necessary to describe the environmental conditions. The operational amplifier in the TIA represents a low noise CMOS type, similar to Analog Devices LTC6240. A quality factor Q of 0.7 gives the best flatness in frequency response. The value of R_f is in the typical size range that delivers output voltages, which can be processed well under reasonable lighting conditions. The PDs are in photoconductive mode. The reverse voltage U_R of the APD is set to achieve nominal gain, and the U_R value of the PIN-PD is chosen to achieve the same capacitance value C_d of 15 pF as the value that yields the APD. In both cases this leads into a viable C_f value of 1.6 pF. Even more important, however, is that this results in the same bandwidth with a cut-off frequency of approximately 1.3 MHz and at the same time an equal slightly higher NBW is produced, which allows direct comparison. The shunt resistance R_i is not taken into account,

as generally R_i is $\gg$ R_f and in GΩ range, thus it is not relevant and is often even not given in data sheets. The irradiances provided by the optical signal and ambient light are assumed to be perpendicular to the detector surface and showing a narrowband characteristic at a wavelength of 450 nm, corresponding to the single wavelength simulation.

For SNR calculations, only the signal component of the output voltage U_out is taken into account, assuming that the DC-component resulting from the ambient light does is not saturate the amplifier and is filtered out before or during the following signal processing. On the noise side, all components are included. Now it is possible to determine the relationships between different signal and ambient light conditions, the SNR, and also to resolve the noise components.

3.3.5 Noise Composition of TIA Amplified PIN-PD and APD

The results of the simulations as described previously are shown in Figs. 3.30 and 3.31. These diagrams show the individual noise components as voltages for the case of a constant SNR of 15 dB with varied ambient light. The required signal irradiances can also be extracted. In case of the PIN-PD for low to medium light, the e_n-noise contribution is dominant and the thermal is predominant. The shot noise of the ambient light starts dominating late at high ambient light levels, and the other noise contributions are less important. In the case of the APD, the situation is clearly different. As expected, all shot noise contributions are much higher, due to the gain. The e_n-noise contribution is relevant at very low ambient light levels, beyond which the ambient light shot noise contribution clearly dominates. The progression of the E_sig as function of E_amb for a constant SNR confirms the frequently encountered statement that APDs, in comparison to PIN-PDs, offer a higher sensitivity that degrades early in the presence of interfering light.

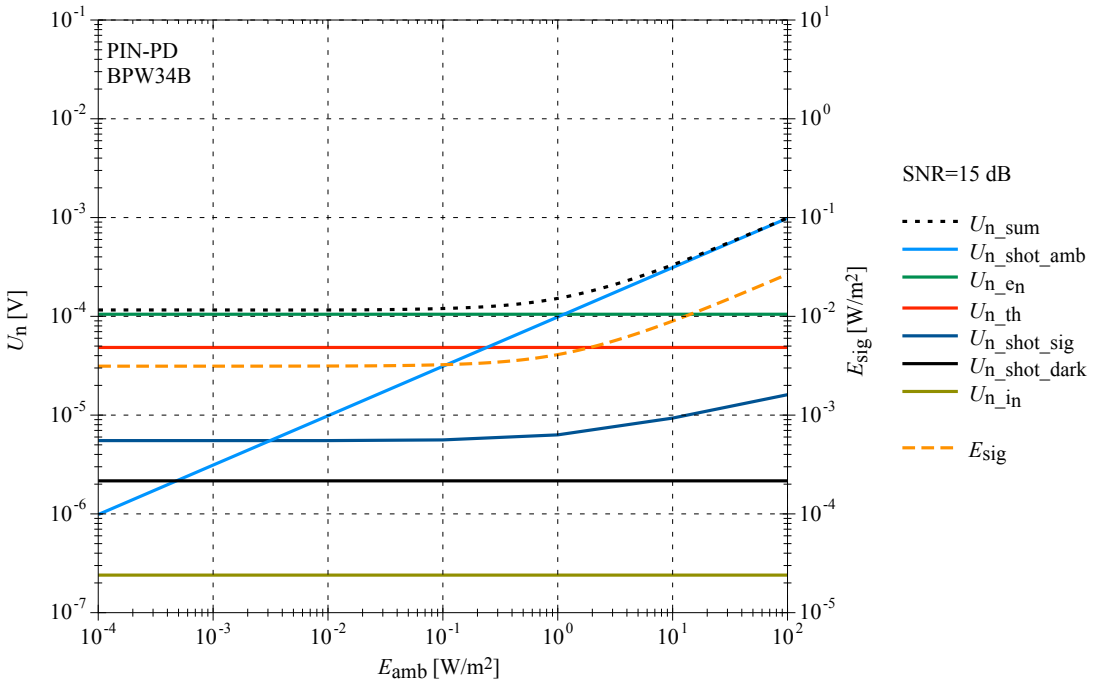

Figure 3.30: General noise composition of TIA combined with PIN-PD.

The reference operational amplifier selected for comparative TIA simulations is a low noise CMOS-type featuring decent noise parameters. A question of practical interest is the influence on the SNR by replacing the OpAmp with a type of different technology and other parameters. This can be answered by means of simulation. Real characteristic values from other OpAmps, within the same 20 MHz GBW-class, are used for this purpose, see Table 3.9. Of course, changes in noise components of the OpAmp can only influence the total noise where they are dominant

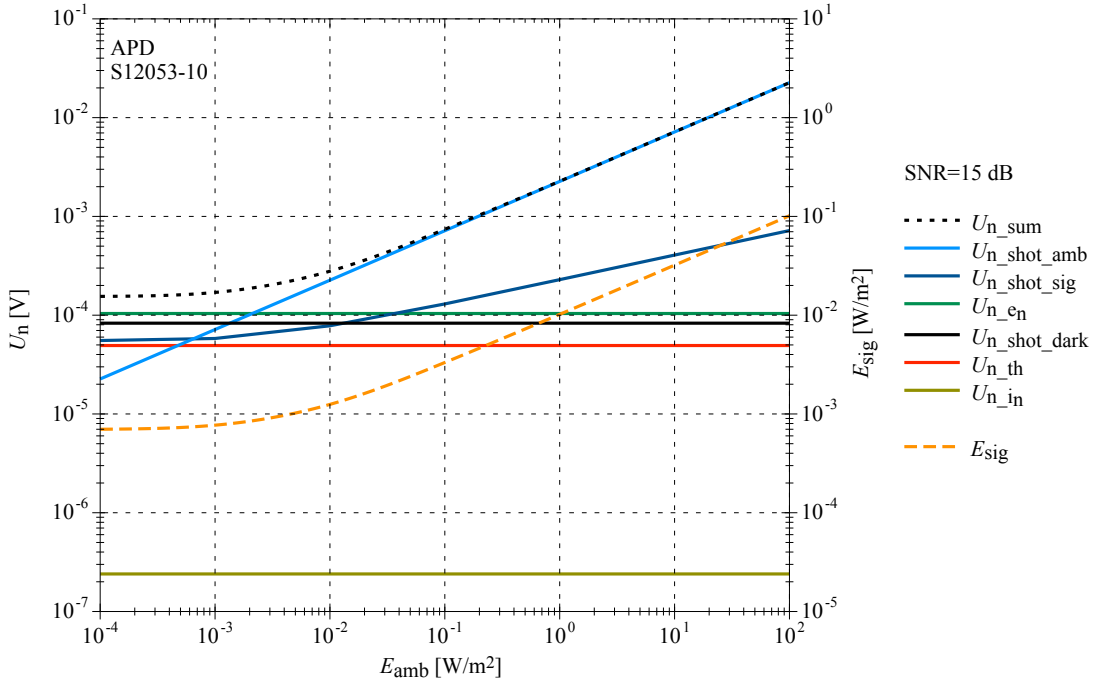

Figure 3.31: General noise composition of TIA combined with APD.

or playing a significant role. In areas where other noises like the shot noise from ambient light are dominant, no large effect may be expected. The outcome of the simulations for PIN-PD and APD, including the different amplifier types, is given in Fig. 3.32. As it turns out, for these configurations, an ultra-low-noise j-FET OpAmp can offer an advantage of several decibel in SNR, at least in the range where shot noise due to ambient light is less significant. This improvement is more pronounced in the PIN-PD case, where the e_n noise contribution is more dominant over the other noise sources.

Table 3.9: OpAmp noise parameters of different technologies.

Partnumber		LTC6240	AD4625	LT1128	
Type		CMOS	J-FET	Bipolar	
Voltage noise density	e_n	6	3.3	0.9	nV/$\sqrt{\text{Hz}}$
Current noise density	i_n	0.0005	0.0045	1.0	pA/$\sqrt{\text{Hz}}$

Further room for SNR improvement is theoretically offered by lowering the temperature, which effects the thermal noise contribution. A reduction from 313 K to 283 K results only in 0.4 dB less thermal noise voltage, and this would only transfer to the total noise if the thermal contribution is dominant. All in all not very effective, especially since active cooling by Peltier elements, for example, would significantly burden the energy budget of mobile systems.

A variation of the GBW can also affect the noise. Deploying substantially more GBW as required, see (3.24), can result in two scenarios. The first is without a change of R_f, the f_{-3dB} and NBW grow, the SNR and the value of C_f decrease. In the second scenario R_f is raised to keep f_{-3dB} and NBW at the former values, which would lead into a decrease of C_f and a larger e_n noise contribution and only result in a minor improvement of the SNR, accompanied by earlier saturation. Both scenarios result in an reduction of C_f, whereby this can be practically limited due to stray capacitances and stability against the swing of the circuit. The best practice remains to run a simulation and observe the circumstances.

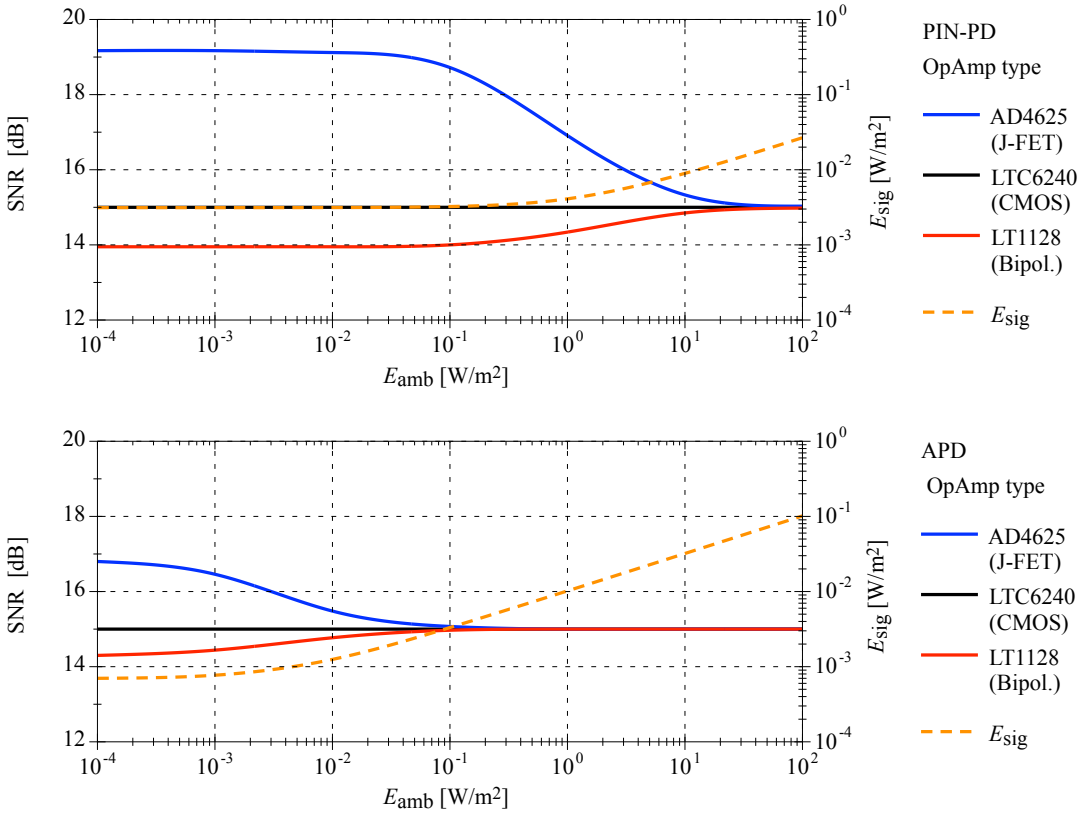

Figure 3.32: Effect of varying the amplifier type, and thereby the corresponding noise density parameters e_n and i_n, on the SNR of PIN-PD and APD driven TIA, under the same light conditions as the CMOS-based reference with a constant SNR of 15 dB.

3.4 The Applicability of PIN-PDs and APDs in Comparison

3.4.1 General Ambient Light Performance of PIN-PD and APD

One of the key questions of system designers, whether to use an APD or PIN-PD, calls for closer examination. In order to set up an as fair as possible comparison of the two types, the detector area as a main parameter should also be taken into account. To achieve this, the selection of detectors from Table 3.8 needs to be extended by large-area types, as presented in Table 3.10. The larger surface area A_{det} causes an increasing capacity C_D. The capacitance of a capacitor increases proportionally with the area, which means that the specific capacitance related to the area is constant. This is also confirmed within a series of PDs of different sizes. However, the values can differ by a factor of 10 between individual product lines.

The APD is assumed to operate at a nominal gain and respective reverse voltage, resulting in a certain capacitance. The PIN-PDs reverse voltage is adjusted to obtain the same value of the APDs C_D, which nearly equals the minimum achievable value of this type. The larger capacitances of both types compared to their smaller derivatives demands a decreasing value of R_f, in order to keep the same cut-off frequency and NBW as before. In terms of the TIA, parameterized as shown in Table 3.8, the size of R_f at 100 kΩ is reduced to 30 kΩ for the large area detectors. Of course this reduction leads into a decrease of the feedback resistors thermal noise contribution, which is not dominant.

Simulations for TIA amplified PIN-PDs and APDs, each in 2 sizes, are executed in order to achieve the SNR progression under different signal and ambient light conditions. The irradiances

Table 3.10: Parameters of additional large-area photodetectors used in the simulation.

Type		PIN-PD	APD	
Manufacturer		Hamamatsu	Hamamatsu	
Partnumber		S3590-08	8664-50k	
Area	A_{det}	100	19.6	mm^2
Responsivity	$\mathcal{R}$	0.28	16	A/W
Capacitance	C_{D}	55	55	pF
Reverse Voltage	U_{R}	25	350	V
Gain	G	1	50	
Excess noise factor	F	-	1.7	

Values valid at a wavelength λ of 450 nm.

provided by the optical signal and ambient light are assumed to be perpendicular to the detector's surface and showing a narrowband characteristic at a wavelength of 450 nm. The results are presented in Figs. 3.33 and 3.34. To help the clarity and to avoid the overlap of the curve families, each is presented in a separate diagram. In each diagram, the necessary signal irradiances for a SNR of 15 dB are marked. Both cases for the extreme ambient light situations are indicated, i.e. without and with very strong ambient irradiance.

A comparison of the results clealy shows differences in the distribution of the curve families. In case of the PIN-PD, they basically run parallel and close to each other and even overlap at low E_{amb} values. In case of the APD, the lines have significantly larger distances between each other and show a bent trajectory for small E_{amb} values. The reason for this bending is the shot noise of the signal component becoming dominant, and this less pronounced effect can also be seen (since ungained) at the top end in the PIN-PDs curves. Essentially, more closely spaced curves mean larger immunity to ambient light. The largest possible variation of the E_{amb} in these examples leads to an E_{sig} value with one order of magnitude difference for the PIN-PDs, whereas it is significantly more than two orders for the APDs.

Looking at the absolute sensitivity values for the particular area class, the APDs perform only better in zero ambient light conditions, with a low E_{amb} value of 0.1 $\mathrm{W/mm}^2$ both detector types are more or less equally sensitive. A considerable increase in sensitivity can generally be achieved within one type by using large-area sensors, despite the reduction of the R_{f} necessary to maintain the bandwidth.

A cross-comparison between large-area PIN-PD and small-area APD shows comparable sensitivity without ambient light, but in terms of ambient light tolerance the PIN-PD is much more robust. Other advantages of PIN-PD are the significantly lower reverse voltage and temperature dependency. From an economic point of view, the large-area PIN-PD also has a slight advantage, since APDs are generally expensive components. At this point it should be mentioned that the costs of the products used in this comparison differ by a factor of one hundred.

A pre-selection of the PDs on the basis of the responsivity and area product in relation to the root of the capacitance is possible in principle, but due to the small number of products to be compared in most cases, the direct application of a simulation is more meaningful.

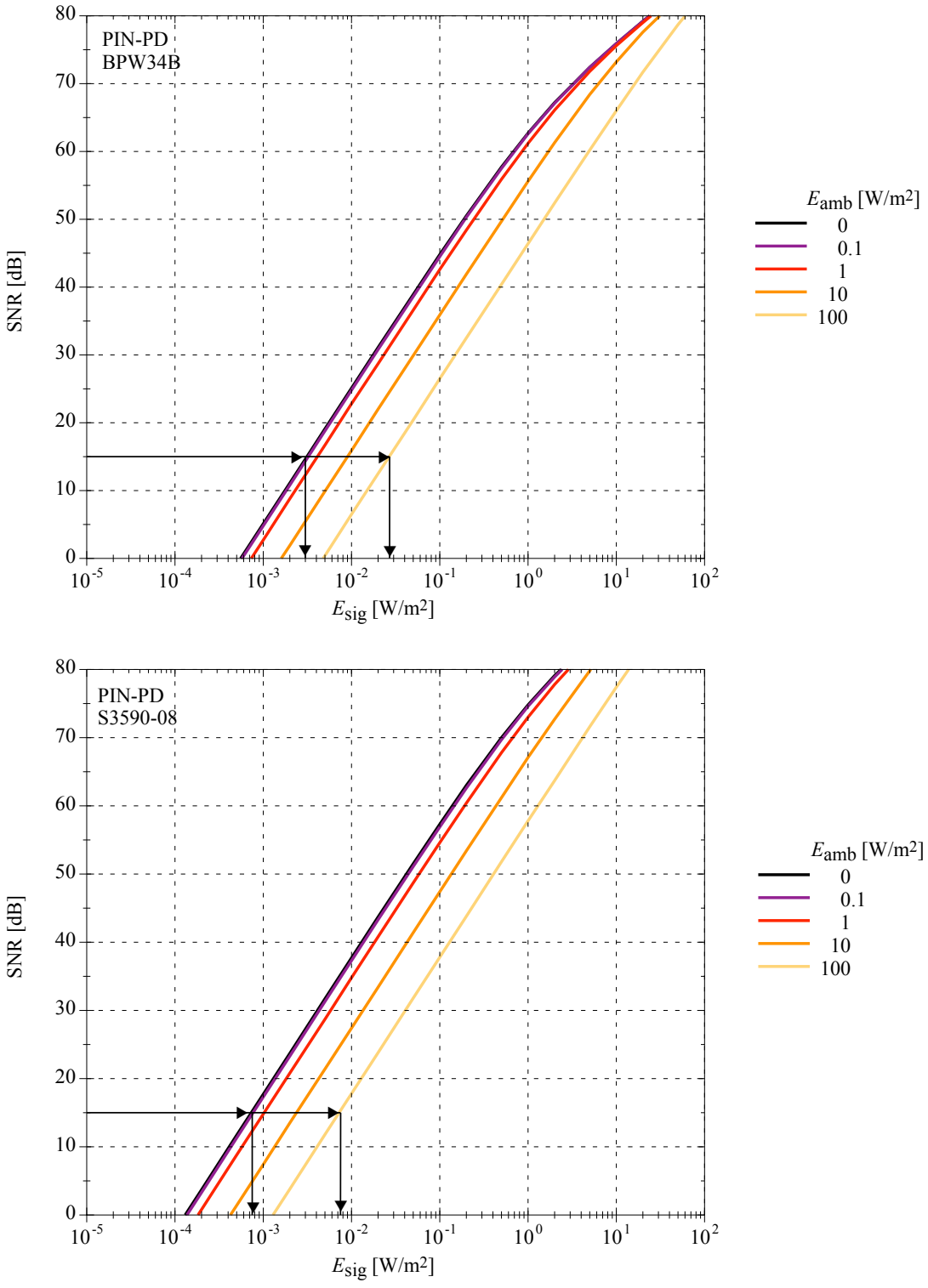

Figure 3.33: General signal-to-noise performance under varying signal and ambient light conditions for two TIA amplified detectors in PIN-technology. The upper diagram is valid for a medium-area (7.45 mm^2) PD, the lower for a large-area (100 mm^2) PD. The arrows indicate the required signal irradiance for 15 dB SNR at the two ambient light extremes.

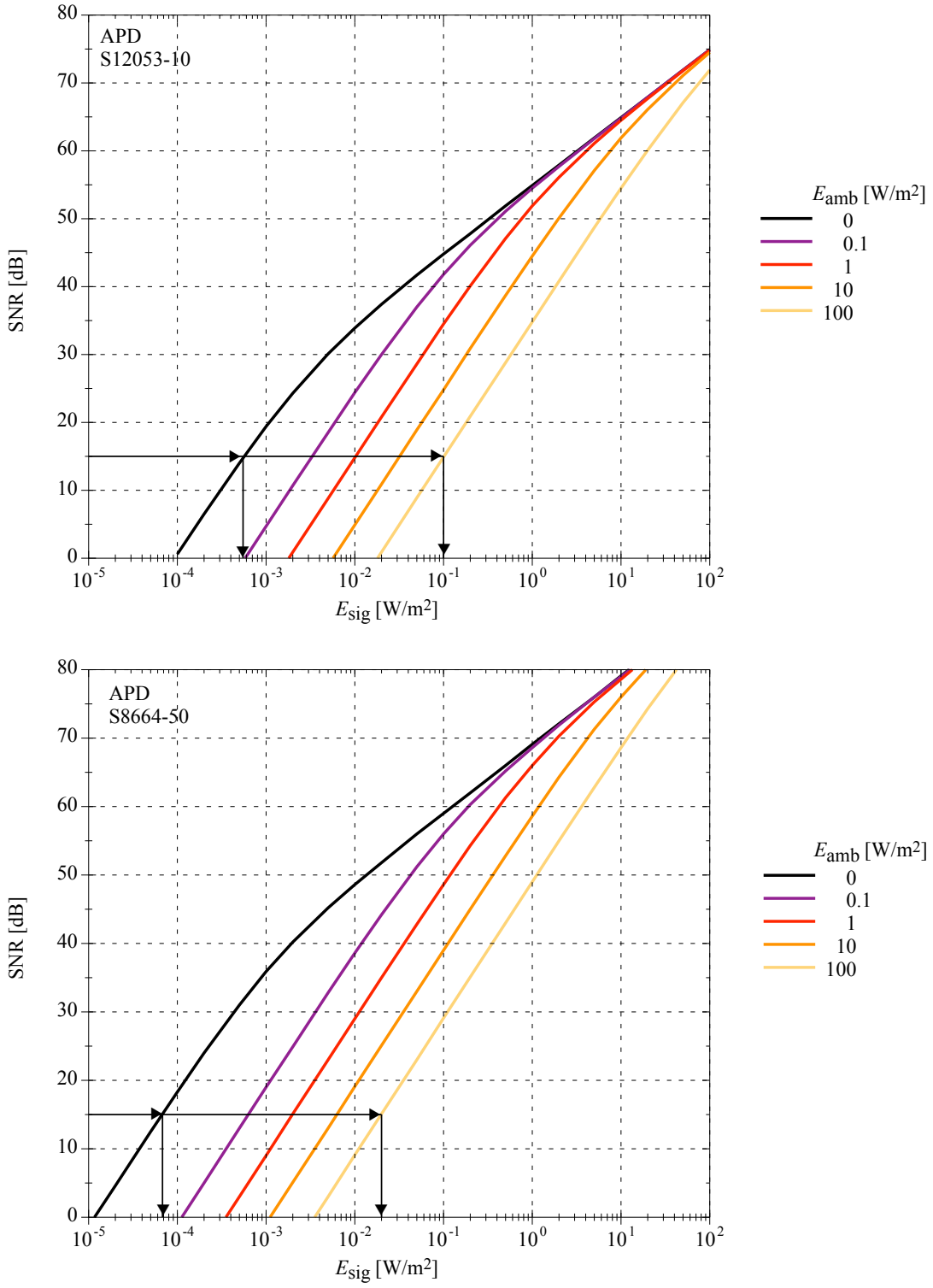

Figure 3.34: General signal-to-noise performance under varying signal and ambient light conditions for two TIA amplified detectors in APD-technology. The upper diagram is valid for a small-area (0.785 mm^2) APD, the lower for a large-area (19.6 mm^2) APD. The arrows indicate the required signal irradiance for 15 dB SNR at the two ambient light extremes.

3.4.2 SNR Performance at UOWC Light Conditions

Transition from in Air Conditions to Underwater Circumstances

A transfer of the TIA amplified PDs into an UOWC system in the underwater environment requires the expression of the abstract irradiance quantities by more descriptive and accessible parameters. In case of the E_{amb} this means a changeover to depth and type of the water, as well as the sensor orientation. For the E_{sig} this leads to the consideration of the LED source setup, the use of the distance to the receiver and also the water parameters. A corresponding scenario is given in Fig. 3.35, where the filter deployed will also be part of the following examinations. The goal is to generate signal-to-noise charts for different PDs, showing the achievable distance as a function of the water depth in a standard geometric configuration.

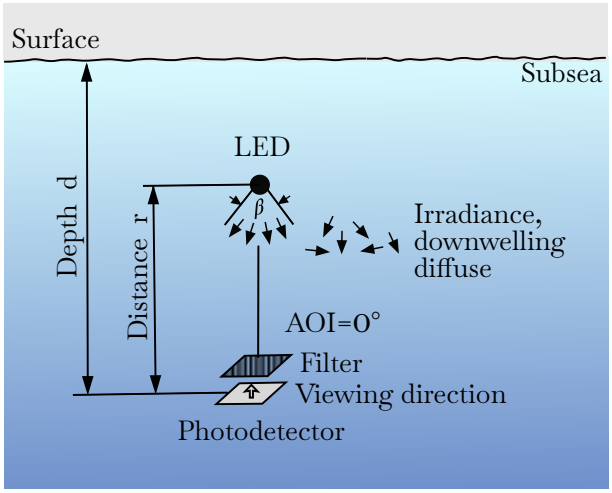

Figure 3.35: Scenario showing the setup and the environmental circumstances for simulation.

The parameters for the TIA and the PDs are given in the Tables 3.7, 3.8 and 3.10, and are reused in the calculations as well as the data of the underwater ambient light field for the intermediate Jerlov III water type given in Section 3.2.1. Further parameters need to be added, which specify the LED-source and the optical bandpass filter, see Tables 3.11 and 3.12, respectively. The ratio of the filters optical bandwidth to the LEDs FWHM is set to 1, relating to the determined OSNR gain maximum in Fig. 3.28. With the sensor looking upwards (generally the worst case) the distance to the source is limited by the depth, referred to as the physical limit in the following section.

Table 3.11: LED source parameters used in the simulation, selected on a realistic scale and corresponding to a cluster of Luxeon Lumileds LXZ1 royal blue.

Center wavelength	λ_{CWL}	448	nm
Spectral width	$FWHM$	18	nm
Optical power	P_{opt}	10	W
Beam angle	β	70°	

The following boundary conditions apply for the determination of E_{amb}: Jerlov III oceanic water type, diffuse ambient conditions, sensor facing upwards (generally the worst case), and a given spectral downwelling irradiance $E_{\mathrm{d}}(\lambda)$ generated by Hydrolight simulation software for different water depths z in certain environmental conditions, cf. Fig. 3.11. The calculation of E_{amb} is done

Table 3.12: Filter and geometrical parameters used in the simulation, modeled as given in (3.10) to (3.16) and Fig. 3.26.

Center wavelength	$\lambda_{\mathrm{PB}_{\mathrm{center}}}$	448	nm
Passband width	PB	18	nm
Angle of incidence	AOI	0°	
PD facing direction		up	

by multiplying $E_{\mathrm{d}}(\lambda)$ with the spectral transmission $T(\lambda)$ for the diffuse case:

$$E_{\mathrm{amb}} = \int_{\lambda_{\mathrm{diff}_{\mathrm{lower}}}}^{\lambda_{\mathrm{diff}_{\mathrm{upper}}}} E_{\mathrm{d}}(\lambda) \cdot T_{\mathrm{diff}}(\lambda)\ \mathrm{d}\lambda. \tag{3.40}$$

The following boundary conditions apply for the determination of E_{sig}: water attenuation parameter K_{d}, no inclination between LED and PD, equal distribution within beam angle, and distance r. The calculation of E_{sig} is given by the product of (2.17) and the multiplication of the normalized spectral intensity of the LED $I_{\mathrm{d}}(\lambda)$, with the spectral transmission $T(\lambda)$ for the directed case:

$$E_{\mathrm{sig}} = \frac{P_{\mathrm{opt}} \cdot e^{-K_{\mathrm{d}} r}}{2\pi r^2 (1 - \cos(\beta/2))} \cdot \int_{\lambda_{\mathrm{PB}_{\mathrm{lower}}}}^{\lambda_{\mathrm{PB}_{\mathrm{upper}}}} I_{\mathrm{LED}_{\mathrm{norm}}}(\lambda) \cdot T_{\mathrm{dir}}(\lambda)\ \mathrm{d}\lambda. \tag{3.41}$$

The simulation is performed for a single wavelength, despite the fact that narrow wavelength bands are used, because only small inaccuracies are expected due to the piecewise linearity. This is particularly true for the LED signal component, whereas for the ambient component an overestimation is likely to occur due to the small center shift of the filter.

The calculations for each data point of the aspired diagrams are carried out in the following order, taking into account the boundary conditions: calculate the E_{amb} for the selected water type and depth by (3.40), then determine the required E_{sig} for the respective SNR by the equations of the TIA, finally perform an iterative calculation of the necessary distance r for the determined E_{sig} by (3.41).

Performance Dependence of Detector Type and Area

The results of the previous calculations are presented in the Figs. 3.36 and 3.37, which provide SNR charts for both detector technologies in different sizes. High SNR requirements significantly reduce the achievable ranges for all detectors. The reduced ambient light in deeper water generally leads to an increase in range for a certain SNR. This effect is particularly pronounced for APDs, but is less for PIN-PDs. The water type, of course, has an effect on the range. A clearer oceanic water Jerlov IB increases it, a murkier coastal one like Jerlov 3C leads to a reduction. The general effect of varying the water type is shown in Fig. 3.41.

A direct comparison of the four variants for a target SNR of 15 dB is given in Fig. 3.38. If one compares the small-area and the large-area detectors against each other, it becomes clear that the PIN-PD technology is significantly more performant in shallow and medium water depths and the corresponding ambient light conditions, and the APD technology only catches up in larger water depths to finally show its advantage in deep dark environments. The comparison of the small APD with the large PIN-PD is particularly interesting, since they are in the same price range. This PIN-PD shows a clear advantage over a wide range by about a factor of 2 with regards to the achievable distance, and even keeps up in quasi-darkness.

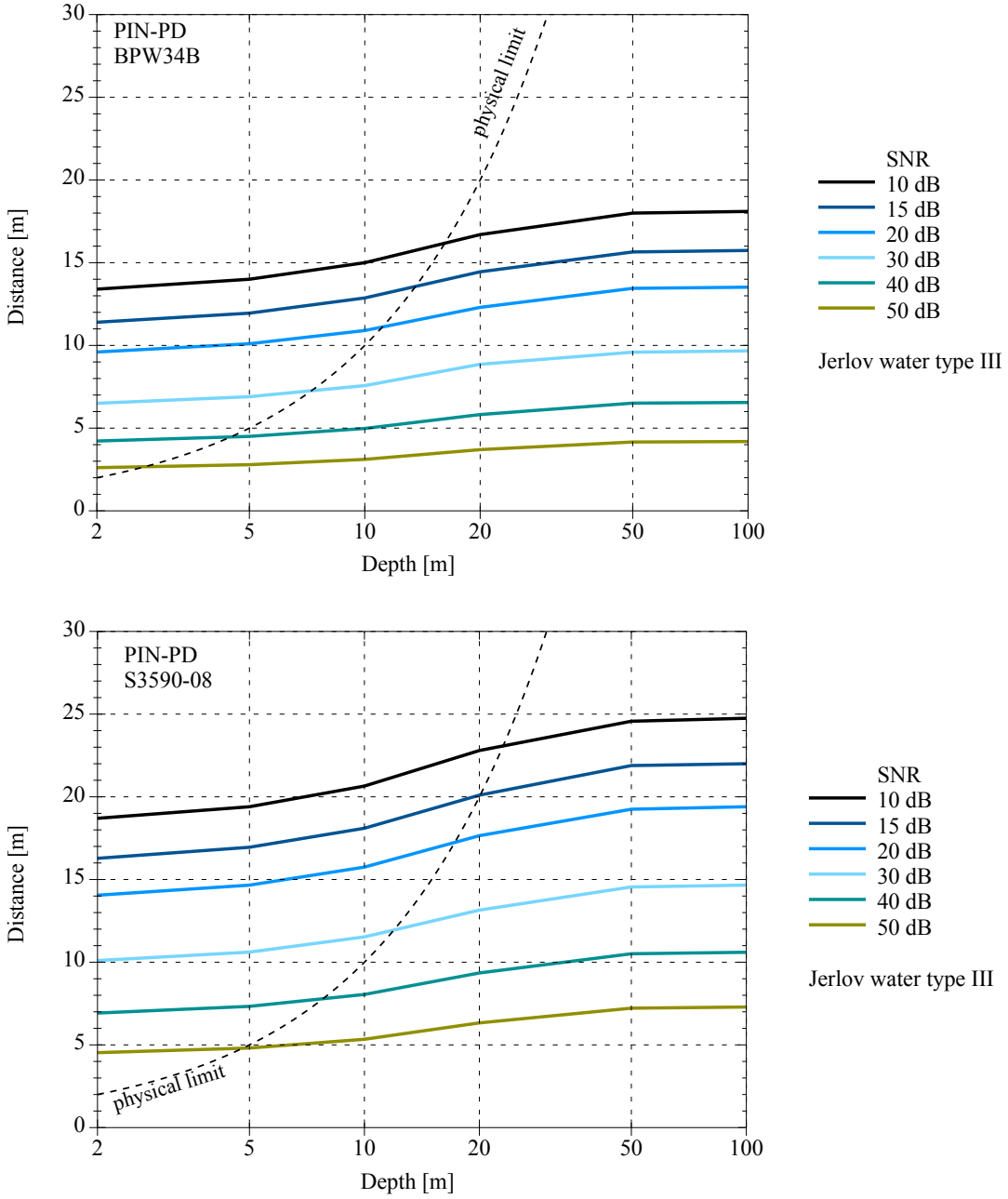

Figure 3.36: Signal-to-noise ratio performance of a small-area (7.45 mm^2) detector in PIN-PD technology in the upper diagram and of a large-area (100 mm^2) detector in the lower diagram. The charts display the achievable distance as a function of the operating depths,which is representative of the ambient light conditions.

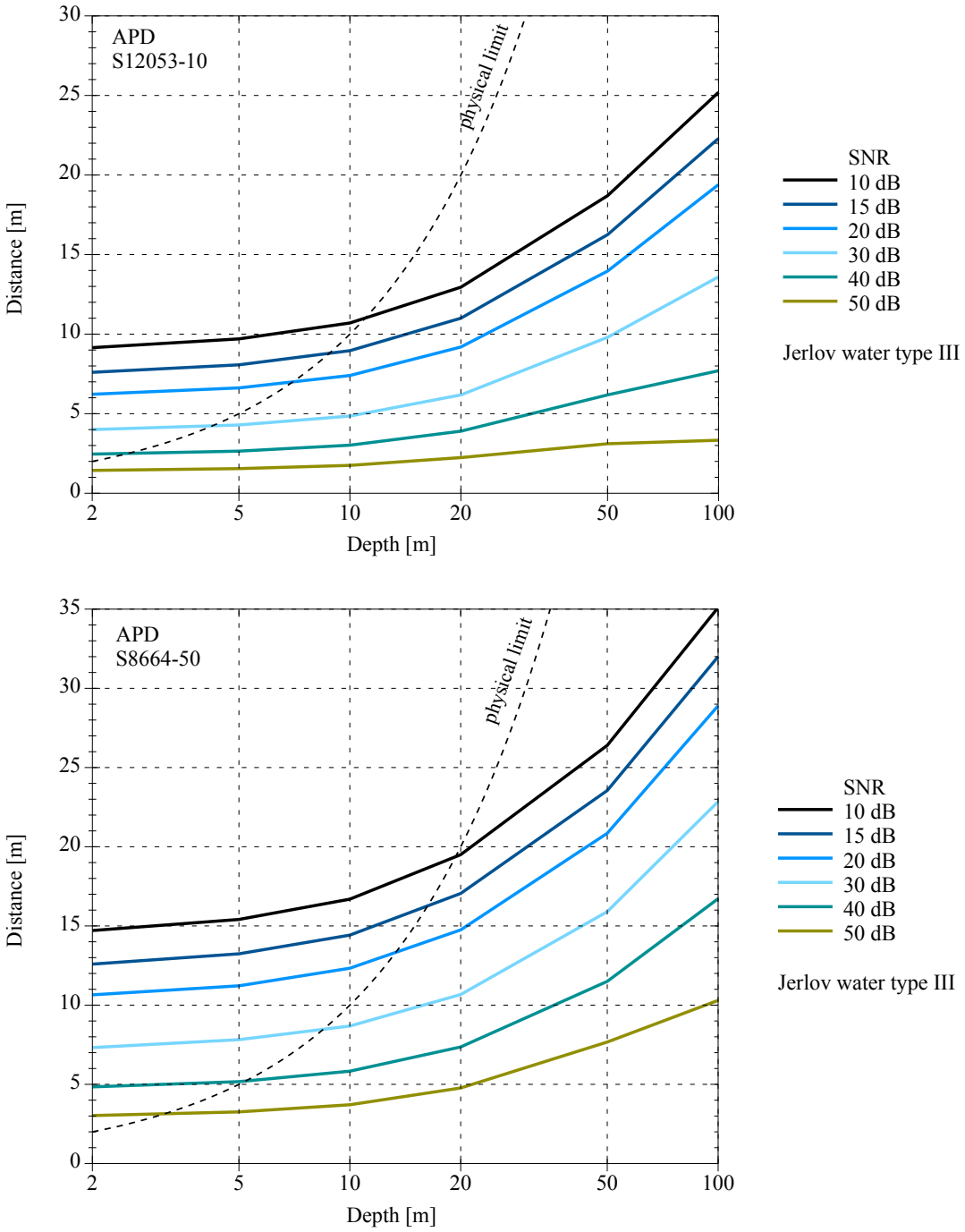

Figure 3.37: Signal-to-noise ratio performance of a small-area (0.785 mm^2) detector in APD technology in the upper diagram and of a large-area (19.6 mm^2) detector in the lower diagram. The charts display the achievable distance as a function of the operating depths, which are representative of the ambient light conditions.

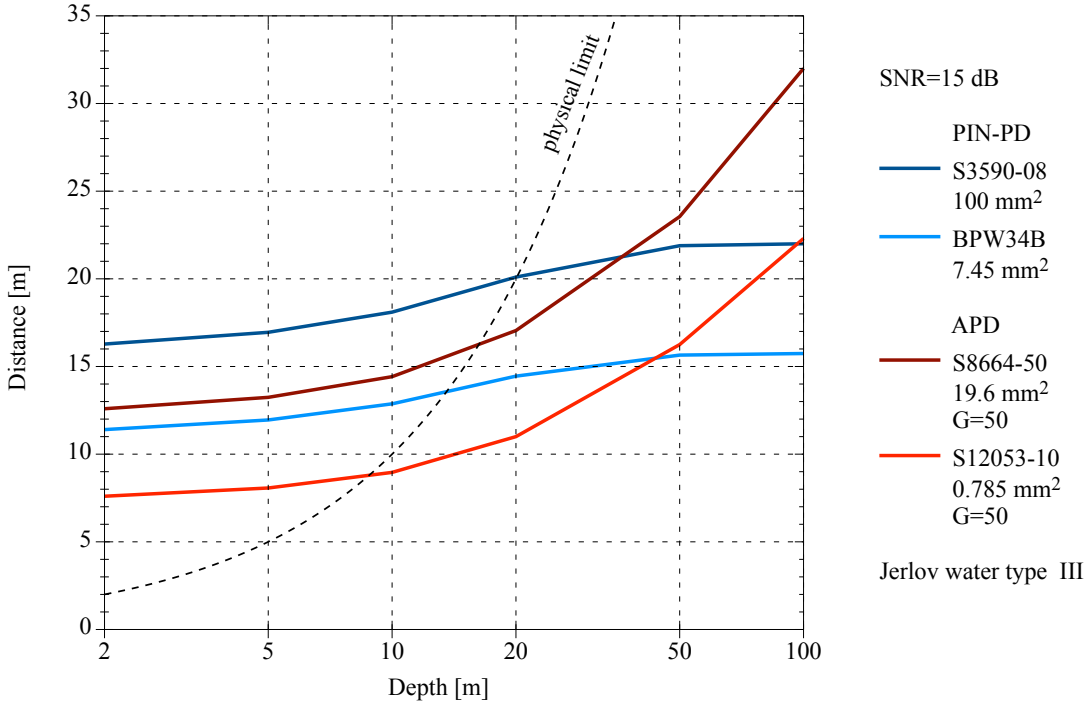

Figure 3.38: Comparative performance of a small-area and a large-area detector each using PIN-PD and APD technologies.

Influence of Detector Orientation

The amount of ambient light a detector collects underwater depends on the viewing direction and the field of view opening angle. The underwater light field is described by the downwelling and upwelling plane irradiances E_d and E_u, as for example, supplied by Hydrolight simulations, see also Table 3.4. They represent the two extreme directions, at least for the more common case of diffuse conditions. The exception would be in shallower depths and clear water where the direct character prevails, and a sensor pointed directly at the sun's incidence can give even higher values compared to facing straight up. The directional components of the underwater ambient light field can be depicted by radiances L, which gives the flux per unit solid angle and area. Hydrolight simulations resolve the light field in 10° vertical and 15° horizontal resolutions. The rotation of a detector in a light field is illustrated in Fig. 3.39. In deeper or stronger scattering water the horizontal direction loses importance, therefore the mean of all the horizontal values is used in further calculations to describe the vertical angular progression. For this purpose, the radiances that lie within the PDs field of view (given by the angle α) are cosine-weighed in respective to the perpendicular of the detector and are summed. The sums for different rotations or viewing angles are normalized to the maximum value, which yields in upwards-looking case. The relative progression of the irradiance on the detectors surface as function of the viewing angle is shown in Fig. 3.40 for different water types, depths and field of views.

Of course in shallower waters the horizontal orientation of the sensor area has an effect, since the radiances oriented to the sun become dominant, whereby the diffuse character remains in many cases. The direct character only prevails in clear water at small depth, see also Fig. 3.10. The horizontal turn of an upwards-looking uniform areal sensor would not change the irradiance exposure and result in a circle on a polar plot of the sensors output current. If the sensor is now tilted vertically and rotated horizontally, an off-centered ellipse or lobe with a more or less pronounced peak is created. To calculate this, the vertically tilted sensor needs to be turned horizontally in the full space light field, which is represented by the radiance distribution. The

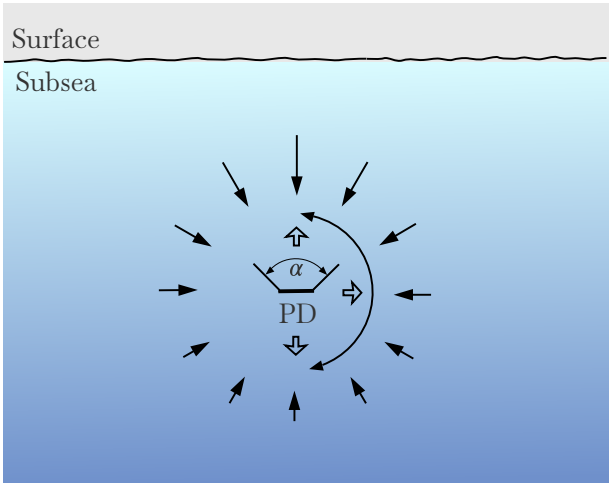

Figure 3.39: Rotation of a photodetector in the vertical ambient radiance light field. The three main facing directions up, horizontal and down are indicated.

respective incident radiances are added up in a cosine-weighted manner.

The influence of the detector's orientation for both technologies in different waters is depicted in Fig. 3.41. The orientation of the planar detector (straight up and down) represents the two extremes. The calculation and the presentation are done in the same way as for Fig. 3.38, and the achievable range at a certain depth is determined for a SNR value of 15 dB. For the APD as well as for the PIN-PD, larger distances result from the downward orientation. This effect is more pronounced with the APD and is also lasting longer at larger water depths. The larger insensitivity to ambient light of the PIN-PD is again evident.

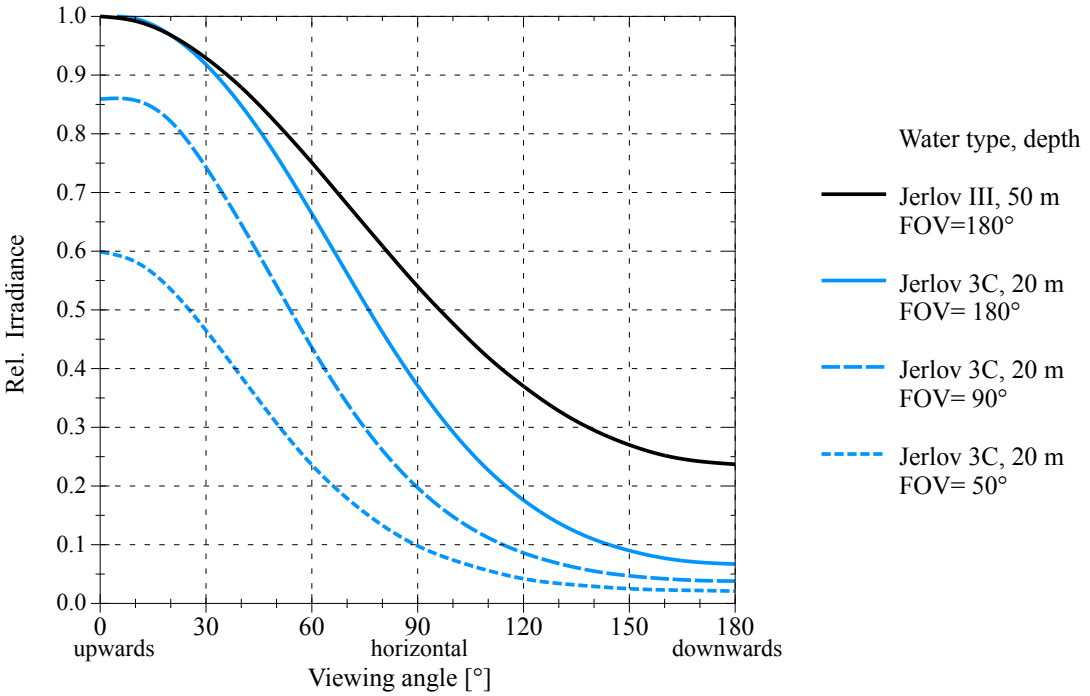

Figure 3.40: Relative irradiance impact on a photodetector as a function of the viewing angle, from upwards-rotated to downwards-looking.

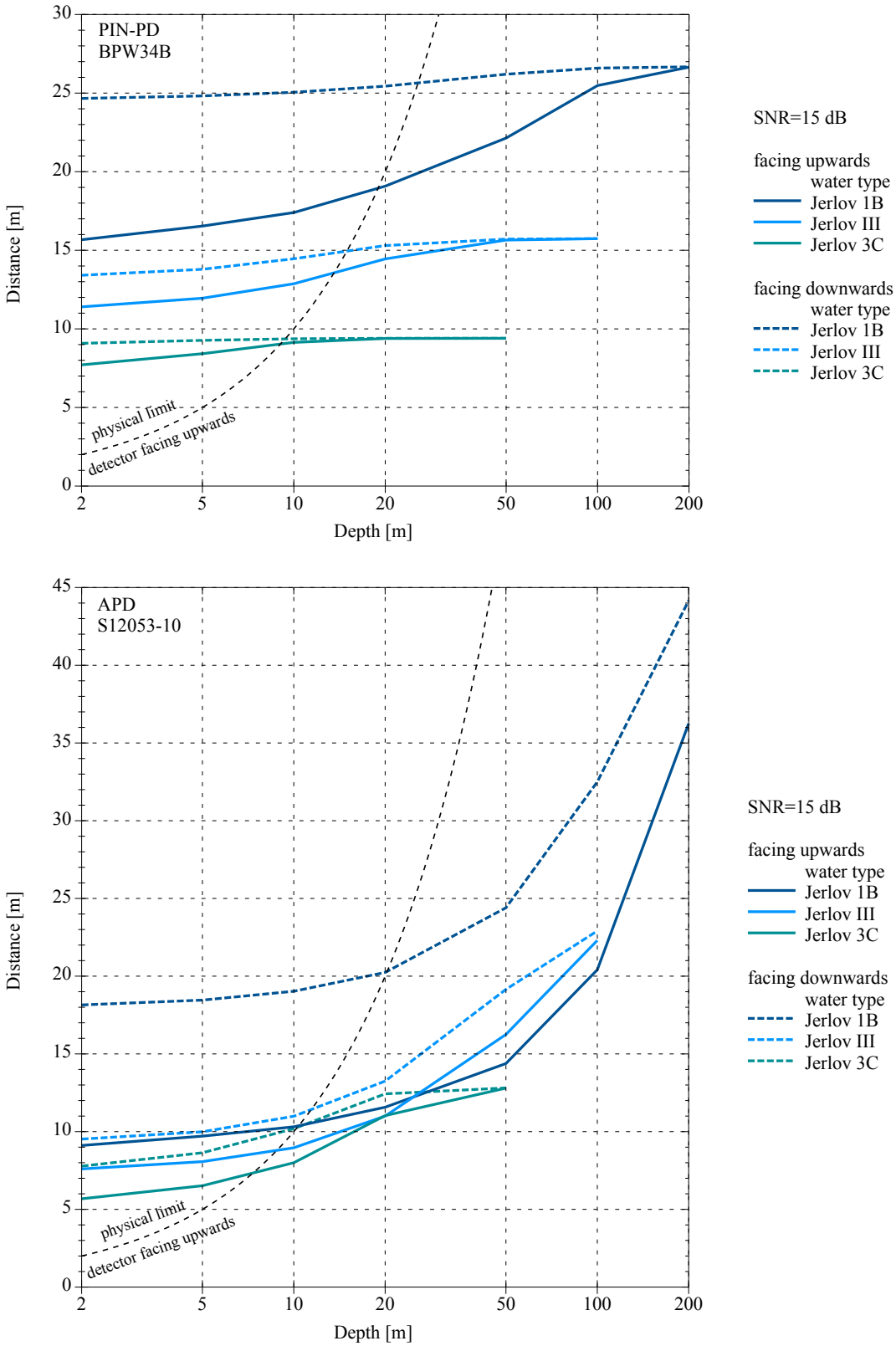

Figure 3.41: Influence of detector orientation on operating range performance, depicted for the extreme viewing directions (straight up and down). Calculated for a signal-to-noise ratio of 15 dB at various depths for Jerlov water types 1B, III and 3C. The upper diagram depicts an example in PIN-PD technology, the lower diagram for APD technology.

Impact of Source Power Variation

To extend the range of an UOWC system, increasing the transmitted optical power is the most obvious method. To illustrate the effects, simulations are carried out under reuse of the previous setups: TIA in Table 3.7, PIN-PD and APD detectors in Table 3.8, thin film optical filter in Table 3.12 and LED source in Table 3.11. The simulations are conducted with a variation of ± 6 dB of the optical source power while maintaining an SNR value of 15 dB to demonstrate the effects on the attainable range. The outcome for both detector types in various depths of oceanic and coastal waters is given in Fig. 3.42.

The curves show a kind of parallel shift for the respective detector and water type, where the distances within a related set of curves decrease both absolutely and relatively from clear to turbid water, corresponding from oceanic Jerlov 1B via III to coastal 3C water type. A look at the link budget, see (2.17), gives two terms that contain the distance r, the inverse square law and Beer's law, where the applied attenuation coefficient c or K_d co-determines the exponential attenuation. In the best possible theoretical case, in conditions without attenuation, quadrupling the power would double the distance. Higher attenuation values cause Beer's law to become dominant, and the yield through power increase drops, and this applies to values from approx. 0.4 1/m for longer distances.

However, there are other aspects to this increase of power. To stay with the example of 10 W optical power, which equals approximately 25 W of electrical power for blue LEDs, a theoretical jump of 6 dB would mean 100 W electrical power. This quickly shows the limits of practical feasibility. Battery-powered underwater vehicles and anchored sensors are generally very sensitive systems in terms of energy consumption, which is in the interest of long operating duration. An LED can be operated with higher power within limits, but this reduces the efficiency, i.e., the ratio of optical to electrical power. The installation of multiple LED elements, on the other hand, may cause space, heat and optical adaption problems.

A similar effect to an increase of the optical LED power can be achieved by variation of the beam angle, which also effects the irradiance. Fig. 3.43 depicts the relative irradiance as a function of the beam angle at conditions of a constant optical source power, and an equal beam distribution within the beam angle and a fixed receiver distance. Of course the reduction of the beam angle has a strong impact on directionality that can cause pointing and tracking issues. Also the number of necessary elements to create a hemispherical characteristic is growing.

Besides the question of distance progression, the issue of an SNR change while keeping the distance at power variations could arise. An increase of 6 dB in the optical source power results in a 12 dB SNR change for the PIN-PD. In case of APD it depends on the operating environmental conditions, at very low light level without shot noise a 6 dB power change also results in a 12 dB SNR change. In areas where shot noise becomes increasingly dominant, it reduces finally to a 6 dB SNR improvement.

The importance and impact of optical source power and energy efficiency suggest two points: the power efficiency could be increased by range- and SNR-adaptive steering of the LED output as well as the implementation of an energy efficient modulation scheme, which for example could include short and large pulses from a high-order PPM scheme.

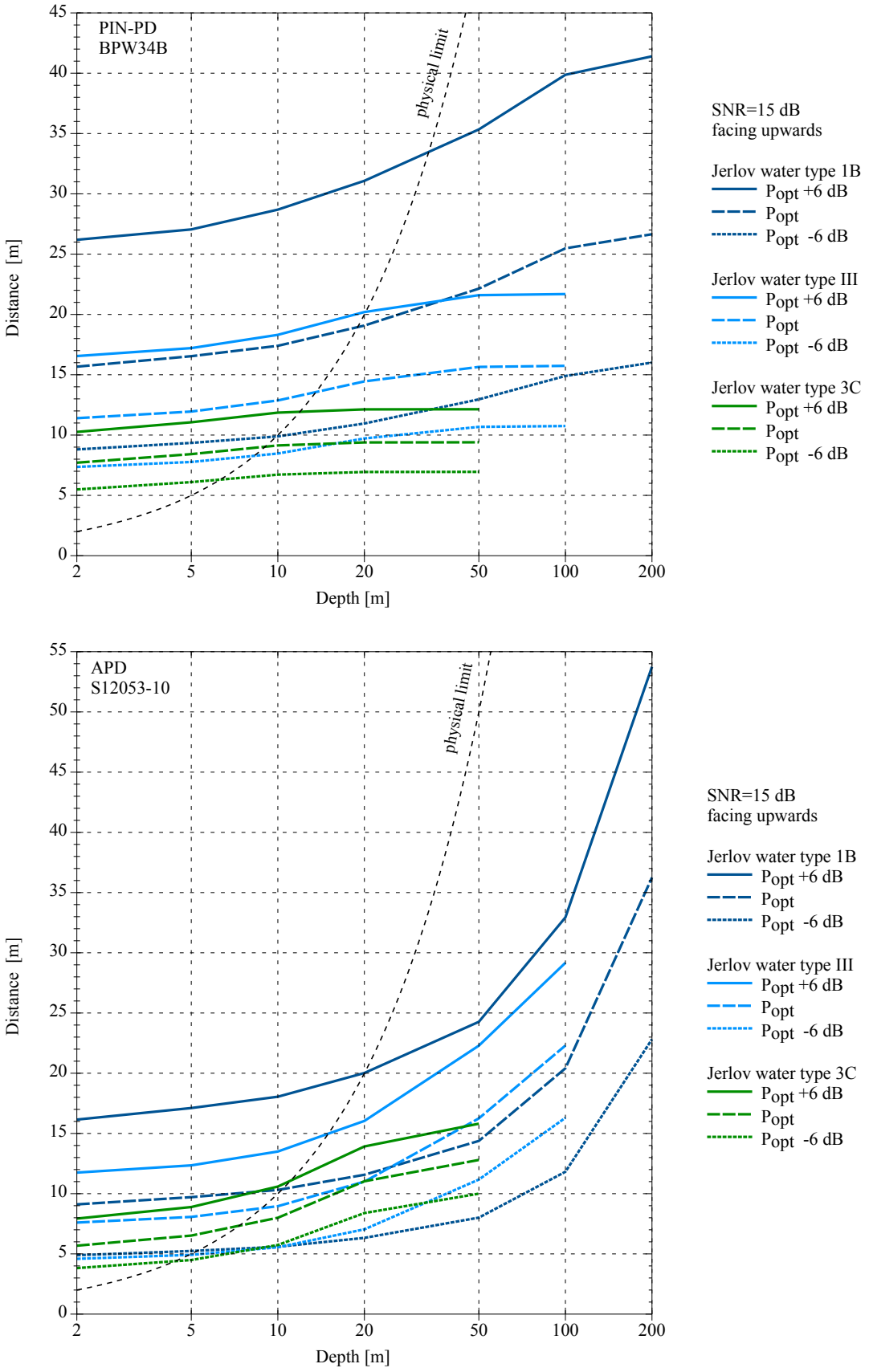

Figure 3.42: Impact of optical source power variation on the achievable range for different water types. Simulated for a constant SNR of 15 dB and an upward facing detector. The upper diagram shows an example for PIN-PD technology, the lower diagram for APD technology.

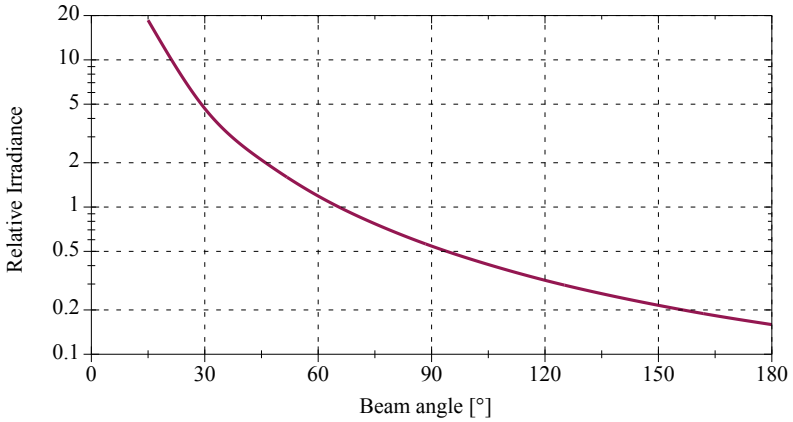

Figure 3.43: Effect of beam angle variation for constant power and equal beam distribution. Y-axis normalized to the value of the beam angle of 65.54° (equal a solid angle of 1 sr).

Filter Bandwidth Variation

The influence of the filter optical bandwidth on the optical signal-to-noise ratio (OSNR), which expresses the suppression of the LED and ambient light components, is depicted in Fig. 3.28. At a ratio of the filter passband to the LED FWHM of approximately 1, the OSNR is maximized. Since the OSNR cannot be transferred directly into the electrical SNR, cf. Section 3.3.1, further studies on the electrical SNR with variable filter bandwidths are necessary. In the following investigations, a ratio of 1 serves as reference. The related experiment can be described as follows: a detector-filter combination is located in a certain water depth in an upwards-looking direction, and an LED source is placed above in a distance that yields a SNR value of 15 dB. Now only the filter bandwidth is changed, like with a rotating filter wheel, and the corresponding SNR is recorded, and the same is determined for a special case without any filter. The variation of the filter bandwidth affects the signal and ambient light component hitting the detectors surface, which changes the SNR of the system. This results in a curve, as the SNR is a function of filter bandwidth, valid for a given water depth. The same principle is now used for different water depths and both detector types, PIN-PD and APD.

The setup and the conditions are the same as used before and are presented in detail at the beginning of this section: a water type of intermediate attenuation (Jerlov III) and thereby a depth-related ambient light spectrum including diffuse ambient light conditions, the sensor facing upwards for a worst case scenario, unchanged TIA and LED parameters, and the known representatives for PIN-PD and APD. The simulation of diffuse transmission is modeled for filter passband widths ranging from 0.2 to 4 times the FWHM of the LED, cf. Section 3.2.5. The detector responsivity at the LED center wavelength is applied to the entire filter bandwidth for a simplified simulation. For the calculation of the special case without any filter a correction factor is used to consider the full bandwidth of the ambient light irradiance.

Numerous calculations have to be carried out to depict the SNR progression for various filter bandwidths at different depths, and for both representative detector types. The outcome of the simulations is given in Fig. 3.44. Both for PIN-PD and APD, an SNR-maximum at a ratio of 1.5 occurs at small depths. With increasing depth and thus overall less ambient light, the optimum ratio changes to 2 and higher. For the PIN-PD, the difference between the SNR-maximum and the point without filter in the 50 m depth curve is small, whereas for the APD, the maximum is still pronounced even in the 100 m curve. This confirms the generally better immunity against ambient light of the PIN-PD application.

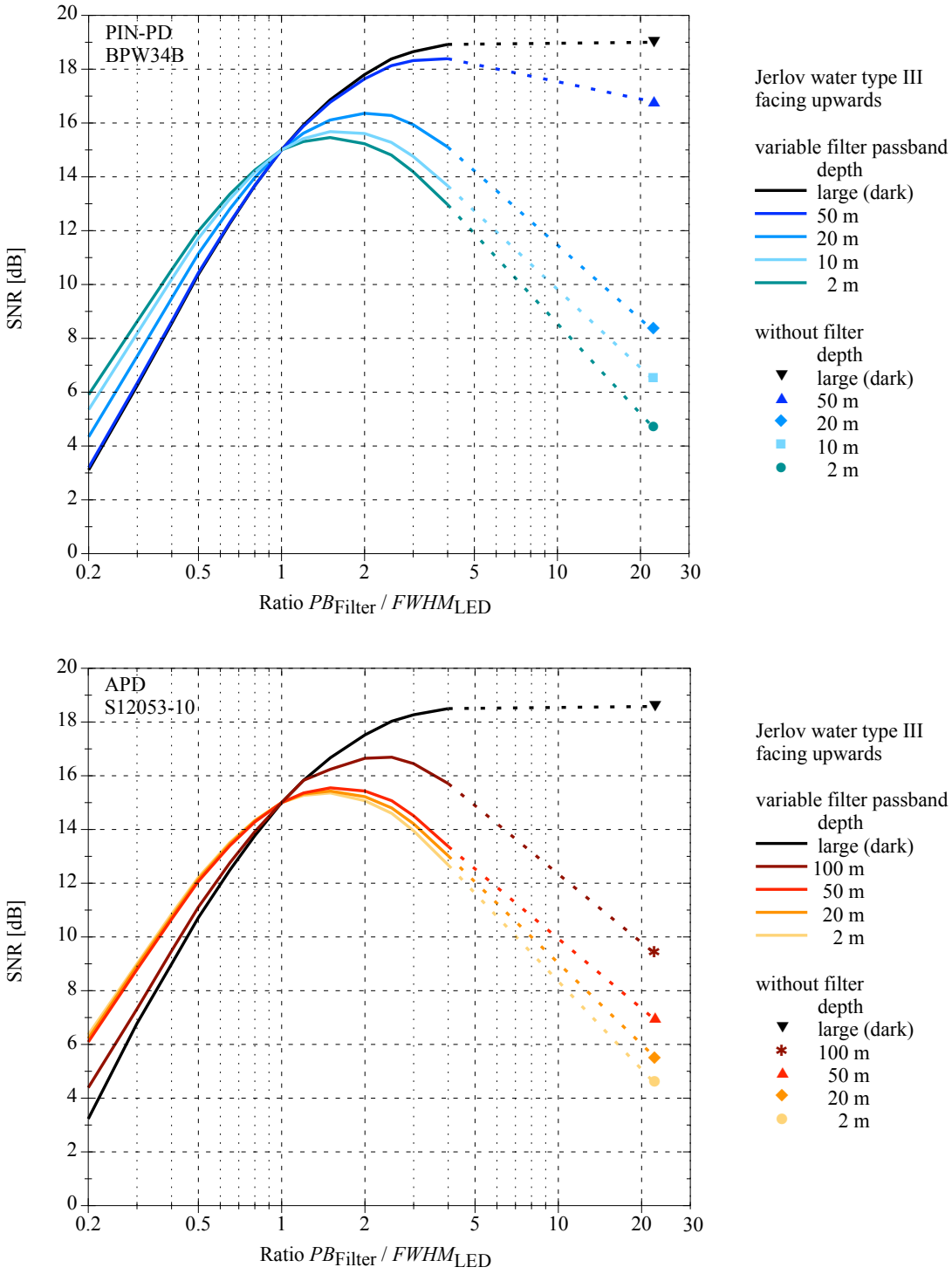

Figure 3.44: Impact of filter bandwidth variation on the achievable signal-to-noise ratio given for water type Jerlov III at different depths and for PIN-PD in the upper diagram, and for APD in the lower diagram. The x-axis represents the ratio of the optical filter passband to the FWHM of the blue LED, which is 18 nm in this simulation. The simulation covers filter passband values of 3.6 nm to 72 nm and the special case without a filter.

3.5 Single-Color Power LEDs used as Photodetectors

Light-emitting diodes are designed as light sources, for instance see [64]. Over the decades, they have evolved from pure indicator lamps to a wide variety of light sources. In recent years, conventional light sources have been increasingly replaced by LEDs. This is due to the following advantages of group III-V compound semiconductor LEDs: LEDs exhibit a high luminous efficacy (in lm/W), they provide long lifetimes, the switching speed is fast, the form-factor is design-friendly, LEDs are available in many different colors, and they operate at lower voltages. However, LEDs can not only be used as photon emitters, but also for photon detection as a photodetector. Of course, they are not optimized for this unintended application. The first publications of this dual-use of solid-state light emission and detection date back to the 1970's by Forrest W. Mims [181], but was rarely put into practice for the next three decades, with a few exceptions.

Employed as photodiodes, the responsivity of LEDs is wavelength-dependent, as they are sensitive to wavelengths equal to, or shorter than, the peak wavelength they emit [182]. For example, green LEDs are sensitive to blue and partially green light, but not to yellow and red light. Mims et al. used this characteristic to develop a sunlight photometer [183]. The breakthrough in terms of communications came in 2003, when Dietz et al. proposed to use LEDs as low-cost bidirectional transceivers [184], which nowadays is known as LED-to-LED communication. Subsequently, diverse sensor applications have been investigated, where LEDs are employed as photodetectors. For instance, LED arrays can be employed as touch-sensitive input and output devices that register reflected light from objects, as invented by Hudson [185]. LEDs were applied as low-cost surface-mount gas sensors by Shepherd et al. [186]. Ben-Ezra et al. used the spectral response to design an LED-based bidirectional reflectance distribution function measurement device [187]. Besides these diverse sensor applications, LED-to-LED communication is in an earlier stage and is still under investigation. The diversity of consumer electronic applications is huge and for the most part is in the low-cost segment. The range extends from toy-to-toy communication employing low data rates [188] to high-speed applications with data rates beyond 100 megabits per second (Mbps) [189, 190]. In order to overcome the limited bandwidth of LEDs, in [189] multicarrier modulation was applied and in [190] receiver-side digital equalization was utilized. In [191] a visible light communication (VLC) system, based on yellow LEDs as a receiver and providing gigabits per second (Gbps), is introduced. In [192] a communication system is presented, where two LED devices are used for bidirectional visible light communication and illumination simultaneously. Visible light communication and related tasks suchs as spectral-based intensity detection for the purpose of high-quality human central lighting is one of the driving forces in LED research [39].

Due to the fact that LEDs are originally not intended to be utilizied as photodetectors, manufacturers do not provide related specifications about their response function, spectral sensitivity, or dynamic range [187]. For this reason, an appropiate experimental characterization of LEDs is essential when utilized as photodetectors [193]. The main topics of the author's experiment series for single-color power LEDs when used as photodetectors [37] were:

- Determination of the wavelength-dependent responsivity (in A/W).
- Comparison of the spectral responsivity with a typical silicon PD and the theoretical bound.
- Investigation of the dynamic properties in terms of rise and fall times and junction capacitance.
- Comparision of the optical field of view (FOV) in emitter and detector mode.
- Examination of a potential impact of light polarization.

Experiments were conducted for two off-the-shelf color LED series with flat lens-free surfaces. Unlike low-power LEDs studied in previous publications [193], no plastic lenses needed to be

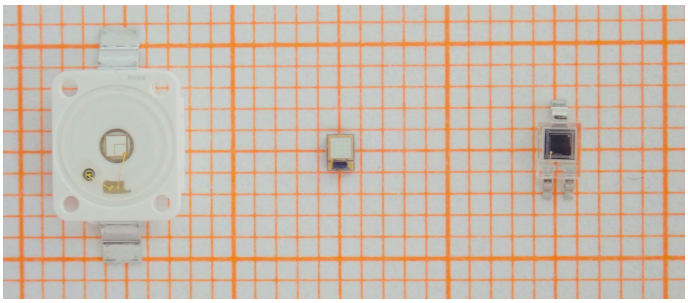

Figure 3.45: This picture shows an LED of the Osram Golden Dragon series on the left side, an LED of the Lumileds Z series in the middle, and the reference photodetector Osram SFH 2400 on the right side. The active area of the devices under test and the grid size is 1 by 1 mm.

removed and the photosensitive area could be precisely taken from the respective data sheet. In the area of optical underwater applications [35, 36], which represents the main interest of this work, single-color high power LEDs are utilized, as they are the first choice for low-cost and short range applications. Furthermore, optical filters are needed for ambient light suppression in this appication range. However, the results reported in the following section and in [37] are universally applicable, in particular for VLC.

Compared to white LEDs, the market only offers a limited selection of single-colored power and high-power LEDs. Regarding the suitability as a photodetector, converted and multiple-die types are beyond the scope of this contribution. The former is due to the conversion layer and generally deep blue excitation LED and the latter because of the in-series connected dies and the resulting problematic use as a current source. Popular low-cost single-die power LEDs in the 1 mm^2 chip size class include the Osram Golden Dragon series and the Lumileds Luxeon Z color series, see also Fig. 3.45. The latter is offered in a rarely found large variety of colors. The few high-power LEDs on the market with larger single dies, for example a 12 mm^2 series offered by Luminus, are mostly available only in the minimal color selections of red, green and blue. Furthermore, this generally high-priced segment is not necessarily interesting for the second application as a photodetector. The two series mentioned, Osram Golden Dragon [194] and Lumileds Luxeon Z [62], and the silicon positive intrinsic negative (Si-PIN) photodetector Osram SFH 2400 [195] were chosen for direct comparison, for specifications refer to Tables 3.13 and 3.14. They share the same active area and shape and are all planar types without primary optics, so they all offer a typical FOV of 120° full width half mean (FWHM). This selection therefore allowed fair comparative measurements to be carried out under repeatable conditions. Experiments were conducted without applying a reverse voltage to the device under test (DUT).

3.5.1 Analysis in the Spectral Domain

Experimental Setup for Spectral Measurements

In order to determine the spectral responsivity of a photodetector, ideally monochromatic light of adjustable wavelength is used. Alternatively, light with a very small optical bandwidth can also be used. To achieve this, a light source with a wide spectrum like a halogen bulb can be combined with a monochromator. These devices utilize the property of light dispersion in prisms or diffraction at gratings to spatially separate the wavelengths. For these experiments, a grating type monochromator Newport Oriel 77250 was used in combination with a halogen source Schott KL1500, see also Fig. 3.46. The externally stabilized light source was operated at 70 W, and a usable continuous spectrum from approximately 400 nm to 750 nm was generated. The light of the monochromator output hit the 1 by 1 mm active area of the DUT at a distance of 50 mm and exhibited an optical bandwidth of a few nanometers. A step size of 10 nm was used as a

Table 3.13: Key parameters of tested LEDs used as photodetector. Data extracted from [62, 194].

Manufacturer Type	Color	Wavelength dom., [nm] peak, [nm]*	Halfwidth spec. typ., [nm]	Lum. flux, typ. [lm, @500mA] Rad. power, typ.* [mW, @500mA]*
Osram LB W5SM	blue	467	25	31
Osram LT W5SM	green	528	33	98
Osram LY W5SM	yellow	590	18	82
Osram LR W5SM	red	628	18	66
Lumileds LXZ1 PB01	blue	470	20	38
Lumileds LXZ1 PE01	cyan	500	30	82
Lumileds LXZ1 PM01	green	530	30	118
Lumileds LXZ1 PL03	amber	588	20	56
Lumileds LXZ1 PH01	red orange	615	20	65
Lumileds LXZ1 PD01	red	633	20	52
Lumileds LXZ1 PA01	deep red	660*	20	350*

Table 3.14: Key parameters of Si-PIN photodetector used for comparison.

Manufacturer Type	Blue enhanced	Responsivity range, [nm]	Responsivity, max. [A/W, @850nm]
Osram SFH 2400	no	380...1100	0.65

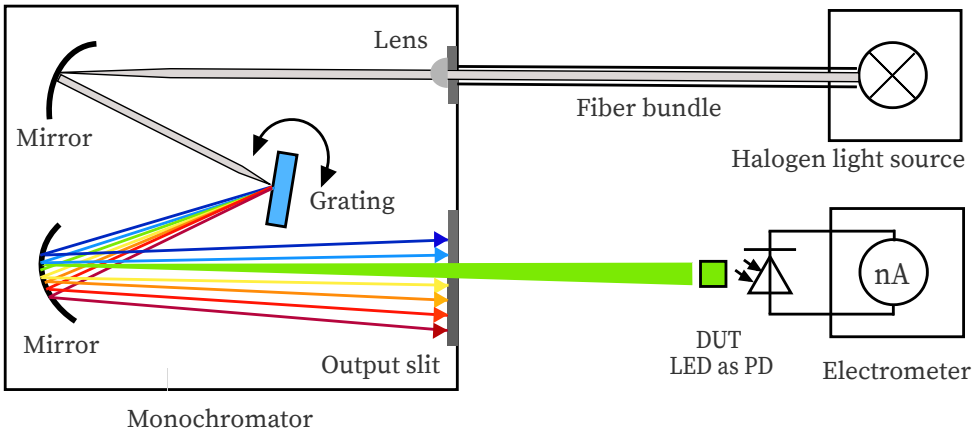

Figure 3.46: Schematic illustration of the measurement setup to determine the spectral sensitivity of a photodetector or LED used as a photodetector. The light source is connected via a fiber bundle to the monochromator. The light output of the monochromators adjustable spectrum hits the device under test, the generated photocurrent is quantified by a nanoampere meter.

reasonable value for processing the available spectrum. The generated photocurrent was measured directly by a Keithley 6517 electrometer in the nanoampere range.

As the main source of inaccuracies in the measurements carried out in the spectral domain, the widely specified responsivity values of the reference photodetector used for comparison can be named. These are a result of the general existing uncertainty of irradiation measurements and variations in the series. Three photodetectors were measured and their mean was used for a reference purpose. A further increase in the number was not undertaken due to the effort involved. The influence of the accuracy of the photocurrent measurement, light source stability, mechanical positioning as well as the wavelength uncertainty of the monochromator and spectrometer were significantly lower and and could be practically neglected in this case. Table C.6 gives an overview.

Examination and Experimental Results of the Spectral Domain

The wavelength-dependent absolute responsitivity of single-color power LEDs deployed as PDs is given in Figs. 3.47 and 3.49. The sensitivity maximum of the DUTs were approximately 50 % to 100 % of the reference Si-PIN-PD at the appropriate peak wavelength, thus representing comparatively high sensitivity values. The theoretical responsitivity bound of an ideal Si-PIN-PD with a quantum efficiency (QE) of 100 % is shown for reference purposes [68]. In Figs. 3.48 and 3.50 the spectral characteristics are normalized to compare the intensity as an LED and the sensitivity as a PD for two series of power LEDs in four and seven colors, respectively. The LED spectrum was measured at a 300 mA forward current and 25°C ambient temperature. Measurements were performed by a Gigahertz Optik BTS 256 Spectrometer. Unfortunately, the full spectral bandwidth of blue to green LEDs as PDs could not be achieved during the measurements, as there was a limitation to wavelengths above 400 nm, due to the confined spectral range of the light source. Nevertheless, the position, the width and the overlap of the spectral intensity and respective sensitivity can be identified. The spectral overlap of all DUTs was small to moderate, resulting in a reduced efficiency if the same LED type is used as a transmitter and receiver. Comparing the normalized progression of the same LEDs as emitter and detector, this effect appears to be more pronounced in the blue-green compared to the yellow-red color range. Examples are given in Fig. 3.51, whereby the extent is difficult to estimate visually. Values for a spectral efficiency J can be calculated using (3.42) with the normalized intensity $I_{\mathrm{e,n}}(\lambda)$ and the normalized responsivity $\mathcal{R}_{\mathrm{n}}(\lambda)$. For both series in the yellow-red regime spectral efficiencies of 54 % to 62 % could be as-

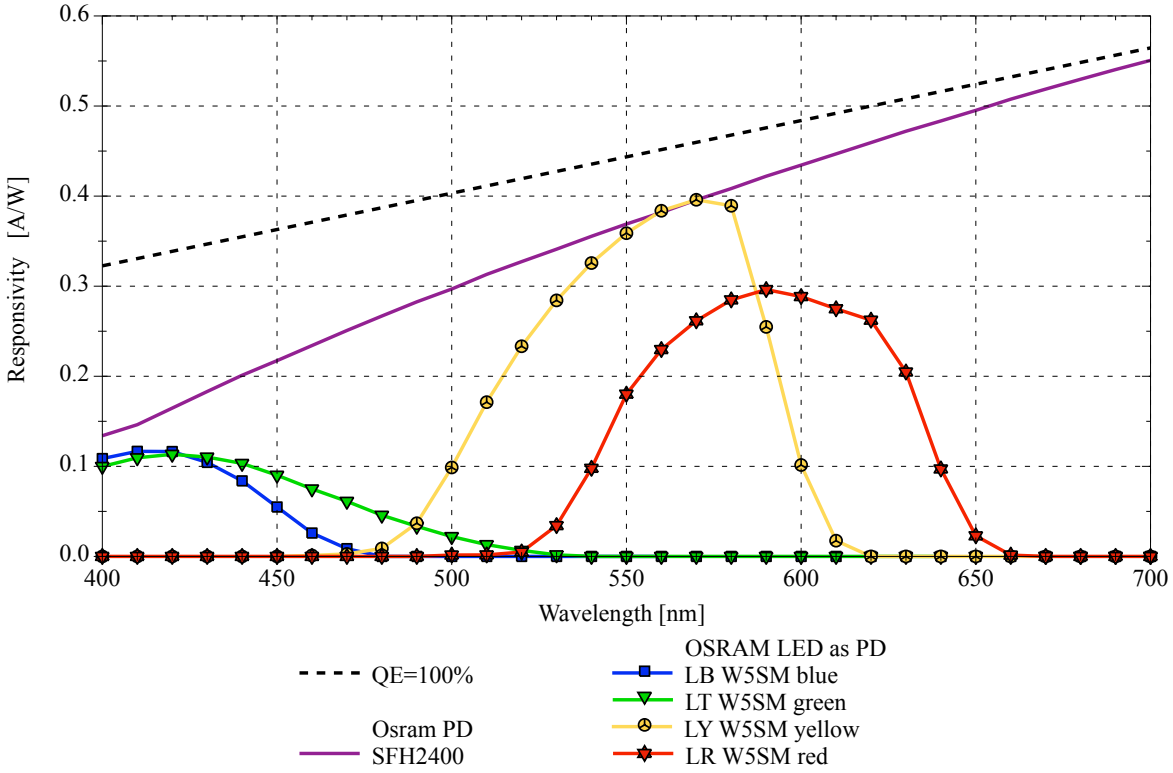

Figure 3.47: Spectral responsivity measurements of Osram Golden Dragon series LEDs in four colors utilized as photodetectors. The measurements are compared with a Si-PIN photodetector and its theoretical bound.

sessed, and values of 5 % to 16 % for the blue-green range. Integral calculations over a wavelength band were performed by summation of discrete elements of 1 nm width.

$$J = \frac{\int_{400\ \mathrm{nm}}^{700\ \mathrm{nm}} I_{\mathrm{e,n}}(\lambda) \cdot \mathcal{R}_{\mathrm{n}}(\lambda)\,\mathrm{d}\lambda}{\int_{400\ \mathrm{nm}}^{700\ \mathrm{nm}} I_{\mathrm{e,n}}(\lambda)\,\mathrm{d}\lambda} \tag{3.42}$$

Viewing the pure bandpass filter features such as width of the passing band and slope, LEDs deployed as a PD can be an alternative to Si-PIN-PDs combined with a colored glass bandpass filter, see Fig. 3.52 and [36]. However, bonded variants are rarely found on the market. Furthermore, colored glass bandpass filters are only available in the blue-green band, and not in the yellow-red band. Fig. 3.52 compares the spectral sensitivity of an LED deployed as a PD with a Si-PIN photodetector combined with a colored glass bandpass filter Hebo G08. However, a thin film filter generally delivers steeper slopes and can be designed over wide ranges with respect to the center wavelength, and are much narrower in the passband, but has the disadvantage of a high price. Investigations of the influence of the temperature on the photodetectors responsivity were not carried out, since they are known to be small and would not justify a considerable effort for a supposedly insignificant result.

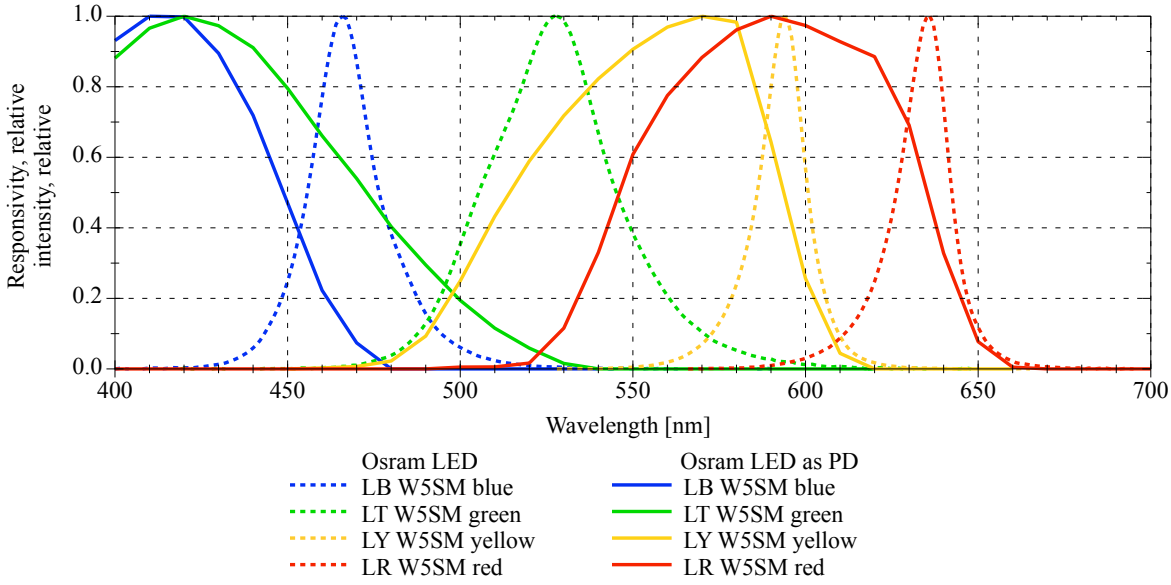

Figure 3.48: Normalized spectral measurements of Osram Golden Dragon series LEDs, deployed as emitters (dashed lines) and as a detectors (solid lines). Presented without measured data points for better clarity.

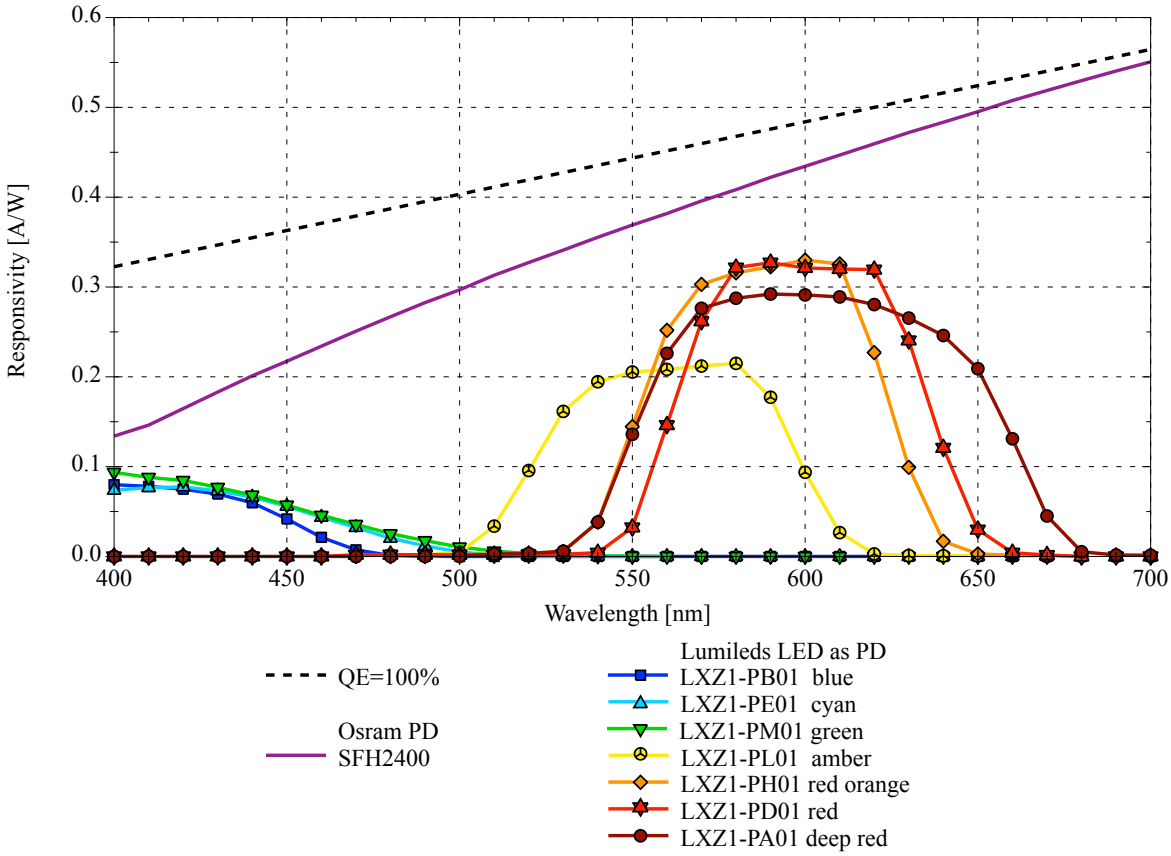

Figure 3.49: Spectral responsivity measurements of Lumileds Z series LEDs in seven colors utilized as photodetectors. The measurements are compared with an Si-PIN photodetector and its theoretical boundary.

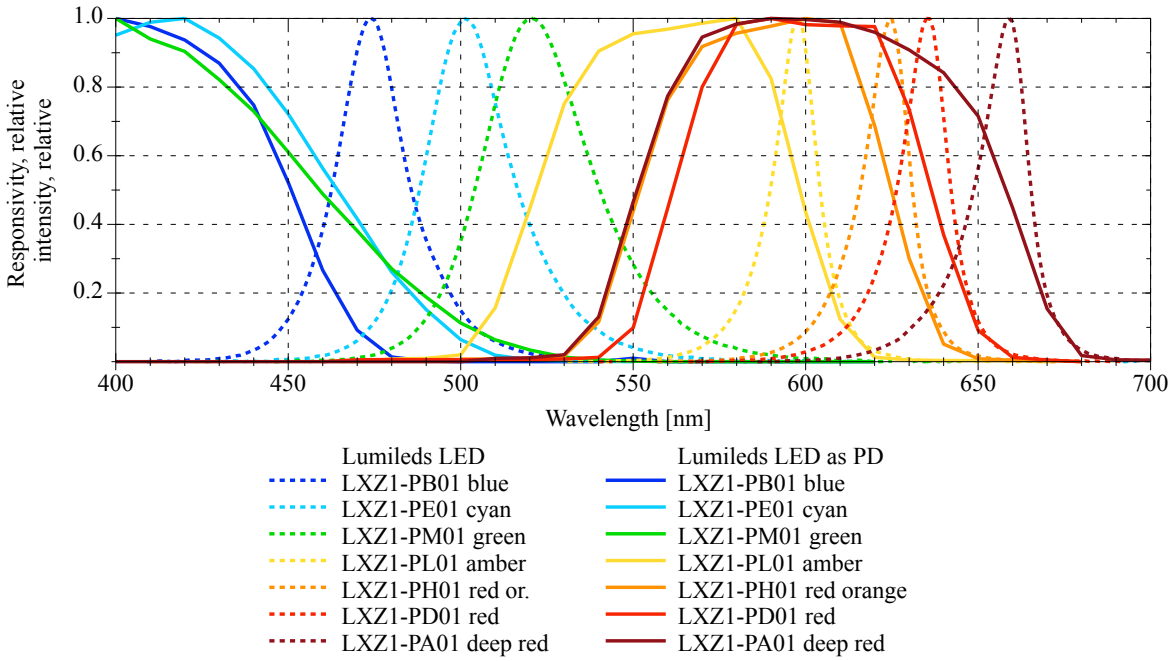

Figure 3.50: Normalized spectral measurements of Lumileds Z series LEDs, deployed as emitters (dashed lines) and as detectors (solid lines). Presentation without measured data points for better clarity.

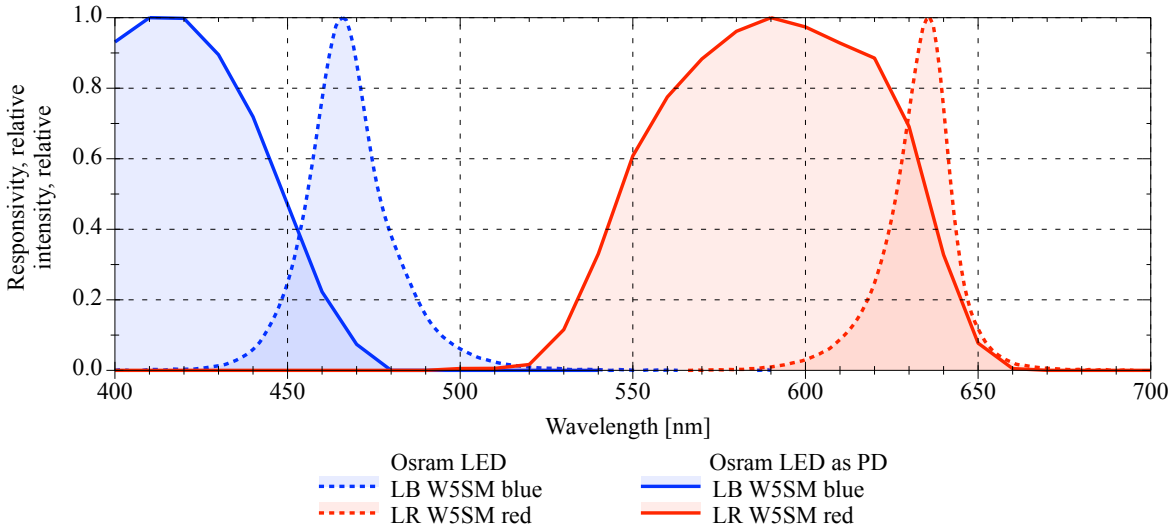

Figure 3.51: Normalized spectral measurements of Osram Golden Dragon series LEDs, deployed as emitters (dashed lines) and as detectors (solid lines). The overlap of the areas illustrates the difference in spectral efficiency of the blue and the red variants.

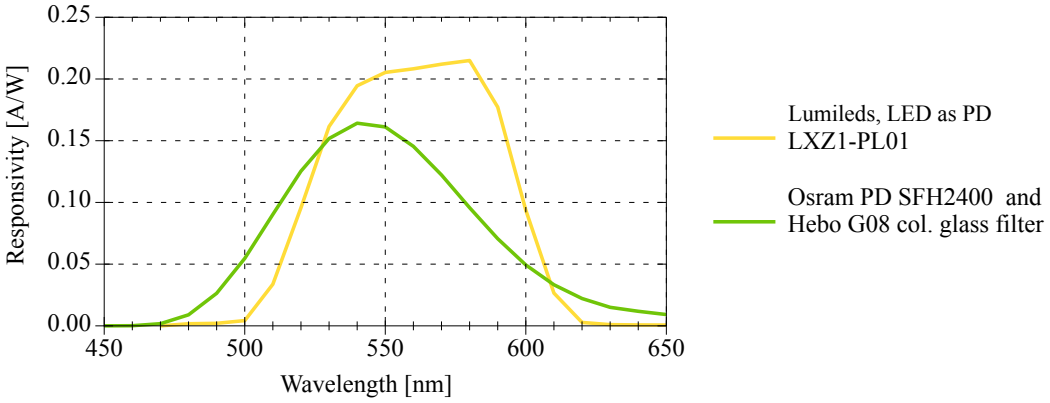

Figure 3.52: Comparison of the measured spectral responsivity of an LED deployed as a PD with an Si-PIN photodetector adapted with a colored glass bandpass filter.

3.5.2 Analysis in the Temporal Domain

Experimental Setup for Temporal Measurements

Measuring the rise time t_{rm} of an impulse response allows the determination of the bandwidth, used here for a photodetector. For this task, a fast light source is ideally used, which offers a short rise time $t_{\mathrm{rs}} \ll t_{\mathrm{rm}}$ and thus results in the neglect of t_{rs}. Typical bandwidths of power LEDs including the driver are known to be in the range of a few MHz to tens of MHz, which results in rise times in the range of tens of nanoseconds. However, since it was the intention to use a power LED as an emitter in this experiment, which represents a relative slow light source, the identification of t_{rs} was necessary. Figure 3.53 depicts the configuration used for these temporal measurements, comprising a signal generator Rigol DG5072, a high-speed MOSFET driver Microchip TC4452 including an LED of the Osram Golden Dragon series as a DUT, a Thorlabs PDA-10A 150 MHz transimpedance amplifier (TIA) PD-module, and a Rohde & Schwarz HMO3004 digital oscilloscope.The signal analysis of the oscilloscope directly provides the 10 % to 90 % rise time of the measured signal.

To measure the rise time of the LED as a PD, representing the DUT, the setup in Fig. 3.54 was used, including the source introduced in Fig. 3.53. The optical bandwidth of the sourcing LED should well overlap the sensitivity band of the DUT. The generated photocurrent was fed into a transimpedance amplifier Texas Instruments THS4631 evaluation board, which offered a gain bandwidth product (GBP) of 210 MHz, and it was configured with a feedback resistance R_{f}

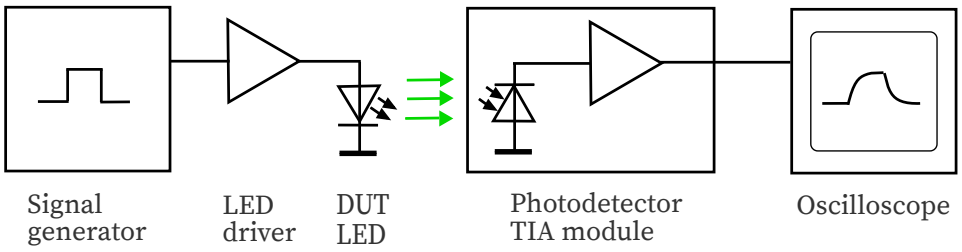

Figure 3.53: Setup for measuring the rise and fall time of LEDs used as light source. The source part of this setup has also been used for investigation of the temporal characteristics of the LEDs used as a PD.

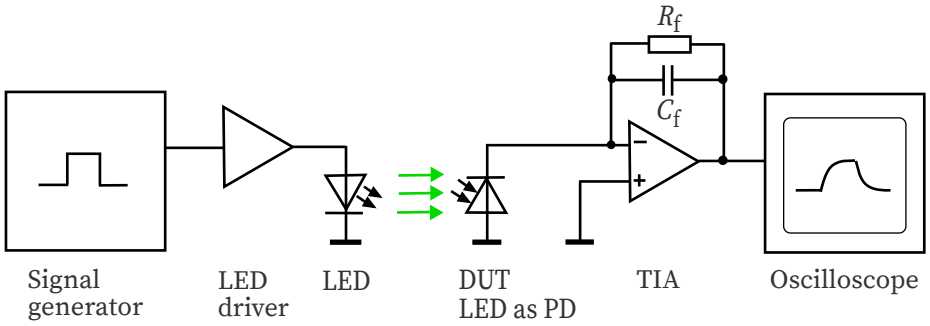

Figure 3.54: Block diagram of the configuration for determination of the rise and fall times of LEDs deployed as PDs. The source is configured as in Fig. 3.53 and the irradiated DUT is connected to a transimpedance amplifier, and the output is recorded by a digital oscilloscope.

of 47 kΩ, as well as a feedback capacitance C_f, to accomplish a quality factor Q of approximately 0.7. The capacitance C of the DUT was measured directly by utilizing a Wavetek LCR55 meter. Using a TIA calculator was found to be helpful at this point, which is available online at [178]. The evaluation of the response signal stored by the oscilloscope delivered the rise and fall times and provided an estimate of the achieved quality factor.

As the main source of uncertainty for the measurements in the temporal domain, the configuration of the feedback capacitor and the resulting quality factor was identified. Timing and capacity values were determined with relatively high accuracy. Table C.6 gives an overview.

Examination and Experimental Results of Temporal Domain

The approximate bandwidth B resulting from 10 % to 90 % rise time measurements can be calculated by:

$$B \approx \frac{0.35}{t_r}. \tag{3.43}$$

This equation is valid for signals with approximately the same rise and fall time [196]. This condition was present in the experiments for the LEDs under investigation. For an experimental determination of the rise time t_{rd} of the photodetector, the rise time t_{rs} of the pulsed light source needs to be taken into account unless $t_{rs} \ll t_{rd}$. The measurable rise time t_{rm} results from the geometric addition of t_{rs} and t_{rd}:

$$t_{rm} = \sqrt{{t_{rs}}^2 + {t_{rd}}^2}. \tag{3.44}$$

In the case of the conducted experiment, which comprised an LED as a source and a fast TIA-PD module as a detector, the shortest measured value of t_{rm} was 40 ns. In conjunction with the calculated value for t_{rd} of 2.3 ns used for the 150 MHz TIA-PD module, t_{rd} was negligible and t_{rm} approached t_{rs}.

In Table 3.15 the measured values t_{rm} of the LEDs used as emitters are shown, given the setup in Figure 3.53. The calculated values for the bandwidths are in the expected range.

In the second part of the experiment, the integrated photodetector TIA module was exchanged by a discrete TIA, which was fed by an LED utilized as PD. In Table 3.16 the measured values for t_{rm} of the two LED series employed as PD are given, the corresponding setup is depicted in Fig. 3.54. The LED sources were matched to the spectral sensitivities, see Table 3.15 and Figs. 3.47 to 3.50. The rise times of the LEDs employed as PDs and the regarding bandwidths were calculated.

Table 3.15: Measured values for 10% to 90% rise time t_{rm} of investigated LEDs used as an emitter.

Manufacturer Type	Color	Wavelength, dom., [nm]	t_{rm}, meas. [ns]	B, calc. [MHz]
Osram LD W5SM	deep blue	455	40	8.75
Osram LT W5SM	green	528	63	5.56
Osram LY W5SM	yellow	590	130	2.69
Osram LR W5SM	red	628	70	5.00

Table 3.16: LEDs used as a photodetector, measured rise time t_{rm}, calculated rise time t_{rd} and calculated bandwidth B, for a TIA configured to approximately $Q = 0.7$.

Manufacturer Type	Color	t_{rs} [ns]	t_{rm} [ns]	t_{rd}, calc. [ns]	B, calc. [MHz]
Osram LB W5SM	blue	40	490	488.3	0.72
Osram LT W5SM	green	40	470	468.3	0.75
Osram LY W5SM	yellow	63	139	123.9	2.83
Osram LR W5SM	red	70	182	168.0	2.08
Lumileds LXZ1 PB01	blue	40	505	503.4	0.70
Lumileds LXZ1 PE01	cyan	40	410	408.0	0.86
Lumileds LXZ1 PM01	green	40	388	377.9	0.93
Lumileds LXZ1 PL03	amber	130	294	263.7	1.33
Lumileds LXZ1 PH01	red orange	70	177	162.6	2.15
Lumileds LXZ1 PD01	red	130	224	182.4	1.92
Lumileds LXZ1 PA01	deep red	130	274	241.2	1.45

In Table 3.17 the measured junction capacitances of the LEDs and the bandwidths as result of the TIA simulation are tabulated for comparison. The simulated bandwidths based on capacitance measurements and the achieved bandwidths for LEDs employed as a PD (driving a TIA in a real LED sourced test setup) show mostly good agreement. The deviation with respect to the determined bandwidths were caused by the difficulty in tuning the TIA exactly to $Q = 0.7$ due to the limited availability of small graded capacitors in the low picofarad range. Both series of LEDs employed as PDs showed larger capacitances in the blue-green regime compared to the yellow-red regime as depicted in Fig. 3.55, which results in longer rise times and lower bandwidths.

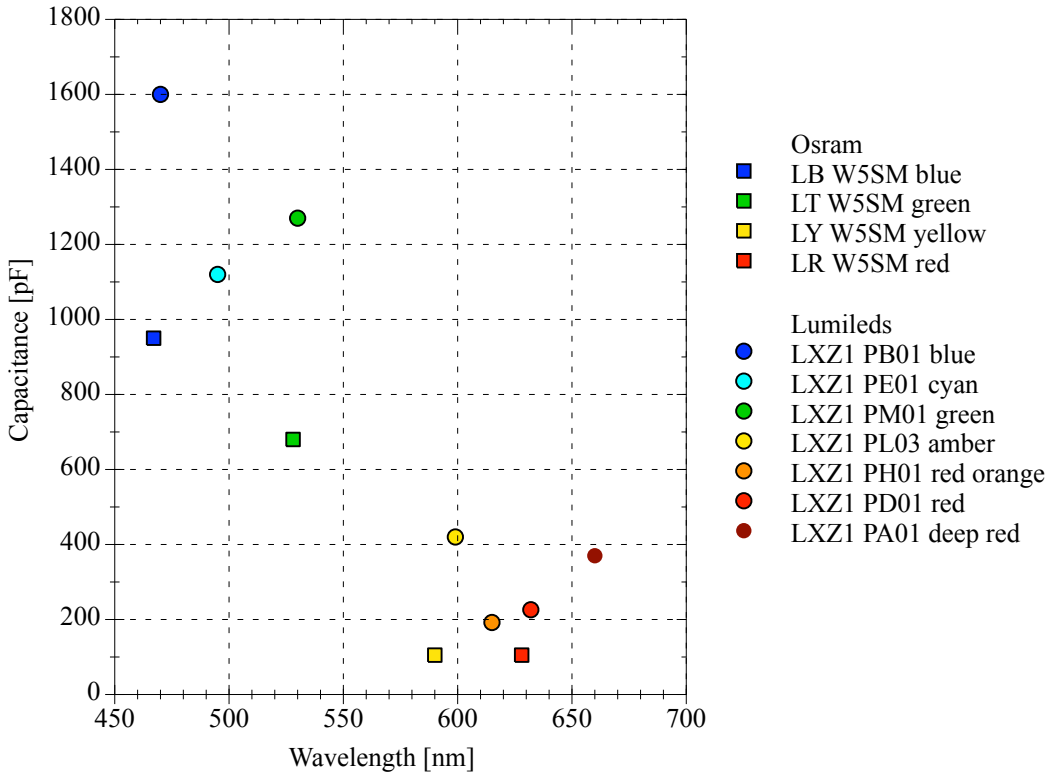

Figure 3.55: Diagram depicts the measured capacitance over the nominal wavelength of two LED series.

Table 3.17: LEDs as a photodetector and the corresponding measured capacitance, used feedback capacitance, and simulated TIA bandwidth for $Q = 0.7$, $GBP = 210$ MHz and $R_f = 47$ kΩ. For comparison: the reference Si-PIN-PD Osram SFH 2400 has a capacitance of 11 pF at zero reverse voltage, resulting in a simulated bandwidth of 7.8 MHz under the same conditions.

Manufacturer Type	Color	C, meas. [pF]	C_f [pF]	B, sim. [MHz]
Osram LB W5SM	blue	950	5.5	0.86
Osram LT W5SM	green	680	4.7	1.02
Osram LY W5SM	yellow	105	1.8	2.58
Osram LR W5SM	red	235	2.8	1.73
Lumileds LXZ1 PB01	blue	1600	7.2	0.67
Lumileds LXZ1 PE01	cyan	1120	6.0	0.80
Lumileds LXZ1 PM01	green	1270	6.4	0.77
Lumileds LXZ1 PL03	amber	420	3.7	1.30
Lumileds LXZ1 PH01	red orange	192	2.5	1.91
Lumileds LXZ1 PD01	red	226	2.7	1.76
Lumileds LXZ1 PA01	deep red	370	3.5	1.38

3.5.3 Analysis in the Spatial Domain

Experimental Setup for Spatial Measurements

One of the main parameters in the application of optical systems is the angle of incidence (AOI). Therefore, to achieve precise alignment and good repeatability, an optical bench was utilized. The light source for spatial measurements was an LED of the series Ledengin LZ4 [63]. The LED colors, blue and amber, were selected so that the wavelength matches the DUT. In order to be able to vary the angle of incidence, the DUT was mounted on a rotatable device, see Fig. 3.56. This setup represents the simplest form of a so-called goniometer. Precise direct measurements of the generated photocurrent were made with a Keithley 6517 electrometer in the corresponding nanoampere range. The determination of the field of view could be carried out based on these measurements with varying AOI. As no major deviations from the radiation characteristic of the DUT as an LED source were expected and in order to minimise the effort, only the smallest possible comparisons within and between the series were made. For comparison within a series, red and green Osram LEDs were used, for the comparison between series green Osram and Lumileds LEDs were used. Values were recorded for AOIs between 0° and 80° taken in 10° increments, and the rotation took place in both directions.

Another test was to verify that the DUT did not react unexpectedly to changes in the direction of polarization. Fig. 3.57 is depicting the setup utilized for this purpose. Non-polarized light from an LED source of appropriate wavelength (matching the DUTs passing band) was used, which was subsequently filtered by a rotatable Edmund Optics glass polarizer 53344. A continuous change of the polarization direction from horizontal to vertical could thus be achieved through rotating the filter up to 90°. Due to the time and effort involved, it was decided not to examine the full series, so only red LEDs of both series were chosen as example DUTs. As a light source, an amber-colored Ledengin LZ4 LED was used, operated under stable conditions in constant current mode. Photocurrents were measured directly with a Keithley 6514 electrometer, values were taken in 10° rotation increments, and the rotation was carried out in both directions.

In principle, the electrometer, which is specialized in measuring tiny currents, enables high accuracies. To ensure that the light source was not drifting during the measurements, values at the zero degree position were checked to be constant between the individual measuring positions. These controls prevented the drift from making significant contributions. The manually rotatable positioning was subject to a certain angular error. Table C.6 provides an overview of the related uncertainties.

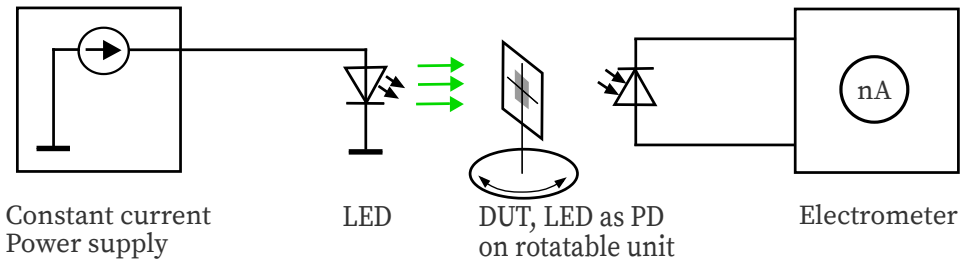

Figure 3.56: This illustration shows the principle system for determination of the directional characteristic of a photodetector. The DUT is rotated so that the irradiation hits the active area at a defined angle.

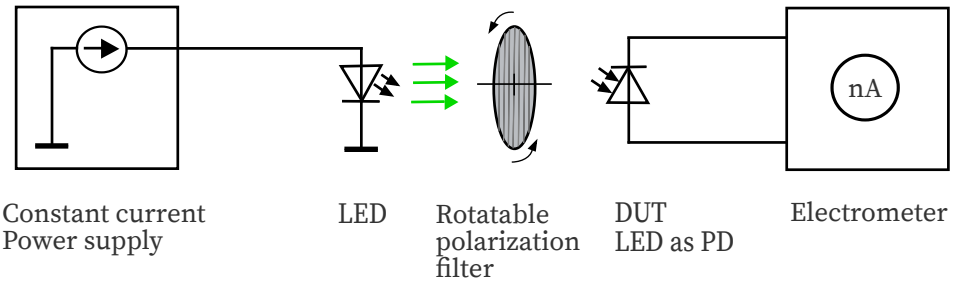

Figure 3.57: This graphic depicts the setup for checking a possible sensitivity to polarization. The light of a unpolarized LED source passes through a polarization filter. The polarization direction depends on the rotation position.

Examination and Experimental Results of Spatial Domain

The measurements of the relative sensitivity as a function of the AOI for the LEDs employed as a PD, showed no significant deviation within the uncertainties from the curves given in the data sheets of the particular LEDs used as emitter, see Fig. 3.58.

When investigating a possible influence of the polarization direction of the incident light on the sensitivity, no indications could be found within the scope of the measuring accuracy. Please refer to Fig. 3.59 and note the very small scaling.

3.5.4 Relevance of the Results for Applicability

Two single-color power LED series were employed as a PD and the spectral, temporal and spatial characteristics were experimentally investigated. The DUT featured unexpected good responsitivity. Previous publications examined mostly low-power and mid-power LEDs, which generally showed less responsivity. Even in comparison to a common Si-PIN photodetector and its theoretical sensitivity boundary, the test objects showed considerable values. The same LED employed as an emitter and a detector, so-called dual-use, is generally applicable through the spectral overlap. However, since this overlap is only small to medium, the same applies to the accompanied efficiency. The yellow-red regime showed significantly larger values compared to the blue-green regime. The "green gap" in efficiency of LEDs used as an emitter, which is centered around 550 nm, occurred correspondingly shifted to lower wavelengths of approximately 500 nm, for LEDs used as PDs. Analogously it could be called "cyan gap" of sensitivity. The examined LEDs utilized as a PD, exhibited another main feature - an inherent optical bandpass characteristic. This can be a cost-efficient alternative to the adaption of secondary filters to PDs. This is especially true since colored glass narrow bandpass filters are generally not available in the yellow-red region, thin film filters are generally expensive, and off-the-shelf PD filter combinations are rare. For the speed, which is important in communication systems, the capacitance has a significant influence. Compared to the Si-PIN-PD reference, the junction capacitance of the examined LEDs employed as PDs was found to be one to two orders of magnitude higher. Accordingly, this leads into a reduced achievable bandwidth. The measurements from the yellow-red regime offer a lower capacitance compared to their counterparts in the blue-green area, thus allowing higher speed. The angle of incidence properties of the LEDs under investigation was discovered to be comparable when operated as an emitter and a detector, as expected. Furthermore, no dependence on the polarization direction could be determined. There is a large potential in LEDs used as PDs for low-cost solutions in visible light communication, daylight filtered or color-selective applications.

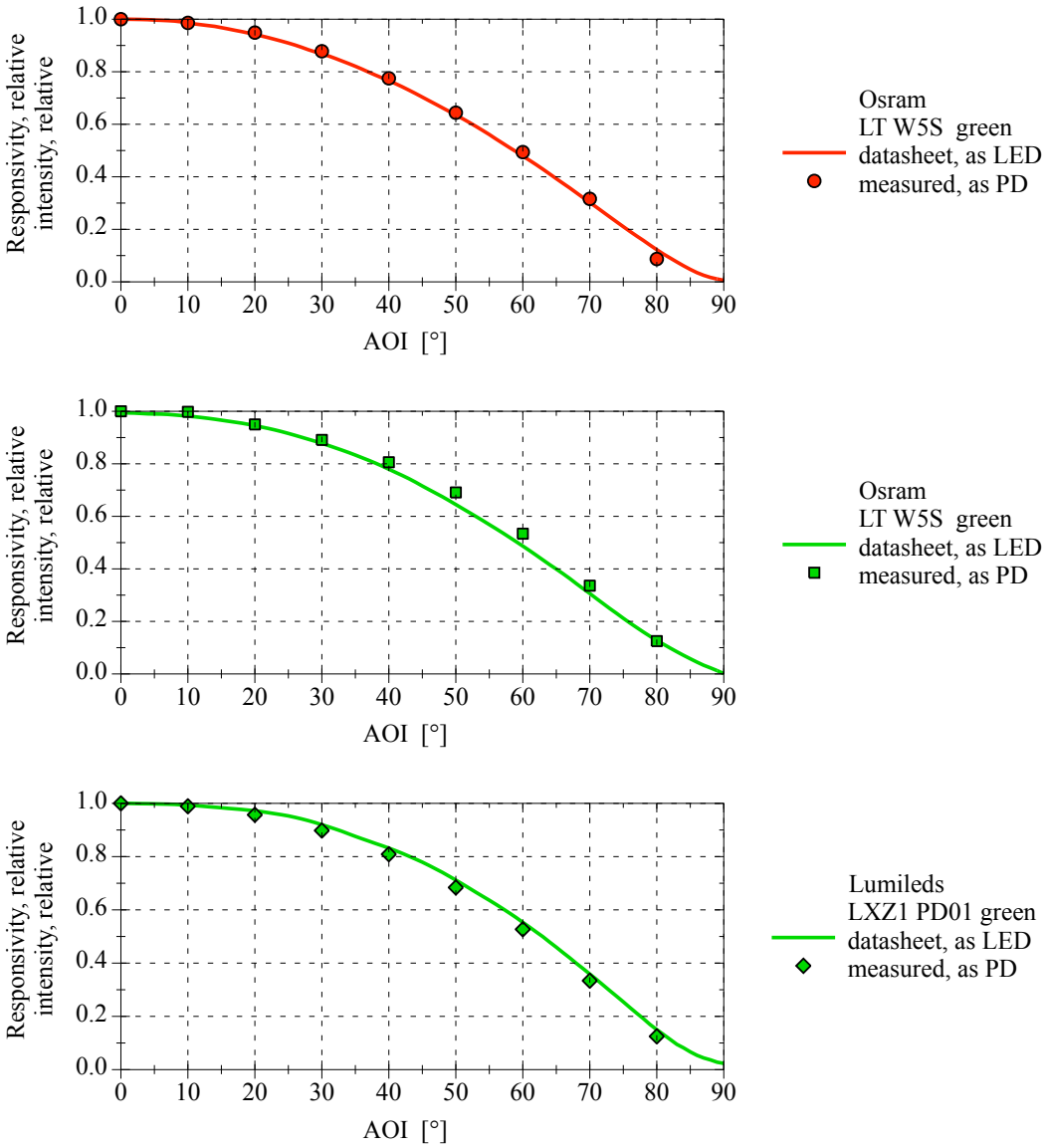

Figure 3.58: Plots overlay the relative responsivity and relative intensity as a function of the AOI for different LEDs deployed as a detector and as a light source. The DUT originate from two series, and within one series the color was varied.

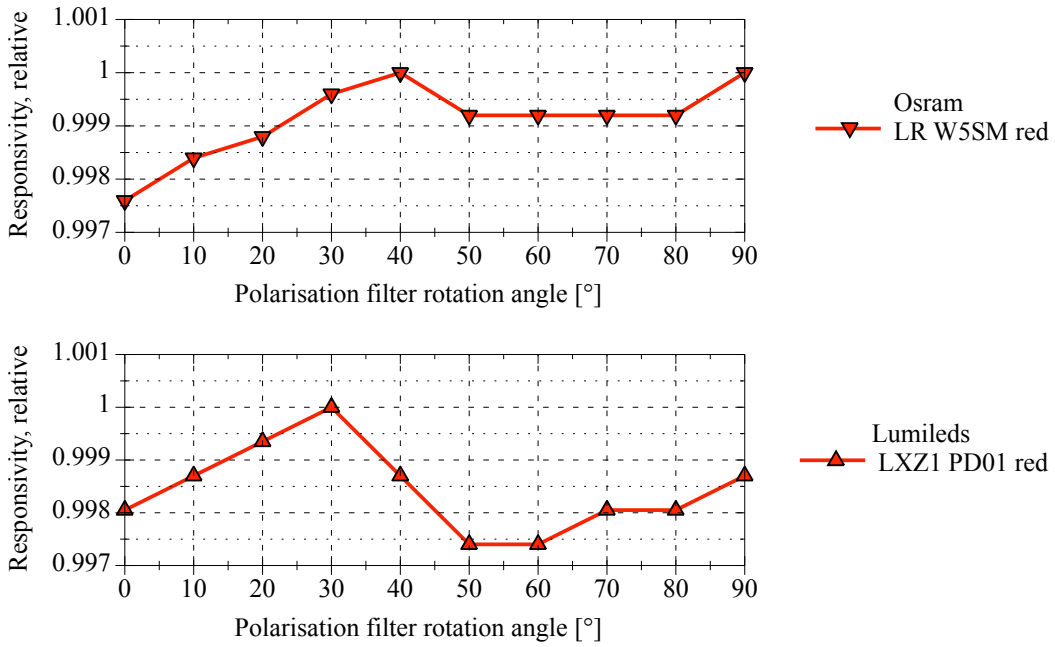

Figure 3.59: Figures show the measured normalized responsivity as a function of the polarization angle for a red Osram LED, as well as for a red Lumileds LED, both employed as a PD.

3.6 Chapter Summary

In this chapter, UOWC system components have been examined with the focus on adaption and optimization. Energy is generally an essential issue in underwater systems. Therefore, a large overall efficiency is targeted in the field of underwater communications. The wavelength has a key impact here. Depending on the water type, the narrow window of least attenuation shifts from blue in oceanic to green in coastal waters. Just in this wavelength range the wall-plug efficiency of LEDs drops, also known as the green-yellow gap. With typical silicon detectors, the responsivity increases moderately in this range, and it finally results in a threefold relationship. For coastal waters, converted green LEDs can represent a solution, despite the lower speed and larger spectral bandwidth.

The operation of UOWC is accompanied by ambient light in most cases, which causes interferences. The ambient underwater light field is subject to many influencing factors: location, sun position, cloudiness, water type and depth. In oceanic waters, the spectrum is predominantly in the blue wavelength range, and in coastal waters it is in the green range. The intensity reduces with increasing depth, and the structure shifts from direct to diffuse. Furthermore, there is a distinct directionality, and downwelling and upwelling irradiances are the common measure here. A method for suppression of these unwanted light components is the employment of optical bandpass filters, which also need to be adapted to the emission spectrum of the LED. Four different filters have been examined in combination with a blue LED for different circumstances - here the water type, the depth and the AOI have been varied. The thin film filters show a larger improvement of the OSNR compared to the absorptive colored glass filters. Their disadvantage is a significant AOI dependence caused by the spectral shift of the transmission zone. An optimal adaption has been achieved with a ratio of 1 for the filter passband to compared to the LED's FWHM. The upper limit for a meaningful utilization can be identified at AOIs of about 30°.

The SNR in the electrical domain is one of the key parameters for the signal processing. For a deeper analysis, PIN-PDs and APDs have been combined with TIAs and investigated at various

light conditions. The total noise results from many contributions: thermal noise, shot noise from ambient light and signal, dark current shot noise and amplifier related noise. A dominant role of the ambient light shot noise component for the APD case is evident. The SNR performance of different detectors have been examined for separated irradiances of ambient and signal light sources. It confirms that PIN-PDs, compared to APDs, are much more robust against ambient light, but with the disadvantage of lesser sensitivity. Large area PIN-PDs can counterbalance this and represent a good compromise. In a next step, the examinations have been extended to conditions prevailing in UOWC. A blue LED acts a light source, a thin film filter is applied in front of different PDs, and the ambient light is represented by the the downwelling irradiance of the respective depth. In terms of achievable distances, a large area PIN-PD performs well, but only in dark conditions a large area APD is more capable. The results of further investigations indicate that the PD facing direction is much more significant in clear oceanic water compared to turbid coastal ones. An increase of the source power is of course a way to enlarge the SNR and distance, which is better for PIN-PDs than for APDs where shot noise can reduce the effect. The last question of this subject relates to the filter passband width in order to optimize the SNR. The simulations provide a passband width of 1.5 to 2 times the LED FWHM to be a good choice.

With emphasis on a possible dual use in UOWC, single-color power LEDs used as photodetectors have been examined. LEDs in different colors of two series have been compared directly with an equally sized PIN-PD. The measurements included the spectral, temporal, and spatial domain, and yielded some unexpected results. The LEDs as PDs exhibited the half or more of the genuine PD responsivity, including a pronounced bandpass character. The width of the passband is larger than the FWHM in LED utilization, the spectral overlap in both modes of operation is color dependent, and it is relatively poor in the blue-green regime. LEDs as PDs suffer from a comparatively high capacitance that limits attainable speeds, and the blue-green regime is more affected. Nevertheless, the results show that they can be an interesting alternative to PD-filter combinations in the low-cost sector.

Chapter 4

UOWC Assemblies

4.1 Underwater Housings

4.1.1 Selection Criteria

For underwater operations, electronic devices and circuits need to be protected against the surrounding corrosive and conductive seawater, as well as from the water pressure in most cases. Therefore housings are an integral part of the UOWC system, however, they receives little attention in the literature [17]. If optical sources or detectors are involved like in UOWC, then additional optical components are essential, especially windows. These so-called optical ports need to be integrated into the housing. The following basic selection criteria for underwater housings apply:

- Maximum operational depth.
- Dimensions, shape, and integrability.
- Utilizable volume, weight, and buoyancy.
- Optically usable field.
- Pressure sensitivity of internal components.
- Accessibility.
- Mechanical robustness.
- Corrosion resistance.
- Availability, producibility.
- Costs.

4.1.2 Basic Concepts and Designs

An overview of the typically deployed housing and port concepts is provided in Fig. 4.1. Most common and widely used are pressure-resistant cavity housings (I-II), with an inner air-filled cavity. Typical materials are aluminum, stainless steel or titanium, but also reinforced synthetics. The selection of the material is mainly based on factors such as operational depth, strength, weight, corrosion resistance, and costs. In principle, long cylindrical housings with a small diameter are well suited for large depths and high pressures. Basically, the ports require flat mounting surfaces, i.e., the side cover of cylinders. This makes housings for deep and optical purposes with a correspondingly large viewing area much more complex, heavier and more expensive.

A special case of this pressure-resistant type is the spherical glass housing (III). It consists of two precisely fitting hemispheres. Subfigure (IV) depicts a fluid-filled thin-walled version of a pressure-neutral housing, where the inner components are exposed to the pressure of the water column. A

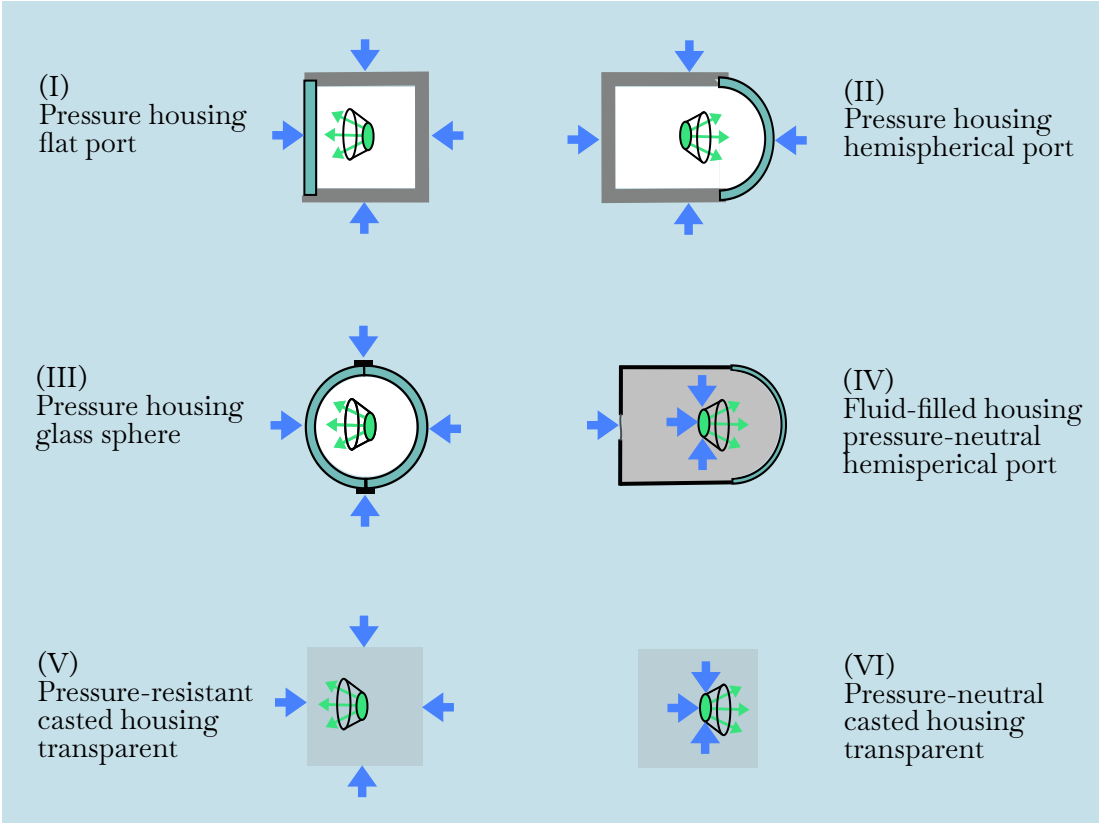

Figure 4.1: Underwater housing concepts for optical applications, illustrated by the example of a green LED including reflector. Blue arrows symbolizie the pressure effect of the water column.

membrane separates the inner and outer fluid and passes on the pressure. The transparent fluids used are in most cases oil-based, but specialized inert electronic liquids are also used in some applications. Since not all electrical components are pressure resistant, this limits the range of usable electronic components. Whereas many semiconductors are applicable, capacitors can be problematic. An advantage of (I) to (IV) is the general accessibility of the components for service or exchange.

A different way is to embed the components in material like epoxy, polyurethane, or silicon. The process of resin-embedding is also known as resin-casting or potting in the community. For optical applications, the potting compound must be either transparent or complemented by a small glass window covering the LED or PD, respectively. Depending on the hardness of the potting compound it can be made pressure resistant (V), where the pressure of the water column is withstood by the cast. Embedding of components in softer flexible materials is realized by the pressure-neutral concept shown in (VI). The concepts of fluid-filling and potting are common and widely used in underwater technology for junction boxes and connectors. For electro-optical and electronic devices the potted design is also increasingly applied. The main advantages are weight, size and costs. The disadvantages on the other hand are limited choice of pressure-tolerant components and inaccessibility for servicing.

4.1.3 Additional Aspects

The heat generated by power electronics such as LED drivers must be dissipated. With metal pressure housing this can be achieved generally simple. A problem which occurs sometimes, due to the humidity of the air inside, is condensation occurring on the cold glass port, which

greatly affects the visibility. This can be prevented by evacuation and flooding with nitrogen, but this requires additional plugs and specialized equipment, and represents an extra effort in the field. Furthermore, the heat dissipation can be impaired by this. Condensation is not a problem with liquid filled housings, and the heat transfer can be improved by utilizing cooling fluids like Fluorinert. Heat dissipation can be an issue in casted housings, and large thin walled areas or a multilayer structure with opaque filled compounds in zones without vision represent possible solutions here. The spatial integration of underwater housings in small vehicles like AUVs is likely to be the most challenging, at least compared to other vehicles likes ROVs or fixed structures. The majority of AUVs are of a torpedo type, which means a narrow cylinder with propulsion in the aft and a certain minimum speed for stable control. Another critical design factor is the buoyancy, because small vehicles are very trim and payload sensitive. Although the typical speed of AUVs is only a few knots, the hydrodynamic design is very important to keep the drag low for high power efficiency of the drive train and the vehicle's stability, particularly for torpedo-shaped vehicles. Therefore, the shape of communication transducers needs to be as small and streamlined as possible. Mechanical impacts due to launching, recovering, transport and seafloor contact are almost unavoidable. The mechanical robustness is hence a relevant property, since glass or plastic thin-walled domes are far more vulnerable than, for example, solid potted solutions. When integrating an UOWC system into the AUV's tight space, the number of cables and connectors, their thickness and routing also need to be considered. Splitting into more smaller sections would increase the housing and cabling effort.

4.2 Optical Ports and Underwater Light Path

4.2.1 Basics, Specific Values and Calculations

Ports are a crucial component in optical underwater applications. Typical instrumentation is employed for the acquisition of physical quantities like attenuation, absorption, turbidity, irradiance or fluorescence [117]. Another major area is the broad range of underwater imaging, where the ports clearly receive the most attention. The reasons are strong effects on distortion and focus [176, 197]. In addition, ports are an important component of equipment for underwater illumination purposes, ranging from a diving torch to an AUV camera flash. This sector exhibits some parallels to UOWC transmitters.

Common Shapes

Flat disks and domes are the most widely used forms of underwater windows, cf. Fig 4.1 illustrations (I) and (II). The domes can be strict hemispheres, but also flattened variants where spherical caps are utilized. Of course, lenses are also used. In addition to the regular shapes, recently also so-called free-form lenses are developed. Pressure-neutral potted housings or just embedded components occupy a special position. The casting can simply represent a thin skin or, depending on the casting mold, it can also take on geometric shapes, see Fig. 4.1 illustration (VI).

Materials

Generally, ports are produced of different types of glass or synthetics. Common materials and their individual refractive index are given in Table 4.1. The typical material thickness ranges from 1 - 20 mm, and the refractive index from 1.4 - 1.6. Glass is known for its best optical properties, and transparent synthetics as a potting compound cannot compete. However, this should be more significant for underwater imaging compared to UOWC. But there are some more properties of interest: UV and aging resistance, shock strength, scratch sensitivity, chemical resistance, adhesive capabilities, machineability, density, and water absorption.

Table 4.1: Typical refractive indices at $\lambda = 589$ nm of selected port materials.

Material	Refractive index n
Silicone potting compound	1.41 - 1.54
Quartz glass	1.46
Polyurethane (PU) potting compound	1.47 - 1.51
Acrylic glass (PMMA)	1.49
Borosilicate-crown glass	1.52
Polycarbonate (PC)	1.58

The loss due to internal absorption in transparent port materials is thickness dependent, and values of a few tenth of a percent are typical in the wavelength range used for UOWC of about 450 - 600 nm. Smaller values also arise with glass, and larger ones with plastics and especially potting compounds, but in principle their importance is minor. This also applies to the wavelength-dependent refraction changes in this wavelength band, which are less than 1%.

The protection of the port against biofouling can be realized through UV-C radiation, see Section 2.1.3. The most effective wavelength for antifouling applications is in the band of 250 nm to 280 nm, therefore utilized window materials need to have a high transmittance in this range. This is only the case for fused-silica quartz glass, not for standard glass and transparent synthetics.

Snell's law, Fresnel's Equations and Radiance

A light ray has to pass two media changes when traveling from the water through a port into an air filled pressure housing, or vice versa. The ray experiences refraction at each of these boundaries, and Snell's law describes the relationship between the angle of incidence and refraction, see (2.1) and Fig. 2.3. The number of transitions can vary with the housing concept; pressure-neutral potted version may only have one, but if more optical elements or media are involved the number increases.

In the following section, the example calculations are conducted for the transmitter side of the flat and dome ports. The reference axis for the calculations is perpendicular to the flat port or radial in the case of the dome port, for both the transmitter and receiver sides, without inclination. At the transmitter side, the source is placed inside the housing, where air represents the first medium. The ray exiting angle is θ_s, the first boundary incident angle is θ_1, and the refracted angle becomes θ_2. After the ray has passed this second medium into the third, the refracted angle θ_3 arises and the resulting angle θ_r is generated. Depending on the port shape, some of these angles may be equal, or there may be additional sub angles like θ_2'. The numeration of the refraction indices is done accordingly from n_1 to n_3. The relationships are illustrated by the diagrams in Figs. 4.2, 4.7 and 4.9.

Since Snell's law only explains the directional change of the incident ray at the interface, the question of the amount of reflected and transmitted light remains open. The answer is given by Fresnel's equations, which describe the transition of electromagnetic waves at the interface in terms of reflectance and transmittance for polarized light. The s- and p-polarized components are considered separately, and can later be merged for unpolarized light, as from an LED. A transition of incident light at θ_1 from a medium of n_1 into another of n_2 results in the transmittance $T_{12}(\theta_1)$ and the reflectance $R_{12}(\theta_1)$. For a subsequent third medium of n_3 this accordingly leads to $T_{23}(\theta_2)$ and $R_{23}(\theta_2)$.

The amount of light can be expressed by the radiance concept, which utilizes so-called light pencils as beams. The radiance L is a radiometric directional quantity, and is power per unit area

per unit solid angle. A part of the incident radiance is refracted and transmitted by the media boundary. The remaining part is reflected, while the law of conservation of energy is satisfied. The relationship of incident and transmitted radiance is finally given by the 'n^2 law for radiance', see (C.16) and [87] for an in-depth discussion. Corresponding sets of adapted equations for the flat and dome port geometry are given in the Appendices C.7 and C.8.

Parameters and Assumptions for Calculations

For the subsequent examinations that focus on the transmitter side, Table 4.2 gives the applied parameters including variation range. These are adapted to real conditions. Assumptions made for the calculations include:

- No internal absorption in port material.
- Isotropic Point source.
- Radiances normalized to source of $L_1 = 1$ [W/m^{2}sr].

Table 4.2: General parameters for port light path examinations, and index order for the transmitter side.

Refraction index, air	n_1	1.0 (no variation)	
Refraction index, port	n_2	1.5 (1.40 - 1.60)	
Refraction index, water	n_3	1.34 (1.33 - 1.35)	
Thickness, port	$t_{\text{fp}}, t_{\text{dp}}$	7 (1 - 20)	[mm]
Radius, dome port, inner	r_{dpi}	50	[mm]

4.2.2 Flat Ports

Transmitter Side

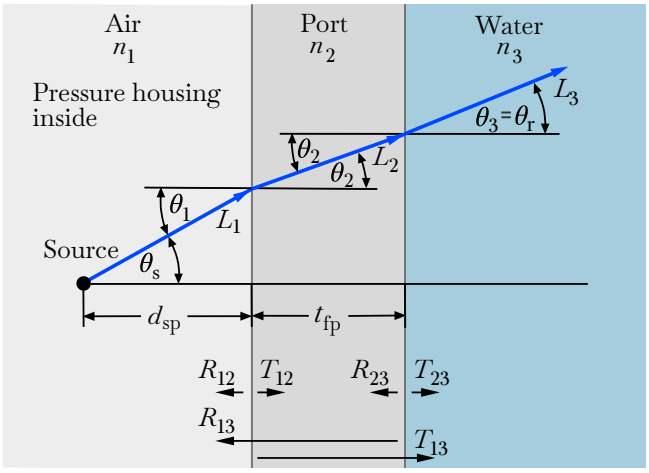

Figure 4.2: Underwater light path geometry for the transmitter side, and the source in a pressure housing including flat port.

The basic case for the transmitter side when using a flat port is depicted in Fig. 4.2, and the parameters for this example calculation are given in Table 4.2. The path of the radiance is symbolized by the blue arrows, starting at the incident L_1 with a source angle θ_s, at the first

boundary surface transitioning into L_2, and at the second to L_3. Snell's law provides θ_2 and θ_3, Fresnel's equations give the transmittances T_{12} and T_{23} as well as the reflectances R_{12} and R_{23}, and finally the 'n^2 law for radiance' yields L_3. Since the port is assumed to be thin, its thickness t_{fp} and the source to port distance d_{sp} are insignificant for now, as the thickness only causes a magnification effect.

The results of these calculations as a function of θ_1 are presented in Fig. 4.3. Overall, there is a strong refraction, the angle θ_3 is in maximum 48.3°, and the total reflection at the n_2 to n_3 boundary is therefore not reached. For small and medium θ_{s} values, there is approximately 95.7 % total transmittance T_{13} and 4.3 % total reflectance R_{13}. It should be emphasized, that for small and medium θ_{s} a ratio L_3/L_1 of approximately 1.7 occurs. The reason for the increased radiance is the reduced solid angle due to refraction, which can be imagined as collimated rays.

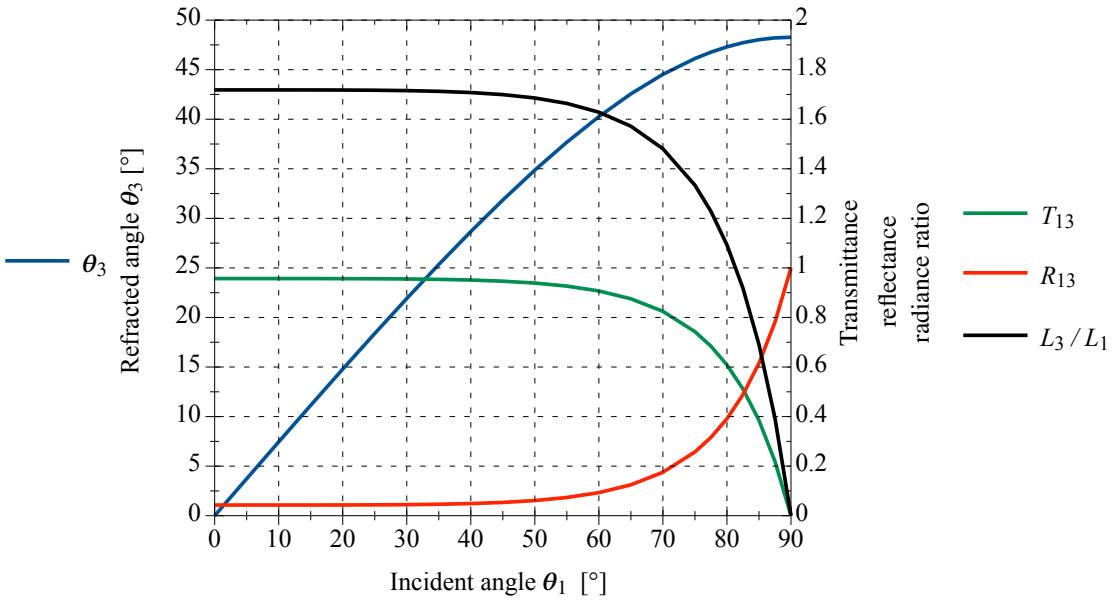

Figure 4.3: Flat port theoretical refraction, transmittance, reflectance, and radiance ratio for transmitter side.

Transmitter Side Parameter Variations

Since the refraction index n_2 of the port depends on the material, and the water n_3 also may be affected by changes, these indices are individually varied in order to determine the respective effects, and the outcome is shown in Fig. 4.4. The port refraction index n_2 variation influences the radiance ratio L_3/L_1 to a small extent, but not the refracted angle θ_3. The water refraction index n_3 variation changes the radiance ratio L_3/L_1 and the refracted angle θ_3, but only both slightly. So in this respect, the port material selection and the operation site choice are barely restricted.

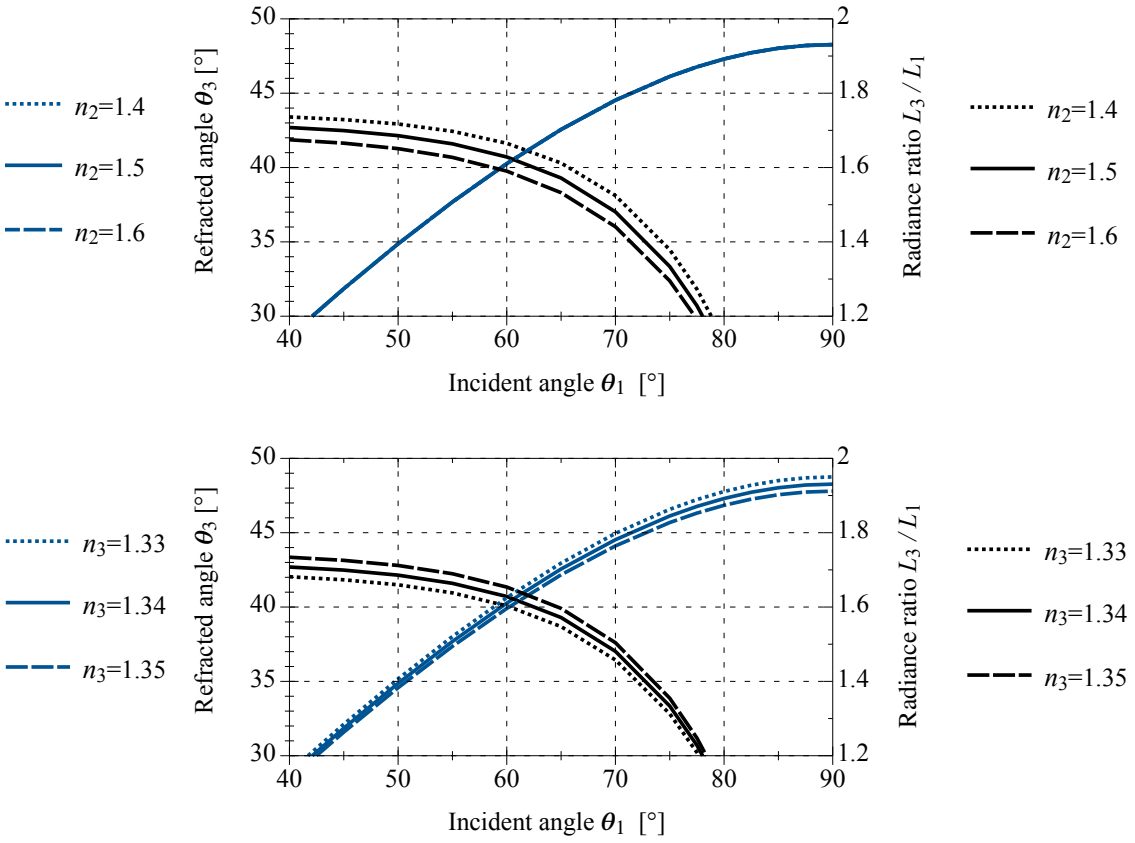

Figure 4.4: Effect of refraction index variation for aflat port. The port material n_2 is varied in the upper diagram, and is for water n_3 in the lower diagram.

Receiver Side

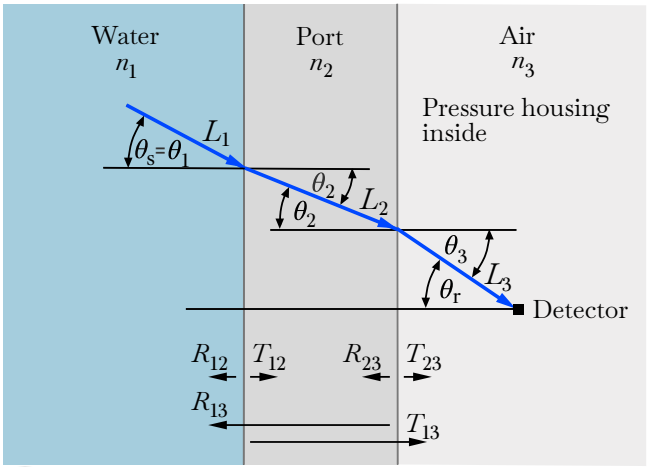

Figure 4.5: Underwater light path geometry of detector in pressure housing including flat port.

A change of the flat port equipped housing to the receiver side configuration affects the direction, the order of the media, and the indices, but the principles stay the same. Fig. 4.5 depicts this situation. Calculations are carried out as for the transmitter side, and the results are presented in Fig. 4.6. A strong refraction is obtained again, at an critical incident angle θ_c of 48.3° and

a resulting angle θ_2 of 41.8°,and the total reflection condition of the port to the air boundary is reached. Further increased incident angles result in total reflection of the equal angle with a minus sign. For small θ_s, there are the same total transmission T_{13} and total reflectance R_{13} values as in the transmitter configuration. Major changes occur at one point, for small and medium θ_s values a ratio L_3/L_1 of approximately 0.53 is calculated. The reason for the decreased radiance is the expanded solid angle due to refraction, which can be visualized as widened rays. A variation of the water n_1 and the port n_2 in the same ranges as before, again only results in small effects. It is worth mentioning that there is a shift of the critical angle by a few degrees when changing n_2 by ± 0.1.

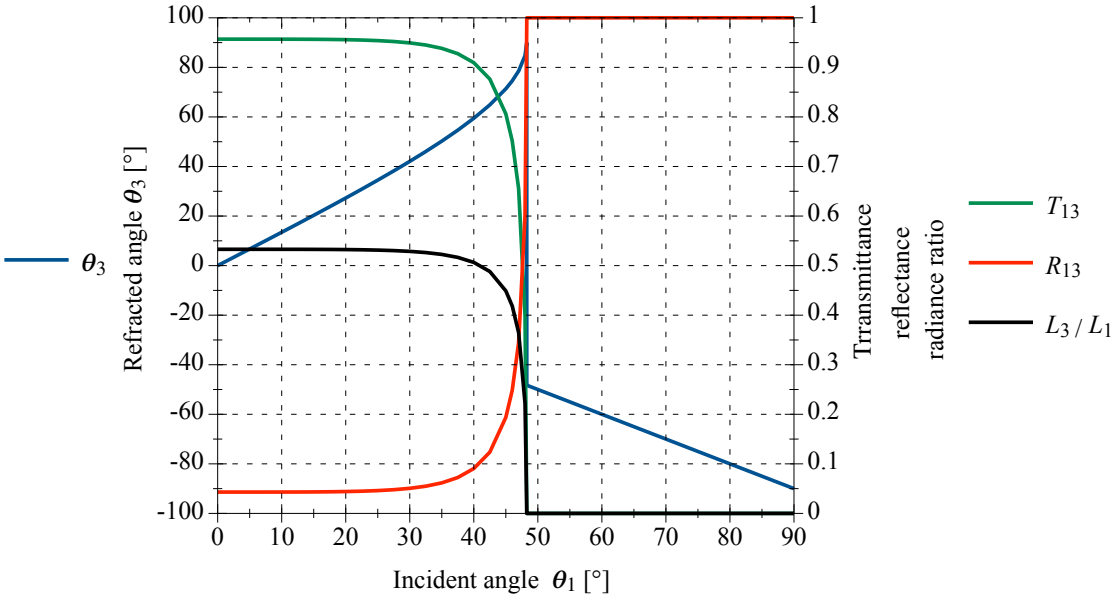

Figure 4.6: Calculated refraction, transmittance, reflectance, and radiance ratio on the receiver side for a flat port.

4.2.3 Dome Ports

Transmitter Side and Centered Source

If an underwater housing is reconfigured from a flat port to a dome port, the geometry changes considerably. For the transmitter side, the special case of a point source located in the dome center is shown Fig. 4.7. As this represents an ideal case, this position is also called the 'sweet spot'.

The light path is symbolized by blue arrows. Since the radiances L_1, L_2, and L_3 are found on a straight line, and the related angles θ_1, θ_2, and θ_3 are zero, no refraction occurs. These relations are consistent, independent from the source angle θ_s, and which is equal to the resulting angle θ_r. Nevertheless, reflections arise at the media transitions. The outcome of example calculations, applying the parameters from Table 4.2 but excluding the irrelevant thickness, is presented in Fig. 4.8. For all incident angles θ_s, there are approximately 95.7 % total transmittance T_{13} and 4.3 % total reflectance R_{13}. A radiance ratio L_3/L_1 of 0.957 occurs.

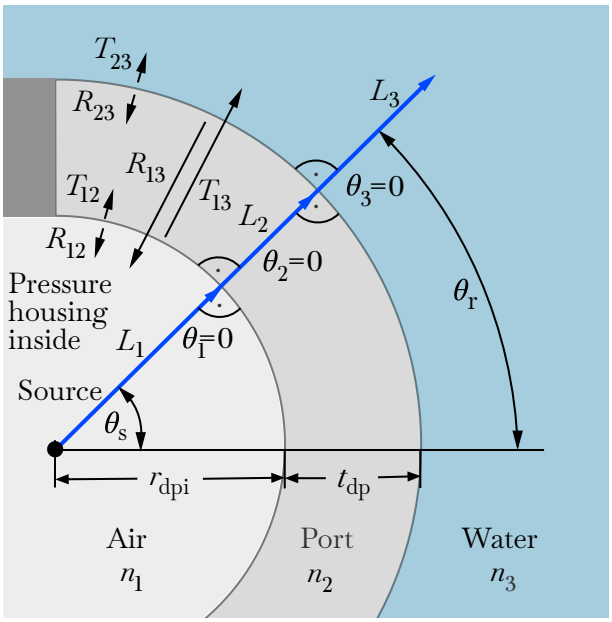

Figure 4.7: Underwater light path geometry of a pressure housing including a dome port and a centered point source.

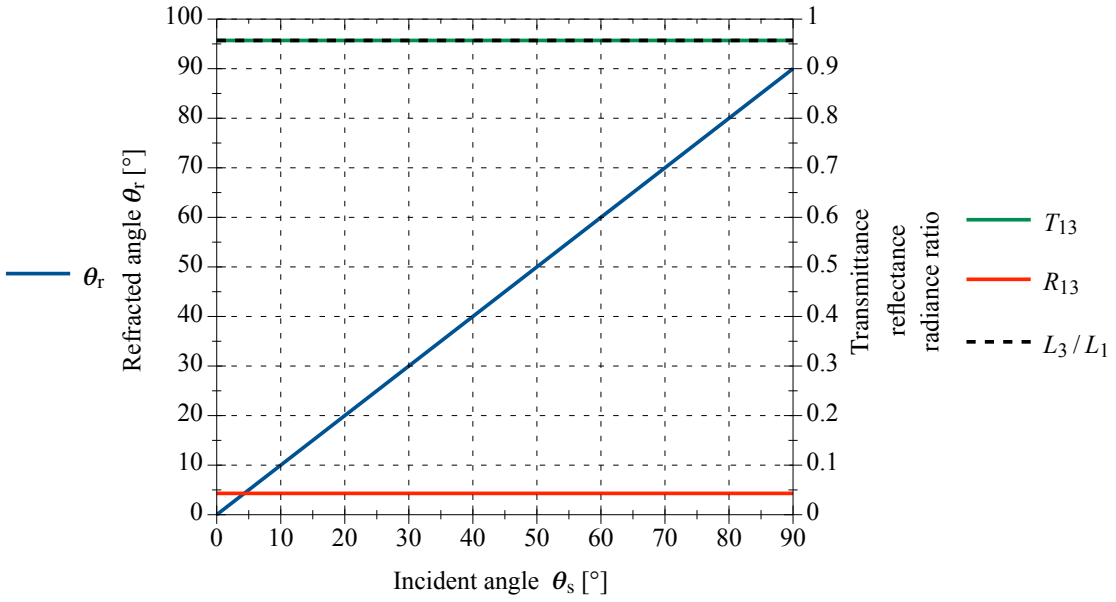

Figure 4.8: Calculated refraction, transmittance, reflectance, and radiance ratio for a dome port housing. An isotropic point source is positioned in the dome center.

Transmitter Side and Source out of the Center

A displacement of the point source or detector from the center of the dome leads to a violation of the ideal case. Two basic types of displacement must be distinguished: the radial form that preserves the rotational symmetry and the lateral form that can create distortions. Due to real dimensions of components, as for example for centered large planar elements, it may be necessary to consider outer areas as lateral displacement.

The examination of this behavior with a radially displaced source is more important for applications in the field, because multiple elements cannot be positioned within, but only radially around the center, and the dome sizes chosen are rather small. The geometric relationships resulting from this case are shown in Fig. 4.9. In addition to the parameters defined previously, the inner dome port radius r_{dpi} and the distance center-to-source d_{cs} needs to be specified, as well as the dome thickness t_{dp}. It can be seen that the source angle θ_{s} is no longer equal to θ_1, and likewise θ_3 is no longer the same as θ_{r}. Furthermore, an auxiliary angle θ_2' is created.

The results of these calculations as a function of θ_{s} presented in Fig. 4.10, are valid for the base parameters in Table 4.2 with a source placed at a d_{cs} of 25 mm, which corresponds to the half inner dome port radius. Overall, there is no overly strong refraction, and it is almost linear for all incident angles θ_{s}. There is approximately 95.7 % of total transmittance T_{13} and 4.3 % of total reflectance R_{13}. The most significant change compared to the ideal case concerns the ratio of transmitted to incident radiance. For small incident angles θ_{s} a ratio L_3/L_1 of approximately 1.27 occurs, and this value decreases in an arcuate curve to zero for a θ_{s} value of 90°.

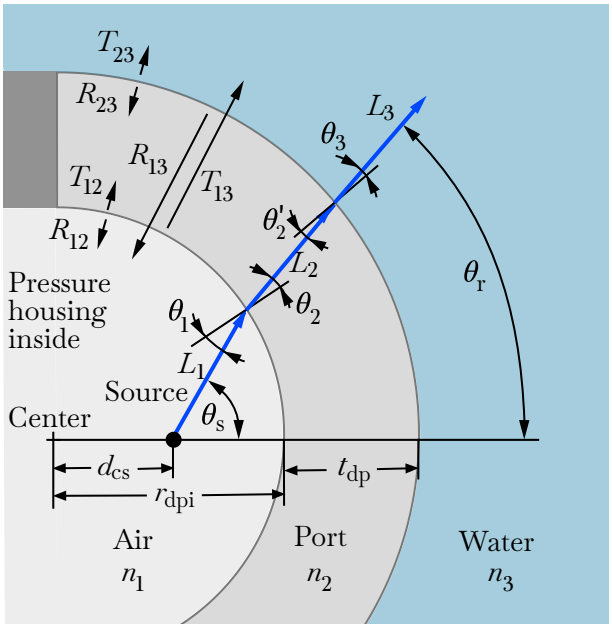

Figure 4.9: Underwater light path geometry of pressure housing including a dome port and a source positioned radially outside of the center.

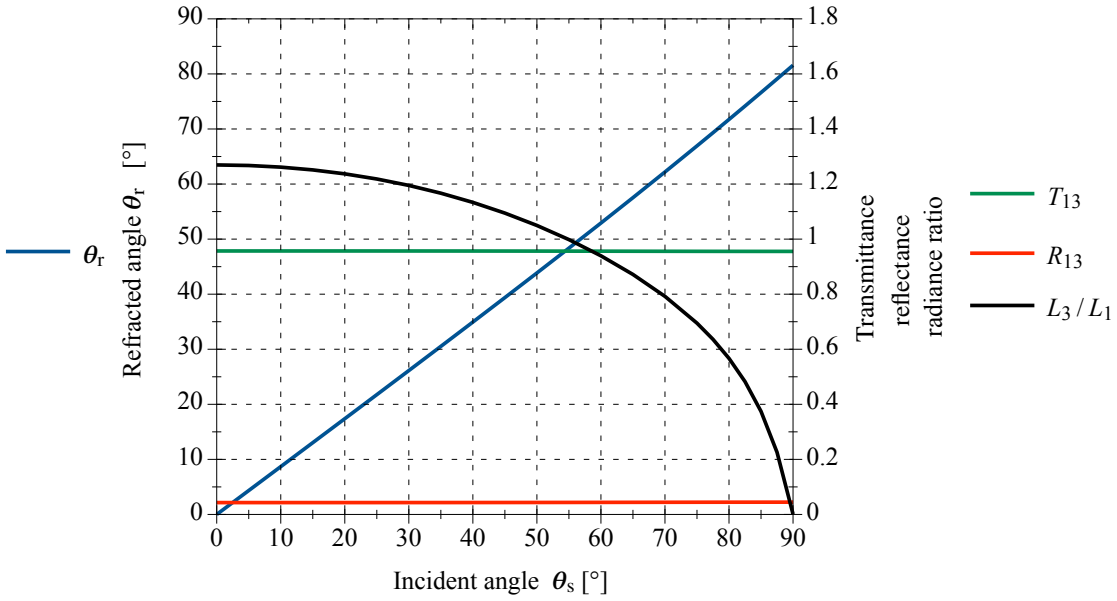

Figure 4.10: Theoretical refraction, transmittance, reflectance, and radiance ratio for a dome port housing. The point source is placed outside the dome center on the half inner radius position.

Source Position Variation

As previously mentioned for the flat port, the important parameters for the dome port are now changed individually. The source position is radially varied, while the base parameters $(n_1, n_2, n_3, r_{\text{dpi}}, t_{\text{dp}})$ are kept constant. Calculations are made for center-to-source distances d_{cs} of 0, 25, 37.5 and 47.5 mm, according to relative values of the inner dome port radius r_{dpi} of 0, 0.5, 0.75, and 0.95. The outcome is given in Fig. 4.11.

The variation of the position over almost the entire range shows a large effect on the refraction and the L_3/L_1 ratio. This can be described by a transformation from the ideal dome port in the direction of a flat port, since the dome becomes relatively flatter as the source approaches the inside of the dome. For many configurations, this intermediate range will occur in reality, due to the space requirements of multiple components in coordination with the size of the dome port. For example, the model shown in Fig. 4.32 exhibits a $d_{\text{cs}}/r_{\text{dpi}}$ ratio of 0.65.

Refraction Index Variation

The refraction index n_2 of the dome port and the water n_3 are individually varied in order to determine possible influences. The results are presented in the form of sections of the meaningful areas, see Figs. 4.12 and 4.13. Both the variation of n_2 and n_3 show hardly any effect on the refraction of θ_s to θ_r and the radiance ratio L_3/L_1 is influenced to a small extent, but the implications are practically negligible.

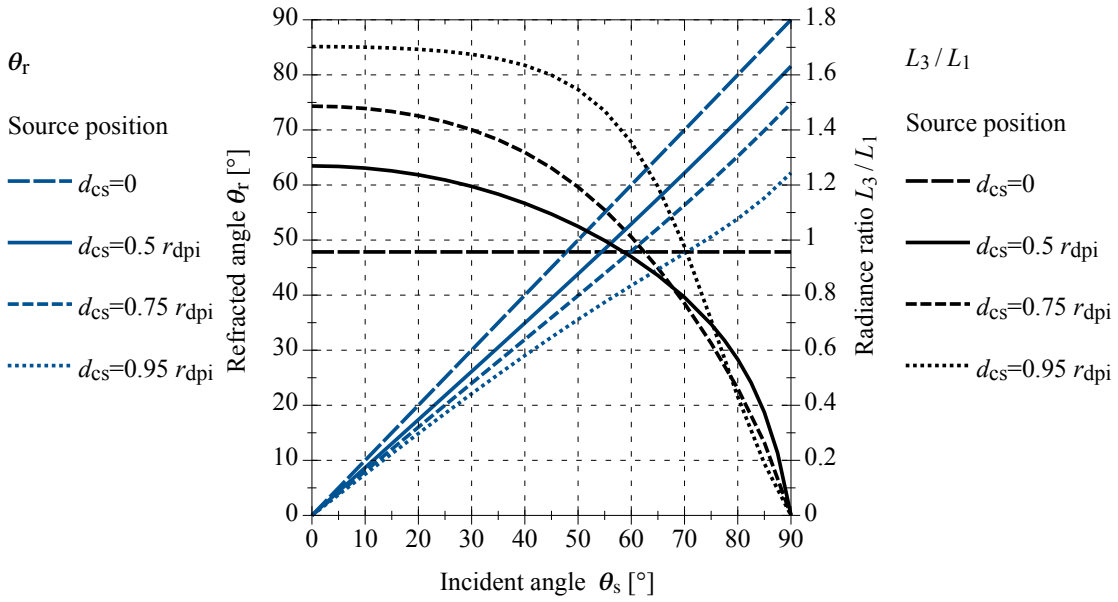

Figure 4.11: Calculated refraction and radiance ratio for a dome port. The source position is radially varied.

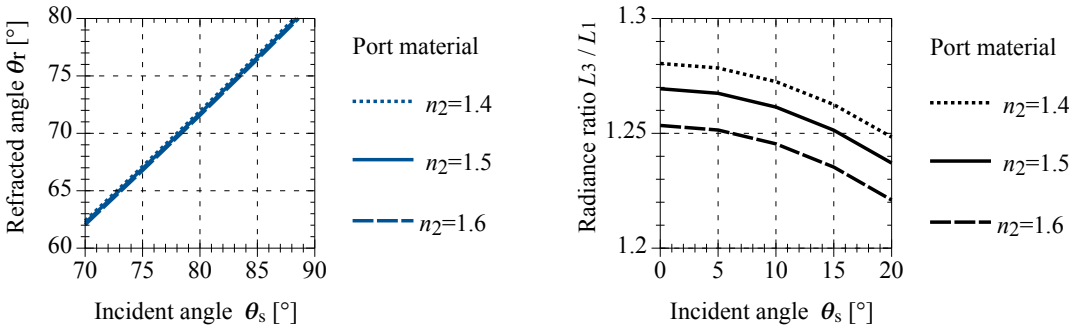

Figure 4.12: Calculated refraction and radiance ratio for a dome port. The refraction index of port material is varied.

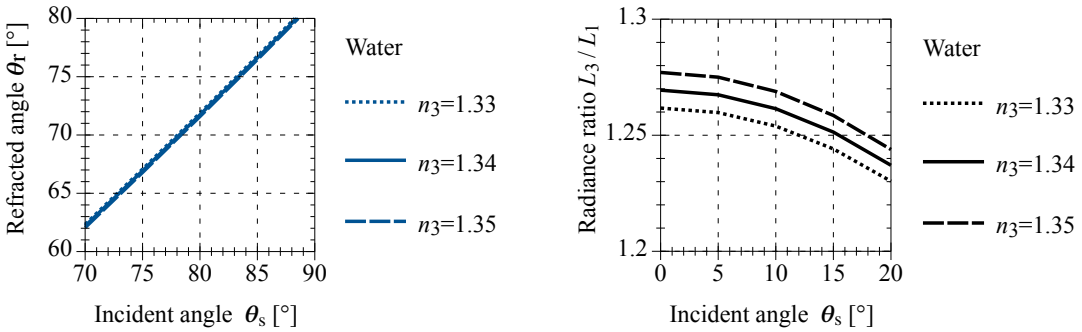

Figure 4.13: Calculated refraction and radiance ratio for a dome port. The refraction index of water is varied.

Dome Thickness Variation

The last parameter to be altered in this series of examinations is the dome port thickness t_{dp}. With a range from 1 - 20 mm, this should cover the values found in reality. For reference, a 100 mm glass dome port specified for a 8000 m depth has a wall thickness of only 7 mm. The results of the calculations are shown in Fig. 4.14. Again, only relatively minor effects are confirmed.

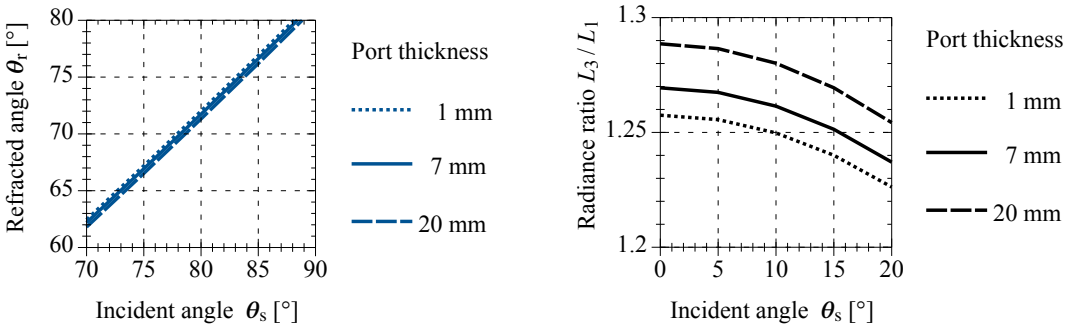

Figure 4.14: Calculated refraction and radiance ratio for a dome port. The port thickness is varied.

Brief Review of Receiver Side

A direction swap for the housing with a dome port to the receiver side configuration changes the direction, the order of the media, and the indices, but the principles stay the same. Figs. 4.15 and 4.16 show the light path for a centered and a radially moved punctual receiver. The ideal situation of a centered detector and incident rays in a perpendicular direction to the dome surface does not cause refraction, thus $\theta_{\mathrm{s}} = \theta_{\mathrm{r}}$. The parameters applied for calculations are the same as before, see Table 4.2. Of course the two media changes result in transmittance and reflectance values, which are apparently equal to the transmitter side, thus T_{13} of 95.7 % and R_{13} of 4.3 %. The same applies to the calculated constant radiance ratio L_3/L_1 of 0.957. The diagram of the transmitter side in Fig. 4.8 is therefore also valid for the receiver side.

Parameter variations at the receiver side are only done for the detector position, not for the refraction indices nor port thickness, due to minor effects only. For a simplified calculation the port is assumed to be thin, thus $\theta_2 = \theta_2'$. The detector position is radially varied, while the base parameters $(n_1, n_2, n_3, r_{\mathrm{dpi}})$ are kept constant. Calculations are made for center-to-receiver distances d_{cr} of 0, 25, 37.5 and 47.5 mm, according to relative values from the inner dome port radius r_{dpi} of 0, 0.5, 0.75, and 0.95. The results for the refracted angle θ_{r} and the radiance ratio L_3/L_1 as a function of the incident angle θ_{s} are presented in Fig. 4.17. The refraction of the incident angle θ_{s} develops relatively linear and gets stronger with increasing distance from the detector to the center. It acts more and more similar to a flat port, which would correspond to $d_{\mathrm{cr}} = r_{\mathrm{dpi}}$. The radiance ratio L_3/L_1 is clearly below 1 for incident angles less than 40°, and this means the incident rays are widened. An impression of this is given in Fig. 4.18.

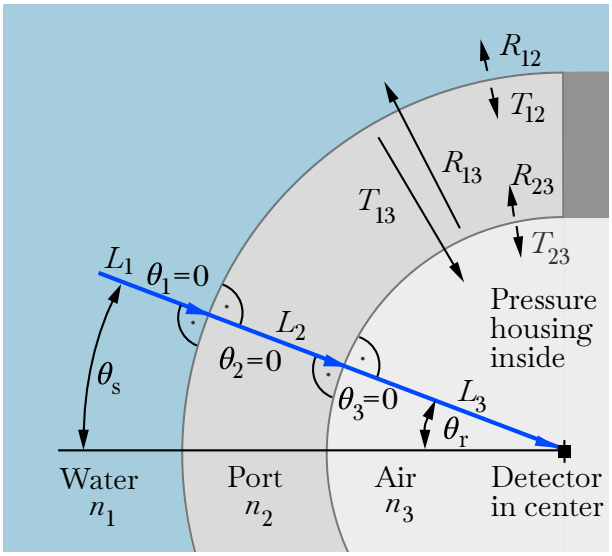

Figure 4.15: Underwater light path geometry of radial incident ray in a pressure housing including a dome port and a detector placed in center.

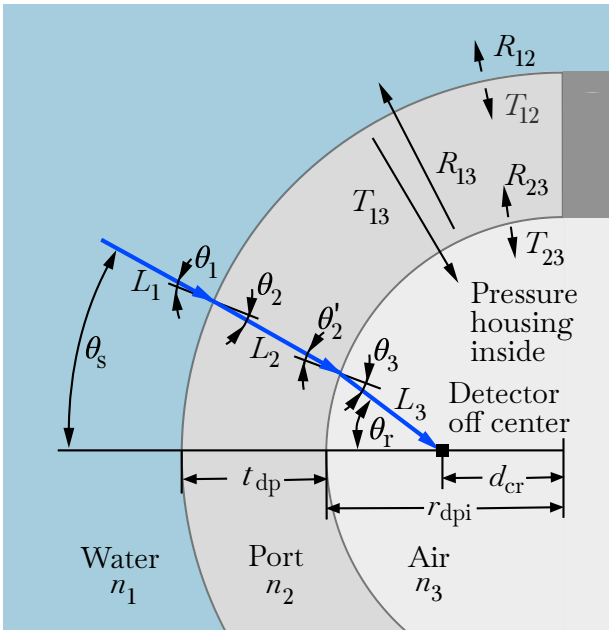

Figure 4.16: Underwater light path geometry of incident ray in a pressure housing including a dome port and a detector placed out of center on a half inner dome radius.

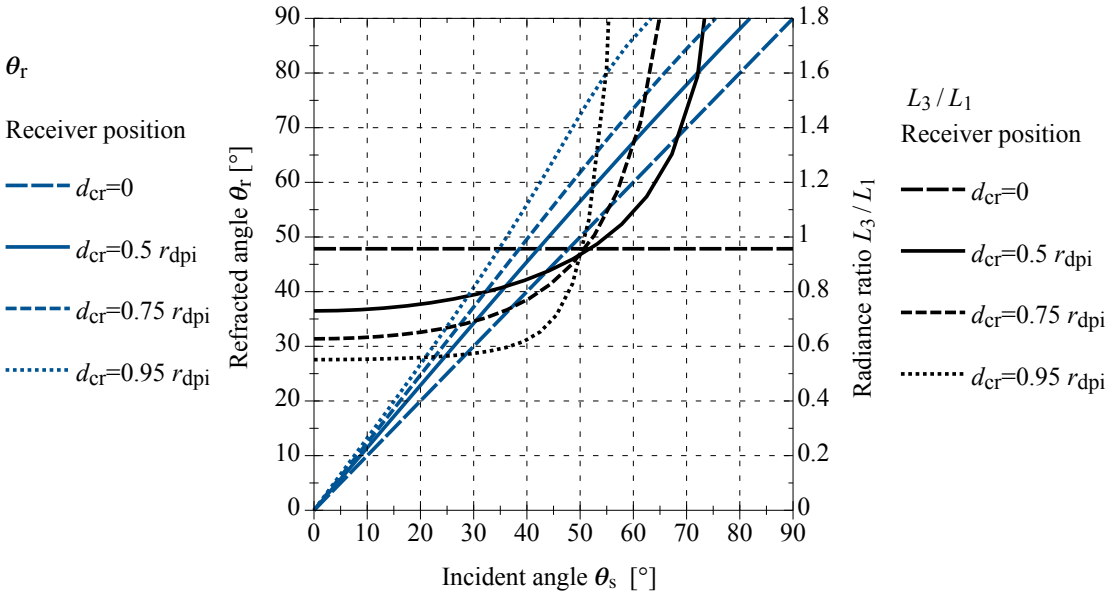

Figure 4.17: Calculated refraction and radiance ratio for a dome port. The receiver position is radially varied.

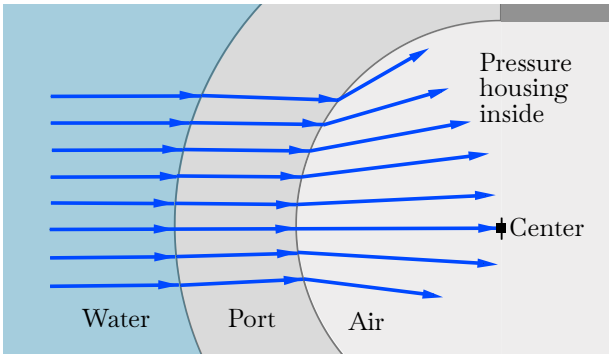

Figure 4.18: Incident rays trajectory for a dome port.

4.2.4 Transparent Embedding

Other than for flat and dome port variants with mathematically predictable relations, calculations are more difficult for pressure-neutral potted variants. Figure 4.19 depicts a typical layout as drawn in cross section, and Fig. 5.26 shows the original. Since the air medium is generally not involved in this design, strong refraction due to large differences in the indices are not expected. In general, these indices are $n = 1.34$ for water and $n = 1.4$ - 1.6 for the transparent material, depending on which is applied. These small medium changes not only limit the refractions, but also keep the reflectance small and the transmittance high. The absorption of synthetic potting materials may not be as low as from glass, but due to small layer thicknesses these are negligible. Flat, concave or convex surfaces can be produced, depending on the mold and process. The component sizes of LEDs and PDs in the millimeter range lead to a process on a relatively small scale. Undercuts and air bubbles can be problematic here, but vacuum processing can be helpful. Air inclusions are not only optically undesired, but pressure cycles in deep sea deployments can cause material stress due to compressibilty, which results in tearing and delamination. Properties like surface tension, shrinkage and viscosity are of major influence. The viscosity of typical optical potting compounds, such as resin-hardener mixtures of 500 to 3000 mPa·s, is roughly comparable to olive oil and fluid honey. The interaction of these properties with the small dimensions is much more appealing than it first appears. These interrelationships must be emphasized because they affect the near field of the LED source, just where the light field develops.

A general analysis such as a source in a housing including a port is not provided here. Pressure-neutral casted LEDs represent individual systems [38], and a reduction to a single point source within a layer is not very meaningful. On the other hand, the precise acquisition of the geometric relations, the corresponding modeling and the simulation require considerable effort. A certain general validity can probably be recognized after working through different variants.

Since the main objective is to determine the geometric intensity characteristics of the source under water, direct measurements represent an alternative here. Experiments in a test basin by means of a goniometer and appropriate underwater sensors are an effective way to achieve this. The influence of the potting can be determined by comparing underwater measurements with corresponding measurements made in air from potted and non-potted LEDs.

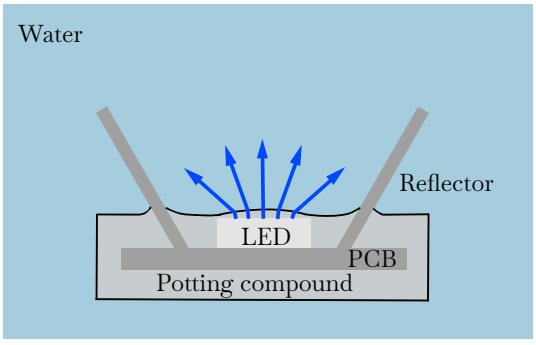

Figure 4.19: Cross section of a pressure-neutral potted LED transmitter.

4.3 Spatial Characteristics of LED Sources and Detectors

4.3.1 Radiation Pattern of LED Source

Sole LED and Secondary Optics

The market offers only a limited range of single-color high power LEDs, which can be designed as single or multiple die types. These are often embedded in some transparent silicon compound,

either with flat or convex formed surface, and types with mounted lenses as a primary optic are also common. The initial cosine-shaped angular intensity distribution of the bare die is, of course, influenced by this. However, only minor impacts can be identified on the basis of the curves from the data sheets of various manufacturers and types. Slight deformations of the cosine take place and the beam angle can also become somewhat smaller, but generally remain in the range of 100° to 120° FWHM. Depending on the application, these rather wide beam angles require reduction through secondary optics. Reflectors and lenses are commonly used to reshape the radiation pattern, and the available beam angles are in the order of approximately 15° to 90° FWHM. Lenses are made of glass or transparent synthetic material, and their fundamental principle is refraction. Reflectors can be produced of glass and metal, but more common usually are different kinds of plastics. The reflective coating required commonly consists of aluminum, but white surfaces are also used. These reflection properties are also subject to a certain wavelength dependence. For use in marine environments, an increased risk of corrosion must be taken into account. The achievable efficiency is generally quoted at 80 to 95%. The resulting characteristic of LED and secondary optic combinations can be very sensitive to mechanical dimensions such as mounting heights, but also to the employed LED type. Further information can be obtained from [198, 199].

Comparison with Generalized Lambertian Source

The radiant intensity of a generalized Lambertian source is described as [79]:

$$I_{\mathrm{e}}(\theta) = I_{\mathrm{e}}(0) \cdot \frac{m+1}{2} \cdot \cos(\theta)^m \tag{4.1}$$

with a mode number m, valid for a full beam angle β, given by:

$$m = \frac{1}{\log_2\left(\cos\left(\frac{\beta}{2}\right)\right)}. \tag{4.2}$$

If the normalized intensity is considered, then the shape is only determined by the term $\cos(\theta)^m$ with the mode number being the only parameter. This model, which is widely used in calculations and simulations, can represent characteristics of genuine sources quite well in some cases, but not in others. This statement is supported by experience gained through goniometer measurements of numerous LED and secondary optics combinations. Corresponding examples for an LZ4 LED in combination with different reflectors of one series are given in Figs: 4.20 and 4.21.

If the values of the measured curves are not directly applicable for calculations or simulations, then a mathematical approximation by a more advanced model is an appropiate solution [200, 201].

Source for Subsequent Analysis

In order to make examinations of the assemblies total characteristics as realistic as possible, an LED already used in the field for UOWC was selected as the reference source. The Ledengin LZ4 is a 10 W-class LED including a primary optic lens [63]. It is available as a non-converted direct color type in four wavelengths, with only the blue and green variants being meaningful choices. The green was preferred to the blue because it is more centrally located in the general transmission window of the water. The beam pattern is not narrowed any further by secondary optics for two reasons. The first is a narrower beam would provoke less refraction effects, which counteracts the objective of the investigations. The second is that the port close to any reflector could create interference and thus make subsequent calculations complicated. The full beam angle is approximatly 105° FWHM in air, the angular intensity curve in air is shown and is used as a reference in Figs. 4.25 to 4.28. There is a small untypical step with a certain recognition value

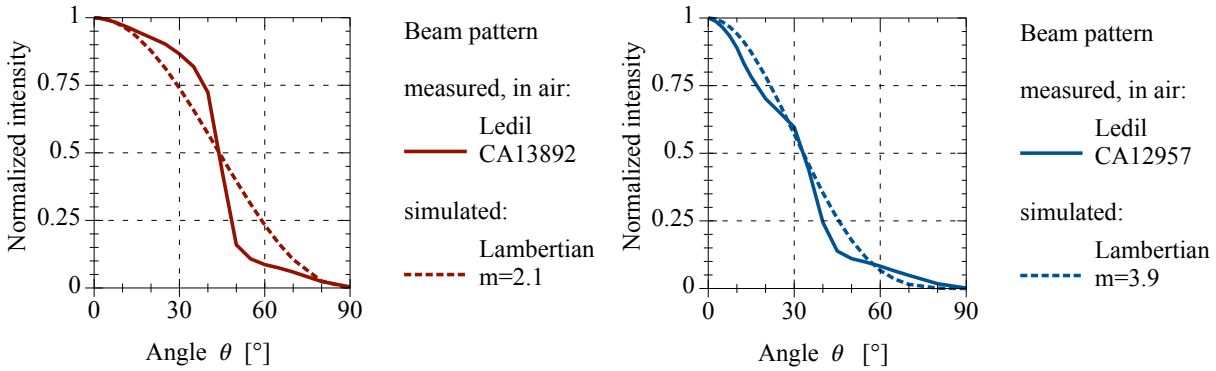

Figure 4.20: Measured and simulated beam patterns of an LED including an extrawide reflector on the left side, and including a wide reflector on the right side.

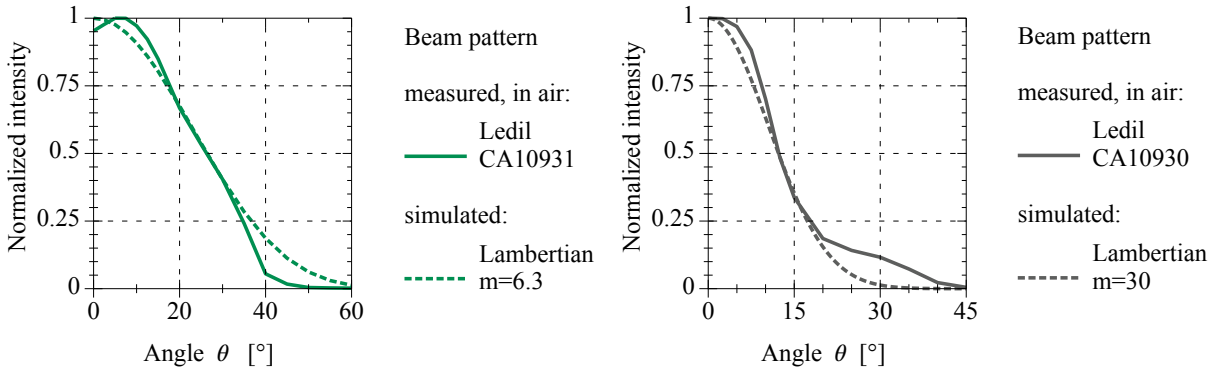

Figure 4.21: Measured and simulated beam patterns of an LED including a medium reflector on the left side, and including a narrow reflector on the right side.

in the curve at 45° to 50°. Crosschecks with other colors of the same LED series have confirmed this, as well as a ring appearing if the pattern is projected onto a wall. Measurements with other sensors and different shielding resolved this detail less. To minimize effects of variations within an LED series, all measurements were performed with selected LEDs. For wet operation the LED was pressure-neutral casted on an aluminum carrier plate, cf. Fig. 4.22. For operation in the housing the LED was mounted on a large massive heat sink, without housing the water acted as direct cooling for the pressure-neutral casted LED. The LED was driven with a precise constant current supply at a forward current of 400 mA. The voltage was monitored to detect potential drift.

Far-Field and Rotation

LEDs in the higher power classes are often built as arrays of single LED dies. These arrays require a certain area and thus no longer represent a point source, when viewed from close proximity. The far-field describes a distance from where the cluster can be modeled or measured as a point source again. This so-called far-field condition depends on radiation pattern, array geometry, and the number of LEDs and the primary optics [202, 203, 204]. For a 2x2 array of Lambertian radiation pattern LEDs this condition is fulfilled at 10 times the distance between the die centers. In case of a Ledengin LZ4 LED this yields 15 mm, but should the port be closer than this distance, calculations as a point source will be subject to error. Measurements of the angular intensity

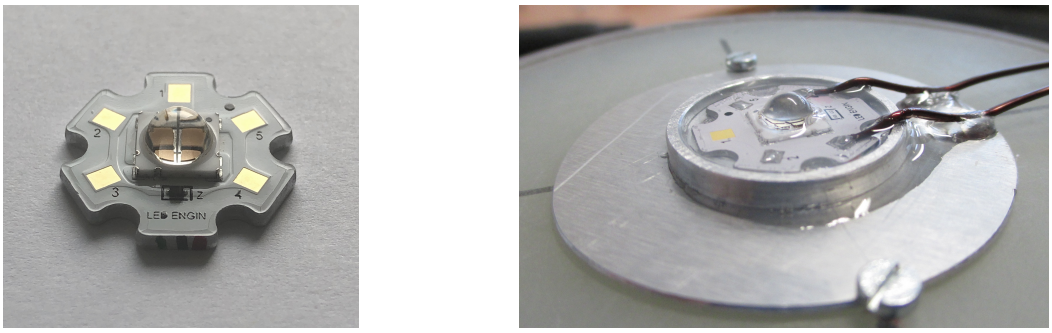

Figure 4.22: Ledengin LZ4 high power LED including primary optic lens, with a bare version shown on the left side, and a pressure-neutral potted version on an aluminum carrier plate on the right side.

distribution of an LZ4 LED at distances of 2.5 cm, 5 cm and 25 cm did not show any significant differences. The same applies to measurements at different rotation angles at 5 cm distance. After placing an additional reflector on the LED and repeating the measurements of the angular intensity distribution at the three distances, clear differences became apparent. The beginning of the far field has clearly shifted to larger distances.

4.3.2 Angular Sensitivity of Photodetector

In UOWC, large-area photodetectors in planar design are employed in most cases, therefore the angular sensitivity is basically following the cosine function. The semiconductor material is generally packaged in ceramic or molded plastic housings or metal cans. The active surface of the chip can be protected by glass windows or by lenses, but also by transparent compounds such as optical silicone or epoxy. These features have a certain influence of the optical path through refraction and masking. Despite this, there are angular sensitivity or responsivity curves missing in many PDs datasheets, it seems to be left up to the user whether to roughly assume the cosine function or to perform sophisticated measurements. Similar to the optical path of the LED, further optical elements are also added to that of the PD. Mostly these are filters, but also include blinds or lenses. When assembling or mounting these optical receiver units, it is essential to keep the number of media transitions low and to avoid large refractive index changes. If the properties of the individual components are known, the resulting characteristic can be calculated, otherwise only the measurement are possible.

4.4 Total Characteristics of Assembly

In the previous sections the ports and the light path in general, as well as the source properties, are described individually, and these are now combined in an UOWC-adequate assembly. The aim is to present the characteristics of common combinations and to identify the agreement between measurements and calculations. For this purpose, the same pressure-neutral casted LED as shown in Fig. 4.22 was used in housings with different ports and in varying positions, and was measured in the underwater operation, as illustrated in Fig. 4.23.

4.4.1 Underwater Measurement Setup

To determine the resulting characteristics of the complete assembly in the intended medium, a specialized setup is needed, such as an underwater goniometer setup, see Fig. 4.24. Within a fixed structure, the assembly to be examined is rotated underwater and the angle-dependent intensity is recorded. In this experiment, measurements were carried out exclusively for the transmitter

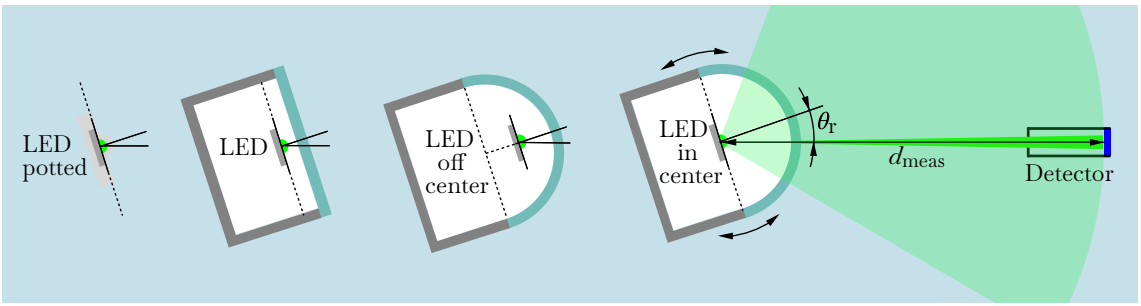

Figure 4.23: Transmitter assemblies in different configurations for underwater goniometer measurements.

side. An indoor basin was used, with a volume of about 2 cubic meters of filtered fresh water, the corresponding refraction index thus results in $n = 1.333$. To avoid reflections from the sides of the basin, the sand covered bottom and the water surface, a geometry including a central position and a relative short measuring distance of $d_{meas} = 267$ mm was selected. This distance was kept the same for all configurations, and it was defined to be between the LED die and the surface of the sensor. A description of the sensor is given in Section 5.3.2. For the intended measurements this irradiance sensor, which features a large FOV, needed to be reconfigured to a radiance sensor. This can be done by adapting a tube with an entrance hole including light baffles. The principal design is described in [87]. The employed tube had a length of 100 mm and an entrance hole of 11.5 mm, with a resulting solid angle of approximately 0.01 sr. Of course the former irradiance calibration is no longer valid, and it now represents an uncalibrated directional radiance sensor. However, the valuable property of linearity over many decades remains, so precise ratio measurements will still be possible. Due to the strong directionality, the sensor is highly robust against interfering light. The room lighting, for example, was only able to cause minimal disturbances. To achieve the resulting angular characteristic of the transmitter assembly it must be rotated. The pivot point for all housing configurations was the LED die, see Fig. 4.23. The whole assembly was rotated in steps up to 90° degree on both sides, while the intensity was recorded. The measuring distance from LED to sensor was kept constant, but the path length through the water was varied by the port configuration. The shortest distance was the dome port and source in the center, the longest was the pressure-neutral potted version. The attenuation coefficient of the basin water could only be estimated, since no measurements were available. It was assumed to be low, maybe not the same as pure water, but a value of $c = 0.15$ 1/m should roughly fit for the used wavelength. The resulting attenuations showed only minor differences of less than 1 %, thus the occurring effect could be neglected.

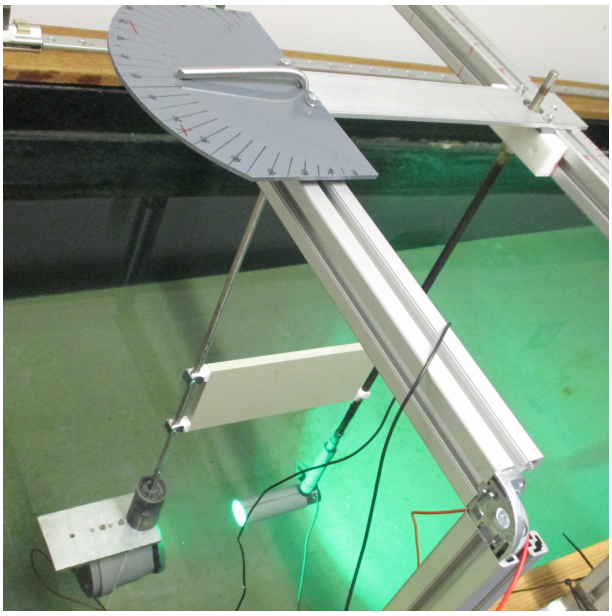

Figure 4.24: Underwater goniometer setup in the test basin.

4.4.2 Comparison of Measurements and Calculations for Transmitter Side

To ensure the measurements of the different configurations remained as comparable as possible, the conditions must be kept the same. This primarily concerns the source, the mechanical setup, the measuring equipment used and the media. The corresponding common parameters are given in Table 4.3.

Table 4.3: Devices and general parameters used for measurements and calculations.

LED Source		Ledengin LZ4	
Wavelength, center	λ	525	[nm]
Detector		Gigahertz Optic RW3703WQ	
Meter		Gigahertz Optic P9710-4	
Distance	d_{meas}	267	[mm]
Refraction index, air	n_1	1.0	
Refraction index, water	n_3	1.333	

Angular Distribution of LED Source and Flat Port

The diagram in Fig. 4.25 shows the normalized intensity as a function of the resulting angle θ_{r} of the transmitter assembly, and the curves from measured values for the flat port configuration in air and underwater. The measured curve of the source without any port in air is also given as reference. Furthermore, the calculated graph for the underwater case is shown for comparison, and the applied equations are described in Appendix C.7. Additional configuration-related parameters can be extracted from Table 4.4.

The measured curve and the calculated curve of the flat port underwater show a reasonably good agreement. Any inaccuracies in the distance d_{sp} and the port n_2 value can be ruled out as the cause of deviations, as these have no effect. The water n_3 value changes within a realistic range and would have hardly any effect, however imprecise angle adjustments and minor measuring distance variations on the goniometer would be possible.

Table 4.4: Flat port parameters.

Manufacturer, spec.		unkown	
Refraction index, supposed	n_2	1.475	
Thickness, flat port	t_{fp}	9	[mm]
Distance, source to port	d_{sp}	15	[mm]

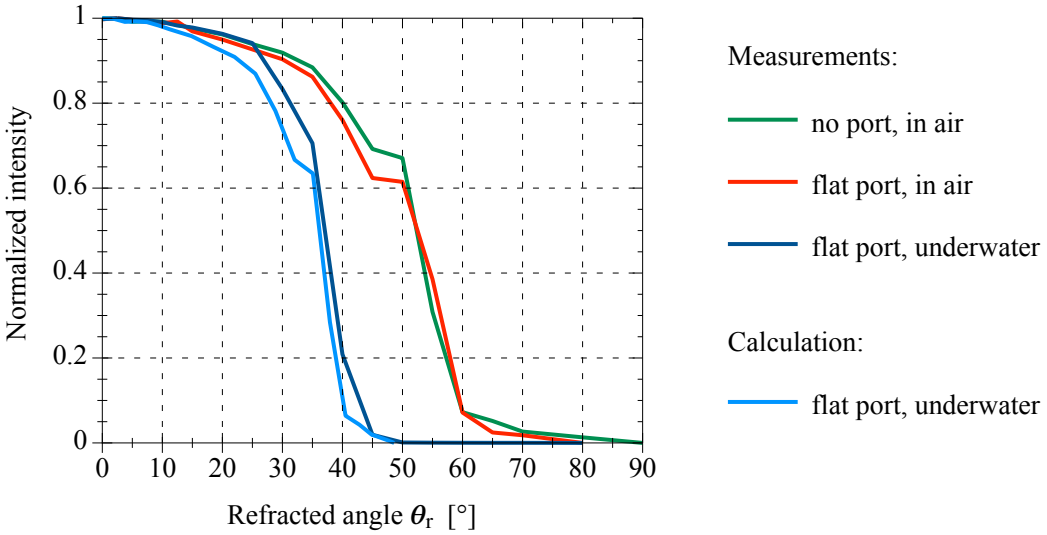

Figure 4.25: Measurements of an LED source with and without flat port, in air and underwater, and a calculated curve for flat port underwater configuration is added for comparison.

Angular Distribution of LED Source and Dome Port

The diagrams in Figs. 4.26 and 4.27 give the normalized intensity as a function of the resulting angle θ_r of the transmitter assembly, as curves from measured values for the dome port configuration in air and underwater, and in each case for two source positions, one at the center as well as one at the half inner dome radius. The measured curve of the source without any port in air is also presented for reference. Furthermore, the calculated graphs for the underwater case are shown for comparison, and the applied equations are described in Appendix C.8. Additional configuration-related parameters can be gathered from Table 4.5. The measured curve and the calculated curve of the dome port underwater for a centered source are almost identical, as well as the curves in air.

The measured curve and the calculated curve of the dome port underwater including the source positioned on the half inner radius are relatively close to each other. Inaccuracies of the three refraction indices and the port thickness only exhibit minor effects. The most probable cause of the deviations is the inaccurate setting of the distance dome center to the source d_{cs}. Imprecise angle adjustments and minor measuring distance variations on the goniometer can also not be excluded.

Table 4.5: Dome port parameters.

Manufacturer, spec.		Vitrovex, 8000m	
Glass, type		Borosilicate 3.3	
Refraction index, 525 nm	n_2	1.475	
Thickness, dome port	t_{dp}	7	[mm]
Radius, inner	r_{dpi}	50	[mm]
Distances, center to source	d_{cs}	0, 25	[mm]

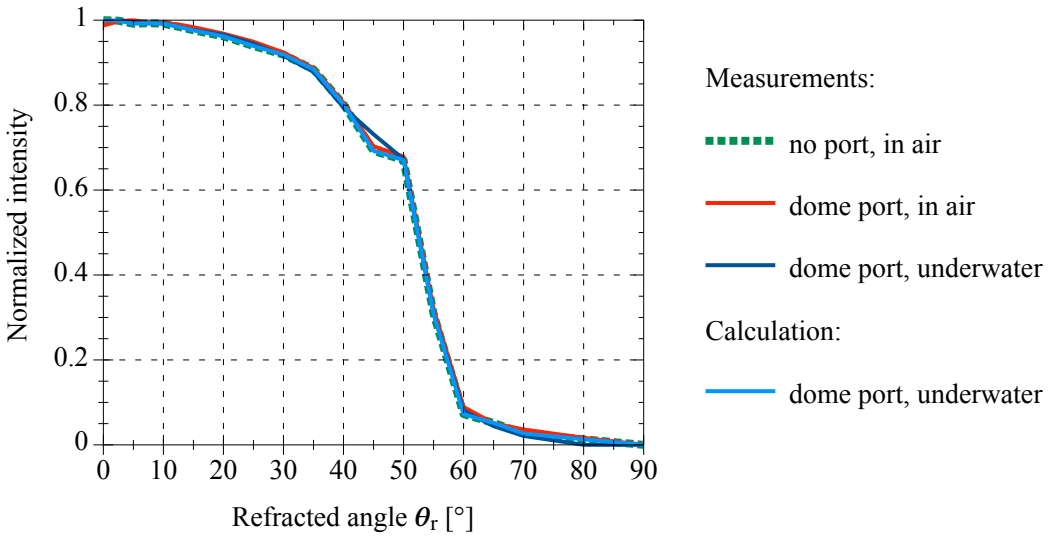

Figure 4.26: Measurements of a centered LED source, with and without a dome port, in air and underwater, and a calculated curve for dome port underwater configuration is added for comparison.

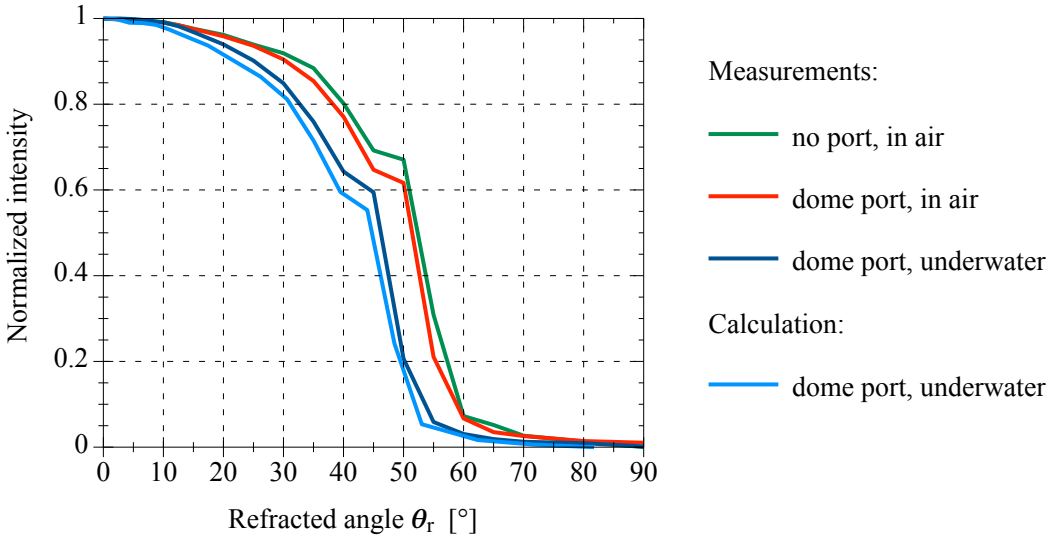

Figure 4.27: Measurements of an LED source positioned on the half radius off center, with and without a dome port, in air and underwater, and a calculated curve for dome port underwater configuration is added for comparison.

Angular Distribution of LED Source in Pressure-Neutral Cast

The diagrams in Figs. 4.28 and 4.29 give the normalized intensity as a function of the resulting angle θ_r of the transmitter assembly, as curves from measured values for the pressure-neutral casted configuration with and without the reflector, and also in air and underwater. The measured curves of the unpotted source in air with and without reflector are also presented for reference. Calculated curves for comparison are omitted. Additional configuration-related parameters can be gathered from Table 4.6.

Since a comparison of measured and calculated curves of the pressure-neutral casted versions underwater is not possible, at least it is possible to compare the curves in air. In order to demonstrate the influence of the potting, in addition to the bare LED equipped transmitter measurements, some experiments were also carried out for a variant equipped with a reflector. A slight influence of the casting can be seen, and it is more pronounced in the bare LED version than in the reflector-equipped version. Based on the experience gained from the measurements of many other potted LED-reflector combinations, these two examples can be considered typical.

Table 4.6: Pressure-neutral cast parameters.

Manufacturer, type		Intercol 5435	
Material		Polyurethane	
Refraction index	n	1.48	
Thickness, estim.	t_{pnc}	1	[mm]

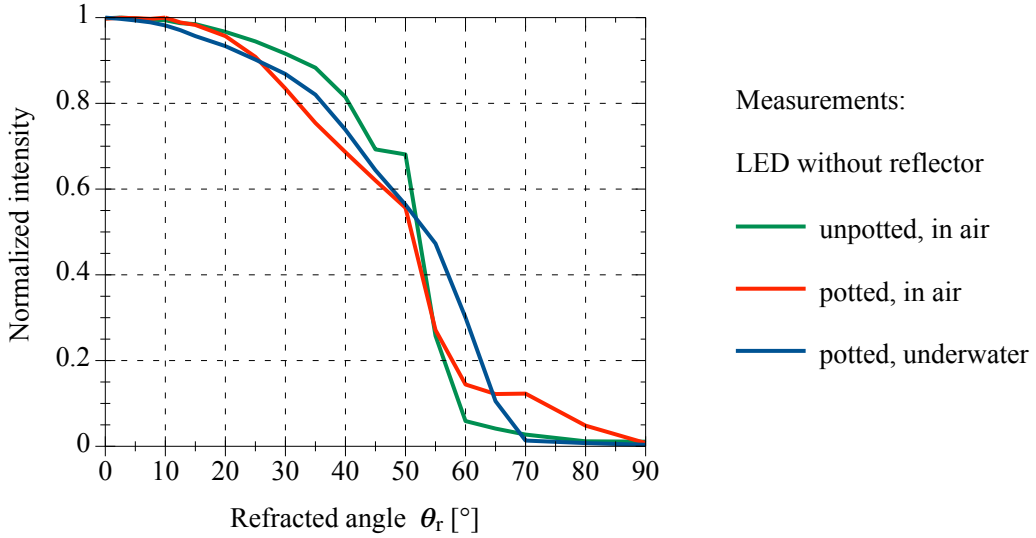

Figure 4.28: Measurements of a bare LED, with and without pressure-neutral cast, and in air and underwater.

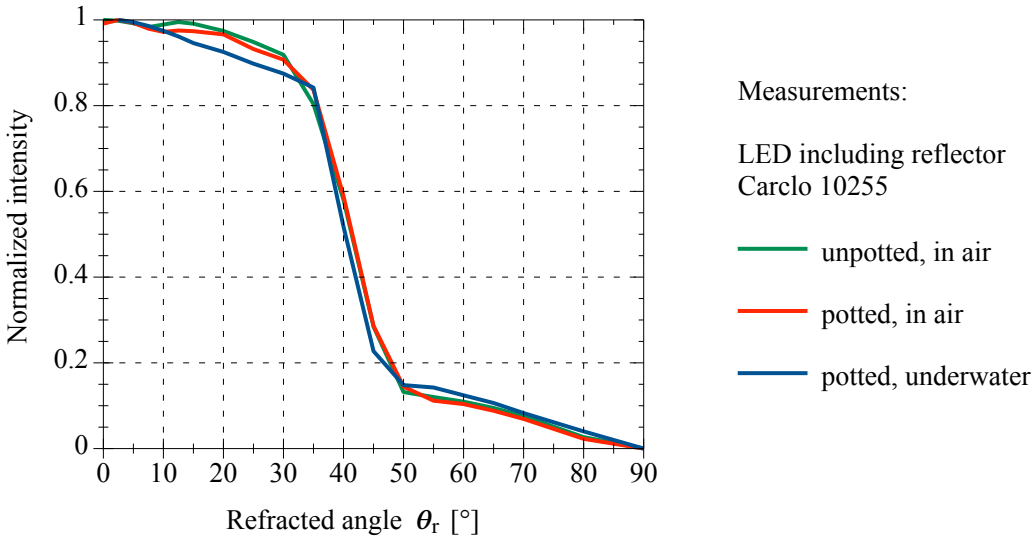

Figure 4.29: Measurements of an LED including reflector, with and without pressure-neutral cast, and in air and underwater.

Intensity Ratios of the Examined Combinations

The source radiance L_1 and the transmitted radiance L_3 of the port equipped housings are located in different media, in air and in water. Therefore absolute measurements would need differently calibrated sensors. As these were not available, and only an uncalibrated sensor modified for radiance could be applied, it was necessary to switch to the use of ratios. The measurements for the flat port, the dome port with source at half inner radius, and the pressure-neutral potted version were normalized to the measurement for the centered dome port configuration. The reasons for this are the ideal properties without angular refraction and a constant magnitude of reflection. For comparison, the relative transmitted radiances for the port versions were also calculated, based on the relative angular intensity distribution of the LED in air and the parameters previously used. Due to the magnification effect of the flat port and the dome port with a non-centered source, a calculation of the apparent shift of the source position is needed, cf. Appendices C.7 and C.8. This shift and the measuring distance provide the correction factor via the inverse square law. The calculated radiance values are also subject to normalization to values from the centered dome port configuration. The curves in Fig. 4.30 depict the radiance ratios as a function of the resulting angle θ_r from transmitter assemblies in different versions for underwater operation. Measured ratios are compared to calculated ratios in the meaningful range of θ_r from 0° to 25°. The measured and calculated curves have the expected order of magnitude and show reasonable agreement. The cause for the deviations are probably related to uncertainties in the setting of the distances, mainly the source to port positioning and the distance from the source to the detector. As with the previous measurements in this section, impacts of angular inaccuracies and incorrect refraction indices are estimated to be minor. Non-linearity of the sensor and supply or temperature-related drift effects of the LED should be negligible.

Due to the high relevance of the dome port and the good transferability for many practical applications, a set of curves for radially varied source positions from the center to near the dome inner surface is given in Fig. 4.31. The respective calculations are based on same source and dome port parameters as used previously, including an LED Ledengin LZ4 without reflector and values given in Table 4.5. The curves are normalized to the initial radiance of the LED at 0°. It is clearly visible that the LED pattern becomes narrower and the intensity increases with growing distance of the source from the center. The characteristic changes from the ideal dome port to the flat

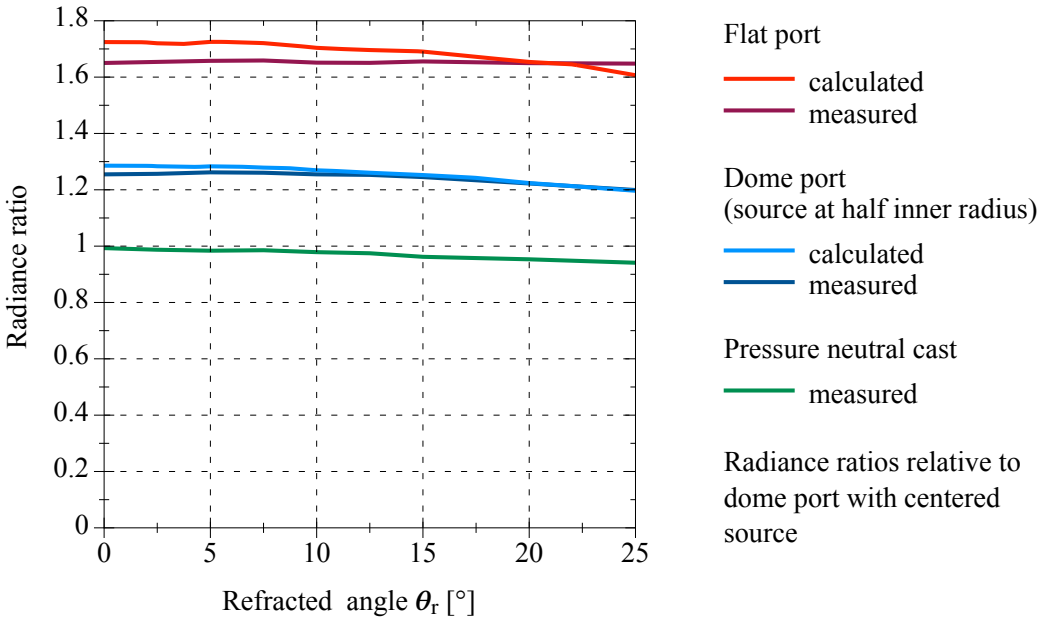

Figure 4.30: Radiance rations of transmitter assemblies in different configurations, including measured and calculated curves.

port.

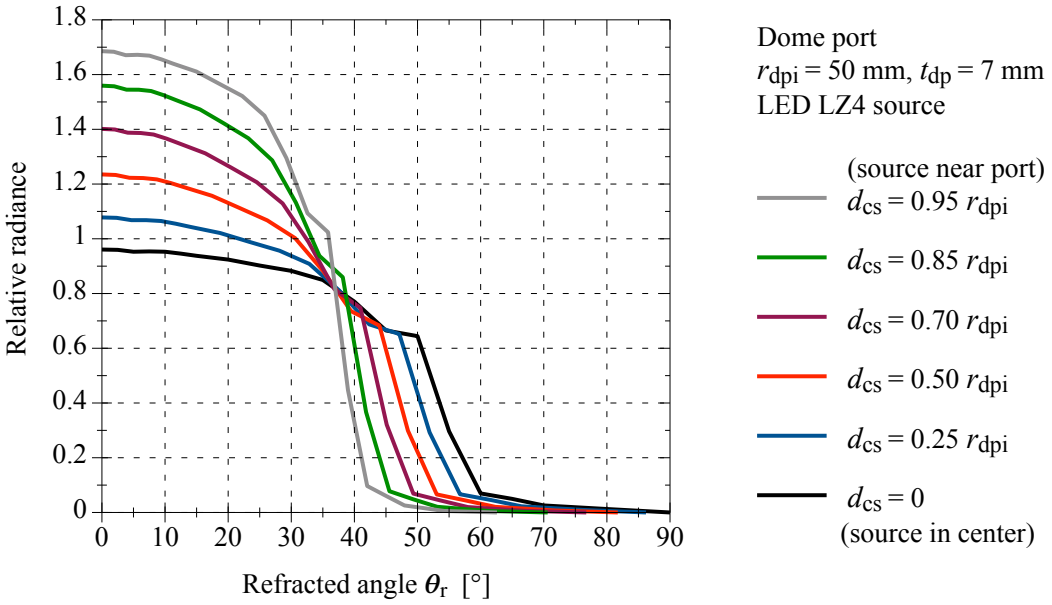

Figure 4.31: Calculated angular radiance progression, for an LED source in dome port configuration underwater, with the source position varied from the center to the near port inner surface.

4.4.3 Implications for Measurements, Design and Implementation

Improvement Proposals for Measurements

The conducted experiments have shown good agreement to the calculations. However, certain simplifications were not applied, such as the thin port assumption, omitting the shift to an apparent position, and the use of general refraction indices. Conversely, this means that the parameters must be known and the principles must be applied in-depth. Accurately acquiring dimensions and properties such as near field characteristic can be associated with difficulties. Therefore, measurements are an essential element in addition to calculations.

Based on the experience gained, a number of improvements can be derived. This includes an overall higher precision of the goniometer setup, exact rotational adjustability, and correct distance settings and rigid carriers. Since rotational symmetry cannot always be assumed, an axial rotatability of the assembly under test is essential for three-dimensional measurements to determine the transition zones in multiple segmented setups. Furthermore, access to calibrated sensors for absolute measurements in air and underwater would be desirable. To extend the capabilities of the measurements to receiver assemblies, an underwater reference light source is necessary. In addition, a large-dimensioned basin is desirable to provide increased measurement depths and distances, including water parameter control.

Considerations for Assembly Design

Underwater housings for optical applications are subject to many selection criteria as given in Section 4.1.1, and one of the major criteria is the optical usable field, which depends on the intended application. In the case of UOWC, we find a certain beam angle on the transmitter side and a certain FOV on the receiver side, and both conically shaped as solid angles. The required size of these angles can be derived from underwater operation scenarios. Besides the direction, the communication distance and the water properties are also of significance. Since vehicles are involved in most scenarios, as presented in Fig. 1.1, there are constraints associated with this. These include: minimum distances to avoid collision damage or getting caught, minimum speeds for non-hovering vehicles, and positioning accuracy. The UOWC technique, mounted on fixed structures, mainly represents only one side of the communication partner. From the above section, it can be concluded that narrow angles, or rather solid angles, which can be related to pointing and tracking problems, should only rarely be used. Wider (solid) angles, starting from a few tens of degrees up to hemispheres or spheres, are required for many applications. This indicates that the flat port is suitable for fewer applications compared to the dome port. The ideal properties of the dome port are increasingly lost as the size of the optical and electronic components grows. The pressure-neutral cast offers many possibilities in optical aspects, but has limitations in other areas.

Finally, the housing including the optical port or alternatively any potted form that are merged with the LED, or respectively the PD, are combined with additional optical elements in an assembly resulting in its own characteristics. Therefore, not only the initial properties of the LED and PD are important, but also those of the components in the optical path. These filters and concentrators of various kinds and numbers may generate additional media transitions. Large changes in the refractive index should be avoided, as these can lead to total reflection depending on the direction. A glass-air transition, as with a flat port in front of a PD for example, can result in a total reflection at an incident angle of 45°. Special angular characteristics of filters in terms of the AOI, of reflectors in terms of the near-field, and of lenses for receivers in terms of wandering focal points also need to be considered. General information and new approaches for concentrators concepts are given in [79, 205, 206, 207], and the filters are discussed in Section 3.2. In addition to the constraints with respect to shape and volume of single-color LEDs, concentrators, large-area photodetectors and optical bandpass filters, there is another aspect of a general

nature, the selection is compromised by a limited product range in these segments.

Implementation of Multiple Segmented Transducers

Based on a general need for large solid angles, this requirement can be roughly divided into two categories. The first is a hemispherical space in the UOWC zone, as with ships and buoys directed downwards from the surface, and complementary for landers and crawlers directed upwards from the seafloor. The second is an in total spherical characteristic in the case of AUVs and nodes in the middle of the water column. At the same time, there are limitations on both the transmitter and the receiver sides. There are power constraints regarding the LED transmitter due to the tight energy budget of battery powered systems such as AUVs, which are directly linked to the crucial operating duration. Photodetectors used on the receiver side require ambient light suppression filters, these can have large influence on the field of view. In summary, it leads to the division into a number of segments that individually yield restrictions and in total meet the demand. Implementation of the UOWC transmitter into or as a sphere is possible in principle, but has disadvantages in the field such as partial blocking by the vehicles hull or shadowing of fins or antennas. Furthermore, a raised mounted or towed UOWC device would be exposed to a greater risk of collision during operation and would be impractical for deployment and recovery. A solution for this is splitting the system into front-rear, upper-lower, or left-right units.

The simultaneous use of separate neighboring sectors enables the possibility of applying MIMO technology or one of the sub-types, see Section 2.1.6. Creating multiple channels also requires more hardware, thus more volume is needed, and an installation in or near the sweet spot of the dome port is becoming increasingly difficult. Energetically, the main advantage is that unused transmitting sectors can be switched off. In the composition of a defined sphere segment from several solid angles, gaps or minima are formed. For example, to achieve a relatively uniform hemispherical characteristic by combining a number of conical sectors, whether from transmitting elements bounded by the beam angle, or from receiving elements bounded by the FOV, distinct overlapping zones would be created automatically. An example: to form a hemispherical coverage from solid angles of 0.842 sr each, which corresponds to 60°, including an overlap of 30 % results in 10 elements.

Factually, this leads to dome ports with a diameter in the order of 100 mm. An own transducer model and a transmitter head are shown in Fig. 4.32. Commercial products, although rare, exhibit the same form factor, see Table 1.2. Of course, this topic can also be found in the literature; one of the first implementations including a hemisperical LED emitter and PMT is described by Farr et al. [157]. Baiden introduced an omni-directional optical transmitter in [208]. An UOWC circular transceiver and a node concept are shown in [40]. Simpson et al. demonstrated segmented smart UOWC transmitters and receivers in [30]. An FSO receiver with overlapping FOV is discussed in [209], and a hemisperical freeform lens for UOWC is proposed in [210].

Figure 4.32: Left: Model of transducer utilizing a 100 mm dome port and comprising 9 pcs. large area PD and 9 LED elements. Right: Pressure-neutral potted transmitter head of 95 mm diameter, including 4 segments of each 4 power LEDs and driver circuits.

4.5 Chapter Summary

In this chapter, assemblies for UOWC have been examined in terms of their optical properties. The main concepts behind housings as indispensable components have been presented, including general selection criteria. Related heat and integration issues have been indicated. The optical window is an integral part of the housing, and in most cases so-called flat ports or dome ports are applied. The material of these ports is typically glass or synthetics, which leads to refraction indices of 1.4 to 1.6, thus significantly different than the indices of 1.0 for air and 1.34 for water. Independent of source or receiver side, light rays have to pass at least two media boundaries, which results in refraction. Snell's law must be applied here, and the Fresnel's equations for transmittance and reflectance. To express the direction and the amount of light, the radiance concept is utilized, including the 'n^2 law for radiance'. Calculations in this respect have been executed for flat and dome ports, both for the transmitter and the receiver sides. The flat and the dome ports exhibit significantly different characteristics, and variations of the refraction indices and the port thickness show only minor effects. The position of a source or detector within the dome port plays a crucial role. Placement in the center, in the so-called 'sweet spot', leads to an almost ideal neutral behavior. Radial displacement towards the dome inner surface results in a transition to flat port characteristics.

Transparent embedded components can represent an alternative to the common pressure housing and port combinations. This special design has advantages and disadvantages, but allows for a variety of makes, so it is difficult to generalize.

The total characteristic of real assemblies has also been examined. For this purpose, goniometric measurements in a test basin were executed. The same power LED including a primary optic was operated in a flat port housing, in a dome port housing at different positions, and as a potted device. The measured angular distributions of these cases, each underwater and in air, were compared to calculations. For the dome and flat ports the outcomes were as expected and showed good agreement. For the casted LED, with and without a reflector, it was seen that the cast caused only minor changes. The difference between measured and calculated radiance ratios are small.

Concerning the assembly design in the UOWC, the following can be extracted: in most cases a hemispherical characteristic is favored, but the attainable beam angels or FOVs of single elements

are rather limited. Taking into account energy aspects and the potential to use MIMO technology, this most likely leads to multiple segmented transducers, either in a dome port pressure housing or a pressure-neutral potted device.

Chapter 5

Underwater Lightfield Simulation

5.1 Monte Carlo Simulation

Monte Carlo techniques are nowadays applied to solve a wide range of problems in many areas of science, besides engineering, physics and computer graphics, also for example in biology and economics. Monte Carlo (MC) methods are computational algorithms that are based on probability and statistics, and numerical results are generated by repeated random sampling. These methods are often used when other approaches are too difficult or are not applicable. This is the case for the light propagation underwater, which is generally described by the radiative transfer equation (RTE) [87]. This is a mathematically challenging equation in an integro-differential form with several variables [101]. The commercial Hydrolight software uses a simplified scalar version of the RTE for calculation of radiance distributions in optical oceanography. There are also other approaches to solve the RTE [211] for UOWC purposes. A comparison of commonly employed numerical solutions in this area is given in [101]. Nevertheless, performing MC simulations is the more popular way to study the underwater optical channel [21]. They offer the possibility to influence the system design by predicting the system performance instead of executing costly and time consuming field tests.

5.1.1 MC Software Solutions

Monte Carlo software adressing the light propagation in media mainly derive from the area of modeling laser based light transport in tissue for medical applications of the nineties [212, 213]. In the past decades, a large number of software solutions following the Monte Carlo approach for photon movement in media have certainly been developed, but most of them are probably not accessible to the public. Since the focus is on the application and not on the development of suitable software, some known solutions are presented briefly in the following section.

PyTissueOptics offers a simple open source Python code for MC tissue optics simulations [214]. This software is intended for education, prototyping and small calculations. The code only implements the basic principles and offers only a limited scope of functions. Furthermore, it is described as slow. To make it usable for sophisticated simulations on a larger scale, a considerable programming effort is required.

PyXOpto is a collection of open source Python tools for performing MC simulations of light propagation in turbid media [215]. It offers a large function range and fast parallel computing, if appropriate devices are available. Simulations are built on programming sequences of function calls. There is no graphical user interface (GUI) implemented nor advanced file handling and data evaluation, as would be helpful for more extensive simulation projects.

Photonator is an open source project, developed for research on underwater optical communication [216]. It is based on Matlab and C and was neither maintained nor further developed over the last decade. The software is tailored to the requirements of the author. Due to these facts, certain necessary adjustments and extensions might be difficult. Matlab licenses and in-depth knowledge are also required.

Montcarl is a very comprehensive program package for MC light scattering simulation, and was originated for the medical research [217]. This package features a GUI for Windows computers,

without requiring special hardware nor programming language skills. It is freely available for usage within the scientific community. This software has been developed and is field proven over a long period of time and continues to be maintained. Furthermore, detailed documentation and the support of the author F. F. M. DeMul is available.

Overall, currently the most promising approach to realize the planned extensive series of simulations is the usage of the Montcarl package. Since it originates from the medical-physical and not the oceanographic field, there are naturally certain hurdles for its use in the underwater environment. There are some adaptions to the dimensions as well as water specific functions required. These necessary changes and extensions were submitted to the author and discussed, and implementation took place in subsequent versions. This creates the prerequisites for an uncomplicated and efficient realization of the simulation tasks for UOWC.

5.1.2 Simulation Assumptions and Adopting the Underwater Environment

A short description of the mechanics underlying the MC simulation in UOWC include: light is treated as an amount of virtual photons, a specific number of photons are generated by a source and are characteristically distributed, and on their way through the water medium they are scattered and absorbed so that only a certain portion reaches the receiver. In Fig. 5.1, the environment as well as the source and receiver setup are shown. In the preparation of the functional description

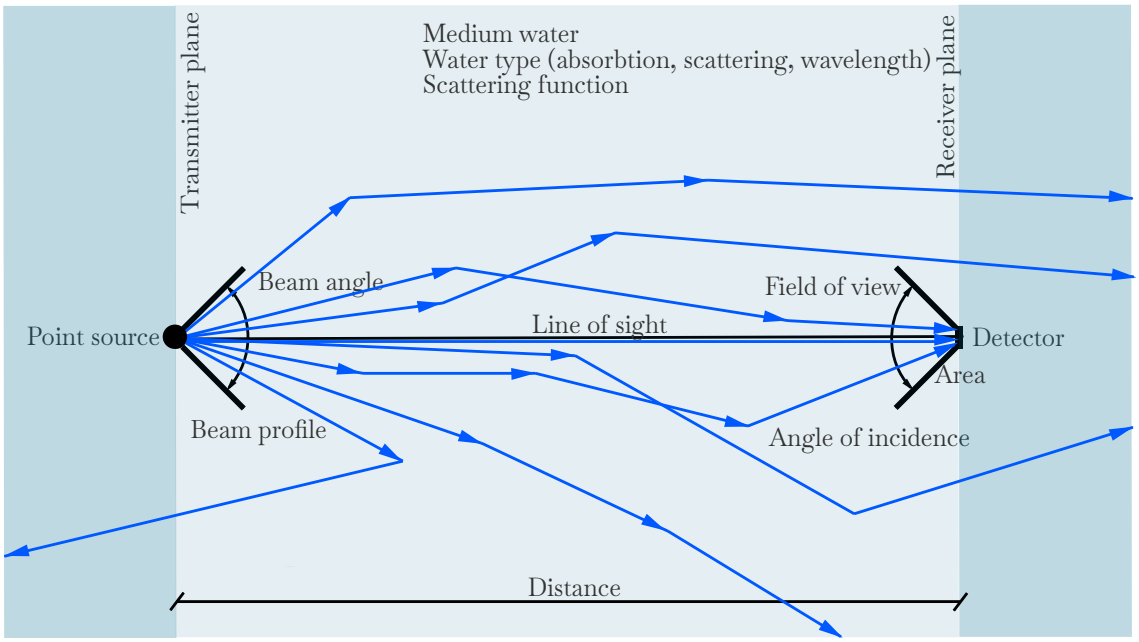

Figure 5.1: Two-dimensional overview of the underwater setup for MC simulations. The blue arrows symbolize photon paths.

and the execution of the MC simulations, some assumptions must be made and preconditions must be presented. The following list gives the individual items including a brief explanation:

- Mid water depths, far away from surface and seafloor, therefore there are no reflections.
- A homogeneous medium, with uniform absorption and scattering in the volume of the water column.
- Water parameters given as wavelength-dependent absorption and scattering values, originated from Jerlov water types.
- Scattering properties of water following the Fournier-Forand model by default.

- Only elastic scattering, and only with a shift in the direction, not in the wavelength (Raman).
- A constant refraction index of the medium, and no turbulence.
- No ambient light.
- No blocking objects.
- Termination of photons behind the transmitter and receiver plane.
- The source and receiver are centrally aligned, without inclination, and a certain distance from each other.
- Ports are not considered, thus without refraction or loss from flat or dome ports.
- The point source, defined by the beam angle and the beam pattern, is isotropic (rectangular pattern) by default.
- The detector is of planar type, defined by the area and the field of view, which is hemispherical by default.
- The number of generated photons, chosen to be close to the software's upper limit, for best possible average values.
- The detector area is adapted for the amount of received photons, for obtain good statistics and small geometric errors.
- The number of repetition runs, to be increased in inefficient cases, within reasonable computational runtimes.
- Only single wavelength validity per simulation run, thus spectral coverage requires considerable additional effort.

Other assumptions or changes are noted, and the exact parameters of the different individual simulations are given in tables within the respective subchapters and in the appendix.

5.1.3 Description of the MC Functional Principle

In the wider field of ocean optics, MC simulations have been used for three decades, even in the more recent special field of optical underwater communication in the last decade. The increasingly available computing power improves the applicability and also the general accessibility. The MC technique advantages follow a simple concept, to be general and instructive, as well as good to implement in software. Possible weaknesses are inefficiency, poor suitability for certain problems, as well as hiding underlying mathematical structures [101].

The MC method has found its way into many different publications. An in-depth theoretical discussion of MC for optical oceanograhpy is covered in [87], and a practical guide providing the methodology and equations with respect to MC software development is included in [218]. MC taylored for UOWC is presented in [60, 219, 220].

In the following section, the principle of operation will be presented in a simplified way. For this purpose, the simulation is divided into three main blocks.

Photon Source and Initial Conditions

A pencil beam is the most simple source for injection of photons into a medium, but this represents only the special case of an ideal laser. More practical and LED-related examples include divergent point sources with isotropic characteristics, i.e., uniform intensity distribution in all directions, or even Gaussian or Lambertian characteristics. The origin takes place at the zero point in the global xyz-coordinate system, see Fig. 5.2. The photon source is represented by many equally sized packages of photons. Each packet has the initial weight w_0 and an individual direction. In total, the packages correspond to the source intensity function or source angular characteristic. The task is to define the initial direction of the photon package with a normalized source intensity

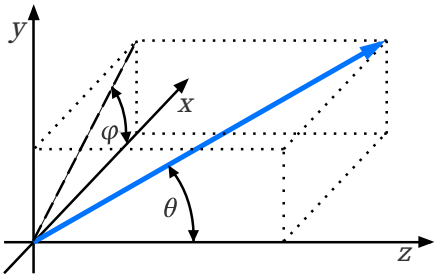

Figure 5.2: Three dimensional position of an initial launched photon package (blue line) in a global xyz-coordinate system.

function, represented by $I(\theta, \varphi)$. The azimuthal angle with respect to the x-axis is φ, and the polar angle with respect to the z-axis is θ. Most sources are rotationally symmetrical around the z-axis, or in other words azimuthally-independent. The azimuthal direction can be represented by a random number from 0 to 2π. Hence the cumulative distribution function (CDF) of the angle φ in the xy-plane is given by:

$$\varphi = 2\pi\mathbb{R}, \tag{5.1}$$

where $\mathbb{R}$ is a random uniform distributed number in the interval from [0,1]. The probability density function (PDF) for the polar angle $p(\theta)$ is [218]:

$$p(\theta) = 2\pi I(\theta)\sin(\theta),\ 0 \geq \theta \geq \pi/2. \tag{5.2}$$

The PDF now needs to be transferred into a CDF $P(\theta)$, so that the angle θ also is accessible by "inverse transform sampling" by a random number:

$$P(\theta) = 2\pi \int_0^{\theta_0} I(\theta)\sin(\theta)\mathrm{d}\theta = \mathbb{R},\ 0 \geq \theta \geq \pi/2. \tag{5.3}$$

Finally, two independent generated random numbers give the φ and θ values for the direction of the initial photon packages. If we now apply the general form to an isotropic source this leads to:

$$\theta = \arccos(1 - 2\mathbb{R}). \tag{5.4}$$

The direction of a photon packet in a source with a Cartesian coordinate frame can also be described by a unit vector. The components of these "direction cosines"-called projection can be calculated by:

$$\mu_\mathrm{x} = \sin(\theta)\cos(\varphi) \tag{5.5}$$

$$\mu_\mathrm{y} = \sin(\theta)\sin(\varphi) \tag{5.6}$$

$$\mu_\mathrm{z} = \cos(\theta). \tag{5.7}$$

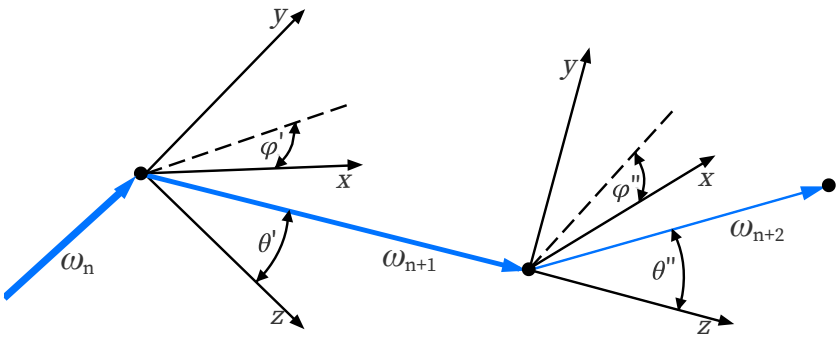

Figure 5.3: Movement of photon package (blue line) between optical events, including weight reduction and scattering into an altered local xyz-coordinate system.

Photon Travel

The process of transporting the packages produced in the source through the medium is carried out in many small steps. Interactions of the photons with particles of the medium represent events as depicted in Fig. 5.3. Photon packages travel from one event labeled n to the next event $n+1$ without being scattered or absorbed, covering the geometric distance s in meters. Regarding [87], the respective CDF and the rearrangement to s are given as:

$$\mathbb{R} = 1 - e^{-sc} \tag{5.8}$$

$$s = -\frac{1}{c} \cdot \ln(\mathbb{R}). \tag{5.9}$$

Here c is the attenuation coefficient and $\mathbb{R}$ is a random number. At the end of the path the event occurs, the photon package weight w is reduced due to the absorption and the direction is deviated due to scattering. The weight loss from one event to the next is given by:

$$w_{n+1} = w_n \cdot \left(1 - \frac{a}{c}\right) = w_n \cdot \omega_0. \tag{5.10}$$

Instead of employing the absorption a to attenuation ratio, the albedo ω_0 can be used. Due to the large number of simulated paths, this approximation can be applied instead of calculating individual path absorptions [60]. The determination of the direction change of the photon packet is the remaining task before the next step to the subsequent event is carried out. The scattering properties of the water medium are given as phase functions, cf. Section 2.2.1. These functions can be based on measurements by Petzold [105] or on analytic functions such as Henyey-Greenstein [108] or Fournier-Forand [109]. These phase functions are probability density functions (PDFs) of photons scattering in polar and azimuthal directions, which are independent from each other. As for the photon source, scattering PDFs needs to be transferred into CDFs. For the azimuthal scattering angle φ' this results in:

$$\varphi' = 2\pi\mathbb{R}. \tag{5.11}$$

Analogous to (5.2) and (5.3), the CDF for the polar scattering angle θ' must be developed from the PDF, i.e., from the phase function $\tilde{\beta}(\Psi)$ or in other notation $\tilde{\beta}(\theta)$. This yields:

$$P(\theta') = 2\pi \int_0^{\theta\prime} \tilde{\beta}(\theta)\sin(\theta)\mathrm{d}\theta = \mathbb{R},\ 0 \geq \theta \geq \pi. \tag{5.12}$$

The derivation of CDFs from the scattering phase functions would result in complicated formulas, if it is possible at all. With the expected number of scattering events, this would require considerable computational time. A popular solution is by the so-called lookup table method [221], which is a numerical evaluation of the equation. A table lists a cumulative value as a function of θ', and for computed random values of $\mathbb{R}$ the relating polar scattering value can be interpolated. Now the new global direction of the photon package can be calculated based on the distance s, the angles θ' and φ', and the direction cosines must be updated. The steps on the way from one event to the next are repeated in a loop. This core process is described in detail in [216, 218, 220].

Photon Termination and Reception

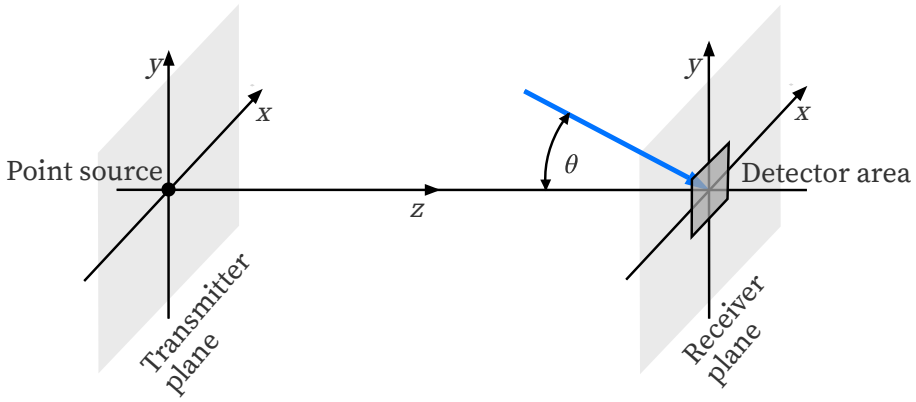

Figure 5.4: Three-dimensional position of a photon package (blue line) arriving at the receiver area in a global xyz-coordinate system.

LED based UOWC setups with usually wider beam angles and relatively small detector areas at medium to large distances are fundamentally inefficient in terms of the ratio of photons generated to photons received. This means that for the majority of photons the path does not end in the receiver, but rather in certain termination conditions. These are necessary to ensure that the computer power is used in the best possible way for photon packets, which have a significant impact on the final result of the simulation. As given in Section 5.1.2 and depicted in Fig. 5.4, photon packets passing the transmitter plane in the $-z$ direction will be terminated. The same applies to photon packages passing the receiver plane without hitting the receiver area in the $+z$ direction. These criteria are based on the fact that multiple backscattering is very unlikely. After a photon packet has been scattered multiple times, including a large weight reduction, but without having fulfilled a termination criteria, a common method called "rouletting" is applied to save valuable computational time. Here, a certain lower limit for the weight is set. If it is undercut, a uniform distributed random number is compared to the threshold value of the rouletting. The weight is either set to zero and the path is terminated as for most cases, or the weight is boosted in the remaining few cases. For example, 9 of 10 packages will be terminated and only one is boosted by a factor of ten. In this way, the total probability is preserved. Finally, photon packages of a certain weight arriving at the detectors area or passing it are considered as received and terminated. For detectors with less than hemisperical reception, it must still be verified that the angle of arrival is within the FOV. In this case, the azimuthal angle is relevant, and the polar angle is insignificant. Regarding Mobley [100], there is no need to apply a cosine factor for the incident angle when counting individual photons in Monte Carlo simulations. Photons are treated as power, and they are automatically accounted for non-perpendicular incident angles by the decreased effective detector area and hits thus become more improbable. The overall process is described in the form of flowcharts in [216, 212].

5.2 Generation of System Attenuation Coefficients via MC Simulation

The basic link equation for an optical underwater communication system, as given in (2.17), includes two distance-related terms: the inverse square for the geometric attenuation, and the negative exponential term e^{-cr} for medium-related attenuation. The application of the beam attenuation coefficient c in laser-based systems may be correct. However, LED-based point-source systems usually have beam angles ranging from a few to 120°, from which the need for an individual coefficient can be identified. This system related value k_{sys} was introduced by Cochenour [104, 222]. The theoretical upper boundary is the beam attenuation coefficient c, and the lower is given by the absorption coefficient a, which physically cannot be undercut. Within these limits, the diffuse attenuation coefficient K_d is located. K_d is a widely documented property for downwelling irradiance, and it represents a fundamental oceanographic parameter to assess the amount of sun light in the water column. The wide gap between values a and c is depicted as colored zones in Figs. 5.5 and 5.6. Irradiance change calculations at the receiver of an example setup with the the application of these extreme values, is given in Figs. 3.1 and 3.2, for oceanic and coastal waters respectively. It is important to apply realistic system attenuation parameters for more accurate irradiance and distance estimations. Therefore, the coefficient k_{sys} is examined in more detail in the following section, and the influencing factors are investigated. The determination of this system-

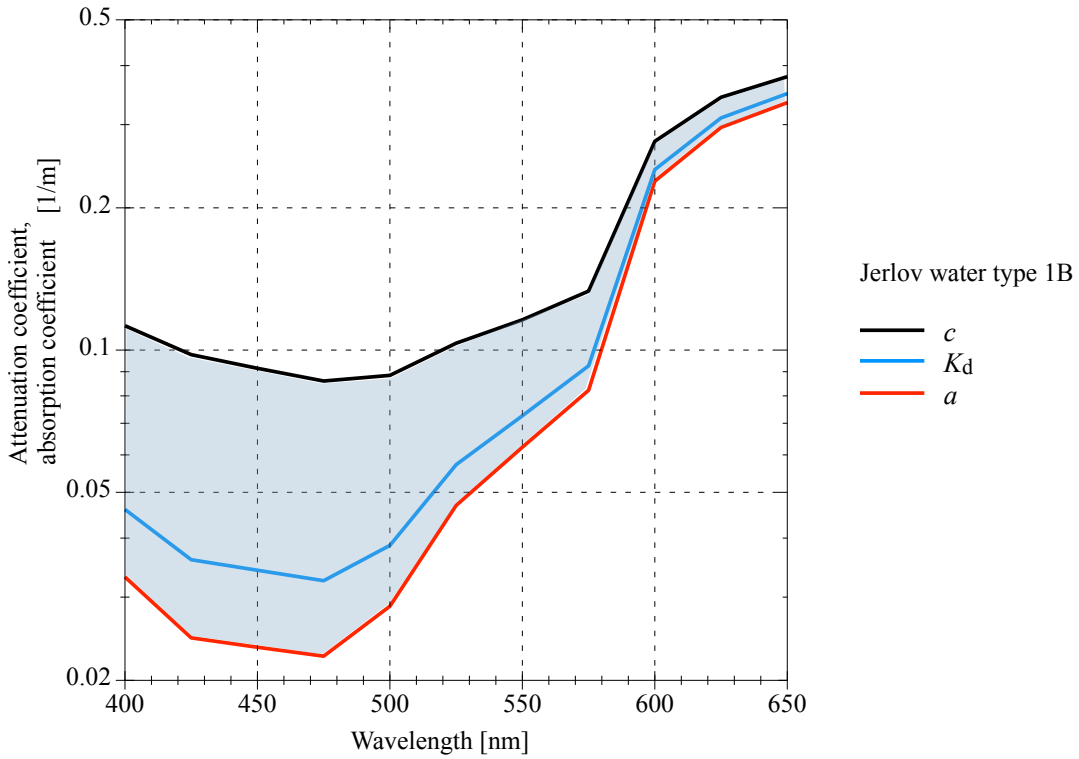

Figure 5.5: The filled area (light blue) depicts the theoretical range of the system attenuation coefficient k_{sys}, valid for oceanic water type Jerlov IB.

dependent attenuation coefficient is performed via MC simulation. Finally, the MC simulation provides the quantity, path and direction information of detected photons in dependence of the amount and characteristic of emitted photons and the attenuation by a medium. Seen physically, a photon represents a power in the unit watt. When photons are distributed or collected in a certain time period they represent an energy, and when detected at a certain area they get an irradiance E in the unit of watts per area. As previously explained, no further cosine correction

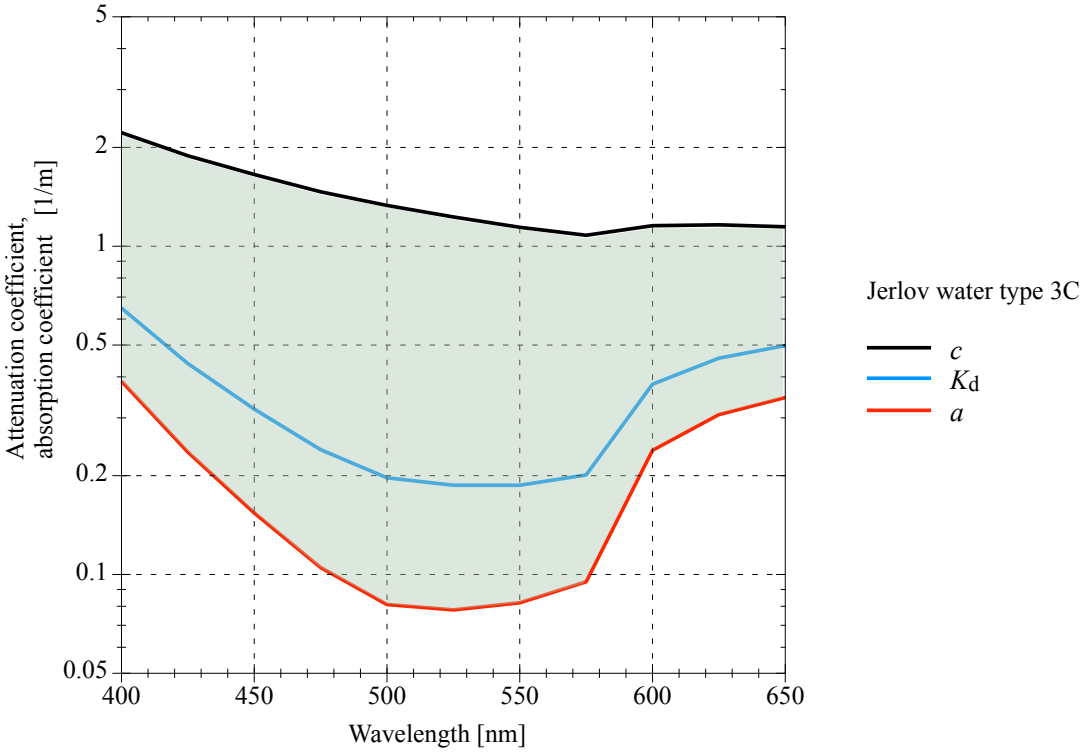

Figure 5.6: The filled area (light green) depicts the range theoretical range of the system attenuation coefficient k_{sys}, valid for coastal water type Jerlov 3C.

is required.

The general link equations will be given in (5.18) and (5.19), and are valid for equal intensity distribution within the beam angle or cone in a three dimensional view. The link equation including the spherical crown (5.19) is the more accurate version for larger beam angles compared to the plane version (5.18). In order to allow for beam shapes that are not uniformly distributed, instead of resolving the above mentioned equations by k_{sys}, the equation (5.13) was used, which instead of being based on one simulation is based on two at different distances but otherwise equal parameters. In this case, the beam angles and detector area are reduced in the equation. The irradiances at the two distances E_{r1} and E_{r2} are substituted by the sums of photons detected $n_{\mathrm{Pr_1}}$ and $n_{\mathrm{Pr_2}}$ in the simulation with otherwise identical parameters. This yields:

$$k_{\mathrm{sys}} = \frac{\ln\left(\frac{n_{\mathrm{Pr_1}} \cdot r_1^2}{n_{\mathrm{Pr_2}} \cdot r_2^2}\right)}{-r_1 + r_2}. \tag{5.13}$$

The following simulations of the k_{sys} are intended to show the effect of the variation of the beam angle and to determine the position compared to the theoretical limits a and c and the frequently available value K_{d}.

5.2.1 Variation of Beam Angle

The more parameters are included in a simulation, the more difficult it is to make a generally valid representation, as in the case of the determination of k_{sys}. The main parameters are the source beam angle and the wavelength. They are varied throughout the simulations for one water type at a time. As before, Jerlov water types 1B and 3C are used as typical representatives for oceanic and coastal water. In each case, the spectral range of the lowest attenuation of the respective water

type is examined. The beam angle is intentionally changed over a wide range to cover the values achievable in the field for LEDs with optical collimation. Further parameters are set to basic values for reasons of presentability and are later systematically varied in order to record their effects. The beam pattern is hereby initially set to rectangular for an ideal source. The scattering is modeled by the Fournier-Forand function, as it is the most feasible for these purposes. The detector's field of view is unrestricted, for a planar detector type thus it is hemispherical. Other parameters such as the distances, the detector areas, and the number of photons and simulation runs are selected within a reasonable scope and limits of the software and computation times. Table 5.1 gives an overview over the parameters applied, which are the reference for the subsequent variations. The

Table 5.1: Parameters used in the simulations for varying the beam angle.

Water type		Jerlov 1B, Jerlov 3C	
Wavelength	λ	425 to 525, 450 to 600	[nm]
Beam angle	β	1, 5, 10, 20, 45, 90	[°]
Beam pattern		rectangular	
Attenuation coefficient	a	Table C.7	
Scattering coefficient	b	Table C.7	
Scattering function		Fournier-Forand	
Distance	r_1, r_2	3, 7	[m]
Detector area	A_{det}	Table C.8	
Field of view	β	180	[°]
MC runs per datapoint		Table C.8	
Photons per run		$5 \cdot 10^7$	

outcome of the simulations is given in Figs. 5.7 and 5.8. It confirms the assumption that the beam angle has a strong influence on the k_{sys} and delivers a set of curves within the theoretical limits. The smallest simulated aperture angle of 1° is basically narrow, but still far from being comparable to a laser beam, thus the clear distance to the beam attenuation coefficient c is also explainable. On the opposite side, the curve of the widest simulated beam angle is just above the attenuation a values. The location of the K_{d}-curve is interesting, as it lies between the curves for 20° and 45° for both water types. Widely used large LED-typical aperture angles like 60° to 90° are located between the a and K_{d} curves. The progression of k_{sys} as a function of the beam angle can be explained as follows: increasing beam angles lead to larger areas surrounding the center, from which photons can also scatter onto the detector surface. This increasingly compensates for the losses of the central area due to scattering, which yields smaller attenuation values.

Running simulations to get meaningful results requires several test runs to tune the parameters. In principle, for the sake of better results, it is desirable to generate as many photons as possible and feed them into the simulation. On the part of the software, the number is limited due to the individual tracking, the resulting data volumes and the subsequent handling including evaluation. The simulation series of this work corresponds to a data volume of over 70 GB and a few weeks of computer runtime for a standard notebook. Each data point is based on many repeated simulation runs, both to improve the mean value and to be able to make statistical statements about the variation of the individual values. The ratio of 2-sigma to mean value of detected photons serves as an indicator. The wide range of the beam angles analyzed causes considerable differences in the efficiency of the simulation, to be understood as the ratio of photons received to photons generated. This requires a careful adjustment of the detector size to the beam angle used. The detector areas used in the simulation are in most cases considerably larger than those of real components. An increase of the detector area with inefficient large beam angles can lead to geometrical problems, since the path length in outer areas deviates from the central one. With very small beam angles

it must be ensured that the detector area is also smaller than the spot of the beam, otherwise, the detector would still capture increasingly scattered photons. The simulations have shown that the extraction of the water-related attenuation becomes more difficult with less turbid water under the same geometric conditions with increasing beam angle and thus decreasing efficiency. This can be counteracted to a limited extent by increasing the number of simulation runs. These impacts are reflected in the parameters applied to the simulations, which are presented in the Appendix C.8. The system coefficients k_{sys} are basically only valid for a single wavelength, and the application to the peak wavelength of single-color LEDs should not be critical due to the typically small spectral half-width and the spectral symmetry. For color-converted LEDs with comparatively large half-widths and asymmetric spectra, it may be necessary to consider the entire spectrum section by section.

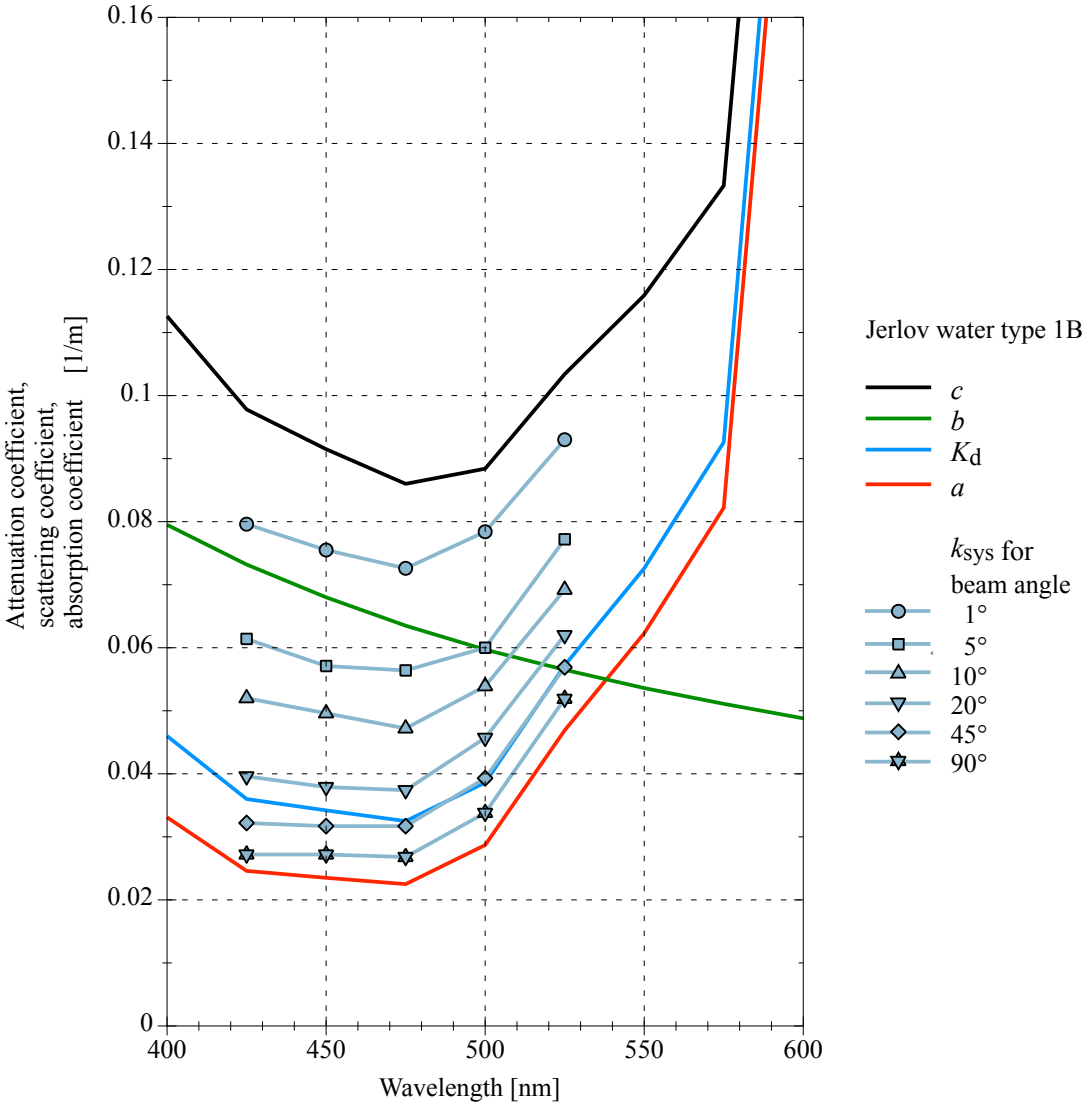

Figure 5.7: Impact of beam angle variation on the system attenuation coefficient k_{sys} in oceanic water type Jerlov 1B.

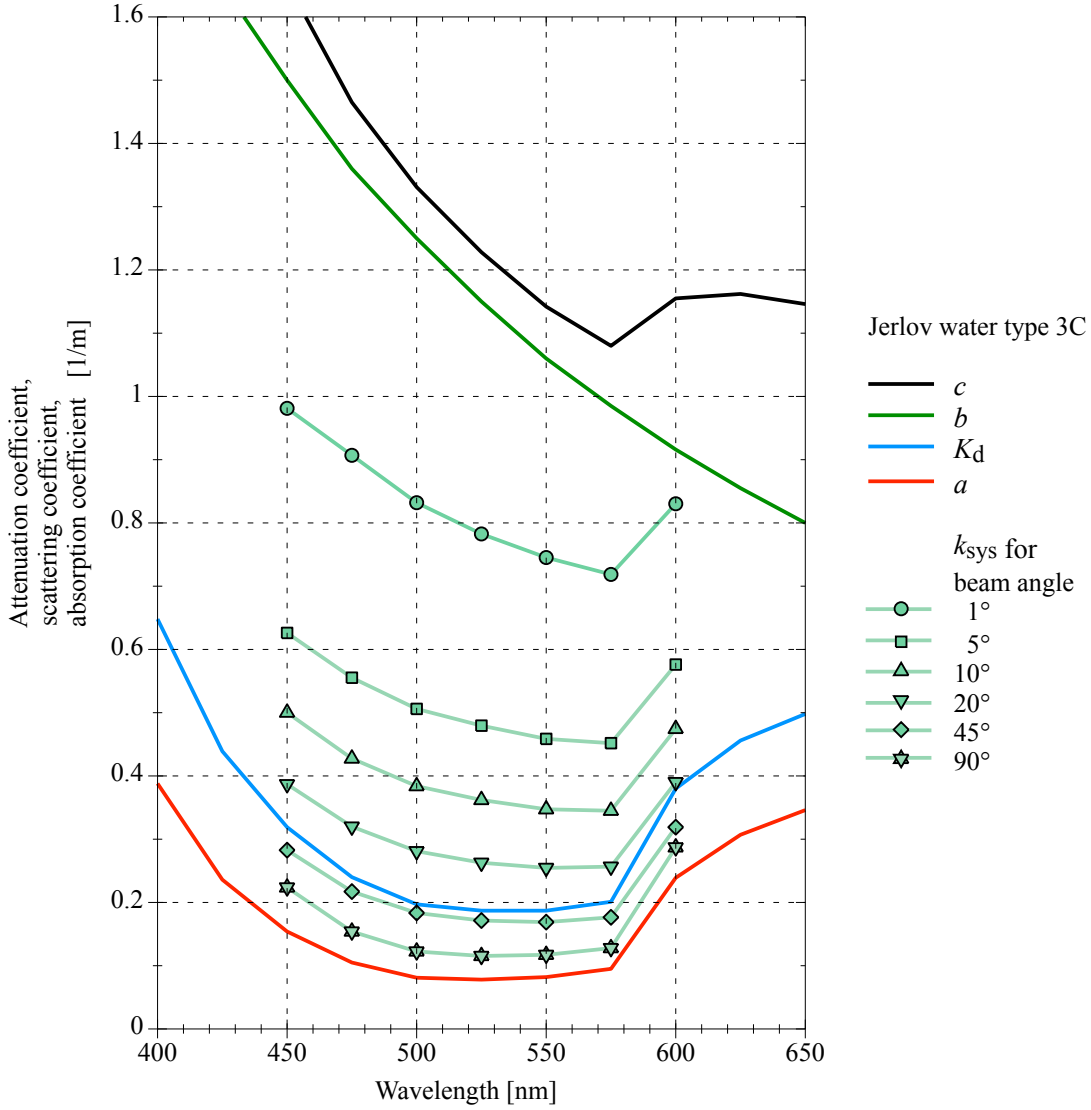

Figure 5.8: Impact of beam angle variation on the system attenuation coefficient k_{sys} in coastal water type Jerlov 3C.

5.2.2 Investigation of Distance Dependence

The system attenuation coefficient k_{sys} can own a minor distance dependence. The cause for such an effect can be imagined as follows: a narrow beam increasingly blurrs with growing distance in strongly scattering media. This acts like a slightly larger beam angle, thus k_{sys} decreases. Cochenour covered this topic in [104], where the beam spread function is characterized, but is related to lasers. In this study, these effects were found to be present even at medium distances in the range of 10 to 20 meters, with strong scattering under coastal or harbor water conditions. In the following section, it will be investigated, whether and to what extent, LED-based systems are affected. The base is formed by MC simulations for a certain distance. The equation (5.13), which generally is applied here for k_{sys} is differential, it needs two distances r_1 and r_2, with the restriction that the distances must be neither equal nor zero. The function can be imagined as follows, the slope between the two values is determined and the k_{sys} value for the distance of interest 0 to r is calculated. The default distances in the simulations r_1=3 m and r_2=7 m correspond to a source to detector distance of r=10 m. A transition of r_1 to 0 and r_2 to r or 10 m in the example, may

provide a better explanation. Other distance pairings of the same sum, such as 4 m and 6 m, could also be similarly used. To examine the dependency, simulations at additional distances for selected beam angles at one characteristic wavelength have been executed, see Table 5.2. In the case of a rectangular beam pattern, the spherical crown based equation (2.18) can be utilized for a single distance. Direct usage is not possible, since the attenuation variable cannot be isolated due to a ln(x)/x problem in the distance r, but iterative calculations are feasible. The application of the iterative and the differential variants provide comparable results. However, the possibilities in terms of large distances are limited due to the generally small number of counted photons, the square distance law, and a limited number of photons that can be generated. The results are given in Fig. 5.9 for both water types and narrow and wide beam angles, respectively. Each row contains values determined in both ways. Each point is based on 20 or more simulation repetitions, and the error bars indicate how the variation of the received photons affects the k_{sys}. In coastal water, as expected, a falling k_{sys} curve is obtained for the narrow beam angle, and constant values for the wide beam angle. In contrast, no clear result can be derived for the less-scattering oceanic water on the basis of the simulations and results presented. An improvement could be achieved by considering much larger distances, but this is where the simulations in this setup reach their limits. The distances covered in relation to the attenuation can be represented by the number of attenuation lengths, see Section 2.2.1. This value is about 2 for oceanic water and 12 for coastal waters, both with a narrow beam.

Table 5.2: Parameters used in the simulations about distance dependence.

Water type		Jerlov 1B, Jerlov 3C	
Wavelength	λ	450, 550	[nm]
Beam angle	β	1, 45	[°]
Beam pattern		rectangular	
Attenuation coefficient	a	Table C.7	
Scattering coefficient	b	Table C.7	
Scattering function		Fournier-Forand	
Distance	r_1, r_2	3, 7, 11, 15 (1B) 3, 5, 7, 9 (3C)	[m] [m]
Detector area	A_{det}	Table C.8	
Field of view	β	180	[°]
MC runs per datapoint		Table C.8	
Photons per run		$5 \cdot 10^7$	

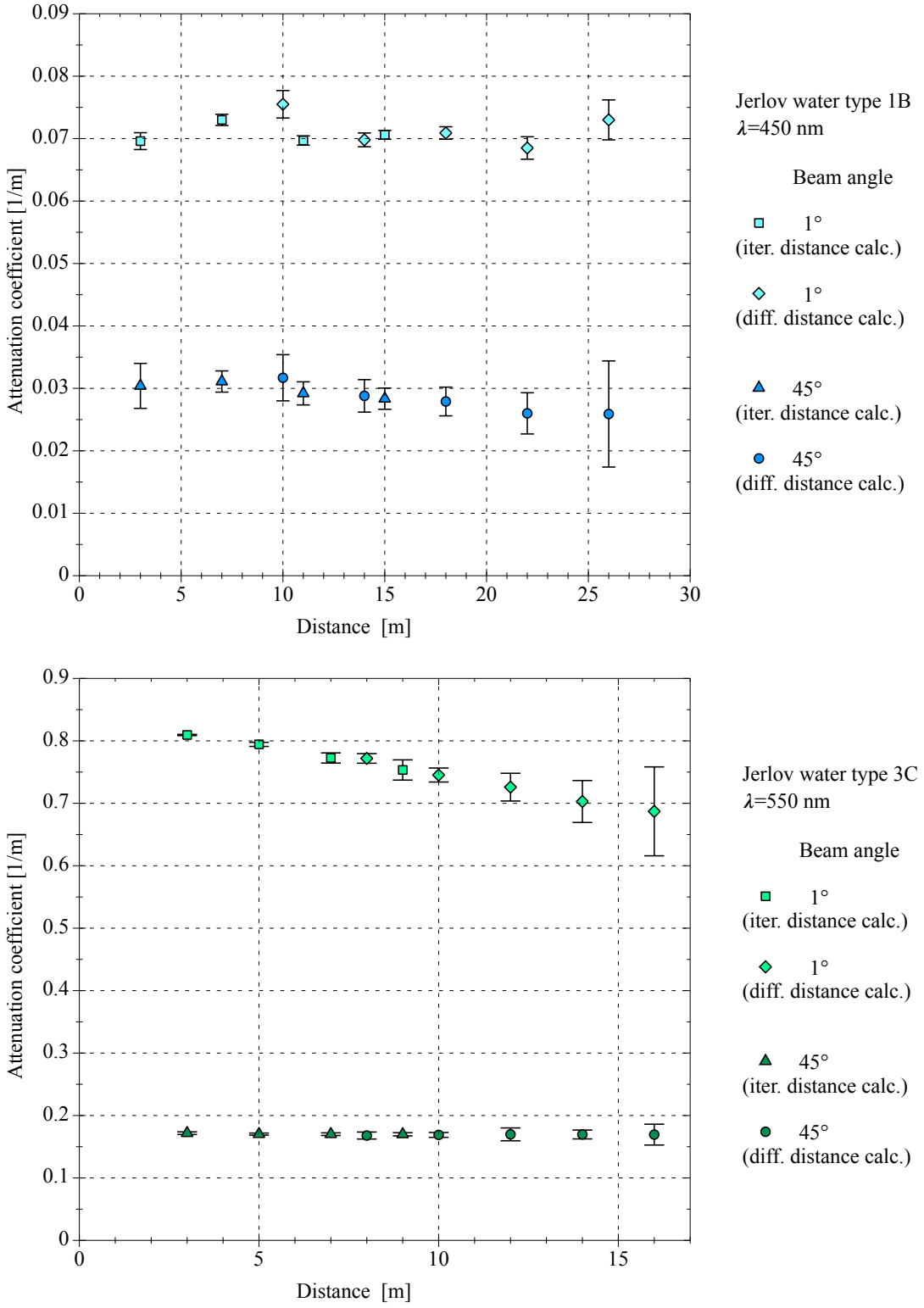

Figure 5.9: Distance dependence of the system attenuation coefficient in oceanic Jerlov 1B and coastal 3C water types.

5.2.3 Impact of Radiation Pattern

The point source used in the simulations is not only characterized by the beam angle, but also by the spatial radiation pattern. The intensity is rotationally symmetrical around the z-axis, but the polar-angle-dependent intensity can develop differently according to the pattern characteristic. In the simplest case this is isotropic and has a rectangular beam pattern, which means intensity is constant within the boundaries. Generally the (full) beam angle β is defined as within the 50% margins of intensity, also known as the full width half mean (FWHM). In the case of the rectangular pattern, the boundary is formed by steep slopes. In contrast to this, the Lambertian characteristic commonly used for divergent sources shows rounded slopes. The beam pattern of real non-laser sources like LEDs (including some beam shaping through reflectors or lenses) in most cases is not ideal and ranges between these two theoretical characteristics, c.f Section 4.3.1. This is not to be confused with the term "beam profile", which belongs to lasers and describes the intensity on a plane perpendicular to the beam (cross section).

In case of MC simulations, this means that the rectangular and Lambertian beam patterns can be used as boundaries, and their influence can be well demonstrated. A drawback of the employed software is that the Lambertian characteristic is not implemented, therefore the offered Gaussian characteristic is used instead. The very basic isotropic profile is of course supported. For parallel beams such as from lasers, the Gaussian bell-shape describes the intensity of the cross section on the beam, or in a projection on the wall. These patterns need to be converted into an angular form, like a rotating measurement of the characteristic on a goniometer at a constant distance. The extent to which the Gaussian and Lambertian characteristics match within the applicable angular range must be reviewed. The calculation of the normalized intensity for both beam patterns is described in Appendices by (C.38) and (C.39), and the parameters are given in Tables C.9 and C.10. For narrower beam angles up to 30° the patterns are more or less similar, the differences increases with a further growing beam angle, but even for a 90° angle the difference is minor, see Fig. 5.10. In the range of values intended for simulations a comparability is therefore given.

To investigate the effects of changing the patterns, individual points were simulated with Gaussian beam pattern instead of the reference setting of a rectangular profile, using the same parameters, cf. Tables 5.1 and 5.3. These points are shown in addition to the segments of the existing curves for oceanic and coastal waters in Figs. 5.11 and 5.12, respectively. 2σ-error bars are included to indicate the accuracy. The wavelengths are chosen for the two water types in the most interesting range, with the lowest attenuation in each case, 450 nm for the oceanic Jerlov 1B and 550 nm for the coastal Jerlov 3C waters. The results of the simulations indicate that in principle weaker and less directional patterns cause a decrease of k_{sys}, whereas the impact is stronger for small beam angles. The effect is much more pronounced in clear oceanic water with less scattering. In coastal water the total effect is significantly less and becomes negligible at large beam angles. Even if only small curve sections and individual points are used here to interpret the effects, these are still characteristic and based on tens of simulation runs in each case. The most obvious explanation for the lower attenuation values of the Gaussian beam is that a kind of widening occurs, despite the defined equal angles of both profiles. The oceanic water is a low scattering regime, this means for photons that have lost the direct path by scattering they are relatively unlikely to get back to the path by scattering again. The rectangular pattern has the largest direct component with the narrowest beam angle and thus the smallest fraction of photons remaining that can potentially be scattered into the path. This could explain the largest impact of a pattern change here, and why the effect decreases for larger beam angles. The situation in coastal water with strong scattering is different. Due to the comparatively frequent scattering processes, the directional component degrades quickly. With large beam angles, this is poor anyway, which ultimately leads to the beam pattern becoming insignificant.

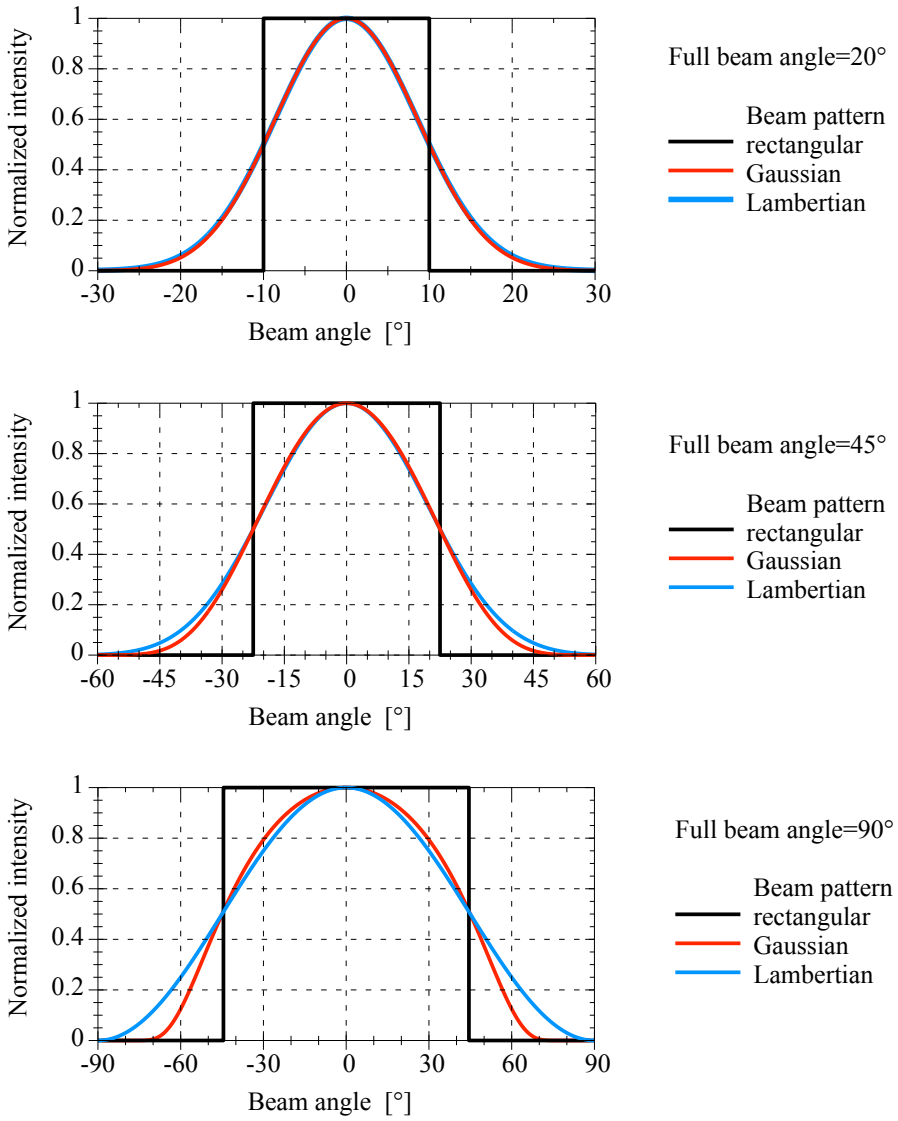

Figure 5.10: Comparison of theoretical beam patterns for various beam angles.

Table 5.3: Parameters used in the simulations for varying the beam pattern.

Water type		Jerlov 1B, Jerlov 3C	
Wavelength	λ	450, 550	[nm]
Beam angle	β	1, 10, 45	[°]
Beam pattern		rectangular, Gaussian	
Attenuation coefficient	a	Table C.7	
Scattering coefficient	b	Table C.7	
Scattering function		Fournier-Forand	
Distance	r_1, r_2	3, 7	[m]
Detector area	A_{det}	Table C.8	
Field of view	α	180	[°]
MC runs per datapoint		Table C.8	
Photons per run		$5 \cdot 10^7$	

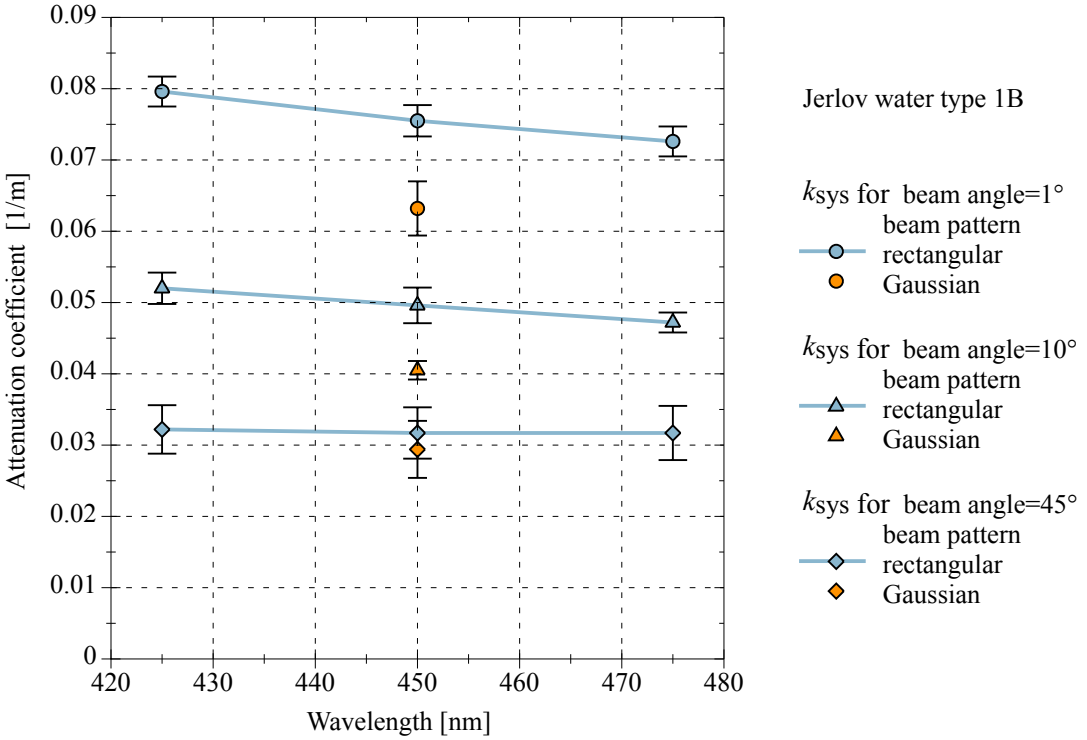

Figure 5.11: Impact of beam pattern variation on the system attenuation coefficient in the oceanic Jerlov 1B water type.

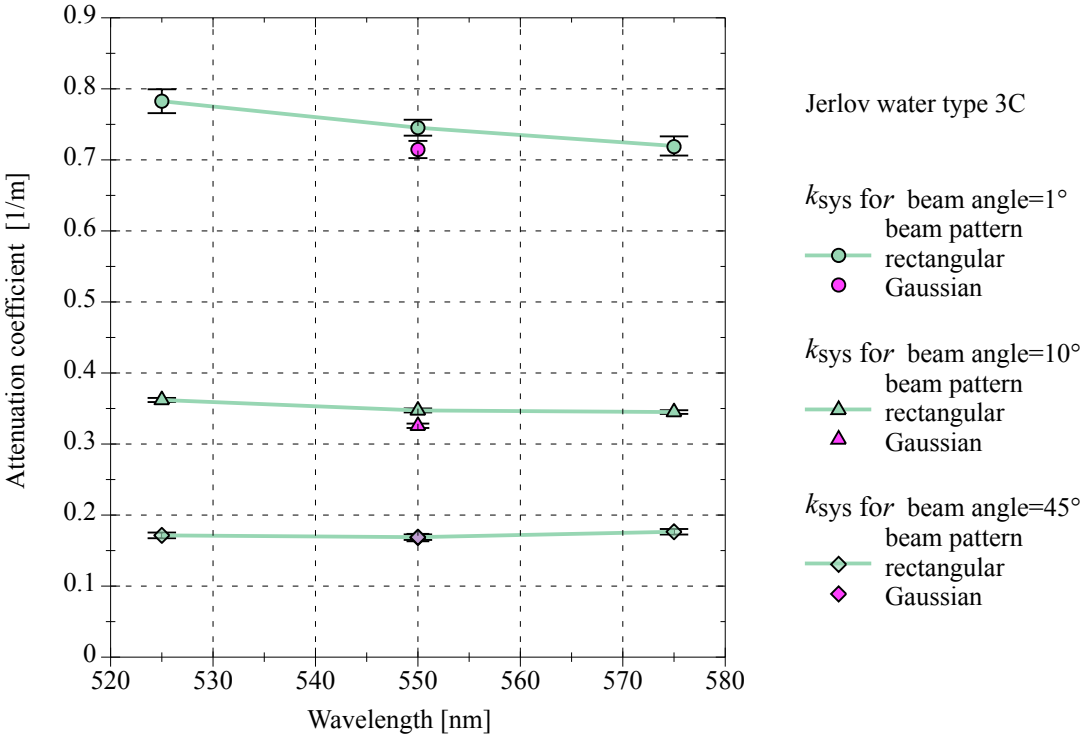

Figure 5.12: Impact of beam pattern variation on the system attenuation coefficient in the coastal Jerlov 3C water type.

5.2.4 Effect of Changes in Field of View

The field of view of a detector directly limits the range of the inclination and determines the spatial operating range of the system in conjunction with the transmitter characteristics and the media properties, as depicted in Fig. 2.12. Limitations of the FOV, which is usually hemispherical in planar detectors, can have different causes and objectives. The FOV can be altered or influenced as a result of filters, shutters, baffles, lenses, or even just through the optical path of the underwater housing, cf. Section 4.2. As a relevant parameter in UOWC, the FOV has been subject of several publications [60, 223, 224]. The focus of this work, including simulations, is on subsequent quantities, such as achievable reception powers. In most cases the FOV has the shape of a cone,

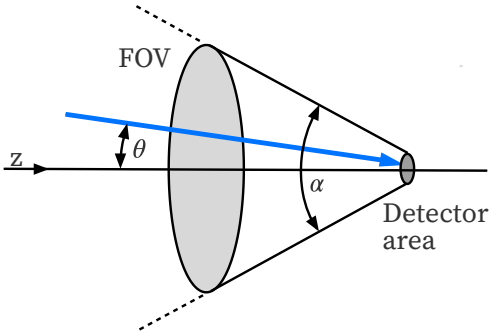

Figure 5.13: Geometry of the receiver field of view including a photon path, symbolized by the blue arrow.

which is symmetrical around the z-axis, see Fig. 5.13. The polar component θ of the incident path is significant, but the azimuthal is not in this case. In MC simulations, only photons reaching the detector area with an angle of incidence smaller than half of the FOV angle α are taken into account. The simulations are performed with a FOV of 180°, and a reduction of the FOV can be achieved by filtering the individual incident photon path data afterwards. This method is more efficient to run compared to several individual simulations for different FOVs. The results of the simulations show the effect of a FOV change on the system attenuation coefficient k_{sys} for various beam angles, see Figs. 5.14 and 5.15. A low scattering regime is represented by the oceanic water type Jerlov 1B, a turbid environment by the coastal water type Jerlov 3C, and detailed simulation parameters are given in Table 5.4.

It can be seen that a FOV reduction from 180° to 90° has practically little to no effect. A further reduction leads to an increase of the k_{sys}, which becomes more pronounced with larger beam angles. Overall, the effect is stronger in coastal waters. The reason for the different responses to a FOV reduction lies in the quantity distribution of the angles of incidence. Figs. 5.16 and 5.17 provide these as characteristic examples, for both water types at small and large beam angles respectively. A decreasing FOV is equivalent to an incremental cutting off of right diagram areas, and the impact on the quantity of photons counted is clearly obvious.

Table 5.4: Parameters used in the simulations for varying the detector field of view.

Water type		Jerlov 1B, Jerlov 3C	
Wavelength	λ	450, 550	[nm]
Beam angle	β	1, 5, 10, 20, 45, 90	[°]
Beam pattern		rectangular	
Attenuation coefficient	a	Table C.7	
Scattering coefficient	b	Table C.7	
Scattering function		Fournier-Forand	
Distance	r_1, r_2	3, 7	[m]
Detector area	A_{det}	Table C.8	
Field of view	α	15, 30, 60, 90, 120, 180	[°]
MC runs per datapoint		Table C.8	
Photons per run		$5 \cdot 10^7$	

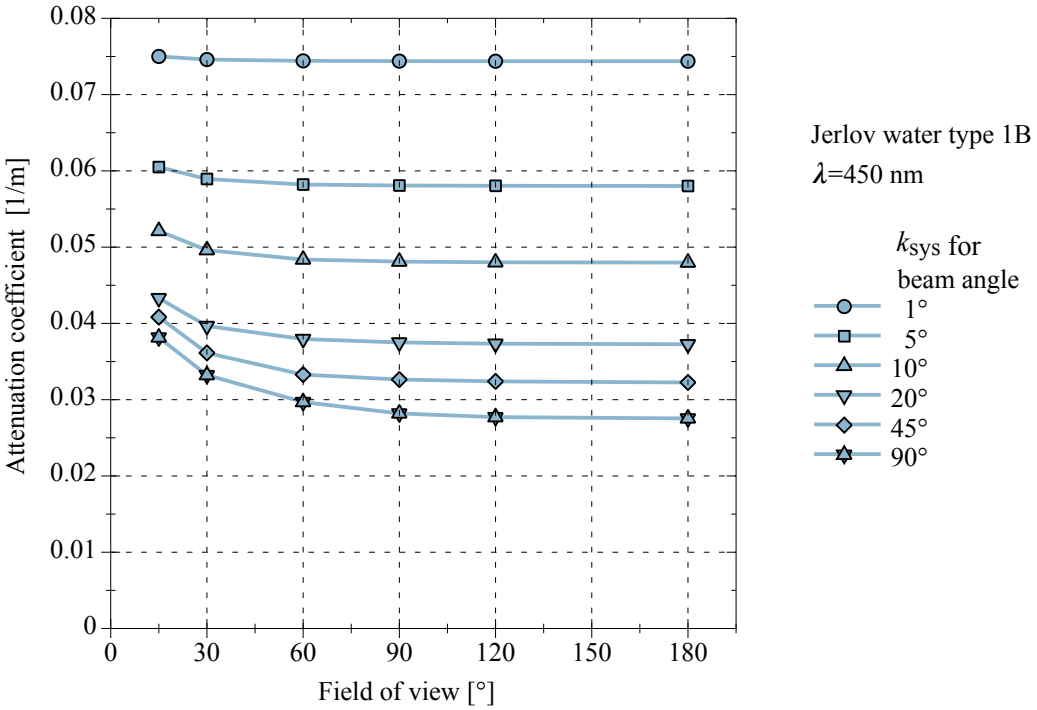

Figure 5.14: System attenuation coefficient as a function of the detector field of view for various beam angles. Simulated for oceanic water type Jerlov 1B at a wavelength of 450 nm.

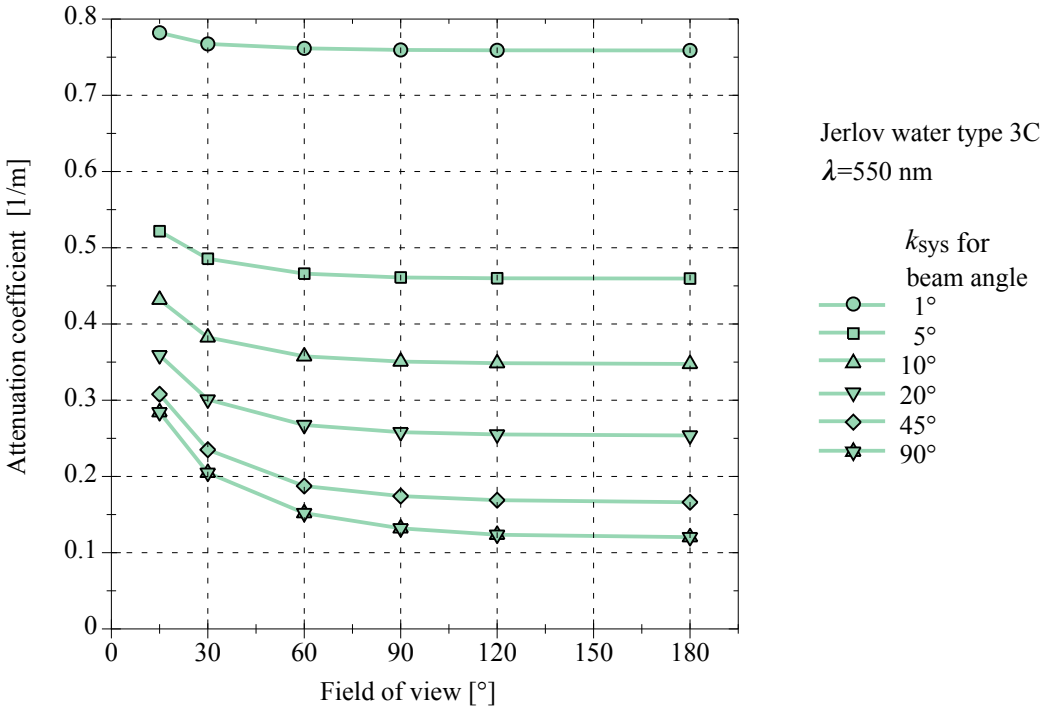

Figure 5.15: System attenuation coefficient as a function of the detector field of view for various beam angles. Simulated for coastal water type Jerlov 3C at a wavelength of 550 nm.

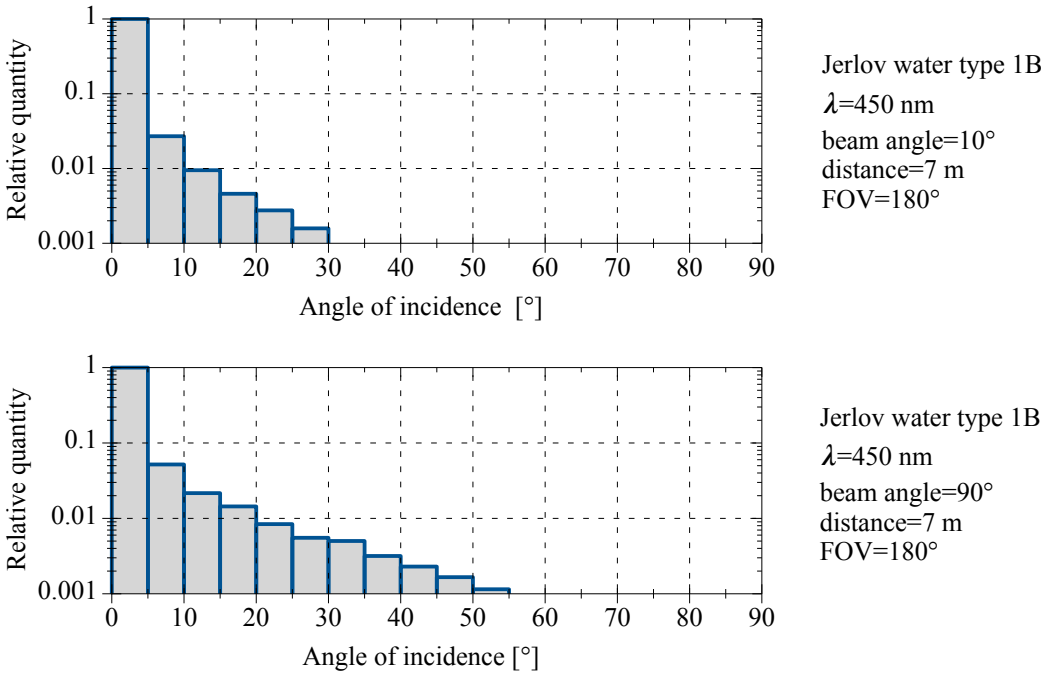

Figure 5.16: Quantitative angle of incidence distribution of detected photons for oceanic water type Jerlov 1B. The upper diagram applies for a narrow beam angle, the lower for a wide angle. Please note the log-scale for better resolution.

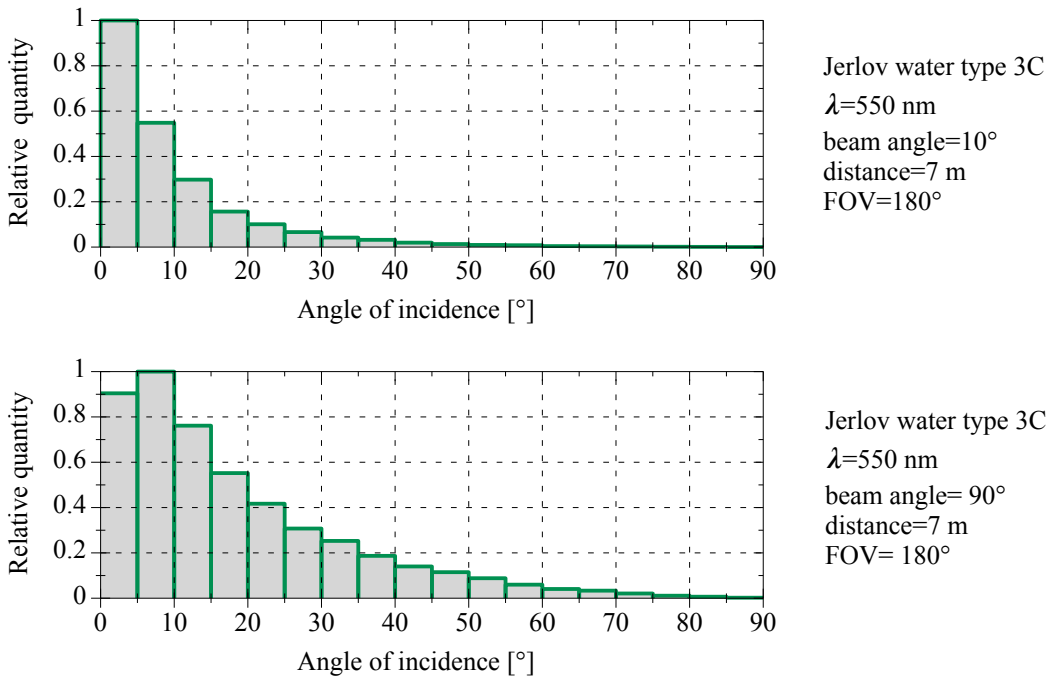

Figure 5.17: Quantitative angle of incident distribution of detected photons for coastal water type Jerlov 3C. The upper diagram applies for a narrow beam angle, the lower for a wide angle.

5.2.5 Influence of Applied Scattering Phase Function

An introduction to the particulate scattering in water from a physical oceanographic perspective is given in Section 2.2.1. The scattering characteristics are described by models and their analytic functions, such as Henyey-Greenstein (HG) and Fournier-Forand (FF). These two widely used models represent the scattering properties in slightly different ways, and possible impacts on MC-simulations for UOWC are the subject of this examination. As a general reference phase function, the measured average by Petzold in 1972 is used. It still represents a good mean of the variability surveyed. The HG phase function model in the one-term version (OTHG) is known to provide a relatively poor fit at small and very large scattering angles, and even worse at very small ones. The commonly applied parameter g_{HG} =0.924 still provides the best approximation. In the meantime, FF has supplanted HG in oceanography. FF is recognized to be more realistic, but is also more complicated. FF enters the comparison with the well established parameters n_{FF} =1.1 and μ_{FF} =3.5835. Further literature in this area is provided by [107, 101].

The phase functions, which represent PDFs, need to be transferred into CDFs, in order to be suitable for computer-based MC simulations. The procedure is described in Section 5.1.3. In the case of HG an analytical form exists to determine the scattering angle θ directly as function of the random number $\mathbb{R}$. This is not the case for FF, and its analytic CDF is considered to be unsolvable for $\mathbb{R}$. A workaround is to create a table that contains closely-spaced values of θ and the related cumulative value, which is supplied by the CDF. These lookup-tables allow the MC software fast access during the simulation runtime. The angle corresponding to the random number is extracted from the table by linear interpolation. A detailed description is given in [221], the respective formulas are included in Appendices (C.40) and (C.41).

The two curves of the CDF from HG and FF show only slight differences when viewed in their complete form. A detailed look at the small angle range makes the differences obvious, see Fig. 5.18. FF clearly prefers small angles in comparison to HG. Half of all scatter events occur in the angular range of 0° to 4°, compared to 0° to 7.5° for HG.

Of course natural waters come with variations, but the phase function can generally be applied to coastal and oceanic waters. The reason lies in the origin, the volume scattering functions, which after normalization to the respective scatter coefficients deliver an independent phase function. Studies have shown that the phase function is only subject to a weak wavelength dependence [106]. Since these minor variations, within the wavelengths used for simulations here, mostly concern the backscatter range, they can be omitted.

To investigate the impact of the phase function model, individual points were simulated with HG instead of the reference setting of FF, and otherwise using the same parameters, cf. Tables 5.1 and 5.5. These points are shown additionally to the segments of the existing curves for oceanic and coastal waters in Figs. 5.19 and 5.20. 2σ-error bars are included to indicate the accuracy. The wavelengths are chosen for the two water types in the most interesting range of the least attenuation in each case: 450 nm for the oceanic Jerlov 1B and 550 nm for the coastal Jerlov 3C.

HG delivers significantly higher k_{sys} values compared to FF, and at larger beam angles the relative increase seems to be reduced. The oceanic and coastal water types show comparable behavior, which confirms the independence of the phase function to the water type. The increase in k_{sys} with HG applied can be explained by the fact that losses increase, so to speak, with small beam angles due to scattering in rather large angles.

Table 5.5: Parameters used in the simulations for comparison of two scattering functions.

Water type		Jerlov 1B, Jerlov 3C	
Wavelength	λ	450, 550	[nm]
Beam angle	β	1, 10, 45	[°]
Beam pattern		rectangular	
Attenuation coefficient	a	Table C.7	
Scattering coefficient	b	Table C.7	
Scattering function		Fournier-Forand, Henyey-Greenstein	
Distance	r_1, r_2	3, 7	[m]
Detector area	A_{det}	Table C.8	
Field of view	α	180	[°]
MC runs per datapoint		Table C.8	
Photons per run		$5 \cdot 10^7$	

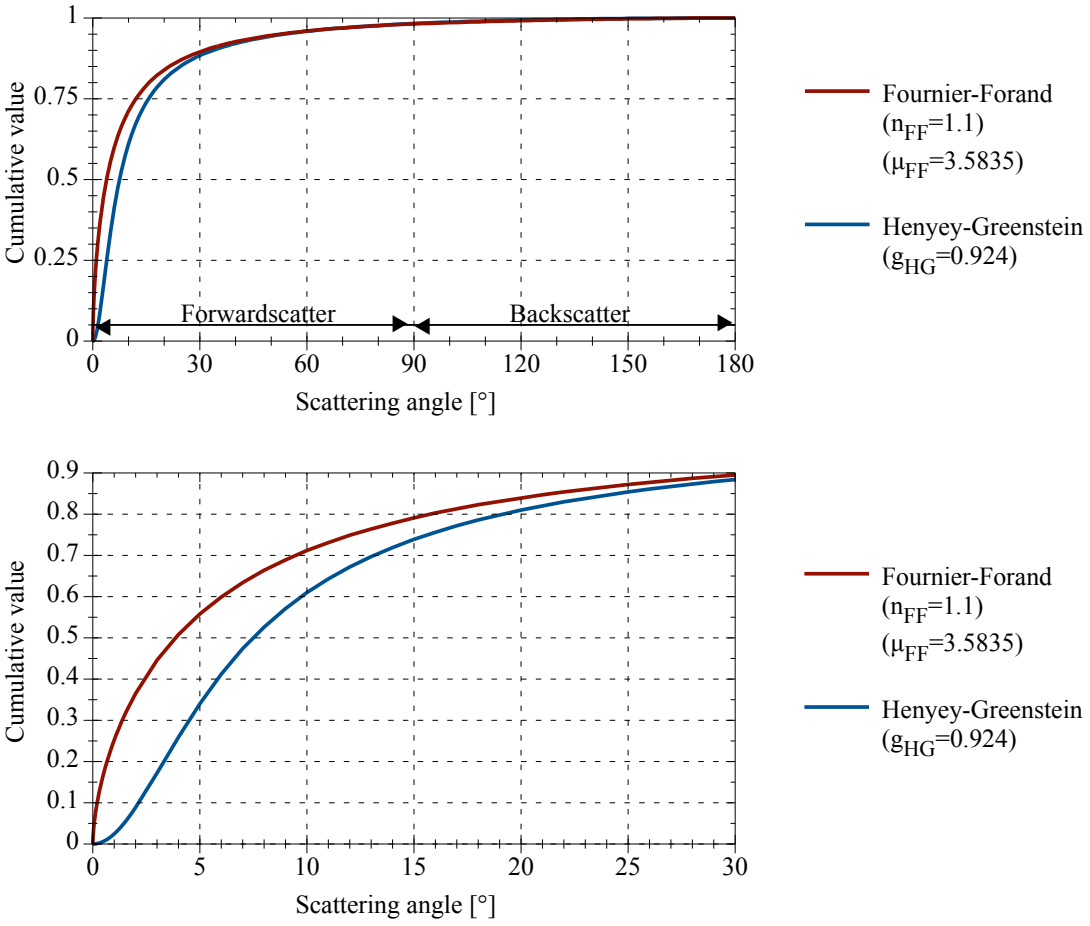

Figure 5.18: Cumulative distribution function for Fournier-Forand and Henyey-Greenstein scattering functions, as an overview in the upper diagram and with more detail in the lower diagram.

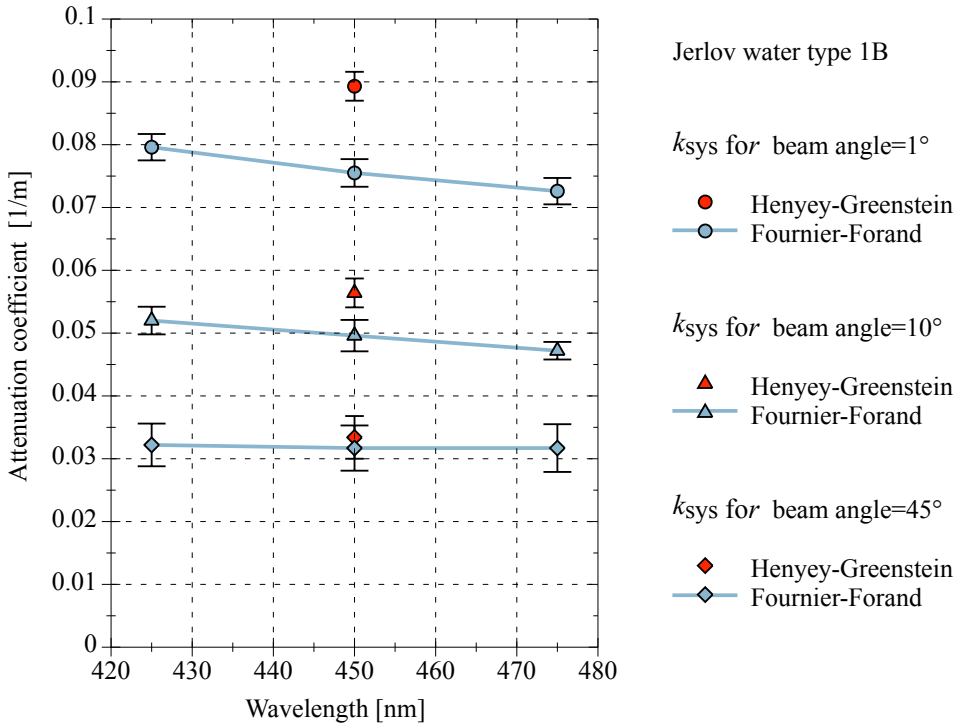

Figure 5.19: Impact of the scattering function variation on k_{sys}-determination via MC simulation for oceanic water type Jerlov 1B.

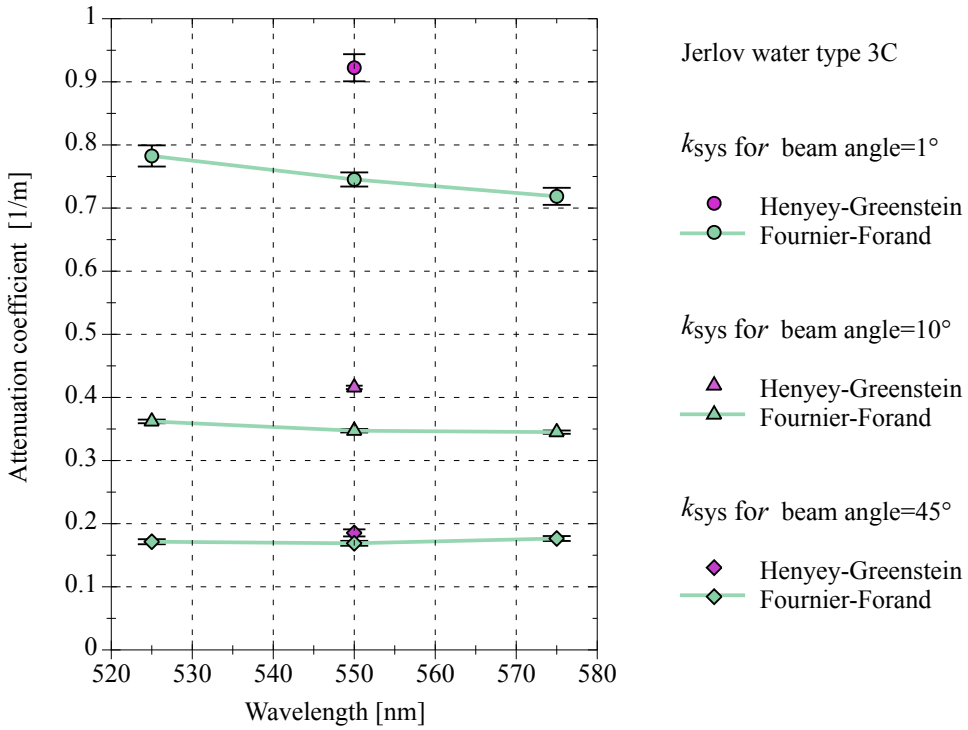

Figure 5.20: Impact of the scattering functions variation on k_{sys}-determination via MC simulation for coastal water type Jerlov 3C.

5.2.6 Examinaton of Temporal Dispersion

The following investigations are not directly related to the previous ones of the parameters regarding the system attenuation coefficient k_{sys}. Instead they are another product of the MC simulations, which provides information on whether the bandwidth of the system is possibly limited by the properties of the channel. Since the temporal dispersion is of fundamental importance, especially for potentially faster laser-based systems, it is also the subject of many publications in the field of UOWC [50, 52, 219, 222, 225]. Nevertheless, realistic conditions of LED-based systems are simulated here in order to show the scale of the arising temporal dispersion.

Although the photons or packets are generated and processed sequentially during the simulation, the evaluation can be based on the assumption that all photons in the MC simulation are generated in the source at the same time t_0, which allows time-resolved responses to be examined. The route of each photon is tracked by the simulation software, that means the segments of the scattered path through the medium from the origin in the source to reaching the receiver. In addition to the path length, the number of scattering events and angular information are also available as data. The decisive speed under water is the phase velocity, cf. (2.3). As a factor entered here, the refraction index n is subject to dependencies such as pressure, salinity and temperature, see Section 2.2.3. For simplicity, a general value of n =1.34 is assumed, which leads to a speed of light value in water of $2.14 \cdot 10^8$ m/s. The time t_{p} needed for a photon to travel a certain path length s_{p} can be calculated by:

$$t_{\mathrm{p}} = \frac{s_{\mathrm{p}}}{c_0} \cdot n, \tag{5.14}$$

where c_0 is the speed of light in air. Photons on the shortest possible path without scattering, given as distance r, produce a transit time of t_1, which cannot be physically undercut. Photons that have undergone one or more scattering events exhibit a longer path length s_{p} and thus a longer transit time t_{p}. The m photons arriving randomly after t_1, with a transit time t_{p}, produce a peak with exponential decay, which represents the temporal scattering, see Fig. 5.21. The parameters

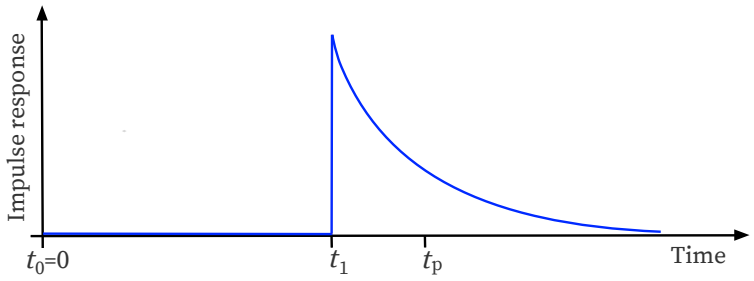

Figure 5.21: Prominent time points within the transit of the photons.

for the simulations of these examples were chosen so that the worst-case scenarios with respect to the delay would occur, but they are still in a realistic range. This means a beam angle of 90° and a FOV of 180°, as well as distances of 10 m for coastal and 30 m for oceanic waters, cf. Table 5.6. These two distances result in t_1 of 44.7 ns and 134 ns, respectively. The generated data of the received photons in each simulation are filtered in different ways. The first is to get the probability distribution as a function of the scattering order. The second is the evaluation of the individual path lengths and the calculation of t_{p}, including the identification of the time delay related to t_1. To obtain the distribution of the photons individual delay values, they are sorted into the respective time slots, which have a width of 0.1 ns. Within a time slot the sum of the photons is calculated. The individual slot sums for all the FOV series are normalized to the maximum value at a FOV of 180° and thus represent relative quantities.

Figure 5.22 depicts the probability of the scattering order of the received photons for two water types each for a wide and narrow beam angle. It shows that in coastal water, despite the

significantly shorter distance, many more scattering events occur. A smaller beam angle leads to a slight shift of the scattering order towards smaller values. The resulting delay in oceanic water is at an overall low level and is hardly influenced by the variation of the beam angle and the FOV, see Fig. 5.23. This is completely different in coastal water as given in Fig. 5.24. Significant delayed portions can be identified here, and furthermore there is a clear dependence of these on the beam angle and the FOV. A reduction of the beam angle or the FOV leads to smaller delayed portions in each case. The reasons for the different behavior of the two water types with regard to the delay can be found in the scattering order. In oceanic water, with on average only a few scattering processes from the incoming photons, the forward character is basically preserved and an FOV variation thus has little effect. Even a large beam angle cannot scatter substantial parts from the outer areas into the receiver. The predominantly high scattering order in the coastal water leads to a contrary response.

The investigations carried out are aimed at the question of the extent to which LED-based UOWC systems are affected by the scatter-induced delay. A comparison between the delays of a few nanoseconds produced under the simulation conditions, with the typical rise and fall times of power-LEDs in the order of tens of nanoseconds, leads to the conclusion that the delay is negligible. Even in the murkiest harbor water the delays may be an order of magnitude larger, and the effect on the system bandwidth would still be small because the detector capacitance represents the hurdle in most cases.

Table 5.6: Parameters used in the simulations and calculations for examination of the scatter induced delay.

Water type		Jerlov 1B, Jerlov 3C	
Wavelength	λ	450, 550	[nm]
Beam angle	β	10, 90	[°]
Beam pattern		rectangular	
Attenuation coefficient	a	Table C.7	
Scattering coefficient	b	Table C.7	
Scattering function		Fournier-Forand	
Distance	r	10, 30	[m]
Detector area	A_{det}	Table C.8	
Field of view	α	20, 60, 180	[°]
MC simulation runs		1	
Photons per run		$5 \cdot 10^7$	
Refraction index	n	1.34	

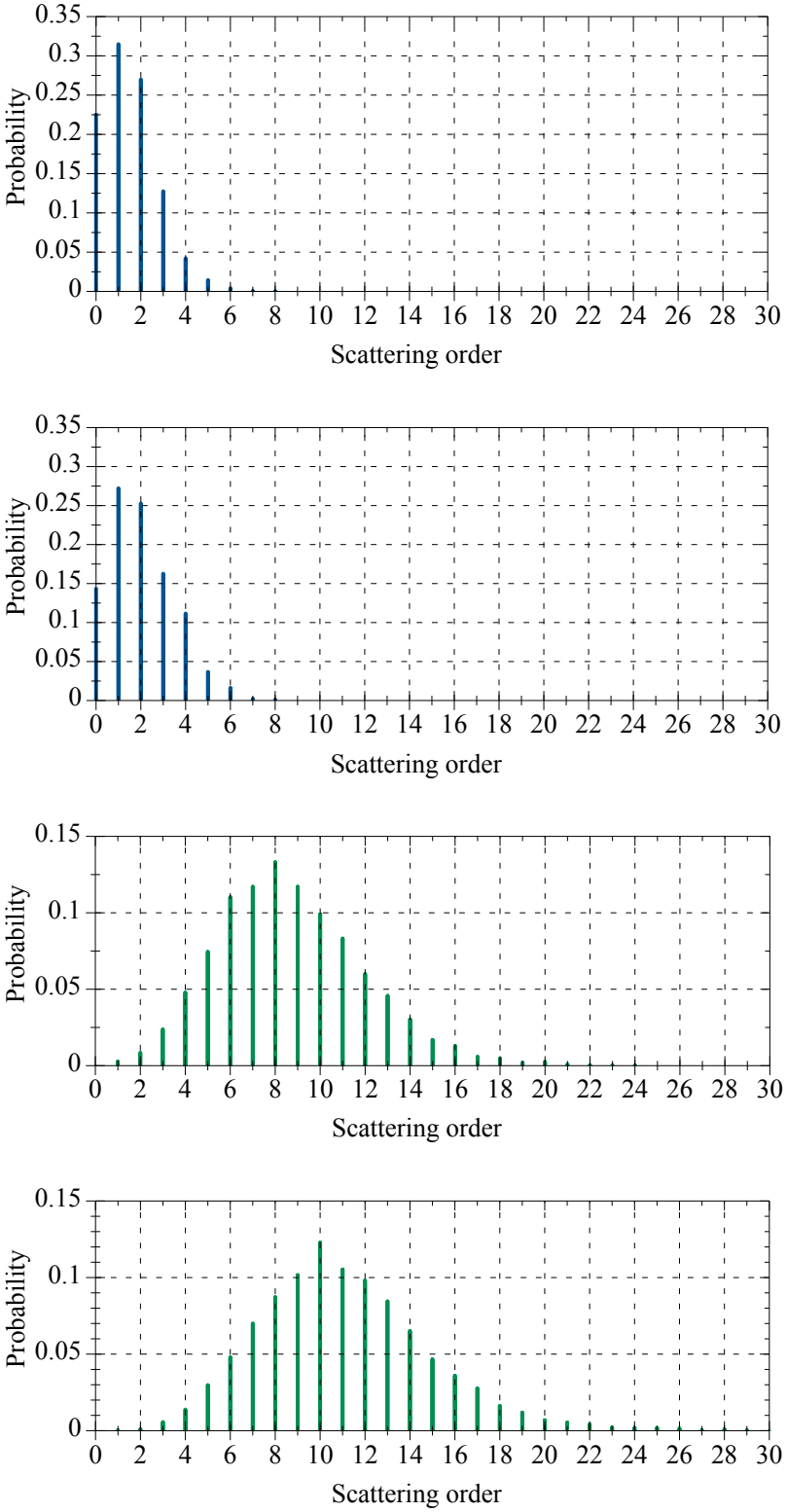

Figure 5.22: Scattering probability distribution based on MC simulations for Jerlov 1B oceanic and Jerlov 3C coastal water types, each for a narrow and wide beam angle.

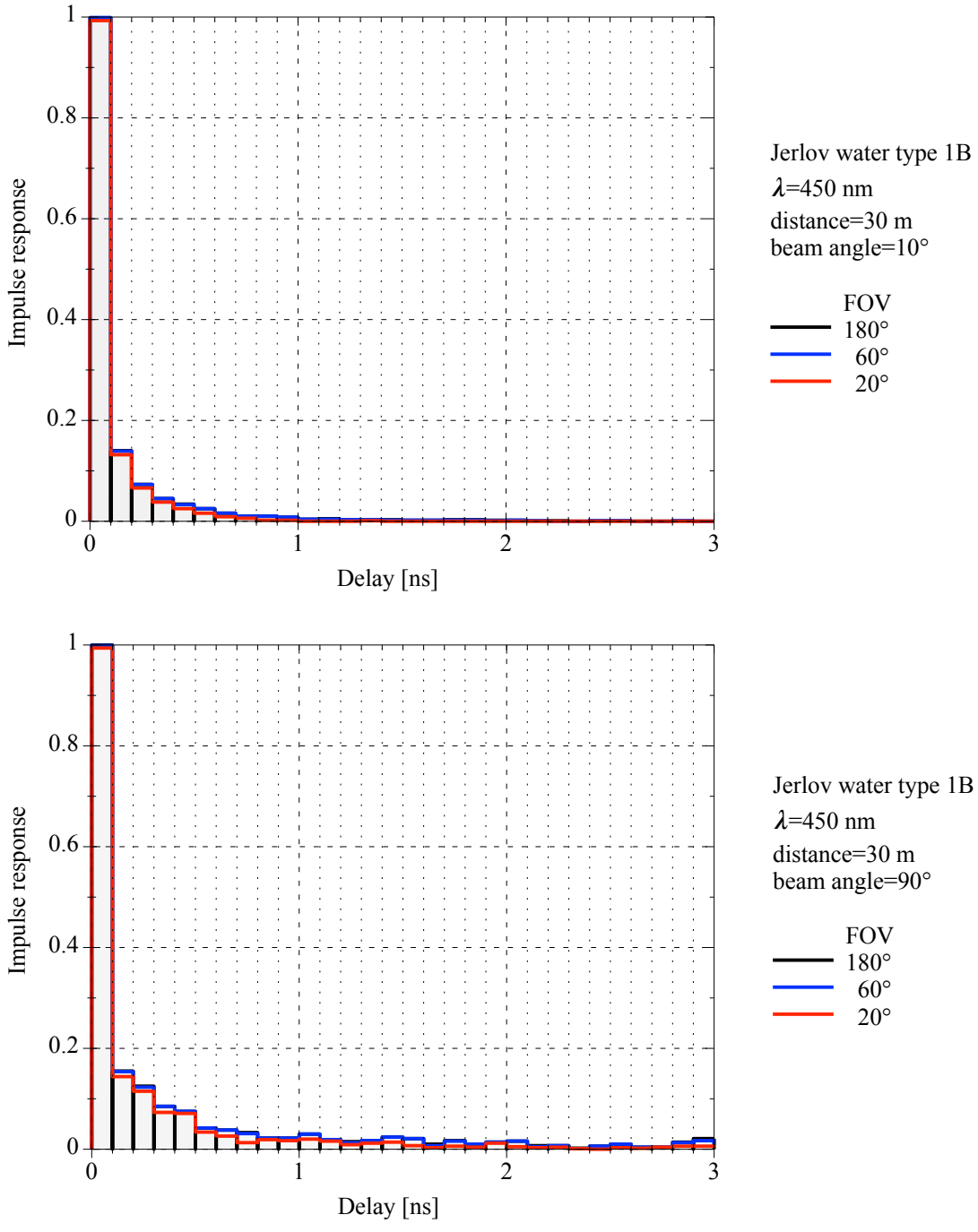

Figure 5.23: Delay distribution for different FOVs, based on MC simulation for Jerlov 1B oceanic water type, each for a narrow and wide beam angle.

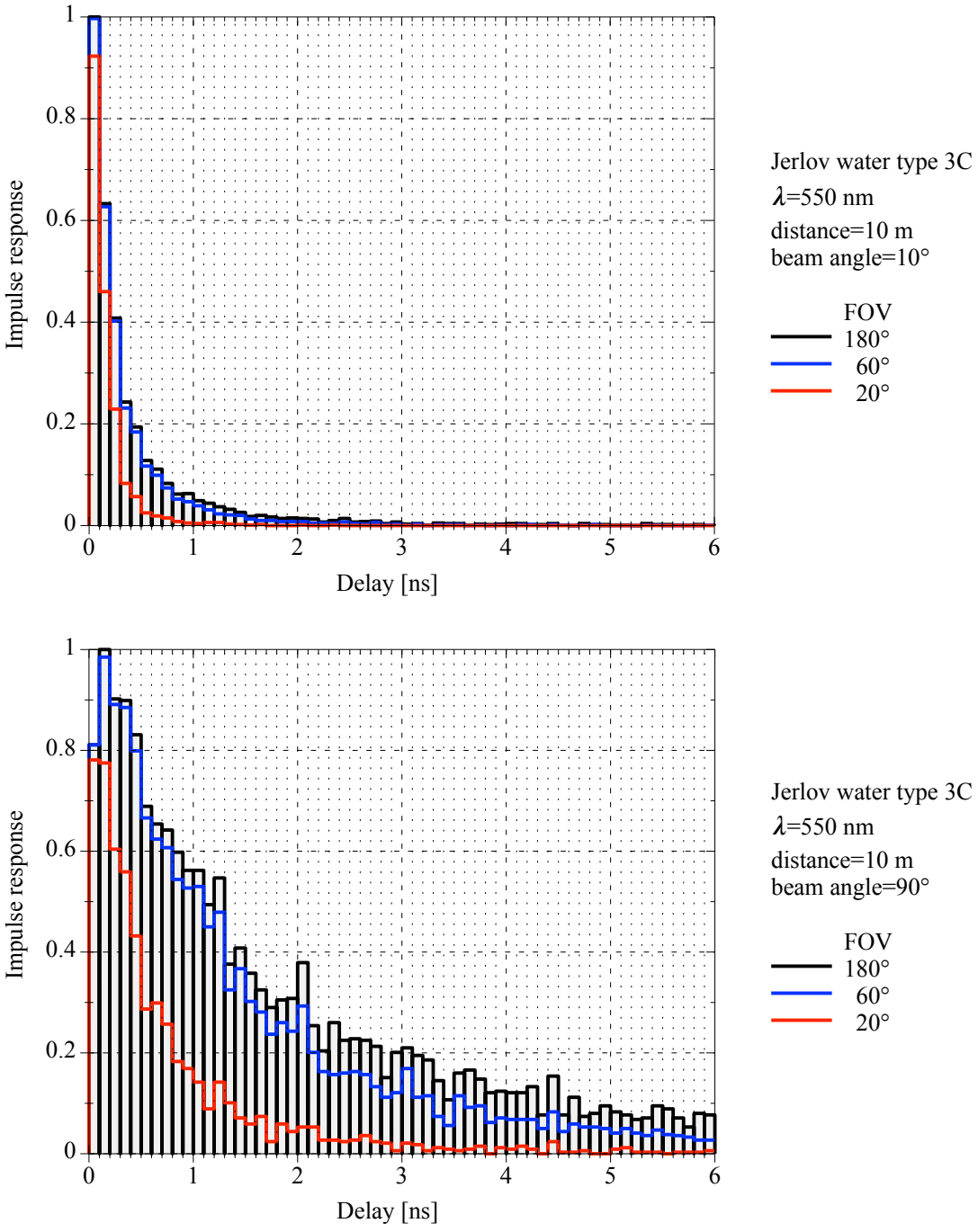

Figure 5.24: Delay distribution for different FOVs, based on MC simulation for Jerlov 3C coastal water type, each for a narrow and wide beam angle.

5.3 Experimental Determination of System Attenuation Coefficients

The method presented here and its appication in the field have their origin in the authour's contribution which examines of the potential of converted green LEDs for use in coastal water [35]. In a comparison of these LEDs with direct color types, the yielding system attenuation coefficient plays a major role. A practical approach to determine this coefficient, referred to as k_{sys}, is described. The instruments and equipment dedicated to underwater use are introduced, repeated field test in natural water are presented, as well as in situ reference measurements by an oceanographic spectrophotometer. The available technical data of the equipment provides good prerequisites for setting up simulations. Finally, the results of the measurements and the simulations are compared.

5.3.1 Development of the Procedure

In the following section, the approach is described on how the system attenuation coefficient k_{sys} can be determined from irradiance measurements at different distances.

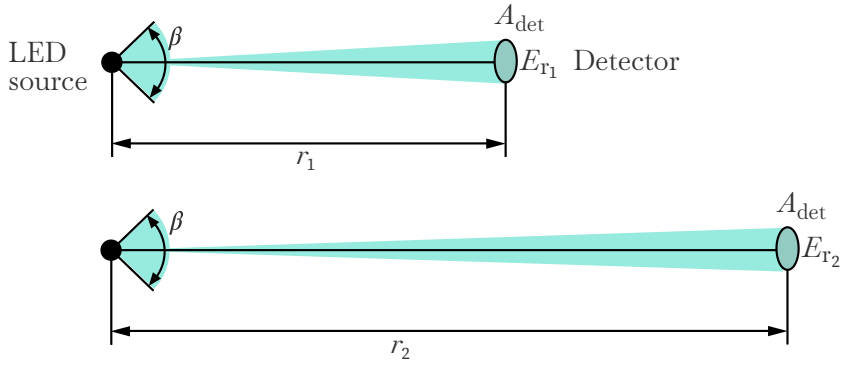

Figure 5.25: Geometric layout of the experimental setup.

The irradiance E (in W/m^2) collected by the active area A_{det} of the PD (in m^2) and the responsivity $\mathcal{R}$ (in A/W) determine the detector current I_{det} (in A):

$$I_{\mathrm{det}} = E \cdot A_{\mathrm{det}} \cdot \mathcal{R}. \tag{5.15}$$

For a point source in vacuum the ratio of the irradiances (E_{r_1} and E_{r_2}) at two distances r_1 and r_2 follows the inverse square law and is given by:

$$\frac{E_{\mathrm{r}_1}}{E_{\mathrm{r}_2}} = \frac{{r_2}^2}{{r_1}^2}. \tag{5.16}$$

An LED is assumed as a point-source with isotropic characteristic within the beam angle β, see Fig. 5.25. The link budget of a system comprises the properties of the transmitter, the medium and the receiver. A setup in a LOS configuration without inclinations represents the base case. For these circumstances and according to [3] this causes a received optical power at the detector of:

$$P_{\mathrm{Ropt}} = \frac{P_{\mathrm{Topt}}}{\pi \cdot r^2 \cdot \tan^2(\beta/2)} \cdot e^{-k \cdot r} \cdot \frac{\pi \cdot D^2}{4}. \tag{5.17}$$

P_{Ropt} is the received power and P_{Topt} is the transmitted power (both in W). The beam angle is represented by β, the distance r is in m, and the general attenuation coefficient k has the unit 1/m. D stands for the detector aperture diameter in m. Let us denote the attenuation coefficient

as k_{sys}, which is valid for the specific setup and the particular conditions for a certain wavelength. Substituting k for k_{sys} and using the detector area A_{det} instead gives:

$$P_{\text{Ropt}} = \frac{P_{\text{Topt}}}{\pi \cdot r^2 \cdot \tan^2(\beta/2)} \cdot e^{-k_{\text{sys}} \cdot r} \cdot A_{\text{det}}. \tag{5.18}$$

In this form, the power is projected onto a flat surface, thus is only correctly applicable for small beam angles up to a few degrees. Without this disadvantage, alternatively the transmitter area term could also represent the area of a spherical crown, which leads to:

$$P_{\text{Ropt}} = \frac{P_{\text{Topt}}}{2 \cdot \pi \cdot r^2 \cdot (1 - \cos(\beta/2))} \cdot e^{-k_{\text{sys}} \cdot r} \cdot A_{\text{det}}. \tag{5.19}$$

The irradiance E at the receiver at a distance r can be expressed as:

$$E_{\text{r}} = \frac{P_{\text{Ropt}}}{A_{\text{det}}}. \tag{5.20}$$

Solving for P_{Ropt} at two distances r_1 and r_2 results in:

$$P_{\text{Ropt\_r}_1} = E_{\text{r}_1} \cdot A_{\text{det}} \tag{5.21}$$

$$P_{\text{Ropt\_r}_2} = E_{\text{r}_2} \cdot A_{\text{det}}. \tag{5.22}$$

Inserting (5.21) into (5.19), and (5.22) into (5.19) yields:

$$E_{\text{r}_1} = \frac{P_{\text{Topt}}}{2 \cdot \pi \cdot r_1^2 \cdot (1 - \cos(\beta/2))} \cdot e^{-k_{\text{sys}} \cdot r_1} \tag{5.23}$$

$$E_{\text{r}_2} = \frac{P_{\text{Topt}}}{2 \cdot \pi \cdot r_2^2 \cdot (1 - \cos(\beta/2))} \cdot e^{-k_{\text{sys}} \cdot r_2}. \tag{5.24}$$

Forming the quotient of E_{r_1} and E_{r_2} leads to:

$$\frac{E_{\text{r}_1} \cdot r_1^2}{E_{\text{r}_2} \cdot r_2^2} = \frac{e^{-k_{\text{sys}} \cdot r_1}}{e^{-k_{\text{sys}} \cdot r_2}}. \tag{5.25}$$

Finally, solving for k_{sys} results in:

$$k_{\text{sys}} = \frac{\ln\left(\frac{E_{\text{r}_1} \cdot r_1^2}{E_{\text{r}_2} \cdot r_2^2}\right)}{-r_1 + r_2}. \tag{5.26}$$

Hence, at least two irradiance measurements at different distances and otherwise identical conditions needs to be carried out to determine the associated k_{sys}. More measurements would of course be useful for confirming the persistence of the determined value. Analogous to E_{r_1} and E_{r_2}, the proportional quantities $I_{\text{det}_{\text{r}_1}}$ and $I_{\text{det}_{\text{r}_2}}$ or $P_{\text{R}_{\text{r}_1}}$ and $P_{\text{R}_{\text{r}_2}}$ can also be used, depending on accessibility. Further rearrangement delivers the attenuation as a ratio of the irradiances at the respective distances r_1 and r_2 [43]:

$$\frac{E_{\text{r}_1}}{E_{\text{r}_2}} = e^{-k_{\text{sys}} \cdot (r_1 - r_2)} \cdot \left(\frac{r_1}{r_2}\right)^2. \tag{5.27}$$

5.3.2 Experimental Setup

The experiments were designed to compare the performance of LEDs of different wavelengths with respect to UOWC in a real environment. In addition to suitable housings, this also requires adapted designs and parameters. The implementation of (5.26) to determine individual system attenuation coefficients demands variable distances as well as reproducible accurate intensity detection at the receiver position. At this point it should be noted that k_{sys} is only valid for the specific test setup, the actual water conditions, and the approximate peak wavelength of the light source, since the LED is not-monochromatic. The source power and the radiation pattern do not need to be known for k_{sys} determination, as long these are not changed during the measurements. However, they are still important for subsequent and more in-depth analysis.

LED source

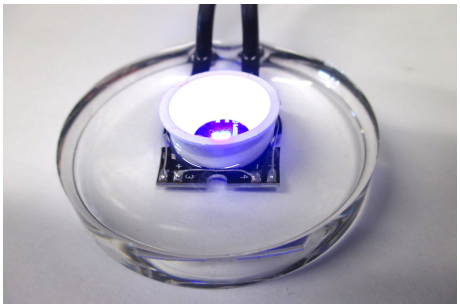

Figure 5.26: LED source including a reflector in pressure-neutral cast technology.

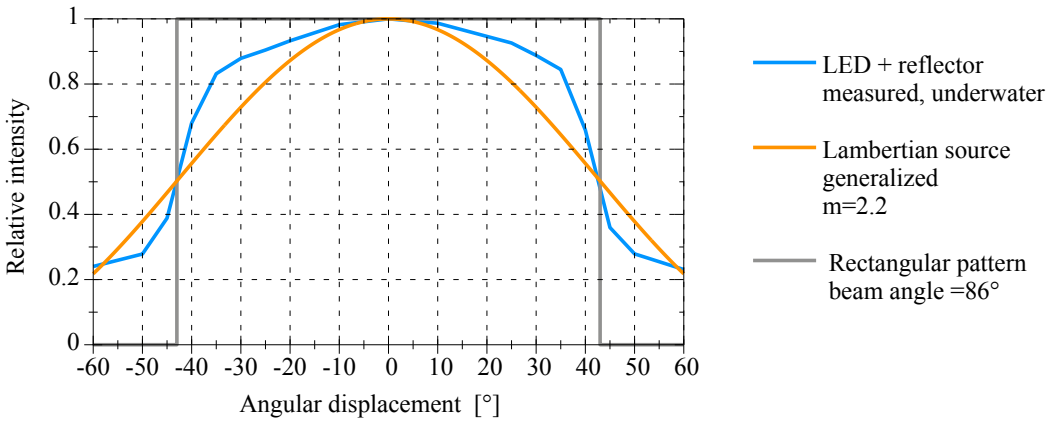

Figure 5.27: Underwater radiation pattern of applied light source, and for comparison a generalized Lambertian source, as well as a rectangular beam pattern.

Corresponding to the wavelengths of the least attenuation window of coastal water, blue and green direct color LEDs and converted green ones were used. Four of each of these power surface mounted device (SMD) LEDs were mounted on a metal printed circuit board (PCB) for better heat dissipation. To reduce the very large beam angle of these planar type LEDs, a reflector was mounted. Finally the assemblies were moulded in transparent polyurethane, according to the concept of a pressure-neutral cast underwater housing, see Fig. 5.26. The resulting beam pattern was recorded underwater on a goniometer installation. Figure 5.27 shows this curve including the base characteristics for the same beam angle. LEDs of Lumileds Luxeon LXZ1 series with part numbers PR01, PM01, PX01 were used [62], and operated at a forward current I_F of 300 mA.

Detector

A precision light meter equipped with an irradiance detector head in a waterproof version was selected as a receiver (Gigahertz-Optik P9710-4 optometer and RW3703 WQ detector head). This sensor features a glass dome port, a cosine correction and a circular diffusor of 11 mm diameter, resulting in 95 mm^2 of detector area, see Fig. 5.28. This means that the characteristics are similar to a typical large area flat substrate PD of a UOWC system. Furthermore, this sensor features a flat responsivity in the visible wavelength range and a calibration curve is offered by the manufacturer. For the comparative measurements to be made, the rather poor absolute accuracy of irradiance measurements is secondary, but the generally good linearity over a wide range is beneficial.

Figure 5.28: Irradiance detector in a dome port housing.

Rig and Application

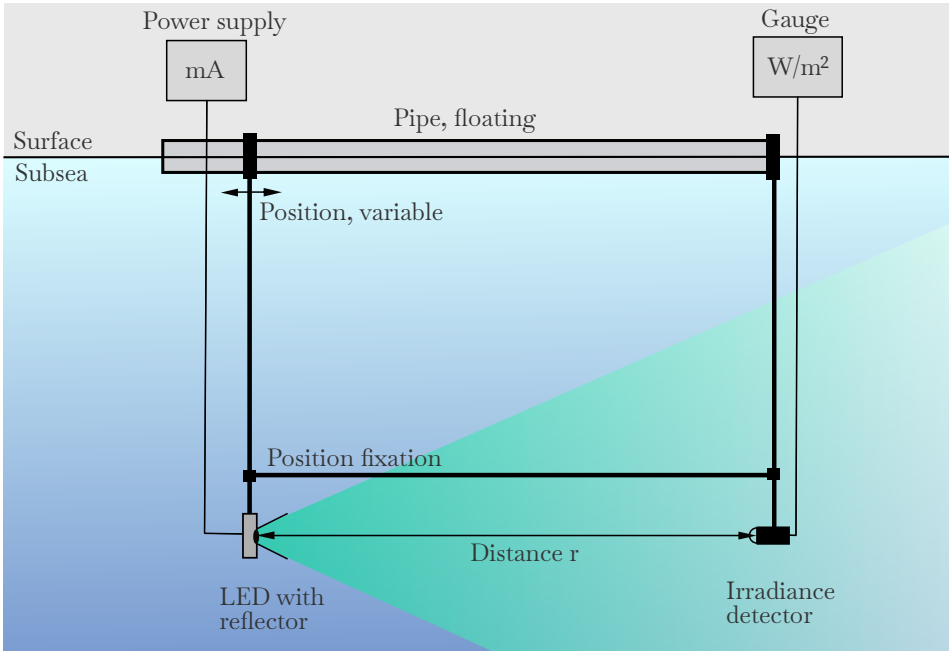

Figure 5.29: Experimental setup for the determination of k_{sys}.

The main factors for planning and executing underwater tests in the Baltic Sea are natural attenuation conditions in the seawater, no reflections from pool walls, and the good accessibility due to geographical proximity. A boundary condition for the test setup is LOS without inclination of the LED source and the light sensor, so carefully alignment is mandatory. Also, depth and distance of the LED(s) and detector should be kept at a certain ratio in order to minimize surface reflections. A sketch of the setup used in the experiment is shown in Fig. 5.29. The base is formed by a floating closed pipe with a length of 3 meter. The LED and the detector are guided on metal rods at a depth of 1 m, and the horizontal distance is variable. An additional fixation is used for accurate distance settings and to suppress oscillations caused by currents. The operation is carried out from a moored boat in deeper water.

Water Parameter Reference Measurements

The water parameters of the same position and depth are subject to multiple natural variations due to: season, currents, particle and freshwater entries etc. Of course the parameters cannot be actively changed, as might be possible in a tank with some effort, cf. Section 2.2.1. In any case, it is important for later work that comprehensible parameters are recorded, e.g., measuring

spectral absorption and attenuation curves by oceanographic instruments [21]. In order to obtain these independent reference values, an underwater spectrophotometer (AC-S, WetLABS, U.S.A.) was used for in situ measurements [226]. During this experimental campaign the instrument was deployed two times with 10 days separation.

5.3.3 Results of Measurement Campaign

Five experiments were undertaken in the summer of 2016 within a two month period in the Eckernfoerde Bay at coordinates 54N28.490 9E50.803. The intention was to evaluate the proposed method, to determine the individual k_{sys} of the three different colored LEDs, and to improve the setup. The hope was to find different conditions on the respective measurement days. As spectrophotometer was only available for a limited period of time, and it could only be deployed on two field test dates with relatively clear water conditions. The measurements on both days look comparable at first view, but they differ significantly in the ratios of absorption to scattering, which leads into a large variation of the albedo. Therefore, further examination of both days is required. The water conditions were found to be in the range of Jerlov water type 1C to 3C, see Fig. 5.30. These two samples show how rough the classification model actually is and that the real curves can take other shapes. After looking at the reference measurements, the changeover to the

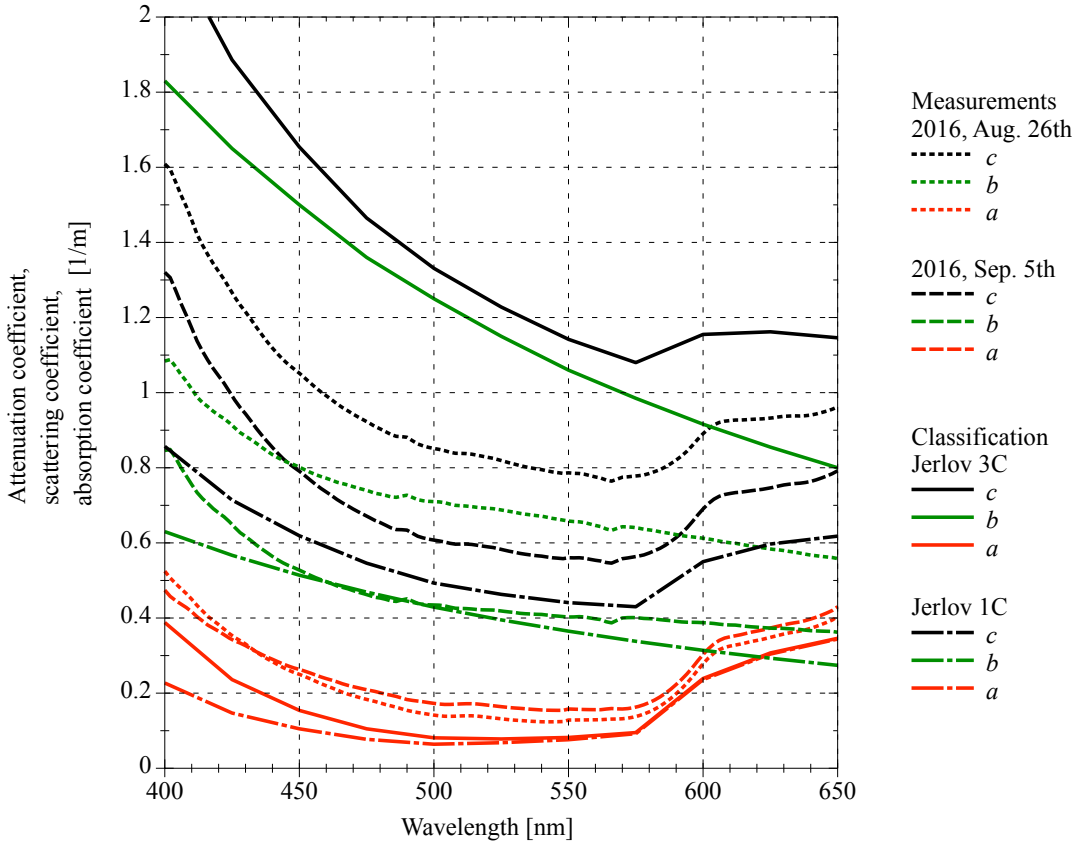

Figure 5.30: Comparison of measured absorption, scattering and attenuation data with the Jerlov water type classification.

core of the measurement series can take place. The three differently colored LEDs form the device under test (DUT), and let us name the related individual system coefficients k_{sysblue}, k_{sysgreen}, and $k_{\text{sysconvgreen}}$, respectively. The approximate peak wavelength of the LEDs (since they are not-monochromatic) are set to 450, 530 and 550 nm for further examinations. The quality of the determined values is largely influenced by three factors: right distances, stable source radiation

and precise detection. In this experiment distances of 0.4 - 0.8 m were used for r_1, and 1.3 - 2.2 m for r_2. The distance squared law, the avoidance of difference formation of equal values and the residual ambient light must be taken into account at the selection. Since the distances are squared in the calculation, accuracy and reproducibility are also important. The next issue is a stable operation of the particular LED source, both during the measurements and especially after adjusting the distances. For this purpose, both the constant forward current I_F and the voltage U_F of the four LEDs in series were monitored, which would allow a correction in the event of a drift, assuming the radiant efficiency of the LED is linear in this narrow range. The irradiances were recorded in a measuring range with constant resolution. Since the measurements were conducted under natural conditions, signal variations due to scattering from particles drifting in the current were averaged by using the maximum integration time of 5 seconds. Despite the fact that the measurements were carried out under difficult conditions in the deepest night, existing moonlight and passing clouds showed unexpectedly large effects. Therefore ambient light values and meter offset had to be taken into account. The light cone under water must be observed during the measurements so that temporary disturbances caused by passing jellyfish, algae and seaweed can be avoided. For each LED source, irradiance measurements were performed at four distances on each measurement day, from which the respective k_{sys} was determined, and the resulting mean value was used. Five measurements were performed at the same location with the same equipment

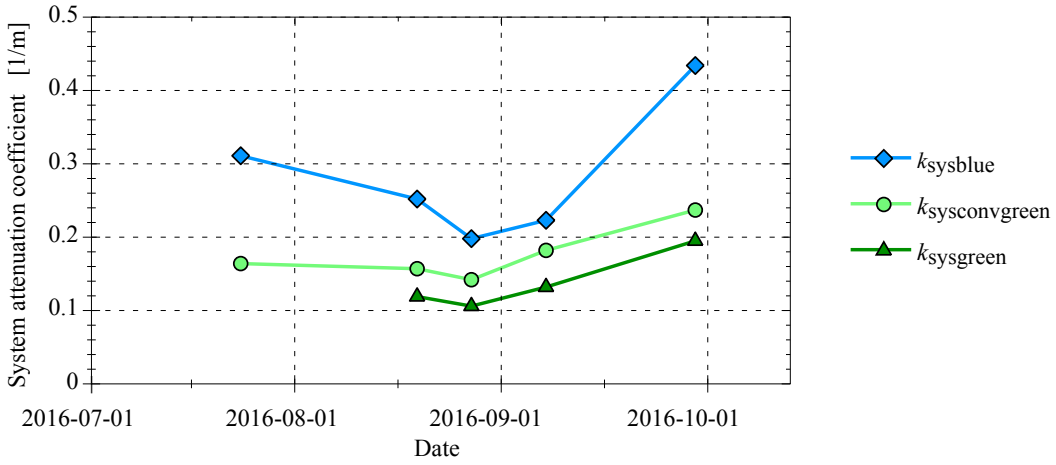

Figure 5.31: Variability over time of the system attenuation coefficient for different LED colors, respectively wavelengths.

over a period of more than two months, allowing a small insight into the natural variability of the water in terms of the impact on k_{sys}, see Fig. 5.31. A variabilty of factor two between the lowest and highest values for one wavelength were observed, and even higher differences are likely to arise within a period of a year. The second even more important result of the measurement series is the position of the data points relative to the reference measurements of the spectrophotometer. This comparison of the determined k_{sys} with the attenuation, absorption and scattering coefficients measured by the AC-S is presented in Fig 5.32. On both days the determined values for k_{sys} were close and slightly below to the absorption coefficient values, which indicates negligible loss due to scattering at these short distances. When comparing the values of k_{sys} for green and converted-green LEDs, converted green show higher k_{sys} values. This effect is related to a significant part of the spectral bandwidth above 580 nm, see Fig. 3.6. Since the absorption increases in this area, it leads to the effective average for converted green beeing higher compared to single wavelengths of 530 or 550 nm. Mostly immune to such impact are the non-converted LEDs due to the small optical bandwidth, independent of the center wavelength. The values determined for $k_{sysblue}$ and $k_{sysgreen}$ are both slightly below the physical bound of the absorption value on both days. Nonlinearity

of the irradiance measurements and uncertainties in the distance settings can be ruled out as the main cause, since typical magnitudes of these do not have a large enough impact. It is more likely that the measured values for E_{r_2} are slightly too high due to a minor portion of total reflections at the water surface. The geometry of the setup should actually prevent this, but the rippled water surface as well as the non-ideal reflector with significant intensity components outside the nominal beam angle promote this. Assuming this proportion is 5 % of the measurement at r_2, and E_{r_2} is reduced accordingly, this would yield a 20 % increase in k_{sys} at the given conditions. Thus the points for $k_{sysblue}$ and $k_{sysgreen}$ would lie above the absorption curve.

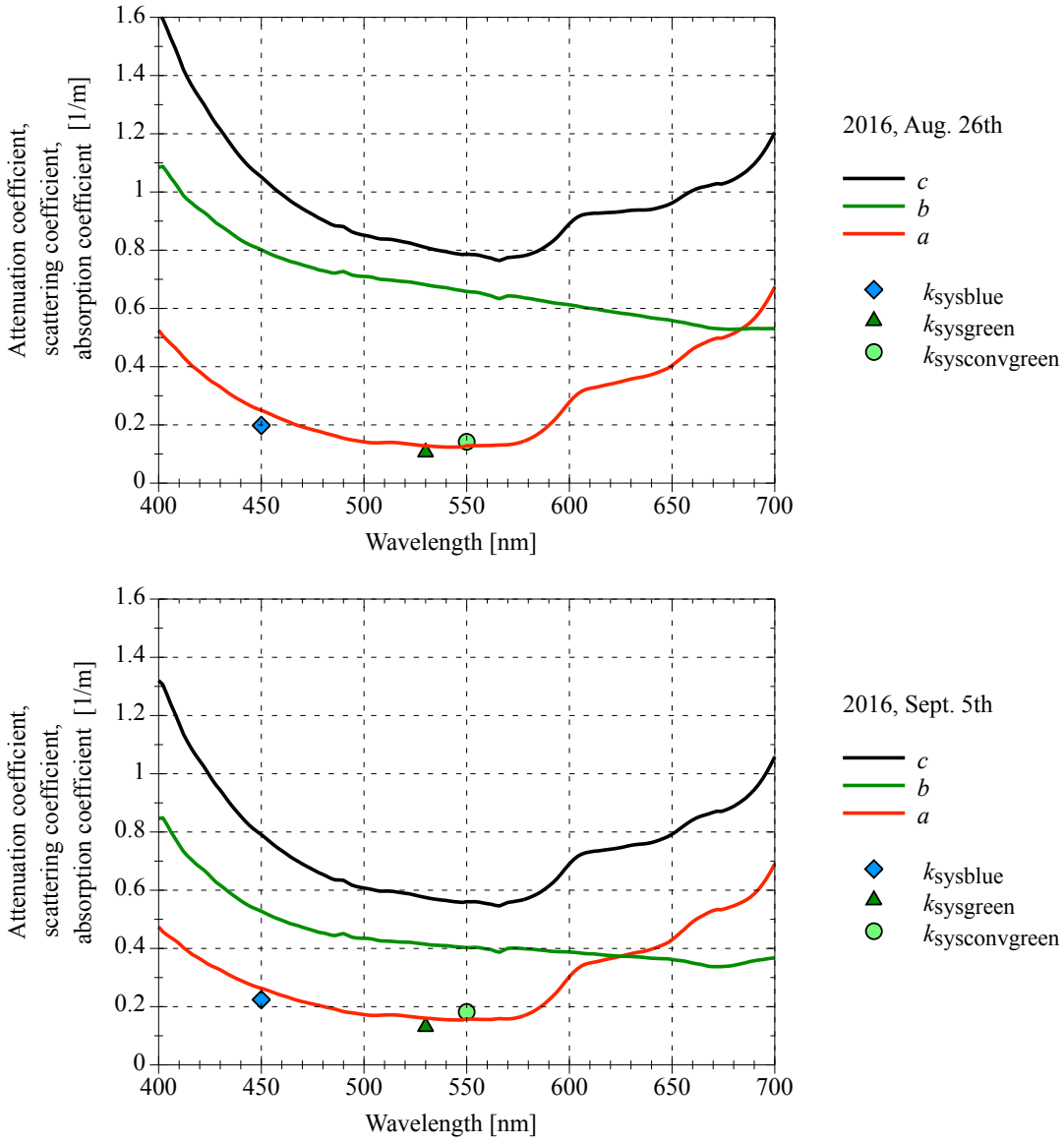

Figure 5.32: Measured absorption, scattering and attenuation curves based on spectral photometer measurements on two days with different conditions. Additionally, the determined k_{sys} datapoints for three different colored LEDs are given. Based on own measurements for [35].

5.3.4 Verification by MC Simulation

The available independently measured water parameters, as well as the known technical data of the LED source and the receiver, allow to set up corresponding MC simulations to verify the determined k_{sys} values. However, not all parameters can be transferred directly, some have to be adjusted, and others are predefined. Therefore, some of the parameter given in Table 5.7 are explained below.

The beam pattern of the source as given in Fig. 5.10, is set to be isotropic (rectangular) for the simulation. The only other possible choice would have been a Gaussian-shaped pattern, and the impact is likely to be small, cf. Fig. 5.12 for Jerlov 3C water type. The detector FOV is set to 180°, to match the sensor characteristic including the dome port. The use of the same small detector area as that of the sensor in conjunction with the wide beam angle would result in inefficient and thus more inaccurate simulations, therefore the area is increased by a factor of 100. The distances are set to 1 and 2 meters, so generally in the same range as the variable distances of the measurements, whereby the smaller distance was increased slightly to reduce geometric errors. As in the previous simulations, it is important to achieve low variances and stable average values in conjunction with the maximum number of photons per run, and a reasonable number of runs.

Figure 5.33 presents detailed sections of Fig. 5.32 for the two days of the spectrophotometer reference measurements including the k_{sys} simulation results, as well as the values determined by irradiance measurement and the absorption curve. The data points represent the average value of four measurement-based values and ten simulation-based values. In addition, the 2-sigma error bars are indicated. The accuracy of the AC-S spectrophotometer is specified as ±0.01 1/m within a spectral range of 400 to 730 nm, thus the error corresponds approximately to the line thickness.

Basically, the conditions of these simulations are fairly similar to those in Section 5.2.1, for water type Jerlov 3C at a beam angle of 90°. Therefore, it can be expected that the simulated k_{sys} values will also be slightly above the absorption curve, which is indeed confirmed. Possible causes for the measurement-based k_{sys} values being too low are explained in Section 5.3.3.

Table 5.7: Parameters used in the MC simulations for verification of the determined k_{sys} values.

Water type		Baltic Sea	
Wavelength	λ	450, 530, 550	[nm]
Beam angle	β	86	[°]
Beam pattern		rectangular	
Attenuation coefficient	a	Table C.12	
Scattering coefficient	b	Table C.12	
Scattering function		Fournier-Forand	
Distance	r	1, 2	[m]
Detector area	A_{det}	100x100	[mm^2]
Field of view	β	180	[°]
MC runs per datapoint		10	
Photons per run		$5 \cdot 10^7$	

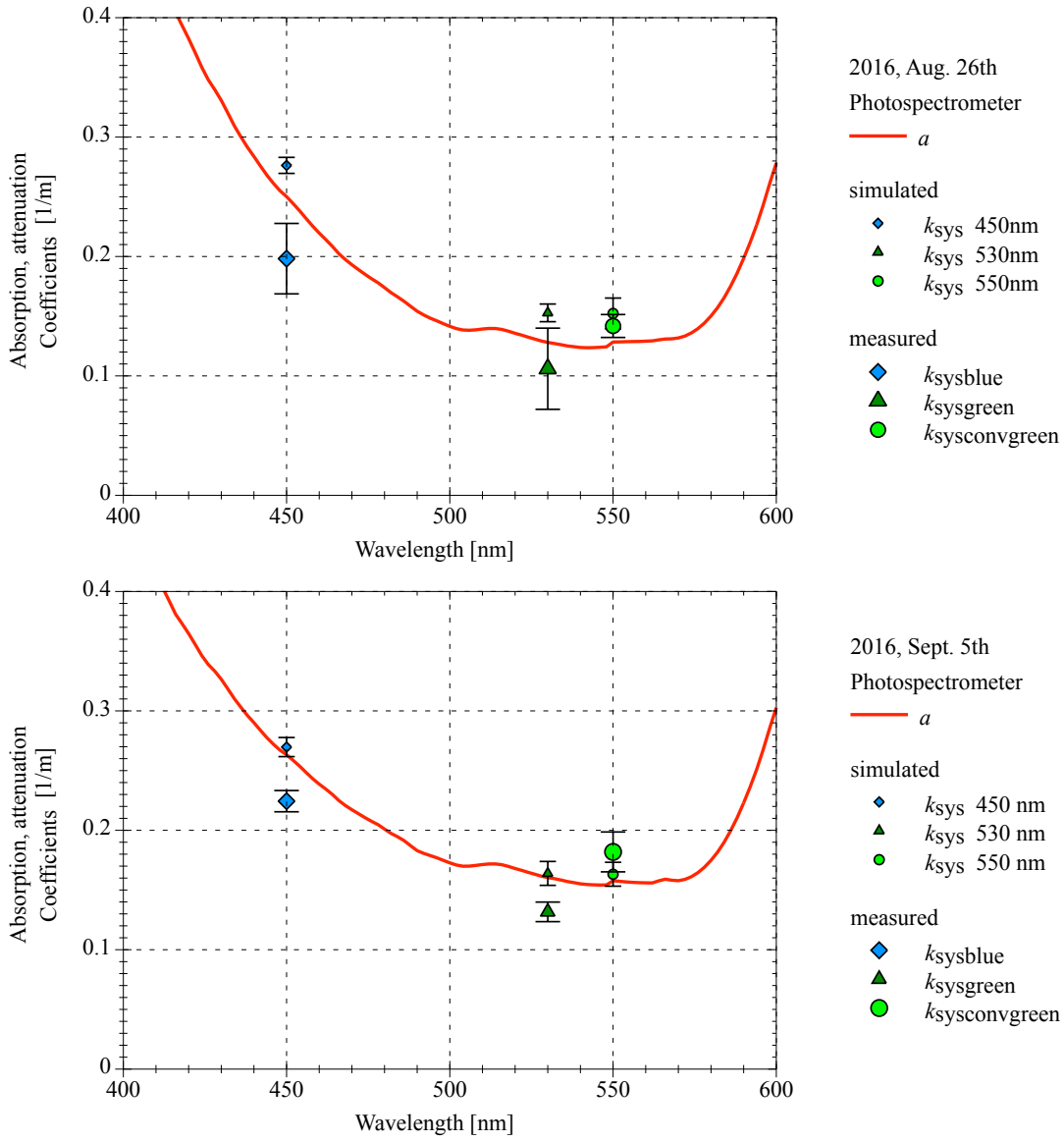

Figure 5.33: Detailed view for comparison of the measured and simulated k_{sys} values for both measurement days, as well as the respective absorption curves for better orientation.

5.4 Chapter Summary

In this chapter, the Monte Carlo simulations for underwater light propagation have been conducted, and the choice of a software solution to realize own simulations is described. Assumptions and adaptions required for the underwater environment are given. The MC functional principle is explained, according to the different stages that the generated photon packages pass through: initializing, traveling, termination and reception.

The aim of the MC application has been to determine the individual system attenuation coefficients k_{sys} in order to enable better predictions by the link budget. Primarily, k_{sys} depends on the water type, the wavelength and the beam angle. The beam attenuation coefficient c and the absorption coefficient a limit the theoretical range of k_{sys}. A large number of individual simulations are required to generate a meaningful spectral chart, and this has been accomplished in examples for a clear oceanic water type and a more turbid coastal type. The strong influence of the beam angle is confirmed, and the simulated curves exhibit correspondingly large spacings. A certain guideline is given by the diffuse attenuation coefficient K_{d}, which roughly coincides with a beam angle of 30°.

To strengthen the validity of the simulations with many influencing factors, it is appropriate to systematically vary individual parameters and to identify the respective effects. Variations of the distance and the FOV only lead to minor effects, whereas changes of the beam pattern or the scattering model can have a larger impact.

MC simulations have been performed including the recording of the complete photon paths, which allows subsequent examination of the delay and the exponential decay of the impulse response. Turbid coastal water in combination with a large beam angle and FOV, and including a long distance, represents a very demanding adverse application. An evaluation provides delay distributions in the order of a few nanoseconds, and thus is not critical for typically achievable LED bandwidths.

The experimental determination of k_{sys} through irradiance measurements at different distances has been developed. The setup for open water tests in the Baltic Sea is described. The results of the measurement series for different LED wavelengths over several weeks are presented, including parallel spectrophotometer reference measurements. The effect of the natural variation of the water on k_{sys} emerges. After parametrizing the properties of the utilized test devices, MC simulations have been run. A comparision of the measurements and simulations shows a relative good agreement, and the reasons for deviations are identified.

Chapter 6

Conclusions and Outlook

6.1 Conclusions

Today, high-performance communication is a key technology in almost all fields. This also applies to the underwater area, where a growing demand from different stakeholders can be recognized. Underwater optical wireless communication is advantageous for various applications, including networking, imaging, navigation and real-time operations.

This thesis investigates the underwater optical channel for LED-based short-range communication in multilateral aspects. The main focus is on the optical and electrical domain in the physical layer. The intention is to provide optimization strategies, to incorporate the interdisciplinarity, to determine limits and feasibility, to bridge theory and practice, and to support processes from design to operation.

In the visible light range, the water medium exhibits only a narrow wavelength band of low attenuation, which shifts from blue in oceanic waters and to green in coastal waters. LEDs matching these wavelengths are burdened by the green-yellow gap in efficiency, and the relation of fed-electrical to emitted-optical power becomes poor. This is an adverse effect, since energy is a major issue in underwater systems. A high overall efficiency is generally the aim, especially with mobile UOWC systems. The wavelength is thus a key parameter, since the photodetector adds a further dependency on it. A threefold relationship arises. An evaluation shows that for oceanic waters blue single-color LEDs are the most favorable choice. This does not apply analogously to green single-color LEDs in coastal waters, their performance is rather weak there. Converted-green LEDs prove to be a solution, as the spectrum of the high-efficient blue LEDs is shifted to green by a conversion layer. The efficiency advantages are contrasted by the speed and a larger spectral bandwidth.

Natural light can penetrate to depths of more than 100 meters, thus interfering UOWC operations. Conditions like location, sun position, cloudiness, water type and depth have a strong influence on the underwater ambient light field. The spectral range is subject to changes with respect to position and width. The intensity decreases with the depth, and the structure transitions from direct to diffuse, but retains a certain directionality. The down- and upwelling irradiances are the important oceanographic quantities here. These unwanted light components generate noise in the detector, which cannot be separated later. Suppression to a certain degree can be achieved by optical bandpass filters, but the emission spectrum of the LED must not be cut too much. The analysis made allowed the determination of an optimum filter adaption. Filters of different types and bandwidths have been combined with a blue LED and examined under variation of water type, depth, and angle of incidence. The optical signal-to-noise ratio was improved by all filters, but the absorptive colored glass filters could not out-perform the sophisticated thin film filters. However, a better filter effect is accompanied by a significant spectral shift of the transmission zone in dependence of the angle of incidence. A weak optimum is found when the thin film filter passband equals the LED optical bandwidth, but AOIs exceeding 30° increasingly deteriorate a meaningful utilization.

UOWC systems include signal processing in the electrical domain, and the signal-to-noise ratio is one of the most important parameters here. This examination refers to the receiver side,

consisting of a photodetector that is exposed to ambient and signal light components, followed by a transimpedance amplifier for the conversion of the tiny detector currents into more viable voltages. PIN-PD and APD detectors of different sizes, specially selected for UOWC purposes, have been examined in an in-depth SNR analysis for various light conditions in order to determine the best option. The noise constituents considered include the thermal noise, ambient and signal light generated shot noise, and the dark current shot noise as well as the amplifier related noise. The gain of an APD also requires special consideration. A general SNR performance of the detectors under test has been computed for separately varied ambient and signal irradiances. A larger robustness against ambient light is generally seen in the PIN-PDs, but better sensitivity is observed in APDs. Large-area PIN-PDs represent are a good choice, as the missing gain is compensated by the large area, and shot noise components remain ungained. The former general conditions have been adapted to an environment prevailing in UOWC for further examination. A turbid oceanic water type is assumed, the ambient light is determined by the downwelling irradiance, a blue LED forms the signal source, and the photodetectors are equipped with a thin film bandpass filter. Due to the numerous dependencies, many parameters needed to be systematically varied in order to cover the diverse realistic circumstances. Simplified conclusions suggest that APDs are more capable in terms of the attainable range, but only in dark deeper water, otherwise large-area PIN-PD are a better performing choice. The detector's viewing direction has the most influence in clear and shallow conditions, and is reduced with depth and turbidity. A source power variation acts directly on the SNR (or range), but shot noise penalizes this effect with APDs. For reasons of efficiency, an increase in SNR should always be aspired on the receiver side first. The last finding within this area concerns the SNR optimization through a filter passband adjustment. The simulations result in a maximum effect at a passband width of 1.5 times the LED FWHM in shallower water for both detector types. Due to the many possible scenarios and influences, a general optimization is difficult or even impossible to achieve. Known or limited operation conditions are the prerequisites for effective optimization.

The possibility that LEDs can be operated as photodetectors has been known for decades, but is rarely noticed. Single-color power LEDs, which feature large die areas, have been examined in this respect with emphasis of a potential dual use in UOWC. A direct comparison of different colored LEDs from two series to an equally sized PIN-PD has been carried out. To obtain a comprehensive impression of the properties, measurements have been conducted in the spectral, temporal, and spatial domains. Unexpected results emerged, in a positive sense. The responsivity of the LEDs used as PDs reached values of more than the half compared to the genuine type, along with a pronounced bandpass character. The passband is significantly wider than the FWHM in the designated LED mode. Of decisive importance, however, is the position of these bands, or in other words the spectral overlap. This property showed a strong color dependence; the blue-green regime offered only a poor overlap, but the yellow-red regime has a much better overlap. The exhibited capacitance is a key factor for fast communication, but the tested devices showed comparatively high capacitances, which correspond to a limiting effect. The spatial domain remained unchanged. In summary, LEDs as PDs are an interesting low-cost alternative to PD-filter combinations for areas where reduced speeds and ranges are sufficient.

Housings and optical ports are indispensable components for UOWC assemblies. Electronic and optical devices need to be protected from the conductive and corrosive sea water. The basic types of pressure-resistant housings including a flat or a dome-shaped port have been compared with the alternative of transparent embedding in terms of the optical path. The light rays underlie changes at the media boundaries due to refraction and reflection. This has been theoretically analyzed for flat and dome ports, both for the transmitter and the receiver sides. The impact of refraction index variations and the significance of the source or detector position is demonstrated. Real LED-equipped source side assemblies in different configurations have been examined thoroughly by underwater goniometer measurements, and the corresponding calculations showed good agreement. Assemblies utilizing a flat or dome port exhibited quite different characteristics, but

the properties of the reference LED source in a thin transparent cast were barely changed. The largest potential for the usage in UOWC, including the favored hemispherical characteristic and the potential of integrating multiple elements, is clearly either with the dome port pressure housing or with a pressure-neutral potted solution.

The link budget is essential in communications, and for the case of UOWC the light propagation underwater is fundamental, which is generally described by the radiative transfer equation. As an alternative to following this mathematically highly demanding path, Monte Carlo simulations offer a method that is widely used and accessible. An MC simulation generates results by repeated random sampling based on probability and statistics. In this application, virtual photons are generated and tracked on their paths from the source to the receiver through the water medium, where absorption and scattering occurs. To access the link budget, the individual system attenuation coefficients k_{sys} need to be determined via MC. k_{sys} is primarily depending on the water type, the wavelength and the beam angle. The boundaries are the beam attenuation coefficient c and the absorption coefficient a. A large number of individual simulations have been executed in order generate meaningful spectral k_{sys} curves for an oceanic water type and a coastal one, respectively. The results show a strong influence of the beam angle and the wavelength. The importance of an individual k_{sys} coefficient versus a simplified application of a, c or the diffuse attenuation coefficient K_{d} is clearly demonstrated. As the simulations performed rely on many further parameters, these were varied individually to identify the respective effects, and finally to strengthen the validity of the simulations. Minor impacts resulted from variations of the field of view and the distance only, and more distinct effects were obtained by the modification of the beam pattern or the scattering model. The complexity and the importance of simulations in this regard is revealed. However, the limitations of MC simulations also become clear, as the amount of photons which can be generated and processed is finite, and the efficiency at large beam angles and distances can become so low that no meaningful quantities can be received for evaluation.

By means of sophisticated MC simulations, versatile data sets have been generated, including complete information on the photon paths. This allowed the subsequent extraction of important properties for signal transmissions; in this case the delay and the exponential decay of an impulse response. A worst case scenario was created, including a long distance in turbid coastal water, a large beam angle and a wide field of view. The analysis yields delay distributions in the single nanosecond range, which can be classified as non-critical in terms of typical LED rise- and fall-times.

Since the k_{sys} depends on the system characteristics and the environmental conditions, it is possible to determine it experimentally for a real case. The method is based on underwater irradiance measurements at different distances, and a setup for open water tests in the Baltic Sea has been developed. Measurement series for different LED wavelengths over several weeks have been carried out, and reference measurements of the particular prevailing water parameters have been undertaken in parallel using a photospectrometer. MC simulations have been executed for the setup parameters and the measured water parameters to obtain k_{sys}. The results show a satisfying agreement of measurements and simulations, which validates the method. Another outcome is evidence of the large impact of the water natural variation on k_{sys}. Furthermore it has been confirmed, how essential independent reference measurements of the water parameters are.

In conclusion, the analyses and results of this thesis provide the UOWC community insight into the underwater optical channel between LED and detector, in the global context as well as in-depth in specific topics. This work also represents a solid foundation for subsequent aspects in the digital domain. The benefits are not only limited to communication system developers, but future users and neighboring areas can also take advantage of it.

6.2 Outlook

Since the establishment of the first UOWC systems more than two decades ago, the technology involved has made progress, but also the needs and applications have evolved. It is an interdisciplinary area, resulting in an uneven distribution of the respective research focuses, the merging of these still represents a weak point. Furthermore, there are certain gaps between theory and implementation, also recognizable in the lack of presented prototypes and documented field operations.

The work presented in this thesis is intended to provide a deeper insight into selected areas, but also to combine different topics. At the time of completion of this thesis, directions for further research can be identified that could provide valuable findings for the overall field.

Ambient Light Suppression

Optical filters, both in colored glass or thin film technology, exhibit fixed characteristics in terms of passband and transmission. They yield a substantial profit with respect to the signal-to-noise ratio when well configured, but cannot be adapted to environmental conditions. This can be achieved by the application of liquid crystal displays as dynamic plane filter, this technology has been applied in VLC [166, 167, 168, 227, 228, 229]. Another technique, the digital micromirror device (DMD), may be an alternative approach for UOWC due to size, speed and optical characteristics. A future approach may be a combination including a lens, an DMD and a bandpass filter in front of a photodetector. Finally, significantly improved suppression would extend the range of faster and more sensitive detectors towards shallow water and daytime operations.

LED as Photodetector

The pronounced bandpass characteristics and viable responsivities of the LEDs used as PDs pave the way for simple spectral measurements. In collaboration with a full spectrum white LED, it should be feasible to evaluate spectral components. The red channel is particularly critical for underwater imaging applications, as the increased attenuation leads to a lower SNR and thus reduced image quality. The spectral information obtained enables an adaption of an artificial light source to the water parameters and the distance, by enriching this spectral range using other color temperatures or a single-color supplement.

UOWC Assemblies

Underwater housings of any type are an unavoidable part of UOWC systems. Criteria, concepts and aspects have been described, as well as how the individual components form an optical assembly and influence the total characteristics. The implementation of compact hemispherical multi-segmented and MIMO-capable transducers, including vehicle integration and AUV field tests, would certainly be a next milestone. Furthermore, it is also to be expected that the additional integration of hybrid technologies will have an impact in this area [230, 17].

A promising alternative concept for further investigation is the use of thick plastic optic fiber. It serves as a light guide between the transmitter and receiver optics and the central housing hosting the LEDs and PDs. Issues to be examined include transmission losses and optical coupling, and in particular the pressure housing feedthrough.

Determination of the System Attenuation Coefficient

In this thesis, curve charts for k_{sys} have been generated by Monte Carlo simulations. These include examples for one oceanic and one coastal water type, and the obvious influence parameters have been investigated. The knowledge gained can be used as a base for further simulations in the

direction of a more comprehensive coverage and finally to improve modeling. In any case, this will allow the community to make better predictions of the signal level and the range. The use is not only limited to UOWC, but also in the field of underwater imaging, where artificial light is applied for object illumination. In addition to intensity calculations, it can also be used for distance related spectral tuning.

Appendix A

Acronyms and Abbreviations

AlGaInP	Aluminum gallium indium phosphide
AOI	Angle of incidence
AOP	Apparant optical property
APD	Avalanche photo diode
ASTM	American Society for Testing and Materials
AUV	Autonomous underwater vehicle
AWGN	Additive white Gaussian noise
BER	Bit error rate
CDF	Cumulative distribution function
CDOM	Colored dissolved organic matter
CHA	Cone half angle
CIE	International Commission on Illumination
CMOS	Complementary metal oxide semiconductor
CPC	Compound parabolic concentrator
CWL	Center wavelength
DEM	Demodulator
DMD	Digital micromirror device
DPIM	Digital pulse interval modulation
DPPM	Differential pulse position modulation
DUT	Device under test
ELF	Extreme low frequency
EM	Electromagnetic wave
FEC	Forward error correction
FET	Field effect transistor
FF	Fournier-Forand
FOV	Field of view
FSO	Free space optics
FWHM	Full width at half maximum
GaP	Gallium phosphide
GBW	Gain bandwidth
GUI	Graphical user interface
HG	Henyey-Greenstein
IEC	International Electrotechnical Commission
IM-DD	Intensity modulation direct detection
InGaN	Indium gallium nitrite
IOP	Inherent optical property
IR	Infrared

ISI	Inter symbol interference
J-FET	Junction field effect transistor
LCD	Liquid crystal display
LD	Laser diode
LED	Light emitting diode
LOS	Line of sight
MC	Monte Carlo
MF	Medium frequency
MI	Magnetic induction
MIMO	Multiple-input multiple-output
MISO	Multiple-input single-output
MOD	Modulator
NAP	Non-algae particle
NBW	Noise bandwidth
NEP	Noise equivalent power
NLOS	Non-line-of-sight
NRZ	Non-return-to-zero
NUV	Near ultraviolet
OC	Optical concentrator
OLED	Organic light emitting diode
OOK	On-off keying
OpAmp	Operational amplifier
OSNR	Optical signal-to-noise ratio
OTHG	One-term Henyey-Greenstein
PB	Pass band
PC	Polycarbonate
PD	Photodetector
PDF	Probability density function
PIN PD	Positive intrinsic negative photodetector
PH	Pressure housing
PMMA	Polymethyl methacrylate
PMT	Photo multiplier tube
PN	Pressure-neutral
POF	Plastic optic fiber
PPC	Parabolic profile concentrator
PPM	Pulse position modulation
PU	Polyurethane
PWM	Pulse width modulation
QE	Quantum efficiency
QLED	Quantum dot light emitting diode
RF	Radio frequency
ROV	Remotely operated vehicle
RSC	Reed Solomon
RTE	Radiative transfer equation
Rx	Receiver
SIMO	Single-input multiple-output

SiPinPD	Silicon positive intrinsic negative photodetector
SiPM	Silicon Photomultiplier
SISO	Single-input single-output
SM	Shift margin
SMD	Surface mounted device
SNR	Signal-to-noise ratio
SS	Sahu-Shanmugam
TCC	Truncated cone concentrator
TIA	Transimpedance amplifier
TIR	Total internal reflection
TTHG	Two-term Henyey-Greenstein
Tx	Transmitter
UOWC	Underwater optical wireless communication
UV	Ultraviolet
UVC	Ultraviolet band C
VIS	Visible
VLC	Visible light communication
VSF	Volume scattering function

Appendix B

Notations

a	Absorption coefficient, total
a_{CDOM}	Absorption coefficient, colored dissolved organic matter component
a_{M}	Absorption coefficient, total, Morel
a_{NAP}	Absorption coefficient, non algae particles component
a_{phyt}	Absorption coefficient, phytoplankton component
a_{w}	Absorption coefficient, water component
A_{chl}	Absorption model constant, chlorophyll specific, Morel
A_{det}	Area of detector
A_{G}	Parameter Gaussian approximation function
A_{LP}	Parameter Logistic power peak approximation function
A_{phyt}	Absorption model constant, Bricaud
b	Scattering coefficient
b_{l}	Scattering coefficient, large particles
b_{p}	Scattering coefficient, particles
b_{s}	Scattering coefficient, small particles
b_{w}	Scattering coefficient, water itself
B	Bandwidth, electrical
B_{phyt}	Absorption model constant, Bricaud
c	Attenuation coefficient
chl	Chlorophyll concentration
c_0	Speed of light
C_{D}	Capacitance of PD
C_{f}	Feedback capacitor of TIA
C_{G}	Parameter Gaussian approximation function
C_{l}	Concentration, large particles
C_{LP}	Parameter Logistic power peak approximation function
C_{s}	Concentration, small particles
d_{asdp}	Distance, apparent source dome port
d_{asfp}	Distance, apparent source flat port
d_{cr}	Distance, center receiver
d_{cs}	Distance, center source
d_{meas}	Distance, measuring
d_{sp}	Distance, source port
D	Diameter of detector aperture
e_{n}	Voltage noise density
e_0	Elementary charge
E	Irradiance

E_{amb}	Irradiance at photodetector, ambient component
E_{b}/N_0	SNR per bit
E_{d}	Irradiance, downwelling
E_{g}	Bandgap energy
E_{LED}	Irradiance of LED
E_{PD}	Irradiance at photodetector
$E_{\mathrm{r_n}}$	Irradiance at distance r_n
E_{s}/N_0	SNR per symbol
E_{sig}	Irradiance at photodetector, signal component
E_{u}	Irradiance, upwelling
f_{G}	Gaussian approximation function LED spectrum
f_{LP}	Logistic power peak approximation function LED spectrum
$f_{-3\mathrm{dB}}$	Cut-off frequency
F	excess noise factor of APD
$FWHM_{LED}$	Full width at half maximum optical bandwidth of LED
g_{HG}	Parameter Henyey-Greenstein CDF
G	Gain, electrical
GBW	Gain bandwidth product
G_{opt}	Gain, optical
h	Planck's constant
$h(t)$	Channel transfer function
i_{n}	Current noise density
i_{F}	Current, forward
i_{PD}	Current, photodetector
I_{amb}	Current of photodetector from ambient light
I_{d}	Dark current of photodetector
I_{db}	Dark current of APD, surface leaking component
I_{det}	Current, detector
I_{ds}	Dark current of APD, bulk leaking component
I_{e}	Radiant intensity, energetic
$I_{\mathrm{e,n}}$	Radiant intensity, normalized
$I_{\mathrm{e,PD}}$	Radiant intensity, energetic, photodetector
$I_{\mathrm{e,R}}$	Radiant intensity, energetic, receiver
$I_{\mathrm{e,T}}$	Radiant intensity, energetic, transmitter
$I_{\mathrm{e,0}}$	Radiant intensity, energetic, initial
I_{G}	Intensity Gaussian beam pattern
I_{L}	Intensity Lambertian beam pattern
$I_{\mathrm{LED_{norm}}}$	Radiant intensity LED, normalized
I_{PD}	Current, photodetector
I_{sig}	Current of photodetector from signal light
I_{Tmax}	Radiant intensity, maximum, transmitter
$I(\theta, \varphi)$	Source intensity function, normalized
J	spectral efficiency
k	General attenuation coefficient
k_{B}	Boltzmann's constant
K_{d}	Diffuse attenuation coefficient

k_{sys}	System attenuation coefficient
L	Cardinality
L_i	Radiance, ith
L_{opt}	Loss, optical
m	Mode number Lambertian pattern
n_{eff}	Refraction index, effective
n_{FF}	Parameter Fournier-Forand CDF
n_i	Refraction index, ith layer
$n_{\mathrm{Pr_n}}$	Number of photons detected at distance r_n
$n(t)$	Noise, additive
N_{R}	Number of receiver elements
N_{Rel}	Noise power, electrical at receiver
N_{shot}	Shot noise power
N_{T}	Number of transmitter elements
N_{therm}	Thermal noise power
NBW	Noise bandwidth
NBW_{e_n}	Noise bandwidth for voltage noise density
p	Pressure
$p(\theta)$	Probabilty density function of (θ)
P_{ambLight}	Power, ambient light
P_{el}	Power, electrical
P_{FF}	CDF of Fournier-Forand scattering model
P_{opt}	Power, optical
$P_{\mathrm{opt.Signal}}$	Power, optical, signal
$P_{\mathrm{opt.Noise}}$	Power, optical, noise
P_{PD}	Power at detector
P_{Rel}	Power, electrical at receiver
P_{Ropt}	Power, optical received
$P_{\mathrm{Ropt\_r_n}}$	Power, optical received at distance r_n
P_{sigLED}	Power, LED signal
P_{Topt}	Power, optical transmitted
$P(\theta)$	Cumulative distribution function of (θ)
PB	Bandwidth, passband
PB_{Filter}	Bandwidth of filter passband
Q	quality factor of pulse response
r	Distance
r_{dpi}	Radius, inner of dome port
r_n	Distance at position n
$r(t)$	Channel output signal
R_{b}	Data rate
R_{f}	Resistance, feedback
R_{i}	Shunt resistance of PD
R_{ij}	Reflectance, from ith to jth layer
$R_{\mathrm{p}ij}$	Reflectance, p-polarized from ith to jth layer
$R_{\mathrm{s}ij}$	Reflectance, s-polarized from ith to jth layer
$R(\lambda)$	Reflectance

$\mathcal{R}$	Responsivity
$\mathcal{R}_\mathrm{n}$	Responsivity, normalized
$\mathbb{R}$	Random uniform distributed number in the interval [0,1]
s	Geometric distance
s_p	Photon travel path length
$s(t)$	Channel input signal
S_CDOM	Absorption model exponential coefficient, CDOM, Bricaud
S_LP	Parameter Logistic power peak approximation function
S_NAP	Absorption model exponential coefficient, NAP, Bricaud
$S_\mathrm{R}(\gamma_\mathrm{R})$	Normalized angular distribution, receiver
$S_\mathrm{R}(\gamma_\mathrm{R,cos})$	Normalized angular distribution, cosine corrected, receiver
$S_\mathrm{T,norm}$	Normalized angular distribution, transmitter
SM	Bandwidth margin provided for filter's shift
t_dp	Thickness of dome port
t_fp	Thickness of flat port
t_p	Time of photon travel
t_pnc	Thickness pressure-neutral cast
t_r	Rise time
t_rd	Rise time of detector
t_rs	Rise time of source
T	Temperature
T_diffpeak	Transmittance of filter,peak, diffuse light
$T_\mathrm{Filterdir}$	Transmittance of filter, directed light
$T_\mathrm{Filterdiff}$	Transmittance of filter, diffuse light
T_{ij}	Transmittance, from ith to jth layer
$T(\lambda)$	Transmittance
U_amb	Voltage, produced by ambient light
$U_{\mathrm{n\_e_n}}$	Voltage, produced by voltage noise density
$U_{\mathrm{n\_i_n}}$	Voltage, produced by current noise density
$U_\mathrm{n\_shot\_dark}$	Shot noise voltage by dark current
$U_\mathrm{n\_shot\_amb}$	Shot noise voltage by ambient light current
$U_\mathrm{n\_shot\_signal}$	Shot noise voltage by signal light current
$U_\mathrm{n\_sum}$	Voltage, sum of all noise sources
$U_\mathrm{n\_th}$	Voltage, produced by thermal noise
U_out	Voltage, output
U_sig	Voltage, produced by signal
v	Phase velocity
V	Volume
W_G	Parameter Gaussian approximation function
W_LP	Parameter Logistic power peak approximation function
x	excess noise index of APD
$x(t)$	Waveform signal
z	Water depth

α	Field of view
$\alpha_{1/2}$	Half angle, field of view
β	Beam angle
$\beta_{\mathrm{d}}, \beta'_{\mathrm{d}}$	Angle, dome port geometry
β_{p}	Volume scattering function, particulate contribution
β_{w}	Volume scattering function, water contribution
$\beta_{1/2}$	Beam half angle
$\beta(\Psi)$	Volume scattering function, total
$\tilde{\beta_{\mathrm{p}}}(\Psi)$	Particle phase function
γ_{R}	Inclination angle, receiver
$\gamma_{\mathrm{R,cos}}$	Inclination angle, receiver, cosine corrected
γ_{T}	Inclination angle, transmitter
δ	Term variable in Fournier-Forand CDF
$\delta(\mathrm{r})$	Thickness element
$\delta(\mathrm{V})$	Volume element
$\delta(\Omega)$	Solid angle element
ϵ	Salinity
η_{el}	Wall-plug efficiency or radiant efficiency
θ	Scattering angle, polar
θ'	Scattering angle, polar, updated after scattering event
θ_{B}	Reflection angle, bottom
θ_{c}	Critical angle
θ_j	Angle, jth, incident or refracted
θ_{r}	Angle, final refracted
θ_{s}	Angle, incident, source
θ_{S}	Reflection angle, surface
κ	Shaping gain factor
λ	Wavelength
λ_{CWL}	Center wavelength
$\lambda_{\mathrm{diffcenter}}$	Center wavelength of filter passband, diffuse
$\lambda_{\mathrm{difflower}}$	Wavelength of filter passband, lower limit, diffuse
$\lambda_{\mathrm{diffupper}}$	Wavelength of filter passband, upper limit, diffuse
$\lambda_{\mathrm{PBcenter}}$	Center wavelength of passband
$\lambda_{\mathrm{PBlower}}$	Wavelength of passband lower limit
$\lambda_{\mathrm{PBupper}}$	Wavelength of passband upper limit
λ_{ref}	Reference wavelength, absorption
λ_0	Reference wavelength, scattering
μ_{FF}	Parameter Fournier-Forand CDF
μ_{x}	Direction cosine, x component
μ_{y}	Direction cosine, y component
μ_{z}	Direction cosine, z component
ν	Term variable in Fournier-Forand CDF
σ	Standard deviation
σ^2	Scintillation index
φ	Scattering angle, azimuthal
φ'	Scattering angle, azimuthal, updated after scattering event

$\Phi_\mathrm{a}(\lambda)$	Radiant power, absorbed
$\Phi_\mathrm{i}(\lambda)$	Radiant power, incident
$\Phi_\mathrm{r}(\lambda)$	Radiant power, reflected
$\Phi_\mathrm{R}(\lambda)$	Radiant power, received
$\Phi_\mathrm{s}(\lambda)$	Radiant power, scattered
$\Phi_\mathrm{t}(\lambda)$	Radiant power, transmitted
$\Phi_\mathrm{T}(\lambda)$	Radiant power, transmitted
Ψ	Scattering angle, polar
ω_n	Weight of photon package at event n
ω_0	Scattering albedo
Ω	Solid angle
Ω_0	Unit solid angle, 1 sr

Appendix C

Definitions and Supplementary Information

C.1 Simulation and LED Parameters for Section 3.1

Table C.1: System simulation parameters for extinction calculations.

Tx optical power	P_{opt}	1.0	W
Wavelength	λ	475, 550 monochromatic	nm
Beam angle	β	70°	
Beam pattern		rectangular, isotropic	

Table C.2: Water parameters for extinction calculations, extracted from [102].

Water type	λ [nm]	c [1/m]	K_d [1/m]	a [1/m]
Jerlov IB	475	0.0860	0.0325	0.0225
Jerlov IB	550	0.1159	0.0726	0.0623
Jerlov 3C	475	1.465	0.240	0.105
Jerlov 3C	550	1.142	0.187	0.082

Table C.3: Parameters of LEDs used for calculations and simulations.

Manufacturer, Type	Color	λ_{peak} [nm]	U_F [V]	Φ_v [lm]	P_{opt} [mW]
Lumileds, LXZ1 PR01	royal blue	448†	2.90	-	575
Lumileds, LXZ1 PB01	blue	474†	3.15	38	-
Lumileds, LXZ1 PE01	cyan	499†	2.95	82	-
Lumileds, LXZ1 PM01	green	519†	3.05	118	-
Lumileds, LXZ1 PX01	lime	541†	2.80	183.8	-
Lumileds, LXZ1 PL02	PC amber	595†	2.90	128	-
Lumileds, LXZ1 PL03	amber	597†	2.15	56	-
Lumileds, LXZ1 PH01	red orange	622†	2.15	65	-
Lumileds, LXZ1 PD01	red	632†	2.20	52	-
Lumileds, LXZ1 PA01	deep red	658†	2.25	-	350
Luminus, SFT10	conv. green	525	2.92	-	413
Osram, LCG H9RN	conv. green	516†	2.90	247	-

Values retrieved from data sheets [62, 147, 146] and by measurements(†). Typical values valid for $I_F = 500mA$ and 25°C.

Table C.4: Wavelength dependent parameters of comprehensive photocurrent simulation for different colored LEDs.

		deep blue	blue	cyan	green	conv. green
λ_{peak}	[nm]	450	475	500	520	515
P_{opt}	[W]	4.0	2.5	1.7	1.6	3.8
R	[A/W]	0.28	0.31	0.33	0.35	0.345
K_d Jerlov 1B	[1/m]	0.0342	0.0325	0.0386	0.0535	0.0498
K_d Jerlov 3C	[1/m]	0.319	0.240	0.197	0.189	0.191

Table C.5: Converted-green LED, split power portion simulation parameters due to wide optical bandwidth.

λ_{center}	[nm]	500	525	550	575	600
λ_{lower}	[nm]	400	512.5	537.5	562.5	587.5
λ_{upper}	[nm]	512.5	537.5	562.5	587.5	700
P_{opt}	[W]	0.961	0.863	0.790	0.585	0.601
R	[A/W]	0.33	0.355	0.38	0.40	0.42
K_d Jerlov 1B	[1/m]	0.0386	0.0572	0.0726	0.0926	0.241
K_d Jerlov 3C	[1/m]	0.197	0.187	0.187	0.201	0.380

C.2 HydroLight Simulation Parameter for Section 3.2.1

HydroLight is a commercial software for radiative transfer simulations in water bodies. It calculates radiance distributions and derived quantities like irradiances and reflectances. Parameters and boundaries applied for ambient light field determinations:

- Jerlov water types IB, III and 3C; absorption and scattering values from [102].
- Sun zenith angles 30°, 50°, and 70°.
- Sky conditions clear and overcast.
- Wind speed 5 m/s.
- Default characteristics of seawater, volume scattering properties of average particles.
- Spectral range 350 to 750 nm, in 5 nm steps.

The applied version was HydroLight 5.2 from Numerical Optics LTD, please refer to [87].

C.3 LED Spectra Modeling Functions and Parameter for Section 3.2.2

Gaussian approximation function $f_{\mathrm{G}}(\lambda)$ regarding [169]:

$$f_{\mathrm{G}}(\lambda) = A_{\mathrm{G}} \cdot e^{-(\frac{\lambda - C_{\mathrm{G}}}{W_{\mathrm{G}}})^2}. \tag{C.1}$$

Parameters used: A_{G}= 1, C_{G}= 447.9 and W_{G}= 10.5.

Logistic power peak approximation function $f_{\mathrm{LP}}(\lambda)$ regarding [169]:

$$f_{\mathrm{LP}}(\lambda) = \frac{A_{\mathrm{LP}}}{S_{\mathrm{LP}}} \left(1 + e^{\frac{\lambda - C_{\mathrm{LP}} + W_{\mathrm{LP}} \cdot ln(S_{\mathrm{LP}})}{W_{\mathrm{LP}}}}\right)^{\frac{-S_{\mathrm{LP}}-1}{S_{\mathrm{LP}}}} \cdot e^{\frac{\lambda - C_{\mathrm{LP}} + W_{\mathrm{LP}} \cdot ln(S_{\mathrm{LP}})}{W_{\mathrm{LP}}}} \cdot (S_{\mathrm{LP}} + 1)^{\frac{S_{\mathrm{LP}}+1}{S_{\mathrm{LP}}}}. \tag{C.2}$$

Parameters used: A_{LP}= 1, S_{LP}= 1.2, C_{LP}= 447.7 and W_{LP}= 5.2.

C.4 Filter Measurement Setup and Simulation for Section 3.2.4

The transmission measurements were performed on an optical bench in the dark by using a Gigahertz Optic Spectrometer BTS256 within the range from 380 to 750 nm. The source to spectrometer distance was in the range of 20 cm, and the rotatable filter carrier was located in between, since only relative measurements were undertaken the distance measure is less critical. Values from 350 to 380 nm were taken from the data sheets provided by the filter manufacturers. As point light sources stabilized halogen units were used. For measurement with diffuse light a sheet of Plexiglas LED 0M200SC (Evonik Industries AG, Darmstadt, Germany) was applied in the source path. Filter simulations were performed with the modeling tool “MyLight” (Semrock Inc., Rochester, USA). To approach a best possible diffuse character a cone half angle (CHA) of 60° was used.

C.5 Signal-to-Noise Calculations in Section 3.2.5

For calculations, the narrow band of the LED spectrum is supposed to have a constant water attenuation factor over this band, so no distortion of the relative spectrum will take place for different distances. Integral calculus over a wavelength band were performed by summation of discrete elements of 1 nm width.

C.6 Measurement Uncertainties for Section 3.5

Table C.6: Measurement uncertainties of the most relevant parameters for the three domains examined. The measurement uncertainties are two standard deviations.

Part	Measure	Unit	Uncertainty	Comment
Electrometer	Photocurrent	nA	± 0.2%	Specs.
Reference photodetector	Responsivity	A/W	± 40%	Specs., min. to typ.
Monochromator	Wavelength	nm	± 0.5	Specs., repeatability
Spectrometer	Wavelength	nm	± 1	Specs.
Oscilloscope	Rise time	ns	± 0.5	Specs, resolution
LCR meter	Capacitance	pF	± 0.2%	Specs.
TIA	Quality factor	-	± 0.1	Estimation
Goniometer	Rotation	°	± 3	Estimation
Polarisation filter	Rotation	°	± 3	Estimation

C.7 Flat Port Light Path Calculation in Section 4.2.2

C.7.1 Transmitter Side

Refraction calculation according to Snell on the transmitter side, as shown in Fig. 4.2, referenced by Fig. C.1, for given n_1, n_2, n_3, θ_1 values:

$$\theta_2 = \arcsin\left(\frac{n_1}{n_2} \cdot \sin(\theta_1)\right) \tag{C.3}$$

$$\theta_3 = \arcsin\left(\frac{n_2}{n_3} \cdot \sin(\theta_2)\right). \tag{C.4}$$

Reflectance and transmittance calculations according to Fresnel [41] on the transmitter side for given $n_1, n_2, n_3, \theta_1, \theta_2$ values:

$$R_{\mathrm{p12}}(\theta_1) = \left(\frac{(\frac{n_2}{n_1})^2 \cdot \cos(\theta_1) - \sqrt{(\frac{n_2}{n_1})^2 - \sin^2(\theta_1)}}{(\frac{n_2}{n_1})^2 \cdot \cos(\theta_1) + \sqrt{(\frac{n_2}{n_1})^2 - \sin^2(\theta_1)}}\right)^2 \tag{C.5}$$

$$R_{\mathrm{s12}}(\theta_1) = \left(\frac{\cos(\theta_1) - \sqrt{(\frac{n_2}{n_1})^2 - \sin^2(\theta_1)}}{\cos(\theta_1) + \sqrt{(\frac{n_2}{n_1})^2 - \sin^2(\theta_1)}}\right)^2 \tag{C.6}$$

$$R_{12}(\theta_1) = 0.5 \cdot (R_{\mathrm{p12}}(\theta_1) + R_{\mathrm{s12}}(\theta_1)) \tag{C.7}$$

$$T_{12}(\theta_1) = 1 - R_{12}(\theta_1) \tag{C.8}$$

$$R_{\mathrm{p23}}(\theta_2) = \left(\frac{(\frac{n_3}{n_2})^2 \cdot \cos(\theta_2) - \sqrt{(\frac{n_3}{n_2})^2 - \sin^2(\theta_2)}}{(\frac{n_3}{n_2})^2 \cdot \cos(\theta_2) + \sqrt{(\frac{n_3}{n_2})^2 - \sin^2(\theta_2)}}\right)^2 \tag{C.9}$$

$$R_{\mathrm{s23}}(\theta_2) = \left(\frac{\cos(\theta_2) - \sqrt{(\frac{n_3}{n_2})^2 - \sin^2(\theta_2)}}{\cos(\theta_2) + \sqrt{(\frac{n_3}{n_2})^2 - \sin^2(\theta_2)}}\right)^2 \tag{C.10}$$

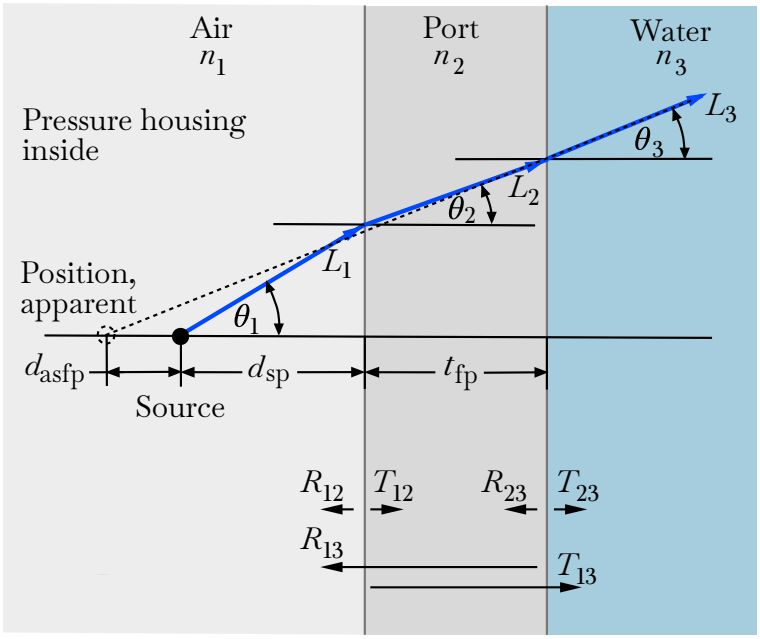

Figure C.1: Flat port geometric relations on the transmitter side.

$$R_{23}(\theta_2) = 0.5 \cdot (R_{p23}(\theta_2) + R_{s23}(\theta_2)) \tag{C.11}$$

$$T_{23}(\theta_2) = 1 - R_{23}(\theta_2) \tag{C.12}$$

$$R_{13}(\theta_1, \theta_2) = (1 - R_{12}(\theta_1)) \cdot (R_{23}(\theta_2) - 1) + 1 \tag{C.13}$$

$$T_{13}(\theta_1, \theta_2) = T_{12}(\theta_1) \cdot T_{23}(\theta_2). \tag{C.14}$$

Radiance calculation according to [101], for the transmitter side and a given $L_1(\theta_1)$:

$$L_2(\theta_1) = \left(\frac{n_2}{n_1}\right)^2 \cdot T_{12}(\theta_1) L_1(\theta_1) \tag{C.15}$$

$$L_3(\theta_2) = \left(\frac{n_3}{n_2}\right)^2 \cdot T_{23}(\theta_2) L_2(\theta_2). \tag{C.16}$$

Calculation of apparent shift of the source position for a flat port:

$$d_{asfp} = \frac{\tan(\theta_1) \cdot d_{sp} + \tan(\theta_2) \cdot t_{fp}}{\tan(\theta_3)} - t_{fp} - d_{sp}. \tag{C.17}$$

C.7.2 Receiver Side

Calculation for the receiver side and thin flat port, as shown in Fig. 4.5, for given n_1, n_2, n_3, θ_1 values: refraction, reflectance, transmittance and radiance calculations are similar to the transmitter side given by (C.3) to (C.16).

C.8 Dome Port Light Path Calculation in Section 4.2.3

C.8.1 Transmitter Side

Refraction calculation according to Snell on the transmitter side, as shown in Figs. 4.7 and 4.9, and referenced by Fig. C.2, for given $n_1, n_2, n_3, \theta_s, r_{dpi}, d_{cs}, t_{dp}$ values:

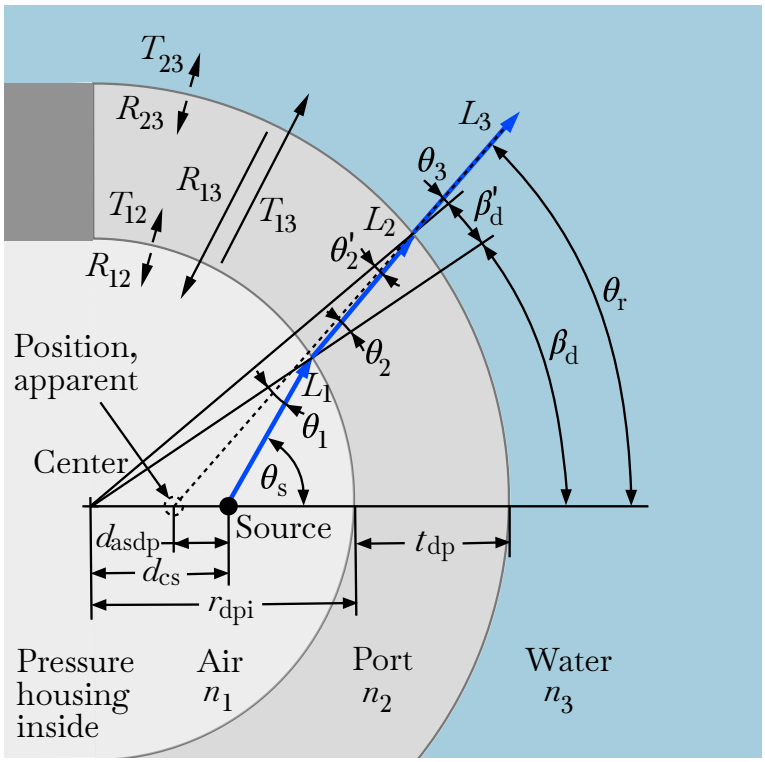

Figure C.2: Dome port geometric relations on the transmitter side.

$$\theta_1 = \arcsin\left(\frac{\sin(180° - \theta_s)}{r_{dpi}} \cdot d_{cs}\right) \tag{C.18}$$

$$\theta_2 = \arcsin\left(\frac{n_1}{n_2} \cdot \sin(\theta_1)\right) \tag{C.19}$$

$$\theta'_2 = \arcsin\left(\frac{r_{dpi}}{r_{dpi} + t_{dp}} \cdot \sin(180° - \theta_2)\right) \tag{C.20}$$

$$\theta_3 = \arcsin\left(\frac{n_2}{n_3} \cdot \sin(\theta'_2)\right) \tag{C.21}$$

$$\beta_d = 180° - (180° - \theta_s) - \theta_1 \tag{C.22}$$

$$\beta'_d = 180° - (180° - \theta_2) - \theta'_2 \tag{C.23}$$

$$\theta_r = \beta_d + \beta'_d + \theta_3. \tag{C.24}$$

Reflectance and transmittance calculations according to Fresnel on the transmitter side:

$$R_{p23}(\theta'_2) = \left(\frac{(\frac{n_3}{n_2})^2 \cdot \cos(\theta'_2) - \sqrt{(\frac{n_3}{n_2})^2 - \sin^2(\theta'_2)}}{(\frac{n_3}{n_2})^2 \cdot \cos(\theta'_2) + \sqrt{(\frac{n_3}{n_2})^2 - \sin^2(\theta'_2)}}\right)^2 \tag{C.25}$$

$$R_{s23}(\theta'_2) = \left(\frac{\cos(\theta'_2) - \sqrt{(\frac{n_3}{n_2})^2 - \sin^2(\theta'_2)}}{\cos(\theta'_2) + \sqrt{(\frac{n_3}{n_2})^2 - \sin^2(\theta'_2)}}\right)^2 \tag{C.26}$$

$$R_{23}(\theta'_2) = 0.5 \cdot (R_{p23}(\theta'_2) + R_{s23}(\theta'_2)) \tag{C.27}$$

$$T_{23}(\theta'_2) = 1 - R_{23}(\theta'_2) \tag{C.28}$$

$$R_{13}(\theta_1, \theta_2') = (1 - R_{12}(\theta_1)) \cdot (R_{23}(\theta_2') - 1) + 1 \tag{C.29}$$

$$T_{13}(\theta_1, \theta_2') = T_{12}(\theta_1) \cdot T_{23}(\theta_2'). \tag{C.30}$$

Formulas for $R_{\mathrm{p}12}(\theta_1), R_{\mathrm{s}12}(\theta_1), R_{12}, T_{12}$ are similar to flat port.

Radiance ratio calculation according to [101], for transmitter side and a given $L_1(\theta_\mathrm{s})$:

$$\frac{L_3(\theta_\mathrm{r})}{L_1(\theta_\mathrm{s})} = T_{13} \cdot \frac{\sin(\theta_\mathrm{s}) \cdot \cos(\theta_\mathrm{s}) \cdot \Delta\theta_\mathrm{s}}{\sin(\theta_\mathrm{r}) \cdot \cos(\theta_\mathrm{r}) \cdot \Delta\theta_\mathrm{r}}. \tag{C.31}$$

Calculation of apparent shift of the source position for a dome port:

$$d_{\mathrm{asdp}} = d_{\mathrm{cs}} - \frac{\sin(\theta_3) \cdot (r_{\mathrm{dpi}} + t_{\mathrm{dp}})}{\sin(180° - \theta_r)}. \tag{C.32}$$

C.8.2 Receiver Side

Refraction calculation on receiver side for thin dome port according to Snell, as shown in Figs. 4.15 and 4.16, and referenced by Fig.C.3, for given $n_1, n_2, n_3, \theta_\mathrm{r}, r_{\mathrm{dpi}}, d_{\mathrm{cs}}$ values and reference:

$$\theta_1 = \arcsin\left(\frac{n_2}{n_1} \cdot \sin(\theta_2)\right) \tag{C.33}$$

$$\theta_2 = \arcsin\left(\frac{n_3}{n_2} \cdot \sin(\theta_3)\right) \tag{C.34}$$

$$\theta_3 = \arcsin\left(\frac{d_{\mathrm{cr}}}{r_{\mathrm{dpi}}} \cdot \sin(180° - \theta_\mathrm{r})\right) \tag{C.35}$$

$$\beta_\mathrm{d} = 180° - (180° - \theta_\mathrm{r}) - \theta_3 \tag{C.36}$$

$$\theta_s = \theta_1 - \beta_\mathrm{d}. \tag{C.37}$$

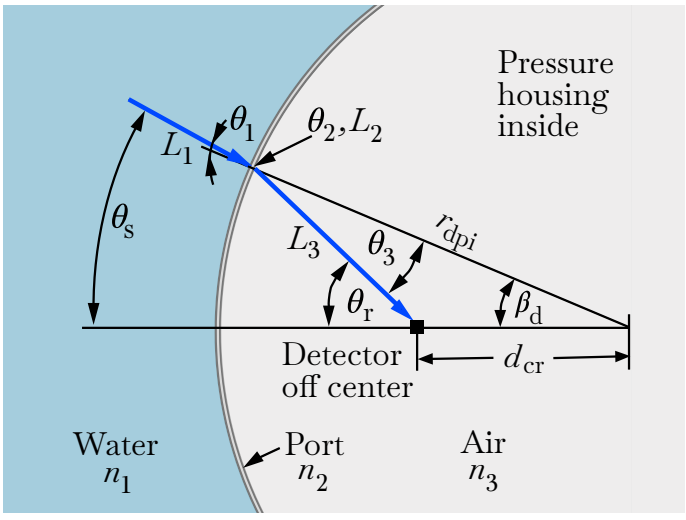

Figure C.3: Dome port geometric relations on the receiver side and a thin dome port.

Reflectance and transmittance calculations according to Fresnel on the transmitter side: formulas for $R_{\mathrm{p}12}(\theta_1), R_{\mathrm{s}12}(\theta_1), R_{12}(\theta_1), T_{12}(\theta_1)$, $R_{\mathrm{p}23}(\theta_2), R_{\mathrm{s}23}(\theta_2), R_{23}(\theta_2), T_{23}(\theta_2), T_{13}(\theta_1, \theta_2)$ are similar to a flat port (C.5) to (C.16), the radiance ratio is given by (C.31).

C.9 Parameters for MC Simulations in Section 5.2

Table C.7: Water parameters used for MC simulations, extracted from [102].

Water type	λ [nm]	a [1/m]	b [1/m]
Jerlov IB	425	0.0246	0.0732
Jerlov IB	450	0.0235	0.0680
Jerlov IB	475	0.0225	0.0635
Jerlov IB	500	0.0287	0.0597
Jerlov IB	525	0.0469	0.0565
Jerlov 3C	450	0.154	1.50
Jerlov 3C	475	0.105	1.36
Jerlov 3C	500	0.081	1.25
Jerlov 3C	525	0.078	1.15
Jerlov 3C	550	0.082	1.06
Jerlov 3C	575	0.095	0.985
Jerlov 3C	600	0.239	0.916

Table C.8: Parameters used for MC simulations.

Beam angle β	[°]	90	45	20	10	5	1
Detector area A_{det}	[mm^2]	300x300	150x150	100x100	100x100	40x40	10x10
MC repetitions Jerlov 1B	[-]	60	60	30	30	20	20
MC repetitions Jerlov 3C	[-]	20	20	20	20	20	20

C.10 Beam Shape Functions and Parameter for Section 5.2.3

Normalized intensity I_{L} as function of the full beam angle β for a Lambertian beam pattern [79]:

$$I_{\text{L}}(\theta) = \cos(\theta)^m. \tag{C.38}$$

Table C.9: Parameters used for the calculation of Lambertian beam patterns.

Beam angle, full β	[°]	90	45	20
Mode number m		2	8.75	45.3

Normalized intensity I_{G} as function of the full beam angle β for a Gaussian beam pattern [231]:

$$I_{\text{G}}(\theta) = \frac{1}{\sqrt{2\pi\sigma^2}} \cdot e^{\frac{-(a\cdot\tan(\frac{\theta}{2}))^2}{2\sigma^2}}. \tag{C.39}$$

Table C.10: Parameters used for the calculation of Gaussian beam patterns.

Beam angle, full	β	[°]	90	45	20
Scale factor	a		0.47	1.135	2.665
Variance	σ^2		0.159155	0.159155	0.159155

C.11 Cumulative Distribution Functions and Parameter for Section 5.2.5

CDF of the Henyey-Greenstein scattering phase function to determine the scattering angle direct for a random number [101]:

$$\theta = \arccos\left(\frac{1+g_{\mathrm{HG}}^2}{2g_{\mathrm{HG}}} - \frac{1}{2g_{\mathrm{HG}}}\left(\frac{1-g_{\mathrm{HG}}^2}{1+g_{\mathrm{HG}}-2g_{\mathrm{HG}}\mathbb{R}}\right)^2\right) \tag{C.40}$$
$$\text{for } -1 \leq g_{\mathrm{HG}} \leq 1, \quad \text{but } g_{\mathrm{HG}} \neq 0, \quad \mathbb{R} \sim U[0,1].$$

Analytic CDF of the Fournier-Forand scattering phase function [101]:

$$P_{\mathrm{FF}}(\theta) = \frac{1}{(1-\delta)\delta^\nu}\left((1-\delta^{\nu+1}) - (1-\delta^\nu)\sin^2(\frac{\theta)}{2}\right) + \frac{1}{8}\frac{1-\delta_{180}^\nu}{(\delta_{180}-1)\delta_{180}^\nu}\cos(\theta)\,\sin^2(\theta) \tag{C.41}$$

$$\text{with} \quad \nu = \frac{3-\mu_{\mathrm{FF}}}{2} \tag{C.42}$$

$$\text{and} \quad \delta = \frac{4}{3(n_{\mathrm{FF}}-1)^2}\sin^2(\frac{\theta}{2}). \tag{C.43}$$

Table C.11: Parameters applied to CDF within MC simulations.

g_{HG}	0.924
n_{FF}	1.1
μ_{FF}	3.5835

C.12 Parameters for MC Simulations in Section 5.3.4

Table C.12: Water parameters used for MC simulations, originated from this thesis in situ measurements in the Baltic Sea. A spectrophotometer of the type AC-S manufactured by Wetlabs was utilized.

Date	λ [nm]	a [1/m]	b [1/m]
2016, Aug. 26th	450	0.2501	0.8016
2016, Aug. 26th	530	0.1281	0.6815
2016, Aug. 26th	550	0.1284	0.6581
2016, Sept. 5th	450	0.2633	0.5276
2016, Sept. 5th	530	0.1604	0.4146
2016, Sept. 5th	550	0.1578	0.4026

References

[1] Levin, L. A. et al. "Global observing needs in the deep ocean". In: *Frontiers in Marine Science* 6 (May 2019), pp. 1–32. DOI: 10.3389/fmars.2019.00241.

[2] Stojanovic, M. and Beaujean, P. P. J. "Acoustic communication". In: *Springer Handbook of Ocean Engineering*. Springer International Publishing, 2016, pp. 359–386. DOI: 10.1007/978-3-319-16649-0_15.

[3] Lanzagorta, M. "Underwater communications". In: *Synthesis Lectures on Communications* 5.2 (Oct. 2012), pp. 1–129. DOI: 10.2200/s00409ed1v01y201203com006.

[4] Palmeiro, A. et al. "Underwater radio frequency communications". In: *OCEANS 2011 IEEE - Spain*. IEEE, June 2011. DOI: 10.1109/oceans-spain.2011.6003580.

[5] Che, X. et al. "Re-evaluation of RF electromagnetic communication in underwater sensor networks". In: *IEEE Communications Magazine* 48.12 (Dec. 2010), pp. 143–151. DOI: 10.1109/mcom.2010.5673085.

[6] Li, Y. et al. "A survey of underwater magnetic induction communications: fundamental issues, recent advances, and challenges". In: *IEEE Communications Surveys & Tutorials* 21.3 (2019), pp. 2466–2487. DOI: 10.1109/comst.2019.2897610.

[7] Hott, M. and Hoeher, P. A. "Underwater communication employing high-sensitive magnetic field detectors". In: *IEEE Access* 8 (2020), pp. 177385–177394. DOI: 10.1109/access.2020.3026623.

[8] Guo, H., Sun, Z., and Wang, P. "Multiple frequency band channel modeling and analysis for magnetic induction communication in practical underwater environments". In: *IEEE Transactions on Vehicular Technology* 66.8 (Aug. 2017), pp. 6619–6632. DOI: 10.1109/tvt.2017.2664099.

[9] Hott, M., Hoeher, P. A., and Reinecke, S. F. "Magnetic Communication Using High-Sensitivity Magnetic Field Detectors". In: *Sensors* 19.15 (Aug. 2019), pp. 1–14. DOI: 10.3390/s19153415.

[10] Hott, M. and Hoeher, P. A. "Channel Modeling and SNR Enhancement for Coil to Magnetic Field Sensor Underwater Communication". In: *Global Oceans 2020: Singapore – U.S. Gulf Coast*. IEEE, Oct. 2020. DOI: 10.1109/ieeeconf38699.2020.9388972.

[11] Hott, M., Placzek, J. M., and Hoeher, P. A. "Self-Driven High-Q On-Off Keying: An Efficient Modulation Scheme for Magnetic (Underwater) Communication". In: *2022 13th International Conference on Information and Communication Technology Convergence (ICTC)*. IEEE, Oct. 2022, pp. 40–44. DOI: 10.1109/ictc55196.2022.9952916.

[12] Hott, M., Placzek, J. M., and Hoeher, P. A. "Single-Frequency-Driven Multi-Resonant FSK: An Easy-to-Operate Wideband Modulation Scheme for Magnetic (Underwater) Communication". In: *2022 13th International Conference on Information and Communication Technology Convergence (ICTC)*. IEEE, Oct. 2022, pp. 354–356. DOI: 10.1109/ictc55196.2022.9952626.

[13] Kaushal, H. and Kaddoum, G. "Underwater optical wireless communication". In: *IEEE Access* 4 (2016), pp. 1518–1547. DOI: 10.1109/access.2016.2552538.

[14] Gussen, C. M. G. et al. “A survey of underwater wireless communication technologies”. In: *Journal of Communication and Information Systems* 31.1 (2016), pp. 242–255. DOI: 10.14209/jcis.2016.22.

[15] Zeng, Z. et al. “A survey of underwater optical wireless communications”. In: *IEEE Communications Surveys & Tutorials* 19.1 (2017), pp. 204–238. DOI: 10.1109/COMST.2016.2618841.

[16] Gkoura, L. K. et al. “Underwater optical wireless communication systems: a concise review”. In: *Turbulence Modelling Approaches - Current State, Development Prospects, Applications*. InTech, July 2017. DOI: 10.5772/67915.

[17] Hoeher, P. A., Sticklus, J., and Harlakin, A. “Underwater optical wireless communications in swarm robotics: a tutorial”. In: *IEEE Communications Surveys & Tutorials* (2021), pp. 1–30. DOI: 10.1109/comst.2021.3111984.

[18] Campagnaro, F., Signori, A., and Zorzi, M. “Wireless remote control for underwater vehicles”. In: *Journal of Marine Science and Engineering* 8.10 (Sept. 2020), p. 736. DOI: 10.3390/jmse8100736.

[19] Campagnaro, F., Steinmetz, F., and Renner, B. C. “Survey on low-cost underwater sensor networks: from niche applications to everyday use”. In: *Journal of Marine Science and Engineering* 11.1 (Jan. 2023), p. 125. DOI: 10.3390/jmse11010125.

[20] Muth, J. “Free-space optical communications: building a deeper understanding of underwater optical communications”. In: *laserfocusworld* 5 (2017), p. 10.

[21] Potter, J. R., Porter, M. B., and Preisig, J. C. “UComms a conference and workshop on underwater communications, channel modeling, and validation”. In: *IEEE Journal of Oceanic Engineering* 38.4 (Oct. 2013), pp. 603–613. DOI: 10.1109/joe.2013.2283094.

[22] Oubei, H. M. et al. “Light based underwater wireless communications”. In: *Japanese Journal of Applied Physics* 57.8S2 (July 2018). DOI: 10.7567/jjap.57.08pa06.

[23] Watson, M. A. et al. “Assessment of laser tracking and data transfer for underwater optical communications”. In: *Unmanned/Unattended Sensors and Sensor Networks X*. Ed. by Carapezza, Edward M., Datskos, Panos G., and Tsamis, Christos. SPIE, Oct. 2014, pp. 1–10. DOI: 10.1117/12.2073675.

[24] Fletcher, A. S., Hamilton, S. A., and Moores, J. D. “Undersea laser communication with narrow beams”. In: *IEEE Communications Magazine* 53.11 (Nov. 2015), pp. 49–55. DOI: 10.1109/mcom.2015.7321971.

[25] Ali, M. F. et al. “Recent advances and future directions on underwater wireless communications”. In: *Archives of Computational Methods in Engineering* (Aug. 2019), pp. 1379–1412. DOI: 10.1007/s11831-019-09354-8.

[26] Alomari, M. M. et al. “Vision and challenges of underwater optical wireless communication - a survey”. In: *International Journal of Computer Applications* 167.8 (June 2017), pp. 8–10. DOI: 10.5120/ijca2017914326.

[27] Khalighi, M. A. et al. “Underwater wireless optical communication, recent advances and remaining challenges”. In: *2014 16th International Conference on Transparent Optical Networks (ICTON)*. IEEE, July 2014. DOI: 10.1109/ICTON.2014.6876673.

[28] Partan, J., Kurose, J., and Levine, B. N. “A survey of practical issues in underwater networks”. In: *Proceedings of the 1st ACM international workshop on Underwater networks WUWNet 06*. ACM Press, 2006. DOI: 10.1145/1161039.1161045.

[29] Jamali, M. V., Chizari, A., and Salehi, J. A. “Performance analysis of multi hop underwater wireless optical communication systems”. In: *IEEE Photonics Technology Letters* 29.5 (Mar. 2017), pp. 462–465. DOI: 10.1109/lpt.2017.2657228.

[30] Simpson, J. A., Hughes, B. L., and Muth, J. F. "Smart transmitters and receivers for underwater free-space optical communication". In: *IEEE Journal on Selected Areas in Communications* 30.5 (June 2012), pp. 964–974. DOI: 10.1109/jsac.2012.120611.

[31] Subsea optical modems. Aquatec Group. URL: https://aquatecgroup.com (visited on 01/09/2020).

[32] Fast underwater wireless communication. Hydromea. URL: https://hydromea.com (visited on 01/21/2020).

[33] Underwater wireless communication system. Marine-link. URL: https://marine-link.com (visited on 01/21/2020).

[34] Optical communications system. Sonardyne. URL: https://sonardyne.com (visited on 01/22/2020).

[35] Sticklus, J., Hoeher, P. A., and Roettgers, R. "Optical underwater communication: the potential of using converted green LEDs in coastal waters". In: *IEEE Journal of Oceanic Engineering* 44.2 (Apr. 2019), pp. 535–547. DOI: 10.1109/joe.2018.2816838.

[36] Sticklus, J., Hieronymi, M., and Hoeher, P. A. "Effects and constraints of optical filtering on ambient light suppression in LED-based underwater communications". In: *Sensors* 18.3710 (Oct. 2018), pp. 1–21. DOI: 10.3390/s18113710.

[37] Sticklus, J., Hoeher, P. A., and Hieronymi, M. "Experimental characterization of single-color power LEDs used as photodetectors". In: *Sensors* 20.5200 (Sept. 2020), pp. 1–13. DOI: 10.3390/s20185200.

[38] Sticklus, J., Kwasnitschka, T., and Hoeher, P. A. "Method and device for potting an LED luminaire potted in a potting compound and LED luminaire". European Patent EP3233414. Jan. 8, 2020.

[39] Hoeher, P. A. *Visible Light Communications: Theoretical and Practical Foundations*. Carl Hanser Verlag GmbH Co KG, 2019. ISBN: 978-3-446-46206-9.

[40] Anguita, D., Brizzolara, D., and Parodi, G. "VHDL modules and circuits for underwater optical wireless communication systems". In: *WSEAS, Transaction on Communications* 9.9 (2010), pp. 525–552. ISSN: 1109-2742.

[41] Schroeder, G. and Treiber, H. *Technische Optik*. Vogel Business Media, 2014. ISBN: 978-3-8343-3335-3.

[42] Gabriel, C. et al. "Misalignment considerations in point-to-point underwater wireless optical links". In: *2013 MTS/IEEE OCEANS - Bergen*. IEEE, June 2013. DOI: 10.1109/oceans-bergen.2013.6607990.

[43] Anguita, D., Brizzolara, D., and Parodi, G. "Prospects and problems of optical diffuse wireless communication for underwater wireless sensor networks". In: *Wireless Sensor Networks: Application-Centric Design*. InTech, Dec. 2010. DOI: 10.5772/14472.

[44] Vali, Z. et al. "Use of Gaussian beam divergence to compensate for misalignment of underwater wireless optical communication links". In: *IET Optoelectronics* 11.5 (Oct. 2017), pp. 171–175. DOI: 10.1049/iet-opt.2016.0132.

[45] Miramirkhani, F. and Uysal, M. "Visible light communication channel modeling for underwater environments with blocking and shadowing". In: *IEEE Access* 6 (2017), pp. 1082–1090. DOI: 10.1109/access.2017.2777883.

[46] Gabriel, C. et al. "Channel modeling for underwater optical communication". In: *2011 IEEE GLOBECOM Workshops (GC Wkshps)*. IEEE, Dec. 2011. DOI: 10.1109/glocomw.2011.6162571.

[47] Li, J. et al. “Channel capacity study of underwater wireless optical communications links based on Monte Carlo simulation”. In: *Journal of Optics* 14.1 (Dec. 2012). DOI: 10.1088/2040-8978/14/1/015403.

[48] Li, Y., Leeson, M. S., and Li, X. “Impulse response modeling for underwater optical wireless channels”. In: *Applied Optics* 57.17 (June 2018). DOI: 10.1364/ao.57.004815.

[49] Cochenour, B., Mullen, L., and Muth, J. “Temporal response of the underwater optical channel for high-bandwidth wireless laser communications”. In: *IEEE Journal of Oceanic Engineering* 38.4 (Oct. 2013), pp. 730–742. DOI: 10.1109/joe.2013.2255811.

[50] Jasman, F. et al. “Scattering regimes for underwater optical wireless communications using Monte Carlo simulation”. In: *International Journal of Electrical and Computer Engineering (IJECE)* 8.4 (Aug. 2018), pp. 2571–2577. DOI: 10.11591/ijece.v8i4.pp2571-2577.

[51] Li, J. et al. “Influence of temporal dispersion on the undersea wireless optical communication and its mitigation using MLSE”. In: *OCEANS 2018 MTS/IEEE Charleston*. IEEE, Oct. 2018. DOI: 10.1109/oceans.2018.8604823.

[52] Tang, S., Dong, Y., and Zhang, X. “Impulse response modeling for underwater wireless optical communication links”. In: *IEEE Transactions on Communications* 62.1 (Jan. 2014), pp. 226–234. DOI: 10.1109/tcomm.2013.120713.130199.

[53] Liu, W. et al. “Non-line-of-sight scattering channel modeling for underwater optical wireless communication”. In: *2015 IEEE International Conference on Cyber Technology in Automation, Control, and Intelligent Systems (CYBER)*. IEEE, June 2015, pp. 1265–1268. DOI: 10.1109/cyber.2015.7288125.

[54] Sun, X. et al. “Non-line-of-sight methodology for high-speed wireless optical communication in highly turbid water”. In: *Optics Communications* 461.125526 (Apr. 2020). DOI: 10.1016/j.optcom.2020.125264.

[55] Arnon, S. and Kedar, D. “Non-line-of-sight underwater optical wireless communication network”. In: *Journal of the Optical Society of America A* 26.3 (Feb. 2009), pp. 530–539. DOI: 10.1364/josaa.26.000530.

[56] Jasman, F. and Green, R. J. “Monte Carlo simulation for underwater optical wireless communications”. In: *2013 2nd International Workshop on Optical Wireless Communications (IWOW)*. IEEE, Oct. 2013, pp. 113–117. DOI: 10.1109/iwow.2013.6777789.

[57] Cox, W. C. et al. “A MEMS blue/green retroreflecting modulator for underwater optical communications”. In: *OCEANS 2010 MTS/IEEE SEATTLE*. IEEE, Sept. 2010. DOI: 10.1109/oceans.2010.5664432.

[58] Johnson, L. J., Green, R. J., and Leeson, M. S. “The impact of link orientation in underwater optical wireless communication systems”. In: *2014 Oceans - St. John’s*. IEEE, Sept. 2014. DOI: 10.1109/oceans.2014.7003030.

[59] Arnon, S. “Underwater optical wireless communication network”. In: *Optical Engineering* 49.1 (Jan. 2010), pp. 150011–150016. DOI: 10.1117/1.3280288.

[60] Cox, W. and Muth, J. “Simulating channel losses in an underwater optical communication system”. In: *Journal of the Optical Society of America A* 31.5 (Apr. 2014), pp. 920–934. DOI: 10.1364/josaa.31.000920.

[61] Doniec, M., Angermann, M., and Rus, D. “An end-to-end signal strength model for underwater optical communications”. In: *IEEE Journal of Oceanic Engineering* 38.4 (Oct. 2013), pp. 743–757. DOI: 10.1109/joe.2013.2278932.

[62] Datasheet Lumileds Z Color Line. High Power Color LED. DS105. Lumileds Holding B.V., 2017. URL: https://www.lumileds.com (visited on 06/12/2020).

[63] Datasheet Ledengin LZ4 series. High-power 4-die LED emitter. OSRAM Opto Semiconductors GmbH, 2022. URL: https://www.osram-os.com (visited on 02/24/2023).

[64] Khanh, T. Q. et al., eds. *LED Lighting. Technology and Perception*. Wiley VCH, 2015. ISBN: 978-3-527-41212-9.

[65] Tian, P. et al. "High-speed underwater optical wireless communication using a blue GaN-based micro-LED". In: *Optics Express* 25.2 (Jan. 2017), p. 1193. DOI: 10.1364/oe.25.001193.

[66] Arvanitakis, G. N. et al. "Gb/s underwater wireless optical communications using series-connected GaN micro-LED arrays". In: *IEEE Photonics Journal* 12.2 (Apr. 2020), pp. 1–10. DOI: 10.1109/jphot.2019.2959656.

[67] Opto-semiconductor modules. Selection guide. Hamamatsu Photonics K. K., 2019. URL: https://www.hamamatsu.com (visited on 04/07/2021).

[68] Hamamatsu, Photonics. *Opto-Semiconductor Handbook*. Japan: Hamamatsu KK, 2014. Chap. 1–3. URL: https://www.hamamatsu.com.

[69] Datasheet BPW34. Silicon PIN Photodiode. Version 1.5. OSRAM Opto Semiconductors GmbH, 2020. URL: https://www.osram.com (visited on 06/18/2021).

[70] Datasheet AD1900-11TO. Avalanche Photo Diode. First Sensor AG, 2011. URL: https://www.first-sensor.com (visited on 11/25/2015).

[71] High-speed response PMT modules for underwater optical communications. Hamamatsu Photonics K.K., 2021. URL: https://www.hamamatsu.com (visited on 06/18/2021).

[72] Hamza, T. and Khalighi, M. A. "On limitations of using silicon photo-multipliers for underwater wireless optical communications". In: *2019 2nd West Asian Colloquium on Optical Wireless Communications (WACOWC)*. IEEE, Apr. 2019. DOI: 10.1109/wacowc.2019.8770202.

[73] Leon, P. et al. "A new underwater optical modem based on highly sensitive silicon photomultipliers". In: *OCEANS 2017 - Aberdeen*. IEEE, June 2017. DOI: 10.1109/oceanse.2017.8084586.

[74] Photodiode Circuit Design Wizard. Analog Devices. URL: https://tools.analog.com/en/photodiode (visited on 07/02/2021).

[75] Hamza, T. et al. "Investigation of solar noise impact on the performance of underwater wireless optical communication links". In: *Optics Express* 24.22 (Oct. 2016), pp. 25832–25845. DOI: 10.1364/oe.24.025832.

[76] Schulze, H. "Some good reasons for using OFDM in optical wireless communications". In: *International OFDM Workshop Hamburg,Germany*. 2011.

[77] Schulze, H. and Hoeher, P. A. "On the General Error Event Probability Evaluation of Optical Intensity Modulation Schemes". In: *IEEE Photonics Journal* 14.5 (Oct. 2022), pp. 1–8. DOI: 10.1109/jphot.2022.3207834.

[78] Proakis, J. G. and Salehi, M. *Digital Communications*. 5th ed. McGraw-Hill, 2007. ISBN: 978-0-07-295716-7.

[79] Barry, J. R. *Wireless Infrared Communications*. Kluwer Academic Publishers, 1994. ISBN: 0-7923-9476-3.

[80] Cox, W. C. et al. "An underwater optical communication system implementing Reed-Solomon channel coding". In: *OCEANS 2008*. IEEE, 2008. DOI: 10.1109/oceans.2008.5151992.

[81] Ghassemlooy, Z. et al. "Digital pulse interval modulation for optical communications". In: *IEEE Communications Magazine* 36.12 (1998), pp. 95–99. DOI: 10.1109/35.735885.

[82] Shiu, D. S. and Kahn, J. M. "Differential pulse-position modulation for power-efficient optical communication". In: *IEEE Transactions on Communications* 47.8 (1999), pp. 1201–1210. DOI: 10.1109/26.780456.

[83] Gabriel, C. et al. "Investigation of suitable modulation techniques for underwater wireless optical communication". In: *2012 International Workshop on Optical Wireless Communications (IWOW)*. IEEE, Oct. 2012. DOI: 10.1109/iwow.2012.6349691.

[84] Simpson, J. A. et al. "5 Mbps optical wireless communication with error correction coding for underwater sensor nodes". In: *OCEANS 2010 MTS/IEEE SEATTLE*. IEEE, Sept. 2010. DOI: 10.1109/oceans.2010.5664429.

[85] Jamali, M. V., Nabavi, P., and Salehi, J. A. "MIMO underwater visible light communications, comprehensive channel study, performance analysis, and multiple-symbol detection". In: *IEEE Transactions on Vehicular Technology* 67.9 (Sept. 2018), pp. 8223–8237. DOI: 10.1109/tvt.2018.2840505.

[86] Liu, W., Xu, Z., and Yang, L. "SIMO detection schemes for underwater optical wireless communication under turbulence". In: *Photonics Research* 3.3 (Apr. 2015), pp. 48–53. DOI: 10.1364/prj.3.000048.

[87] Mobley, C. D. *Light and Water. Radiative Transfer in Natural Waters*. Academic Press Inc., 1994. ISBN: 978-0125027502.

[88] Mobley, C. D. "Radiative transfer in the ocean". In: *Encyclopedia of Ocean Sciences*. Elsevier, 2001, pp. 2321–2330. DOI: 10.1006/rwos.2001.0469.

[89] Roesler, C. S., Perry, M. J., and Carder, K. L. "Modeling in situ phytoplankton absorption from total absorption spectra in productive inland marine waters". In: *Limnology and Oceanography* 34.8 (Dec. 1989), pp. 1510–1523. DOI: 10.4319/lo.1989.34.8.1510.

[90] Smith, R. C. and Baker, K. S. "Optical properties of the clearest natural waters (200–800 nm)". In: *Applied Optics* 20.2 (Jan. 1981), pp. 177–184. DOI: 10.1364/ao.20.000177.

[91] Pope, R. M. and Fry, E. S. "Absorption spectrum (380–700 nm) of pure water II integrating cavity measurements". In: *Applied Optics* 36.33 (Nov. 1997), pp. 8710–8723. DOI: 10.1364/ao.36.008710.

[92] Bricaud, A. et al. "Variability in the chlorophyll-specific absorption coefficients of natural phytoplankton: Analysis and parameterization". In: *Journal of Geophysical Research* 100.C7 (1995), pp. 13321–13332. DOI: 10.1029/95jc00463.

[93] Bricaud, A., Morel, A., and Prieur, L. "Absorption by dissolved organic matter of the sea (yellow substance) in the UV and visible domains". In: *Limnology and Oceanography* 26.1 (Jan. 1981), pp. 43–53. DOI: 10.4319/lo.1981.26.1.0043.

[94] Babin, M. et al. "Variations in the light absorption coefficients of phytoplankton, nonalgal particles, and dissolved organic matter in coastal waters around Europe". In: *Journal of Geophysical Research* 108.C7 (2003). DOI: 10.1029/2001jc000882.

[95] Morel, A. "Light and marine photosynthesis: a spectral model with geochemical and climatological implications". In: *Progress in Oceanography* 26.3 (Jan. 1991), pp. 263–306. DOI: 10.1016/0079-6611(91)90004-6.

[96] Prieur, L. and Sathyendranath, S. "An optical classification of coastal and oceanic waters based on the specific spectral absorption curves of phytoplankton pigments, dissolved organic matter, and other particulate materials". In: *Limnology and Oceanography* 26.4 (July 1981), pp. 671–689. DOI: 10.4319/lo.1981.26.4.0671.

[97] Johnson, L. J., Green, R. J., and Leeson, M. S. "Underwater optical wireless communications: depth dependent variations in attenuation". In: *Applied Optics* 52.33 (Nov. 2013), pp. 7867–7873. DOI: 10.1364/ao.52.007867.

[98] Yap, Y. X., Jasman, F., and Marcus, T. C. E. "Impact of chlorophyll concentration on underwater optical wireless communications". In: *2018 7th International Conference on Computer and Communication Engineering (ICCCE)*. IEEE, Sept. 2018. DOI: 10.1109/iccce.2018.8539297.

[99] Haltrin, V. I. "Chlorophyll-based model of seawater optical properties". In: *Applied Optics* 38.33 (Nov. 1999), pp. 6826–6832. DOI: 10.1364/ao.38.006826.

[100] Mobley, C. D. *Handbook of Optics*. Vol. 1: *The Optical Properties of Water*. McGraw-Hill, 1995. Chap. 43.

[101] Mobley, C., Boss, E., and Roesler, C. *Ocean Optics Web Book*. 2020. Chap. Overview of Optical Oceanography. URL: www.oceanopticsbook.info (visited on 05/04/2020).

[102] Solonenko, M. G. and Mobley, C. D. "Inherent optical properties of Jerlov water types". In: *Applied Optics* 54.17 (June 2015), pp. 5392–5401. DOI: 10.1364/ao.54.005392.

[103] Stramski, D. et al. "The role of seawater constituents in light backscattering in the ocean". In: *Progress in Oceanography* 61.1 (2004), pp. 27–56. DOI: 10.1016/j.pocean.2004.07.001.

[104] Cochenour, B. M., Mullen, L. J., and Laux, A. E. "Characterization of the beam-spread function for underwater wireless optical communications links". In: *IEEE Journal of Oceanic Engineering* 33.4 (Oct. 2008), pp. 513–521. DOI: 10.1109/joe.2008.2005341.

[105] Petzold, T. J. *Volume scattering functions for selected ocean waters*. Tech. rep. SIO-REF-72-78. Scripps Institution of Oceanography La Jolla Ca Visibility Lab, 1972.

[106] Chami, M. et al. "Spectral variation of the volume scattering function measured over the full range of scattering angles in a coastal environment". In: *Applied Optics* 45.15 (May 2006), pp. 3605–3619. DOI: 10.1364/ao.45.003605.

[107] Mobley, C. D., Sundman, L. K., and Boss, E. "Phase function effects on oceanic light fields". In: *Applied Optics* 41.6 (Feb. 2002), pp. 1035–1050. DOI: 10.1364/ao.41.001035.

[108] Haltrin, V. I. "One-parameter two-term Henyey-Greenstein phase function for light scattering in seawater". In: *Applied Optics* 41.6 (Feb. 2002), pp. 1022–1028. DOI: 10.1364/ao.41.001022.

[109] Haltrin, V.I. "An analytic Fournier-Forand scattering phase function as an alternative to the Henyey-Greenstein phase function in hydrologic optics". In: *IGARSS '98. Sensing and Managing the Environment. 1998 IEEE International Geoscience and Remote Sensing. Symposium Proceedings. (Cat. No.98CH36174)*. IEEE, 1998. DOI: 10.1109/igarss.1998.699623.

[110] Sahu, S. K. and Shanmugam, P. "Semi-analytical modeling and parameterization of particulates in-water phase function for forward angles". In: *Optics Express* 23.17 (Aug. 2015), pp. 22291–22307. DOI: 10.1364/oe.23.022291.

[111] Laux, A. et al. "The a, b, c s of oceanographic lidar predictions: a significant step toward closing the loop between theory and experiment". In: *Journal of Modern Optics* 49.3-4 (Mar. 2002), pp. 439–451. DOI: 10.1080/09500340110088498.

[112] Mullen, L., Alley, D., and Cochenour, B. "Investigation of the effect of scattering agent and scattering albedo on modulated light propagation in water". In: *Applied Optics* 50.10 (Mar. 2011), pp. 1396–1404. DOI: 10.1364/ao.50.001396.

[113] Jerlov, N. G. *Marine Optics*. 2nd ed. Vol. 14. Elsevier, 1976. Chap. 10, pp. 127–150. ISBN: 0-444-41490-8.

[114] Aas, E. et al. "Optical water types of the Nordic Seas and adjacent areas". In: *Oceanologia* 55.2 (May 2013), pp. 471–482. DOI: 10.5697/oc.55-2.471.

[115] Matsushita, B. et al. “A simple method for distinguishing global Case-1 and Case-2 waters using SeaWiFS measurements”. In: *ISPRS Journal of Photogrammetry and Remote Sensing* 69 (Apr. 2012), pp. 74–87. DOI: 10.1016/j.isprsjprs.2012.02.008.

[116] Smart, J. H. “Underwater optical communications systems part 1: variability of water optical parameters”. In: *MILCOM 2005 - 2005 IEEE Military Communications Conference*. IEEE, 2005. DOI: 10.1109/milcom.2005.1605832.

[117] Moore, C. et al. “Optical tools for ocean monitoring and research”. In: *Ocean Science* 5.4 (Dec. 2009), pp. 661–684. DOI: 10.5194/os-5-661-2009.

[118] Capone, A. et al. “Measurements of light transmission in deep sea with the AC9 transmissometer”. In: *Nuclear Instruments and Methods in Physics Research Section A: Accelerators, Spectrometers, Detectors and Associated Equipment* 487.3 (July 2002), pp. 423–434. DOI: 10.1016/s0168-9002(01)02194-5.

[119] Austin, R. W. and Halikas, G. “The index of refraction of seawater”. In: *Scripps Digital Collection* (1976). URL: https://escholarship.org/uc/item/8px2019m (visited on 05/05/2020).

[120] Quan, X. and Fry, E. S. “Empirical equation for the index of refraction of seawater”. In: *Applied Optics* 34.18 (June 1995), pp. 3477–3480. DOI: 10.1364/ao.34.003477.

[121] Korotkova, O., Farwell, N., and Shchepakina, E. “Light scintillation in oceanic turbulence”. In: *Waves in Random and Complex Media* 22.2 (May 2012), pp. 260–266. DOI: 10.1080/17455030.2012.656731.

[122] Elamassie, M. et al. “Effect of eddy diffusivity ratio on underwater optical scintillation index”. In: *Journal of the Optical Society of America* 34.11 (Oct. 2017), pp. 1969–1973. DOI: 10.1364/josaa.34.001969.

[123] Vali, Z. et al. “Experimental study of the turbulence effect on underwater optical wireless communications”. In: *Applied Optics* 57.28 (Sept. 2018), pp. 8314–8319. DOI: 10.1364/ao.57.008314.

[124] Vali, Z. et al. “Modeling turbulence in underwater wireless optical communications based on Monte Carlo simulation”. In: *Journal of the Optical Society of America A* 34.7 (June 2017), pp. 1187–1193. DOI: 10.1364/josaa.34.001187.

[125] Vali, Z. et al. “System parameters effect on the turbulent underwater optical wireless communications link”. In: *Optik* 198.163153 (Dec. 2019). DOI: 10.1016/j.ijleo.2019.163153.

[126] Jamali, M. V. et al. “Statistical studies of fading in underwater wireless optical channels in the presence of air bubble, temperature, and salinity random variations”. In: *IEEE Transactions on Communications* (2018), pp. 1–1. DOI: 10.1109/tcomm.2018.2842212.

[127] Oubei, H. M. et al. “Scintillations of RGB laser beams in weak temperature and salinity-induced oceanic turbulence”. In: *2018 Fourth Underwater Communications and Networking Conference (UComms)*. IEEE, Aug. 2018. DOI: 10.1109/ucomms.2018.8493227.

[128] Oubei, H. M. et al. “Simple statistical channel model for weak temperature-induced turbulence in underwater wireless optical communication systems”. In: *Optics Letters* 42.13 (June 2017), pp. 2455–2458. DOI: 10.1364/ol.42.002455.

[129] Baykal, Y. “Scintillations of LED sources in oceanic turbulence”. In: *Applied Optics* 55.31 (Oct. 2016), pp. 8860–8863. DOI: 10.1364/ao.55.008860.

[130] Tang, S., Zhang, X., and Dong, Y. “Temporal statistics of irradiance in moving turbulent ocean”. In: *2013 MTS/IEEE OCEANS - Bergen*. IEEE, June 2013. DOI: 10.1109/oceans-bergen.2013.6607967.

[131] Weng, Y. et al. "Impact of turbulent-flow-induced scintillation on deep-ocean wireless optical communication". In: *Journal of Lightwave Technology* 37.19 (Oct. 2019), pp. 5083–5090. DOI: 10.1109/jlt.2019.2928465.

[132] Simpson, J. A., Hughes, B. L., and Muth, J. F. "A spatial diversity system to measure optical fading in an underwater communications channel". In: *OCEANS 2009*. IEEE. 2009, pp. 1–6. DOI: 10.23919/OCEANS.2009.5422262.

[133] Oubei, H. M. et al. "Performance evaluation of underwater wireless optical communications links in the presence of different air bubble populations". In: *IEEE Photonics Journal* 9.2 (Apr. 2017), pp. 1–9. DOI: 10.1109/jphot.2017.2682198.

[134] Zedini, E. et al. "A new simple model for underwater wireless optical channels in the presence of air bubbles". In: *GLOBECOM 2017 - 2017 IEEE Global Communications Conference*. IEEE, Dec. 2017. DOI: 10.1109/glocom.2017.8254240.

[135] ASTM G173-03 , Standard Tables for Reference Solar Spectral Irradiances: Direct Normal and Hemispherical on 37 Tilted Surface. ASTM International, 2012. DOI: 10.1520/g0173-03r12.

[136] Farr, N. E. et al. "Non-visible light underwater optical communications". In: *2016 IEEE Third Underwater Communications and Networking Conference (UComms)*. IEEE, Aug. 2016. DOI: 10.1109/ucomms.2016.7583454.

[137] Kedar, D. "Subsea ultraviolet solar-blind broadband free-space optics communication". In: *Optical Engineering* 48.4 (Apr. 2009), p. 046001. DOI: 10.1117/1.3120482.

[138] Campagnaro, F. et al. "Measurement-based simulation of underwater optical networks". In: *OCEANS 2017 - Aberdeen*. IEEE, June 2017. DOI: 10.1109/oceanse.2017.8084671.

[139] Campagnaro, F. et al. "Simulation of multimodal optical and acoustic communications in underwater networks". In: *OCEANS 2015 - Genova*. IEEE, May 2015. DOI: 10.1109/oceans-genova.2015.7271518.

[140] Darecki, M., Stramski, D., and Sokolski, M. "Measurements of high-frequency light fluctuations induced by sea surface waves with an Underwater Porcupine Radiometer System". In: *Journal of Geophysical Research* 116 (Nov. 2011). DOI: 10.1029/2011jc007338.

[141] Hieronymi, M. and Macke, A. "On the influence of wind and waves on underwater irradiance fluctuations". In: *Ocean Science* 8.4 (July 2012), pp. 455–471. DOI: 10.5194/os-8-455-2012.

[142] Gernez, P. and Antoine, D. "Field characterization of wave-induced underwater light field fluctuations". In: *Journal of Geophysical Research* 114.C6 (June 2009). DOI: 10.1029/2008jc005059.

[143] Bartlett, J. S. et al. "Raman scattering by pure water and seawater". In: *Applied Optics* 37.15 (May 1998), pp. 3324–3332. DOI: 10.1364/ao.37.003324.

[144] Rosenkrantz, E. and Arnon, S. "Optimum LED wavelength for underwater optical wireless communication at turbid water". In: *Laser Communication and Propagation through the Atmosphere and Oceans III*. Ed. by Eijk, Alexander M. J. van, Davis, Christopher C., and Hammel, Stephen M. SPIE, Oct. 2014. DOI: 10.1117/12.2062587.

[145] CIE. *1988 2 Deg. Spectral Luminous Efficiency Function For Photoptic Vision*. 1990. ISBN: 978-3-900734-23-7.

[146] Datasheet LCGH9RN. High Flux LED. Osram Opto Semiconductors., 2019. URL: https://www.osram-os.com (visited on 09/24/2021).

[147] Datasheet SFT10. High Power Monochromatic SMD LED. Luminus Devices Inc., 2017. URL: https://www.luminus.com (visited on 03/27/2018).

[148] Chun, H. et al. “Visible light communication using a blue GaN uLED and fluorescent polymer color converter”. In: *IEEE Photonics Technology Letters* 26.20 (Oct. 2014), pp. 2035–2038. DOI: 10.1109/lpt.2014.2345256.

[149] OBrien, D. C. et al. “Visible light communications: challenges and possibilities”. In: *2008 IEEE 19th International Symposium on Personal, Indoor and Mobile Radio Communications*. IEEE, Sept. 2008. DOI: 10.1109/pimrc.2008.4699964.

[150] Datasheet BPW34B. Silicon PIN Photodiode with Enhanced Blue Sensitivity. Ver. 1.7. OSRAM Opto Semiconductors GmbH, 2019. URL: https://www.osram.com (visited on 06/18/2021).

[151] Datasheet PS13-6b. Silicon PIN Photodiode. Rev. 30/01. First Sensor AG, 2018. URL: https://www.first-sensor.com (visited on 10/23/2019).

[152] Datasheet S3590-08. Large area Si PIN Photodiode. Rev. Mar.20. Hamamatsu Photonics KK, 2020. URL: https://www.hamamatsu.com (visited on 10/05/2021).

[153] Datasheet S6967. Si PIN Photodiode. Rev. May 21. Hamamatsu Photonics KK, 2021. URL: https://www.hamamatsu.com (visited on 10/01/2021).

[154] Datasheet C30739ECERH Series. Short Wavelength Enhanced Silicon Avalanche Photodiode. Excelitas Technologies, 2016. URL: https://www.excelitas.com (visited on 10/05/2021).

[155] Witas, K. et al. “Low noise omnidirectional optical receiver for the mobile FSO networks”. In: *Optical Sensors 2013*. Ed. by Baldini, Francesco, Homola, Jiri, and Lieberman, Robert A. SPIE, May 2013. DOI: 10.1117/12.2017086.

[156] Anguita, D., Brizzolara, D., and Parodi, G. “Optical wireless communication for underwater wireless sensor networks: hardware modules and circuits design and implementation”. In: *OCEANS 2010 MTS/IEEE SEATTLE*. IEEE, Sept. 2010. DOI: 10.1109/oceans.2010.5664321.

[157] Farr, N. et al. “Optical modem technology for seafloor observatories”. In: *Proceedings of OCEANS 2005 MTS/IEEE*. IEEE, 2005. DOI: 10.1109/oceans.2005.1639874.

[158] Beshr, M., Michie, C., and Andonovic, I. “Evaluation of visible light communication system performance in the presence of sunlight irradiance”. In: *2015 17th International Conference on Transparent Optical Networks (ICTON)*. IEEE, July 2015. DOI: 10.1109/icton.2015.7193685.

[159] Islim, M. S. et al. “The impact of solar irradiance on visible light communications”. In: *Journal of Lightwave Technology* 36.12 (June 2018), pp. 2376–2386. DOI: 10.1109/jlt.2018.2813396.

[160] Chung, Y. H. and Oh, S. “Efficient optical filtering for outdoor visible light communications in the presence of sunlight or articifical light”. In: *2013 International Symposium on Intelligent Signal Processing and Communication Systems*. IEEE, Nov. 2013. DOI: 10.1109/ispacs.2013.6704649.

[161] Giles, J.W. and Bankman, I.N. “Underwater optical communications systems part 2: basic design considerations”. In: *MILCOM 2005 - 2005 IEEE Military Communications Conference*. IEEE, 2005. DOI: 10.1109/milcom.2005.1605919.

[162] Cossu, G. et al. “Sea-trial of optical ethernet modems for underwater wireless communications”. In: *Journal of Lightwave Technology* 36.23 (Dec. 2018), pp. 5371–5380. DOI: 10.1109/jlt.2018.2871088.

[163] Cossu, G. et al. “Full-fledged 10Base-T ethernet underwater optical wireless communication system”. In: *IEEE Journal on Selected Areas in Communications* 36.1 (Jan. 2018), pp. 194–202. DOI: 10.1109/jsac.2017.2774702.

[164] Ge, P. et al. "Optical filter designs for multi-color visible light communication". In: *IEEE Transactions on Communications* 67.3 (Mar. 2019), pp. 2173–2187. DOI: 10.1109/tcomm.2018.2883422.

[165] Mahapatra, S. K. and Varshney, S. K. "Theoretical study on the effectiveness of optical filters to suppress orientation-based solar light noise". In: *Applied Optics* 60.27 (Sept. 2021), pp. 8600–8608. DOI: 10.1364/ao.438164.

[166] Forkel, G. J. M., Krohn, A., and Hoeher, P. A. "Optical interference suppression based on LCD-filtering". In: *Applied Sciences* 9.15 (Aug. 2019), p. 3134. DOI: 10.3390/app9153134.

[167] Krohn, A. et al. "LCD-based optical filtering suitable for non-imaging channel decorrelation in VLC applications". In: *Journal of Lightwave Technology* 37.23 (Dec. 2019), pp. 5892–5898. DOI: 10.1109/jlt.2019.2941734.

[168] Krohn, A. et al. "Impact of liquid crystal based interference mitigation and precoding on the multiuser performance of VLC massive MIMO arrays". In: *IEEE Photonics Journal* 14.5 (Oct. 2022), pp. 1–12. DOI: 10.1109/jphot.2022.3199614.

[169] Reifegerste, F. and Lienig, J. "Modelling of the temperature and current dependence of LED spectra". In: *Journal of Light & Visual Environment* 32.3 (2008), pp. 288–294. DOI: 10.2150/jlve.32.288.

[170] Datasheet Hoya B-440. Color filter glass. Hoya Corpotation Optics Section, 2020. URL: https://www.hoyaoptics.com (visited on 11/12/2021).

[171] Macleod, H. A. *Thin-Film Optical Filters*. 4th ed. CRC Press Taylor and Francis, 2010, pp. 1–772. ISBN: 978-1-4200-7302-7.

[172] General filter information. Semrock Idex Corporation. URL: https://semrock.com/ (visited on 02/15/2022).

[173] Technical Data Thorlabs FB450-10. Bandpass filter. Thorlabs Inc., 2021. URL: https://www.thorlabs.com (visited on 11/12/2021).

[174] Technical Data Thorlabs FB450-40. Bandpass filter. Thorlabs Inc., 2021. URL: https://www.thorlabs.com (visited on 11/12/2021).

[175] Datasheet Semrock 457-50. Single-band bandpass filter. Semrock Idex Corporation, 2021. URL: https://www.semrock.com (visited on 11/12/2021).

[176] Menna, F. et al. "Geometric and optic characterization of a hemispherical dome port for underwater photogrammetry". In: *Sensors* 16.1 (48 Jan. 2016), pp. 1–21. DOI: 10.3390/s16010048.

[177] Graeme, J. *Photodiode Amplifiers: Op Amp Solutions*. McGraw-Hill, Inc., 1995. ISBN: 978-0-07-024247-0.

[178] Transimpedance Circuit Output Noise-Voltage Calculator. JavaScience. URL: https://www.jensign.com/noise/noisecalculator.html (visited on 08/16/2021).

[179] Anguita, D. et al. "Optical wireless underwater communication for AUV Preliminary simulation and experimental results". In: *OCEANS 2011 IEEE - Spain*. IEEE, June 2011. DOI: 10.1109/oceans-spain.2011.6003598.

[180] Xu, F., Khalighi, M. A., and Bourennane, S. "Impact of different noise sources on the performance of PIN- and APD-based FSO receivers". In: *Proceedings of the 11th International Conference on Telecommunications*. IEEE. 2011, pp. 211–218. ISBN: 978-3-85125-161-6.

[181] Mims, F. M. *LED Circuits and Projects*. New York, NY, USA: H. W. Sams, 1973. ISBN: 978-0672210068.

[182] Miyazaki, E., Itami, S., and Araki, T. “Using a light-emitting diode as a high-speed, wavelength selective photodetector”. In: *Review of Scientific Instruments* 69.11 (Nov. 1998), pp. 3751–3754. DOI: 10.1063/1.1149174.

[183] Mims, F. M. “Sun photometer with light-emitting diodes as spectrally selective detectors”. In: *Applied Optics* 31.33 (Nov. 1992), p. 6965. DOI: 10.1364/ao.31.006965.

[184] Dietz, P., Yerazunis, W., and Leigh, D. “Very low-cost sensing and communication using bidirectional LEDs”. In: *UbiComp 2003: Ubiquitous Computing*. Springer Berlin Heidelberg, 2003, pp. 175–191. DOI: 10.1007/978-3-540-39653-6_14.

[185] Hudson, S. E. “Using light emitting diode arrays as touch-sensitive input and output devices”. In: *Proceedings of the 17th annual ACM symposium on User interface software and technology - UIST04*. ACM Press, 2004. DOI: 10.1145/1029632.1029681.

[186] Shepherd, R.L. et al. “Low-cost surface-mount LED gas sensor”. In: *IEEE Sensors Journal* 6.4 (Aug. 2006), pp. 861–866. DOI: 10.1109/jsen.2006.877849.

[187] Ben-Ezra, M. et al. “An LED-only BRDF measurement device”. In: *2008 IEEE Conference on Computer Vision and Pattern Recognition*. IEEE, June 2008. DOI: 10.1109/cvpr.2008.4587766.

[188] Corbellini, G. et al. “Connecting networks of toys and smartphones with visible light communication”. In: *IEEE Communications Magazine* 52.7 (July 2014), pp. 72–78. DOI: 10.1109/mcom.2014.6852086.

[189] Chun, H. et al. “Demonstration of a bi-directional visible light communication with an overall sum-rate of 110 Mb/s using LEDs as emitter and detector”. In: *2014 IEEE Photonics Conference*. IEEE, Dec. 2014. DOI: 10.1109/ipcon.2014.6995247.

[190] Stepniak, G. et al. “Transmission beyond 100 Mbit/s using LED both as a transmitter and receiver”. In: *IEEE Photonics Technology Letters* 27.19 (Oct. 2015), pp. 2067–2070. DOI: 10.1109/lpt.2015.2451006.

[191] Milovancev, D. et al. “Gb/s visible light communication with low-cost receiver based on single-color LED”. In: *Journal of Lightwave Technology* 38.12 (June 2020), pp. 3305–3314. DOI: 10.1109/jlt.2020.2994974.

[192] Li, S., Pandharipande, A., and Willems, F. M. J. “Two-way visible light communication and illumination with LEDs”. In: *IEEE Transactions on Communications* 65.2 (Feb. 2017), pp. 740–750. DOI: 10.1109/tcomm.2016.2626362.

[193] Kowalczyk, M. and Siuzdak, J. “Photo-reception properties of common LEDs”. In: *Opto-Electronics Review* 25.3 (Sept. 2017), pp. 222–228. DOI: 10.1016/j.opelre.2017.06.009.

[194] Datasheet Osram Golden Dragon. W5SM Series. OSRAM Opto Semiconductors GmbH, 2019. URL: https://www.osram-os.com (visited on 06/12/2020).

[195] Datasheet SFH2400. Silicon PIN Photodiode with Enhanced Blue Sensitivity. Ver. 1.7. OSRAM Opto Semiconductors GmbH, 2019. URL: https://www.osram.com (visited on 06/18/2021).

[196] Orwiler, B. *Vertical Amplifier Circuits*. Beaverton, OR, USA: Tektronix Inc., 1969.

[197] She, M. et al. “Refractive geometry for underwater domes”. In: *ISPRS Journal of Photogrammetry and Remote Sensing* 183 (Jan. 2022), pp. 525–540. DOI: 10.1016/j.isprsjprs.2021.11.006.

[198] Bielawny, A. “Reflectors in lightning design”. In: *Advanced Optical Technologies* 8.6 (2019), pp. 469–481. DOI: 10.1515/aot-2018-0052.

[199] Janecek, M. “Reflectivity spectra for commonly used reflectors”. In: *IEEE Transactions on Nuclear Science* 59.3 (June 2012), pp. 490–497. DOI: 10.1109/tns.2012.2183385.

[200] Moreno, I. and Sun, C. C. "Modeling the radiation pattern of LEDs". In: *Optics Express* 16.3 (2008), pp. 1808–1819. DOI: 10.1364/oe.16.001808.

[201] Rachev, I. et al. "Improvement of the approximation accuracy of LED radiation patterns". In: *Electronics* 8.3 (Mar. 2019), pp. 1–9. DOI: 10.3390/electronics8030337.

[202] Moreno, I. and Sun, C. C. "LED array: where does far-field begin?" In: *Eighth International Conference on Solid State Lighting*. Ed. by Ferguson, Ian T. et al. SPIE, Aug. 2008. DOI: 10.1117/12.795944.

[203] Moreno, I., Sun, C. C., and Ivanov, R. "Far-field condition for light-emitting diode arrays". In: *Applied Optics* 48.6 (Feb. 2009), pp. 1190–1197. DOI: 10.1364/ao.48.001190.

[204] Sun, C. C. et al. "Analysis of the far-field region of LEDs". In: *Optics Express* 17.16 (July 2009), pp. 13918–13927. DOI: 10.1364/OE.17.013918.

[205] Donati, S., Martini, G., and Randone, E. "Improving photodetector performance by means of microoptics concentrators". In: *Journal of Lightwave Technology* 29.5 (Mar. 2011), pp. 661–665. DOI: 10.1109/jlt.2010.2103302.

[206] Dong, F. et al. "Monte Carlo-based impulse response modeling for underwater wireless optical communication". In: *Progress In Electromagnetics Research M* 54 (2017), pp. 137–144. DOI: 10.2528/pierm16112403.

[207] Manousiadis, P. P. et al. "Optical antennas for wavelength division multiplexing in visible light communications beyond the Étendue limit". In: *Advanced Optical Materials* 8.4 (Dec. 2019), p. 1901139. DOI: 10.1002/adom.201901139.

[208] Baiden, G., Bissiri, Y., and Masoti, A. "Paving the way for a future underwater omnidirectional wireless optical communication systems". In: *Ocean Engineering* 36.9-10 (July 2009), pp. 633–640. DOI: 10.1016/j.oceaneng.2009.03.007.

[209] Witas, K. and Nedoma, J. "Free space optic receiver with strongly overlapped photodetectors field of view". In: *Applied Sciences* 9.2 (Jan. 2019), pp. 343–355. DOI: 10.3390/app9020343.

[210] Han, B. et al. "Experimental demonstration of quasi-omni-directional transmitter for underwater wireless optical communication based on blue LED array and freeform lens". In: *Optics Communications* 434 (Mar. 2019), pp. 184–190. DOI: 10.1016/j.optcom.2018.10.037.

[211] Illi, E., Bouanani, F. E., and Ayoub, F. "A high accuracy solver for RTE in underwater optical communication path loss prediction". In: *2018 International Conference on Advanced Communication Technologies and Networking (CommNet)*. IEEE, Apr. 2018. DOI: 10.1109/commnet.2018.8360253.

[212] Wang, L., Jacques, S. L., and Zheng, L. "MCML—Monte Carlo modeling of light transport in multi-layered tissues". In: *Computer Methods and Programs in Biomedicine* 47.2 (July 1995), pp. 131–146. DOI: 10.1016/0169-2607(95)01640-f.

[213] Prahl, S. A. "A Monte Carlo model of light propagation in tissue". In: *Dosimetry of Laser Radiation in Medicine and Biology*. Ed. by Mueller, Gerhard J., Sliney, David H., and Potter, Roy F. SPIE, Jan. 1989. DOI: 10.1117/12.2283590.

[214] PyTissueOptics. DCC-Lab. URL: https://github.com/DCC-Lab/PyTissueOptics (visited on 10/25/2022).

[215] Bürmen, Miran, Pernuš, Franjo, and Naglič, Peter. "MCDataset: a public reference dataset of Monte Carlo simulated quantities for multilayered and voxelated tissues computed by massively parallel PyXOpto Python package". In: *Journal of Biomedical Optics* 27.08 (Apr. 2022). DOI: 10.1117/1.jbo.27.8.083012.

[216] Cox, W. C. *Simulation, Modeling, and Design of Underwater Optical Communication Systems*. North Carolina State University, 2012.

[217] DeMul, F. F. M. "Monte Carlo simulations of light scattering in turbid media". In: *Handbook of Coherent-Domain Optical Methods*. Springer New York, Nov. 2013, pp. 593–661. DOI: 10.1007/978-1-4614-5176-1_15.

[218] Leathers, R. A. et al. *Monte Carlo radiative transfer simulations for ocean optics: a practical guide*. Tech. rep. NRL/MR/5660-04-8819. Naval Research Lab Washington DC Applied Optics Branch, 2004, pp. 1–50.

[219] Gabriel, C. et al. "Monte Carlo-based channel characterization for underwater optical communication systems". In: *Journal of optical Communications and Networking* 5.1 (Dec. 2013), pp. 1–12. DOI: 10.1364/jocn.5.000001.

[220] Qadar, R. et al. "Monte Carlo-based channel estimation and performance evaluation for UWOC links under geometric losses". In: *International Journal of Communication Systems* 31.6 (Feb. 2018), pp. 1–18. DOI: 10.1002/dac.3527.

[221] Chen, P. et al. "Semi-analytic Monte Carlo model for oceanographic lidar systems: lookup table method used for randomly choosing scattering angles". In: *Applied Sciences* 9.1 (Dec. 2019), pp. 1–13. DOI: 10.3390/app9010048.

[222] Cochenour, B. and Mullen, L. *Advanced Optical Wireless Communication Systems*. Ed. by Arnon, S. et al. Cambridge University Press, 2012. Chap. Free space optical communications underwater. ISBN: 978-0521197878.

[223] Jasman, F., Green, R. J., and Leeson, M. S. "Impact of receiver field of view on underwater optical wireless communications". In: *Microwave and Optical Technology Letters* 59.4 (Feb. 2017), pp. 837–840. DOI: 10.1002/mop.30410.

[224] Vali, Z. et al. "Receiver parameters effect on underwater optical wireless communication performance in the presence of transmitted gaussian beam". In: *2018 11th International Symposium on Communication Systems, Networks & Digital Signal Processing (CSNDSP)*. IEEE, July 2018. DOI: 10.1109/csndsp.2018.8471803.

[225] Tang, S., Zhang, X., and Dong, Y. "On impulse response for underwater wireless optical links". In: *2013 MTS/IEEE OCEANS - Bergen*. IEEE, June 2013. DOI: 10.1109/oceans-bergen.2013.6607980.

[226] Roettgers, R., McKee, D., and Wozniak, S. B. "Evaluation of scatter corrections for ac-9 absorption measurements in coastal waters". In: *Methods in Oceanography* 7 (Sept. 2013), pp. 21–39. DOI: 10.1016/j.mio.2013.11.001.

[227] Krohn, A., Pachnicke, S., and Hoeher, P. A. "Genetic Optimization of Liquid Crystal Matrix Based Interference Suppression for VLC MIMO Transmissions". In: *IEEE Photonics Journal* 14.1 (Feb. 2022), pp. 1–5. DOI: 10.1109/jphot.2021.3126211.

[228] Harlakin, A., Krohn, A., and Hoeher, P. A. "Liquid Crystal Display Based Angle-of-Arrival Estimation of a Single Light Source". In: *IEEE Photonics Journal* 14.3 (June 2022), pp. 1–12. DOI: 10.1109/jphot.2022.3172511.

[229] Harlakin, A. et al. "Compressive Sensing based Angle-of-Arrival Estimation of a Single Light Source using a Liquid Crystal Display". In: *WSA & SCC 2023; 26th International ITG Workshop on Smart Antennas and 13th Conference on Systems, Communications, and Coding*. 2023, pp. 161–166. ISBN: 978-3-8007-6050-3.

[230] Hott, M., Harlakin, A., and Hoeher, P. A. "Hybrid Communication and Localization Underwater Network Nodes based on Magnetic Induction and Visible Light for AUV Support". In: *2020 International Conference on Information and Communication Technology Convergence (ICTC)*. IEEE, Oct. 2020, pp. 66–68. DOI: 10.1109/ictc49870.2020.9289328.

[231] Zurmuehl, R. *Praktische Mathematik f. Ingenieure und Physiker*. Springer, 1984. ISBN: 3-540-03435-8.

Author's Publications and Patents

[P1] Kwasnitschka, T., Köser, K., Sticklus, J., Rothenbeck, M., Weiß, T., Wenzlaff, E., Schoening, T., Triebe, L., Steinführer, A., Devey, C., and Greinert, J. "DeepSurveyCam - A deep ocean optical mapping system". In: *Sensors* 16.2 (Jan. 2016), p. 164. DOI: 10.3390/s16020164.

Abstract: Underwater photogrammetry and in particular systematic visual surveys of the deep sea are by far less developed than similar techniques on land or in space. The main challenges are the rough conditions with extremely high pressure, the accessibility of target areas (container and ship deployment of robust sensors, then diving for hours to the ocean floor), and the limitations of localization technologies (no GPS). The absence of natural light complicates energy budget considerations for deep diving flash-equipped drones. Refraction effects influence geometric image formation considerations with respect to field of view and focus, while attenuation and scattering degrade the radiometric image quality and limit the effective visibility. As an improvement on the stated issues, we present an AUV-based optical system intended for autonomous visual mapping of large areas of the seafloor (square kilometers) in up to 6000 m water depth. We compare it to existing systems and discuss tradeoffs such as resolution vs. mapped area and show results from a recent deployment with 90,000 mapped square meters of deep ocean floor.

[P2] Sticklus, J., Hieronymi, M., and Hoeher, P. A. "Effects and constraints of optical filtering on ambient light suppression in LED-based underwater communications". In: *Sensors* 18.3710 (Oct. 2018), pp. 1–21. DOI: 10.3390/s18113710.

Abstract: Optical communication promises to be a high-rate supplement for acoustic communication in short-range underwater applications. In the photic zone of oceanic and coastal waters, underwater optical communication systems are exposed by remaining sunlight. This ambient light generates additional noise in photodetectors, thus degrading system performance. This effect can be diminished by the use of optical filters. This paper investigates light field characteristics of different water types and potential interactions with optical underwater communication. A colored glass and different thin film bandpass filters are examined as filter/detector combinations under varying light and water conditions, and their physical constraints are depicted. This is underlined by various spectral measurements as well as optical signal-to-noise ratio calculations. The importance of matching the characteristics of the light emitting diode (LED) light source, the photodetector, and the filter on the ambient conditions using wider angle of incidents is emphasized.

[P3] Liu, H., Sticklus, J., Köser, K., Hoving, H. J. T., Song, H., Chen, Y., Greinert, J., and Schoening, T. "TuLUMIS - a tunable LED-based underwater multispectral imaging system". In: *Optics Express* 26.6 (Mar. 2018), p. 7811. DOI: 10.1364/oe.26.007811.

Abstract: Multispectral imaging (MSI) is widely used in terrestrial applications to help increase the discriminability between objects of interest. While MSI has shown potential for underwater geological and biological surveys, it is thus far rarely applied underwater. This is primarily due to the that fact light propagation in water is subject to wavelength dependent attenuation and tough working conditions in the deep ocean. In this paper, a novel underwater MSI system based on a tunable light source is presented which employs a monochrome still image camera with flashing, pressure neutral color LEDs. Laboratory experiments and field tests were performed. Results from the lab experiments show an improvement of 76.66 percent on discriminating colors on a checkerboard by using the

proposed imaging system over the use of an RGB camera. The field tests provided in situ MSI observations of pelagic fauna, and showed the first evidence that the system is capable of acquiring useful imagery under real marine conditions.

[P4] Sticklus, J., Hoeher, P. A., and Roettgers, R. "Optical underwater communication: the potential of using converted green LEDs in coastal waters". In: *IEEE Journal of Oceanic Engineering* 44.2 (Apr. 2019), pp. 535–547. DOI: 10.1109/joe.2018.2816838.
Abstract: Compared to the open ocean where blue light-emitting diodes (LEDs) perform well for data communications, in coastal and harbor environments optical transmission becomes worse and the color of lowest attenuation shifts to green. Another problem concerns the "green–yellow gap" of LEDs, as the quantum efficiency of current commercially available green LEDs is poor. Since energy consumption is an important factor, particularly for battery-powered systems, using blue LEDs is a tradeoff. Recently, phosphor-converted green LEDs, which are pumped by highly efficient blue LEDs, have been introduced to the market, and this type of LED promises better performance. This paper compares the use of blue, green, and converted green LEDs for applications in optical underwater communication systems in coastal waters. Theoretical aspects of the overall LED-water-detector channel are presented. A method for determining individual system coefficients is developed, and the impact on the communication system performance is explained. Practical approaches are introduced, complemented by measurements in the Baltic Sea.

[P5] Sticklus, J., Kwasnitschka, T., and Hoeher, P. A. "Method and device for potting an LED luminaire potted in a potting compound and LED luminaire". European Patent EP3233414. Jan. 8, 2020.
Abstract: The invention relates to an LED luminaire potting method having the following steps: introducing a configured luminaire to be potted with an optically transparent potting compound into an at least partly optically transparent potting mold. The potting mold is arranged in a vacuum chamber, and the luminaire is fixed in the potting mold such that the luminaire does not come into contact with the walls of the potting mold; introducing an optically transparent potting compound into the potting mold until at least the luminaire is surrounded; and detecting a quantity of bubbles and the quality of the bubble prevention of the optically transparent potting compound by means of an optical sensor or image detector, wherein the pressure in the vacuum chamber is controlled in order to influence the bubbles and/or a pivot/inclination device is controlled in order to move the vacuum chamber and -or the potting mold in order to expel detected gas/air bubbles out of the optically transparent potting compound. The invention further relates to an LED luminaire and a method for producing a potted LED luminaire.

[P6] Sticklus, J., Hoeher, P. A., and Hieronymi, M. "Experimental characterization of single-color power LEDs used as photodetectors". In: *Sensors* 20.5200 (Sept. 2020), pp. 1–13. DOI: 10.3390/s20185200.
Abstract: Semiconductor-based light emitting diodes can be used for photon emission as well as for detection of photons. In this paper, we present a fair comparison between off-the-shelf power light emitting diodes (LEDs) and a silicon photodetector with respect to their spectral, temporal, and spatial properties. The examined LED series features unexpected good sensitivity and distinct optical bandpass characteristic suitable for daylight filtering or color selectivity. Primary application is short range optical underwater communication, but results are generally applicable.

[P7] Song, Y., Sticklus, J., Nakath, D., Wenzlaff, E., Koch, R., and Köser, K. "Optimization of multi-LED setups for underwater robotic vision systems". In: *Pattern Recognition. ICPR International Workshops and Challenges*. Springer International Publishing, Feb. 2021, pp. 390–397. DOI: 10.1007/978-3-030-68790-8_30.

Abstract: In deep water conditions, vision systems mounted on underwater robotic platforms require artificial light sources to illuminate the scene. The particular lighting configurations significantly influence the quality of the captured underwater images and can make their analysis much harder or easier. Nowadays, classical monolithic Xenon flashes are gradually being replaced by more flexible setups of multiple powerful LEDs. However, this raises the question of how to arrange these light sources, given different types of seawater and depending on different flying altitudes of the capture platforms. Hence, this paper presents a rendering based coarse-to-fine approach to optimize recent multilight setups for underwater vehicles. It uses physical underwater light transport models and target ocean and mission parameters to simulate the underwater images as would be observed by a camera system with particular lighting setups. This paper proposes to systematically vary certain design parameters such as each LED's orientation and analyses the rendered image properties (such as illuminated image area and light uniformity) to find optimal light configurations. We report first results on a real, ongoing AUV light design process for deep sea mission conditions.

[P8] Hoeher, P. A., Sticklus, J., and Harlakin, A. "Underwater optical wireless communications in swarm robotics: a tutorial". In: *IEEE Communications Surveys & Tutorials* (2021), pp. 1–30. DOI: 10.1109/comst.2021.3111984.

Abstract: Underwater swarm robotics is an emerging topic. Compared to individual autonomous vehicles, high-capacity communication links are required between the mobile agents. In this tutorial, suitable communication technologies are studied, with emphasis on LED-based underwater optical wireless communications. A comprehensive overview about challenges, advances, and practical aspects of underwater swarm robotics employing optical wireless communications is provided. The tutorial includes the following topics: (1) Channel modeling fundamentals; (2) Physical layer transmission techniques for underwater optical wireless communications; (3) Data link layer aspects and hybrid transmission schemes; (4) Ambient light and interference suppression; and (5) Realization aspects. Finally, suggestions regarding future work are given. The tutorial is intended for readers with a background or interest in electrical and information engineering.